République Algérienne Démocratiques et Populaire

Ministère de l'Enseignement Supérieur et de la Recherche Scientifique

Université Kasdi Merbah Ouargla

Faculté des Mathématiques et Sciences de La Matière

Thèse

Présentée pour l'obtention du diplôme de

DOCTORAT

Domaine : Sciences de la Matière

Filière : Chimie

Spécialité : Chimie Analytique

Evaluation de l'activité antioxydante et étude *in vitro* et *in silico* de l'interaction de quelques N-(ferrocènylméthyl)anilines avec l'hémoglobine et l'albumine de sérum

Soutenu le

Présentée Par : KHENNOUFA Ali

Devant le jury :

SAIDI Mokhtar,	Professeur,	Université de Ouargla,	présidant
BECHKI Lazhar,	Professeur,	Université de Ouargla,	Rapporteur
LANEZ Touhami,	Professeur,	Université de El Oued,	Co-Rapporteur
YOUSFI Mohammed	Professeur,	Université de Laghouat,	examinateur
SALHI Nesrine	Professeur,	Université de Ouargla,	examinatrice
DERRADJI Hadef	M.C.A,	Université de Ouargla,	examinateur
LANEZ Elhafnaoui	M.C.B,	Université de El Oued,	invité

People's Democratic Republic of Algeria

Ministry of Higher Education and Research Scientist

University Kasdi Merbah Ouargla

Faculty of Mathematics and Science of Matter

Thesis

Presented For Graduation From

Doctorate

Domain: Sciences of Matter

Branch : Chemistry

Specialty: Analytical chemistry

Thesis subject:

Evaluation of the antioxidant activity and *in vitro* and *in silico* study of the interaction of some N-(ferrocenylmethyl)anilines with hemoglobin and serum albumin

Graduated

Presented by KHENNOUFA Ali

In front of the jury

Mokhtar SAIDI,	Professor,	University of Ouargla,	President
Lazhar BECHKI,	Professor,	University of Ouargla,	Raporter
Touhami LANEZ,	Professor,	University of El Oued,	Co-Raporter
Mohammed YOUSFI	Professor,	University of Laghouat,	Examiner
Nesrine SALHI	Professor,	University of Ouargla,	Examiner
Hadef DERRADJI	M.C.A,	University of Ouargla,	Examiner
Elhafnaoui LANEZ	M.C.B,	University of El Oued,	invite

الاهداء

إلى من أنارت حياتي، وكانت بحرا صافيا يجري بفيض الحب، وبسمة الشفاء إلى من منحتني القوة والعزيمة لمواصلة الدرب **أمي الحبيبة**

إلى سندي و مسندي واتكائي قوتي و ضلعي الثابت الذي لا يميل، إلى من علمني الصبر والصمود وكان عوني بعد الله **أبي الغالي**

لكل العائلة الكريمة التي ساندتني ولاتزال من أخوة و أخوات ليزا .. صبري.. مديحة .. هالة .. آمنة .. كمال .. إيهاب .. هنادي .. يوسف

إلى رفقاء الدرب: عبد الرؤوف، العيد ،لخضر ،يوسف ،محمد ...

الى كل أصدقاء المخبر: الحفناوي، مسعود، رابح، حسن، عبد اللطيف، نجيبة ...

الى كل اصدقائي في العمل نجيب، سعيد، بشير، كمال، عماد ...

الى من شجعني و كان حافزا لي مديري الشيخ صالحي لزهاري

الى كل من نساهم قلمي وسقطو مني سهوا

خنوفة علي

شكر و عرفان

الحمد لله حمدا كثيرا طيبا مباركا فيه ونصلي ونسلم على المبعوث رحمة للعالمين معلم البشرية سيدنا محمد صلى الله عليه و سلموا على آله و صحبه أجمعين ومن تبعهم بإحسان إلى يوم الدين أما بعد:

الحمد و الشكر لله سبحانه وتعالى الذي منحنا نعمة الصحة والعافية والصبر لاستكمال هذا العمل أما بعد:.

أتقدم بجزيل الشكر والامتنان في المقام الأول إلى أستاذي المحترمين المشرفين على انجاز هذا العمل

"العانز التوهامي " واللذان لم يبخل علي بنصائحمها القيمة النابعة من تجربهما في "بشكي لزهر " أستاذي البحث العلمي و متابعهما لمراحل إنجاز هذا البحث و صبرهما الطويل فلكما مني ميدان الفاضلين أزكى عبارات الشكر و التقدير .

كما أشكر أعضاء لجنة المناقشة لقبولهم مناقشة هذا العمل بداية برئيسها الأستاذ ..... وكذلك المناقشين الأستاذ..... و الأستاذ

كما أتقدم بالشكر الجزيل إلى كافة عائلة مخبر تثمين وترقية الموارد الصحراوية و على رأسهم السيد النيرة "علي طليبة" و الدكتورة "عائشة عدائكة" و السيد "صادق الناني" على المجهودات لمساعدتي في إتمام هذا العمل المتواضع

خنوفة علي

ABSTRACT

In the present work, we describe the synthesis, characterization, and antioxidant activity of a series of N-ferrocenylmethylnitro- and cyanoanilines and their N-acylated derivatives. We also studied their interaction with bovine serum albumin (BSA) and hemoglobin (HHb) using electronic spectroscopy and cyclic voltametry techniques. Results from spectroscopic and cyclic voltammetry measurements indicated the establishments of physical interactions between the synthesized compounds and BSA through electrostatic and hydrogen bonds. Calculated binding free energy confirms these types of electrostatic interactions and further confirms the spontaneous character of the interactions. The obtained results were validated by molecular docking analysis which further allowed the visualisation of the interactions between the nearby residues of the binding sites of the BAS and the studied compounds. Cyclic voltammetry was additionly used to evaluate the antioxidant activity of the acylated derivatives. All investigated compounds showed promising scavenging activity against superoxide anion radicals.

Key words: BSA, HHb, cyclic voltammetry, uv-visible, molecular docking, antioxidant activity, ferrocene derivative

ملخص

في العمل الحالي ، قمنا باصطناع والتوصيف ودراسة النشاط المضاد للأكسدة لـ سلسلة من cyanoaniline و N-ferrocenyl methylnitro ومشتقاته N-آسيلات درسنا أيضًا تفاعلهم مع ألبومين مصل الأبقار (BSA) والهيموغلوبين (HHb) باستخدام تقنية مطيافية الأشعة فوق البنفسجية و المرئية وتقنيات قياس الفولتميتري الحلقي أشارت نتائج القياسات الطيفية وقياسات الفولتميترية الحلقية إلى وجود تفاعلات فيزيائية بين المركبات و BSA من خلال الروابط الكهروستاتيكية والهيدروجينية.

تؤكد الطاقة الربط المحررة المحسوبة لهذه نوع من أنواع التفاعلات انها ذات طابع كهروستاتيكية وتؤكد كذلك عفوية التفاعل. تم التحقق من صحة النتائج التي تم الحصول عليها عن طريق تحليل الالتحام الجزيئي . مما سمح أيضًا بتصور التفاعلات بين الجذور القريبة لمواقع الفعالة لـHHb ولـBSA والمركبات المدروسة .تم استخدام مقياس الفولتميتري الحلقي لتقييم النشاط المضاد للأكسدة للمشتقات .أظهرت جميع المركبات التي تم فحصها نشاطًا واعدًا في تثبيط الجذور الحرة $O_2^{-\cdot}$.

الكلمات المفتاحية: BSA، HHb ، الفولتمتري الحلقي ، الأشعة فوق البنفسجية المرئية ، الالتحام الجزيئي ، النشاط المضاد للأكسدة ، مشتق الفيروسين.

TABLE OF CONTENTS

LIST OF ABBREVIATIONS

Name	abbreviations
Ferrocene	Fc
Derivatives before acylation	FcDB
Derivatives after acylation	FcDA
N-ferrocenylmethylaniline	FMA
N-(ferrocenylmethyl)-2-nitroaniline	FM2N
N-(ferrocenylmethyl)-3-nitroaniline	FM3N
N-(ferrocenylmethyl)-4-nitroaniline	FM4N
2-(ferrocenylmethylamino)benzonitrile	FM2C
3-(ferrocenylmethylamino)benzonitrile	FM3C
4-(ferrocenylmethylamino)benzonitrile	FM4C
N-ferrocenylmethyl -N-phenylbenzamide	FMAA
N-ferrocenylmethyl-3-nitro-N-(4-nitrophenyl)benzamide	FM3NA
N-ferrocenylméthyl-4-nitro-N-(4-nitrophenyl)benzamide	FM4NA
N-ferrocenylmethyl-N-(3-cyanophenyl)-4-nitrobenzamide	FM3CA
N-ferrocenylmethyl-N-(4-cyanophenyl)-4-nitrobenzamide	FM4CA
Bovine serum albumin	BSA
human hemoglobin	HHb
dichloromethane	DCM
Phosphate-Buffered Saline (KH_2PO_4/K_2HPO_4)	PBS
N,N-Dimethylformamide	DMF
tetra-N-butylammonium tetrafluoroborate	TBFP
Cyclic voltammetry	CV
Anodic peak potential	E_{pa}
Cathodic peak potential	E_{pc}
Anodic peak current	I_{pa}
Cathodic peak current	I_{pc}
Free Gibbs energy change	ΔG
Glassy carbon electrode	GC
Ultraviolet	UV
Infrared	IR
Nuclear magnetic resonance	NMR
Binding constant	K_b
Density functional theory	DFT
diffusion coefficient	D
Half-maximal inhibitory concentration	IC_{50}

LIST OF FIGURES

LIST OF TABLES

General introduction

The interaction of drugs with bio-macromolecules has gotten a lot of interest [1–3]. In terms of structure and biological properties, serum albumin is one of the most studied bio-macromolecule [4]. Furthermore, serum albumin contributes significantly to colloid osmotic blood pressure and aids in the transportation, distribution and metabolism of a variety of exogenous and endogenous compounds that can bind to albumins , such as drugs [5]. The drug-albumin complex can also be used as a model for the study of drug-protein interactions which are important in pharmacy, pharmacology, and biochemistry [6–8]. the study can also aid in the explanation of the relationship between protein structures and functions [9–11].

One the families of organometallic chemicals being studied for their applications is ferrocene and its N-derivatives that have attracted the interest of researchers as antioxidant [12], anticancer[13], antibacterial[14], antimalarial[15] drug candidates. They are also an excellent ligand for investigation using experimental methods due to its stability, aromaticity, low toxicity, lipophilicity, and redox activity.

Various analytical techniques have been employed in prior research to investigate interactions [16–18], but these methods often have drawbacks related to the expense of the instrumentation, complexity of the analyses, reagent availability, and characterization of small molecule-protein interactions. To address these limitations, UV-vis spectroscopy and electrochemical methods were utilized to study drug-protein interactions between BSA and drugs due to their direct monitoring capability, high sensitivity, and simplicity[14-19].

Our research focuses on the study of the interaction between N-ferrocenylmethylnitro- and cyanoanilines and their N-acylated derivatives, as ligand, and BSA through finding the binding constant (Kb) and free binding energy change (ΔG) of the ligand-BSA. The obtained results are expected to assist in the understanding of the ligand-biomolecule interaction at the molecular level, as well as in the design of new drugs that bind selectively to predetermined sequences. To validate the obtained experimental results and further visualize the type of interactions, we used molecular modelling. Our goals were to gather evidence of interaction in terms of binding parameters, probing the binding site, binding modes and intermolecular binding distance.

In this doctorate thesis, we studied the interaction of Hb and BSA with twelve (12) ferrocene derivatives synthesized in the Saharan resource valorisation and technology laboratory (VTRS), namely: N-ferrocenylmethylaniline, N-ferrocenylmethyl-2-nitro-aniline, N-ferrocenylmethyl-3-nitro-

aniline, N-ferrocenylmethyl-4-nitro-aniline, 2-(ferrocenylmethylamino)benzonitrile, 3-(ferrocenylmethyl-amino)benzonitrile, 4-(ferrocenylmethylamino)benzonitrile and their acylated forms N-ferrocenylmethyl-N-phenylbenzamide, N-ferrocenylmethyl-3-nitro-N-(4 nitrophenyl)benzamide, N-ferrocenylméthyl-4-nitro-N-(4-nitrophenyl)benzamide, N-ferrocenylmethyl-N-(3-cyano-phenyl)-4-nitrobenzamide, N-ferrocenylmethyl-N-(4-cyanophenyl)-4-nitrobenzamide. We used NMR analyses, UV/VIS spectroscopy, IR spectroscopy and cyclic voltammetry experiments to characterize the newly obtained compounds. Furthermore, cyclic voltammetry and UV/VIS spectroscopy techniques were used to investigate the products BSA and Hb binding properties which were followed by DFT calculations and molecular docking studies.

The study comprises six chapters, which constitute its overall structure.

- Chapter 1: bibliographical overview of ferrocene and ferrocene derivatives, Hb, and BSA
- Chapter 2: theoretical context of the experimental techniques used to characterize the interaction
- Chapter 3: procedures of the synthesis and characterization of ferrocene derivatives.
- Chapter 4: interactions study of ferrocene derivatives with BSA using electrochemical, spectroscopic and molecular docking techniques.
- Chapter 5: interactions study of ferrocene derivatives with Hb using spectroscopic and molecular docking techniques.
- Chapter 6: antioxidant activities study of ferrocene derivatives using cyclic voltammetry.

Chapter 1

Bibliographical overview of ferrocene and ferrocene derivatives, Hb, and BSA

1.1 Ferrocene

1.1.1 History of ferrocene:

A novel compound with iron and two cyclopentadienide ligands was discovered in 1951. Kealy and Pauson [19] and Miller et al [20] groups of chemists almost simultaneously came to identical results, albeit by accidentally. The novel compound was insoluble in water, air-stable and sublimable, with outstanding solubility in organic solvents, according to both groups. Although the initial reports mentioned its high and surprising stability, the right structure was not revealed until Wilkinson and Fischer independently suggested it soon after. Wilkinson used chemical, physical and spectroscopic methods to determine the accurate structure of dicyclopentadienyl iron, while Fischer used X-ray crystallography to characterize the compound.

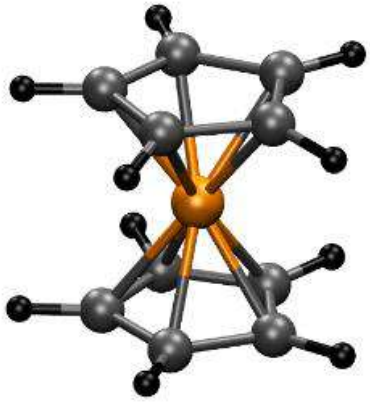

Figure 1.1-1: 3D representation of Ferrocene molecule

Wilkinson suggested a configuration where the iron atom was positioned between two cyclopentadienyl (Cp) ligands, forming a sandwich structure. The bonding between metal d orbitals and π-electrons in the p orbitals of Cp ligands was strong due to their excellent overlap. After further investigation, Wilkinson, Woodward, and their colleagues concluded that the correct structure was a π-complexed sandwich structure [21]. Additionally, Wilkinson found that the iron center of the compound could easily be oxidized from +2 to +3, creating various derivatives of Fc from the blue cation[22] . Fischer's X-ray diffraction experiments confirmed the sandwich structure and proposed a double-cone shape[23].

Through his research, Woodward found that cyclopentadienyl rings shared aromatic properties with benzene, which led him to discover electrophilic aromatic substitution reactions. This discovery,

along with other similarities between the Cp rings and benzene, inspired Woodward's postdoctoral fellow Mark Whiting to name the compound "ferrocene." The term "metallocenes" was later used to describe all transition metal dicyclopentadienyl compounds [24].. The contributions of Wilkinson and Fischer to organometallic chemistry earned them the Nobel Prize in Chemistry in 1973. Today, the term "sandwich compound" is widely used to refer to a broad range of compounds. The discovery of a new type of bonding between metals and organic unsaturated molecules gave organometallic chemistry a fresh perspective.

Ferrocene has two Cp rings which can be arranged in either an eclipsed (D_{5h}) or staggered (D_{5d}) orientation. The energy required for rotation around the Fe-Cp axis is very minimal, less than 4kJ.mol^{-1}. This low energy allows either conformation to be displayed in the ground state structures of ferrocene.[25,26].

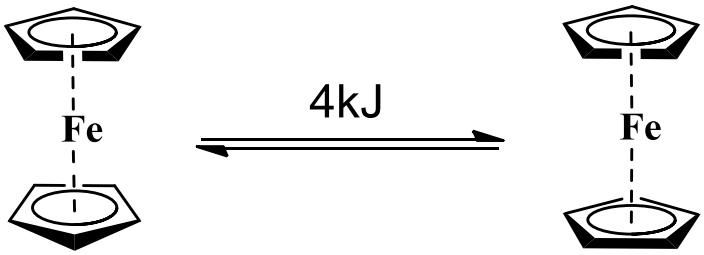

Figure 1.1-2: Ferrocene in the eclipsed (right D5h) and staggered (left D5d) forms.

1.1.2 Electronic Structure of Ferrocene

Ferrocene consists of two cyclopentadienyl anions, each having six d-electrons, bonded to a Fe2+ ion with six d-electrons as well. The compound follows the 18-electron rule where all valence electrons are either in bonding or non-bonding orbitals. Due to the absence of anti-bonding orbitals, the compound remains stable. The bonding within ferrocene can be analyzed through a molecular orbital diagram (**Figure 1.1-3**). which shows the molecular orbitals formed from the interactions between the ligand and metal orbitals. Symmetry considerations, relative energies, and overlap integrals of the ligand-orbitals and the 3d, 4s, and 4p orbitals of the central iron can be used to predict the formation of molecular orbitals.

The lowest energy orbitals in ferrocene molecule are ligand-based, specifically a_{1g} and a_{2u}, as the metal orbitals with the required symmetry ($3d_z^2$/4s and $4p_z$) have significantly higher energy levels. Due to poor overlap with the ligand e_{2g} orbitals, the e_{2g} orbitals remain metal-based, specifically d_{x2-y2} and d_{xy}. The stability of the ferrocene molecule is largely attributed to the formation of two strong bonds resulting from the overlap of ligand e_{1g} orbitals with the iron atom's d_{xz} and d_{yz} orbitals.

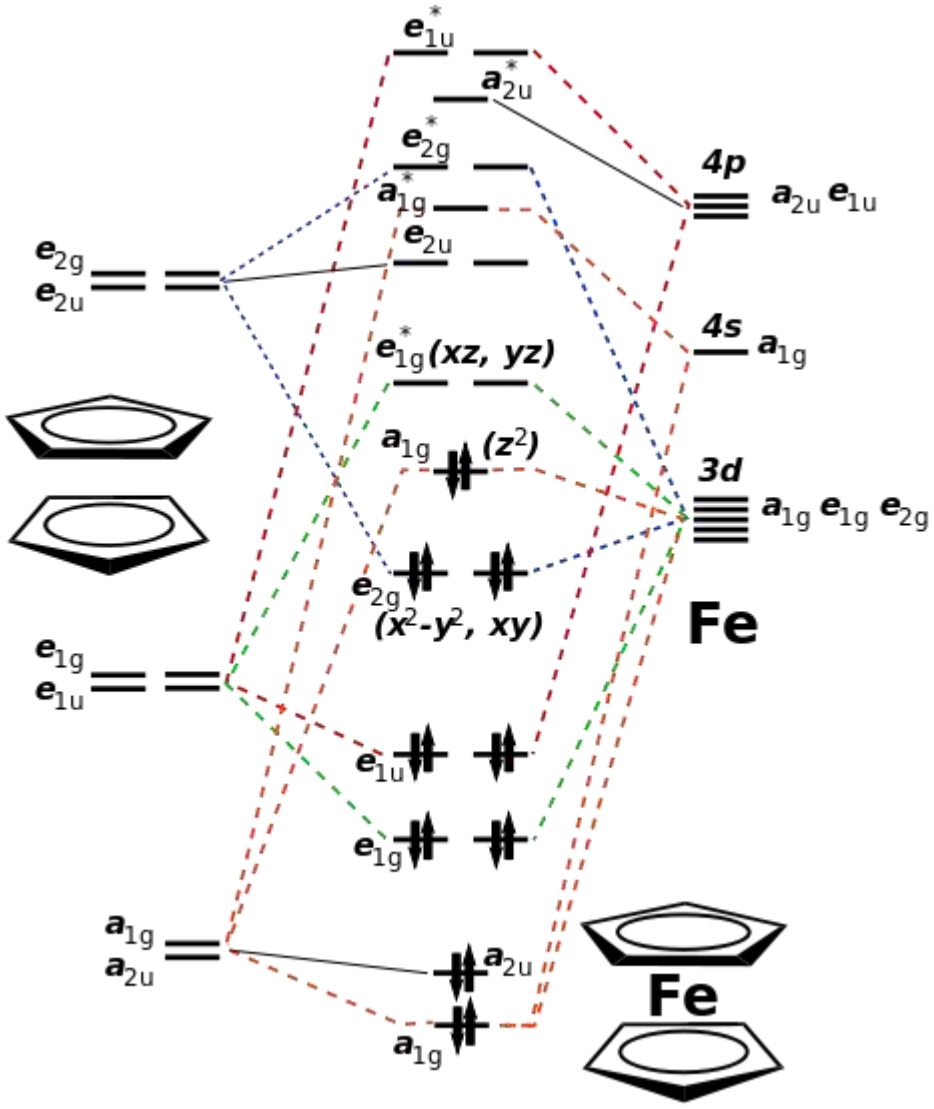

Figure 1.1-3: Molecular orbital of ferrocene molecule [27]

Ferrocene's frontier orbitals include the e2g which has weak bonding, a'_{1g} which is non-bonding and e'_{1g} level which is weakly anti-bonding and unoccupied. Since these orbitals have comparable energies, it is possible to deviate from the 18-electron rule.

1.1.3 Chemistry of Ferrocene

1.1.3.1 Methods of synthesis of ferrocene

In the synthesis of ferrocene, there are two main routes that are typically used:

The first involves the retro Diels-Alder reaction of dicyclopentadiene followed by deprotonation of the weakly acidic cyclopentadiene with an alkali metal. Ferrocene is produced after treatment with iron (II) chloride:

$$FeCl_2 + 2NaC_5H_5 \rightarrow [(\eta^5\text{- } C_5H_5)2Fe] \qquad \textit{1.1-1)}$$

The second method is named metal vapor synthesis, and it involves heating the reactants to high temperatures before combining them on a cold surface:

$$Fe + 2C_5H_6 \rightarrow [(\eta^5\text{- } C_5H_5)2Fe] + H_2 \qquad \textit{(1.1-2)}$$

Finally, ferrocene can be synthesized using an auxiliary base which produces the cyclopentadienyl anion in situ:

$$FeCl_2 + 2C_5H_6 + 2C_5H_5NH \rightarrow [(\eta^5\text{- } C_5H_5)2Fe] + 2[C_5H_5NH_3]Cl \qquad \textit{(1.1-3)}$$

1.1.3.2 Reactivity of ferrocene

In comparison to benzene, ferrocene is more reactive towards electrophilic substitution due to the availability of a greater number of electrons. The rate of reaction for ferrocene is 3×10^6 times faster than that of benzene. There are three proposed mechanisms for explaining electrophilic substitution in ferrocene (E'+'). The first mechanism involves the interaction of electrophilic substituents with weakly bonding electrons of the iron atom, followed by the transfer to the Cp ring with the electrophilic substituent in the endo position, resulting in the formation of substituted ferrocene after proton elimination (Route I). The second mechanism suggests that electrophilic attack occurs on the less hindered exo face of the ligand's ring, without involving direct participation of the metal, and the product is formed after proton loss (Route II). The third mechanism involves the addition of the electrophile to the endo face of the ligand, without any metal interaction (Route III). (Figure 1.1-4).

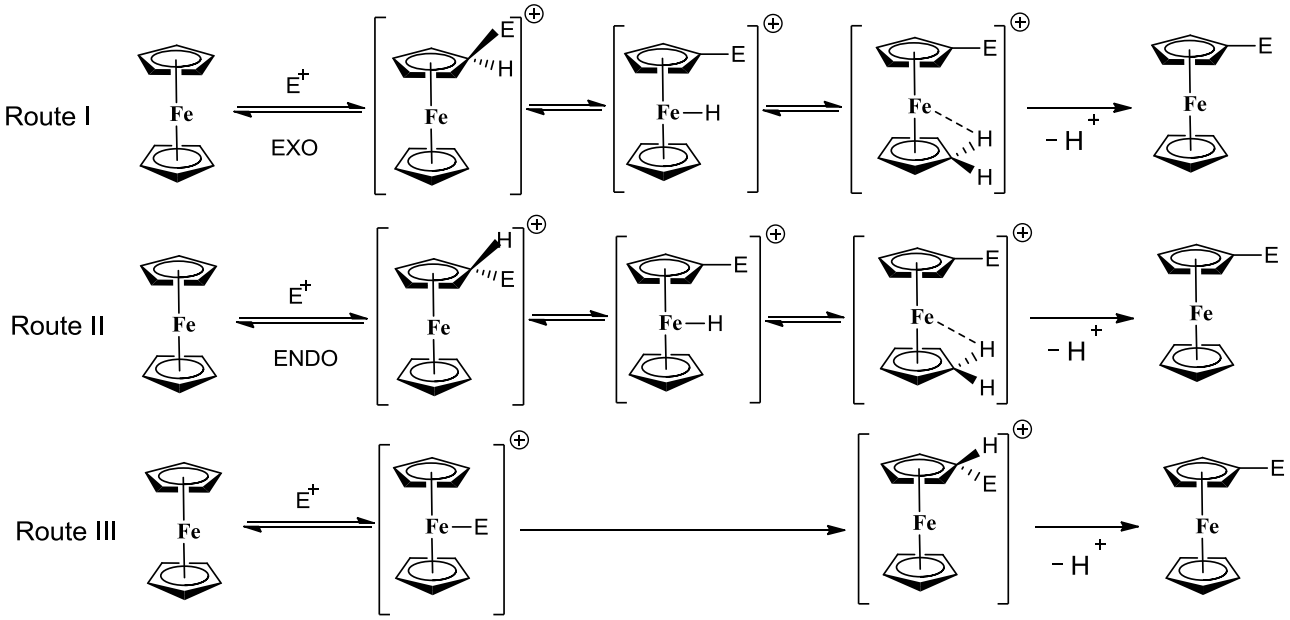

Figure 1.1-4: Proposed mechanisms for electrophilic substitution of ferrocene.

Ferrocene's strong smell and high level of reactivity have made it possible to create many derivatives that serve as important intermediate compounds in organic synthesis[28,29]. These derivatives are easy to make and reactive enough to produce valuable intermediates for creating new organic compounds that would be difficult to make using traditional methods.

One of the commonly used initial substances for creating many different types of ferrocene derivatives is the widely recognized ferrocenylmethyltrimethylammonium iodide, which belongs to the category of quaternary salts. This specific salt is produced through the process of aminomethylation of ferrocene.[30]. (**Figure 1.1-5**).

The ferrocenylmethyltrimethylammonium salt has a trimethylamine component that can be easily replaced by various nucleophiles, including cyanide anions, alkoxide, amines, carbanionic reagents, and Grignard reagents. Our research used the ferrocenylmethyltrimethylammonium salt as a starting material to prepare all the derivatives studied.

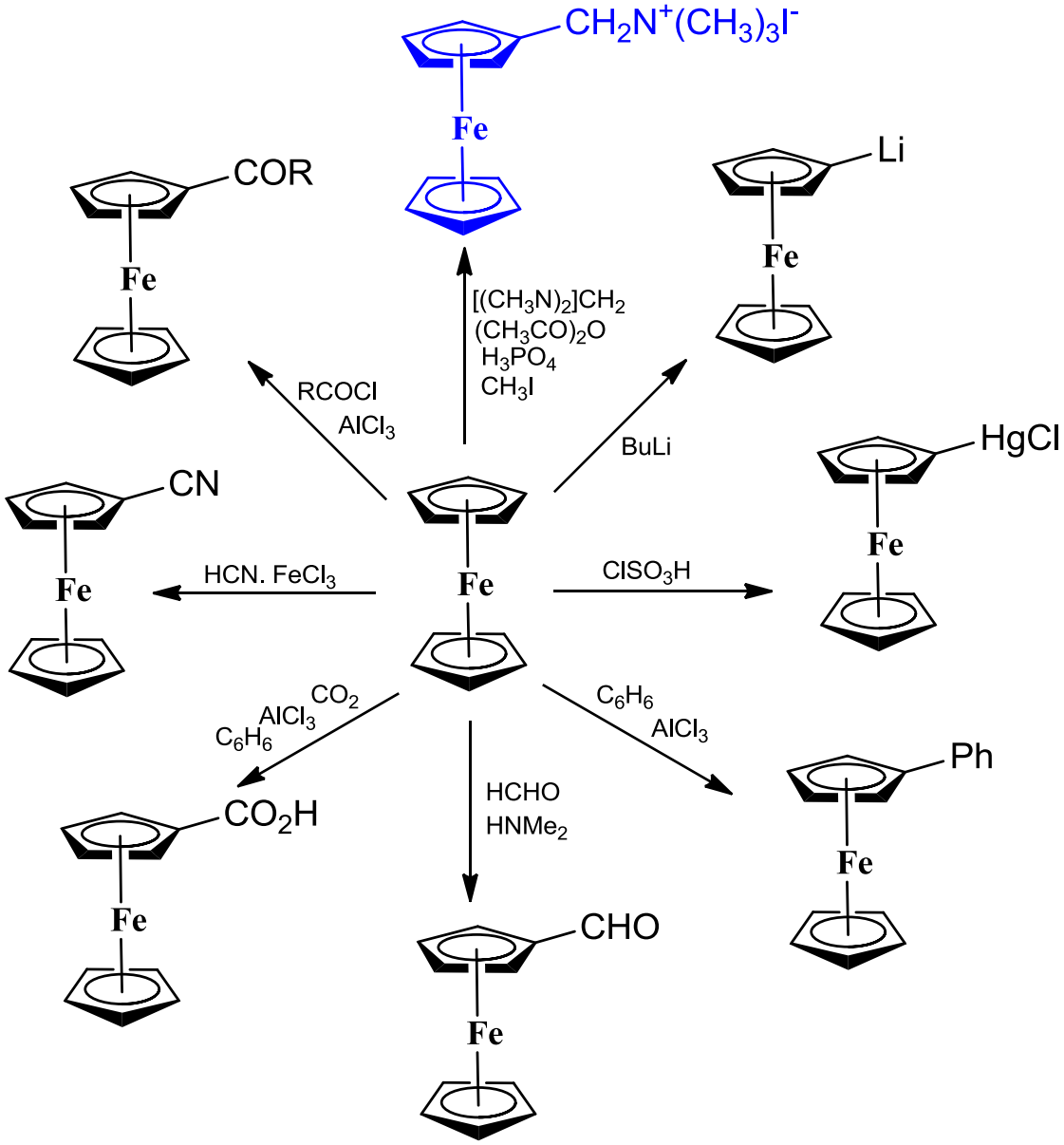

Figure 1.1-5: Selected ferrocene reactions

1.1.4 Application in medicinal chemistry:

Because of the novelty introduced by its presence, medicinal chemists are also open to including ferrocene in their drug design strategies. Ferrocene is a nontoxic, stable compound with good redox properties. Now, scientists are working to develop new compounds that are effective against a wide range of cancers while also having fewer side effects.

Ferrocenes are also known to have a wide range of biological activities, and ferrocene has received special attention due to its neutral chemical stability and non-toxicity. Many ferrocene derivatives have antioxidant[24-26], cytotoxic[31,32], antitumor[33], antimalarial[34], antifungal[35]

and DNA-cleaving activity[36]. Ferrocene derivatives are also used to control the HIV virus which causes AIDS[37]. There are numerous examples in the literature of ferrocene being used in drug design strategies. In one research of nonsteroidal anti-inflammatory agents, replacing the aromatic ring with ferrocene had no influence on anti-arthritic or platelet aggregatory activities in the resulting compounds[38]. Studies with ferrocene-containing penicillin, cephalosporins, and rifamycin revealed that the addition of ferrocene provided no additional benefit[39,40]. When ferrocene was added to famous drugs like tamoxifen and chloroquine, however, significant changes in activity profiles were observed.

The biological properties of ferrocene derivatives containing nitrogen, where the nitrogen is connected through a carbon spacer unit and not directly substituted into one of the cyclopentadienyl rings of ferrocene, have been thoroughly studied and have shown a lot of potential. [41]. **(b)**

Figure 1.1-6 Ferroquine(b) was developed as part of a project to find a replacement for the Fc approved antimalarial drug chloroquine [42]. Ferroquine has successfully completed phase II clinical trials as of 2011[43].

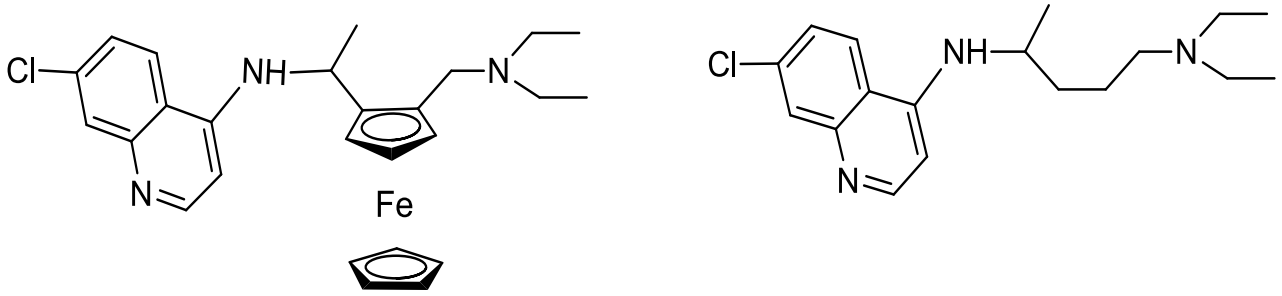

(a) **(b)**

Figure 1.1-6 Structures of ferroquine (a) and chloroquine (b)

Ferrocifen, a potential drug target based on ferrocene, has shown great promise. Similar to ferroquine, it is derived from tamoxifen, an Fc approved drug used for breast cancer treatment. Ferrocifen belongs to a group of metallocenes that are being studied for their potential use in cancer treatment (**Figure 1.1-7**). [43]

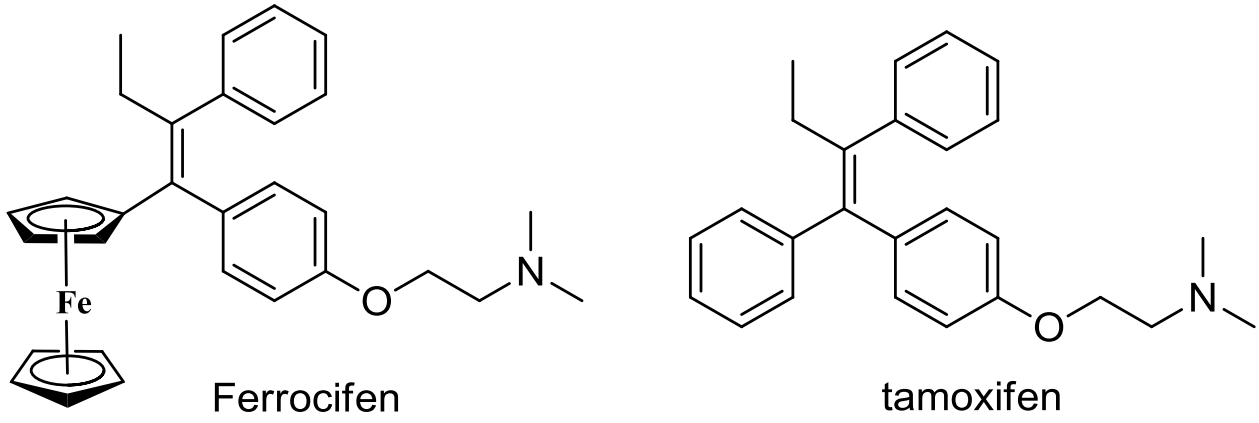

Figure 1.1-7: Structure of ferrocifen and tamoxifen

The field of medicinal chemistry is seeing a rise in interest regarding N-ferrocenylmethylnitroanilines derivatives due to their biological activity as antioxidants [44–46] and potential anticancer drug candidates[8]. Multiple papers discussing the therapeutic benefits of nitrogen containing ferrocene derivatives have been published recently[47–51].

1.2 Proteins

Proteins are crucial molecules that have a vital function in the structure, arrangement, and operation of all living organisms. Their functional diversity categorizes them as transport proteins, storage proteins, hormones, toxins, enzymes, etc. Proteins are generally composed of amino acid monomers organized in a particular manner to execute a precise biological task.[29–31].

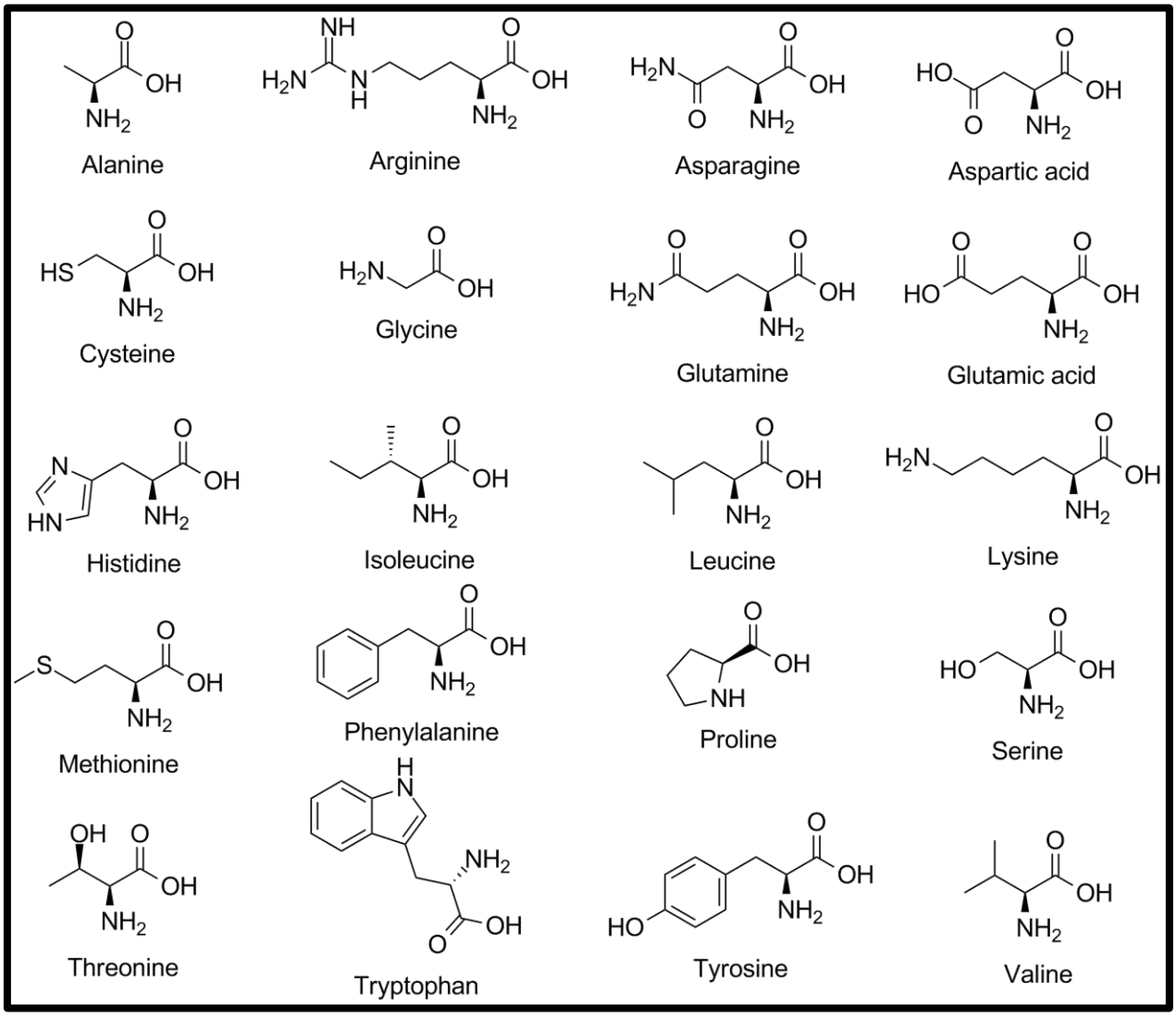

Figure 1.2-1: Amino acids.

In total, there are 20 L-amino acids with structural similarities that include bonding an amino group, a carboxyl group, and a variable side chain to an α-carbon[54]. However, protein differs from this basic structure as it possesses a unique ring at the N-end amine group, which results in a fixed conformation for the CO-NH amide moiety[53].**Figure 1.2-1** clarifies the classification of amino acids as polar, nonpolar, hydrophobic, hydrophilic and charged. Peptide bonds covalently bond amino acids

together in chains. Short chains (less than 30 amino acids) are referred to as peptides, whereas longer chains are referred to as polypeptides or proteins. Peptide bonds are formed when the carboxyl group of one amino acid and the amino group of the next amino acid interacted[55]. **Figure 1.2-2** illustrates the four differentiated dimensions that contribute to the composition of a protein's configuration, including primary structure, secondary structure, tertiary structure, and quaternary structure. This information is crucial to understanding the intricate makeup of protein molecules.

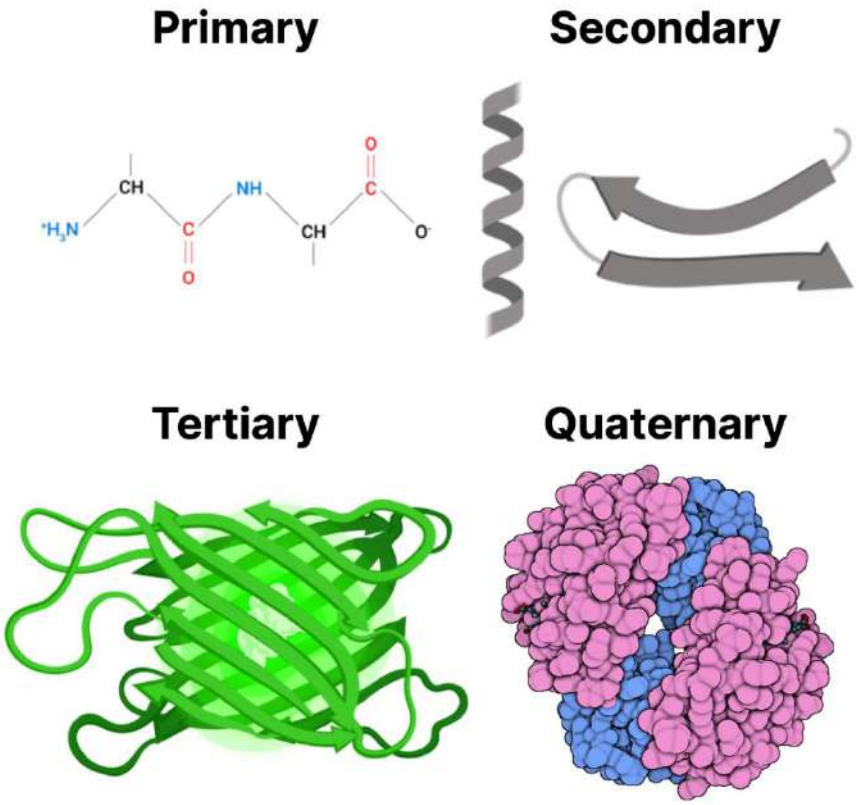

Figure 1.2-2: Protein structures

When examining the composition of a protein, it is important to consider its primary, secondary, and tertiary structures. The primary structure refers to the sequence of amino acids and the presence of covalent linkages such as disulphide bonds. The secondary structure involves areas of the protein that fold or coil, including alpha helices and pleated sheets, which are stabilized by hydrogen bonding[56]. Tertiary structure refers to the final three-dimensional shape of the protein, which is formed by numerous non-covalent interactions between amino acids. These interactions can also lead to the formation of quaternary structure, which involves the binding of multiple polypeptides to create a larger protein.[57,58].

1.2.1 Protein-Ligand Binding

Protein-ligand interactions are vital to almost all biological processes. Several strategies and ideas have been developed for a better understanding of protein-ligand identification at the molecular level. Supportive protein-drug interactions control cellular processes via molecular mechanisms involving protein conformational transitions between low and high-affinity states. The availability of protein-drug complex structures allows for the development of small molecule drugs for treating diseases. HSA interacts with a wide range of therapeutic agents (drugs) in a reversible manner. Recognizing the pharmacokinetics and pharmacodynamics of drugs needs a deep comprehension of drug-protein interaction mechanisms. When drug molecules enter the bloodstream, they are either bound to plasma proteins or exist in free form. Only free drug molecules interact with therapeutic targets to produce remedial effects, as unbound drugs diffuse passively into organ tissue and undergo metabolism. As a result, understanding drug pharmacokinetics and pharmacodynamics requires an understanding of drug binding to albumins[59]. At the atomic level, precise data about the fundamental protein-ligand recognition events is required for understanding biological function [60]. Consequently, studies on the plasma protein-drug binding site are expected to determine the binding parameters that are important when studying a drug profile [61]. The drug-HSA interaction is important in drug bioavailability because the bound portion of drugs acts as a depot, whereas the free portion of drugs participates in its pharmacological effects[62]. Due to the low protein binding, drugs are metabolized and eliminated from the body too quickly, and their long-term therapeutic effect is lost. Moreover, drugs with high protein binding, on the other hand, are gradually metabolized and excreted, increasing the drug's half-life and causing undesirable effects[63]. Drug absorption, distribution, metabolism and excretion properties can be significantly influenced by their binding to serum proteins. Furthermore, there is an evidence of conformational changes in serum albumin caused by drug interactions, which may influence its biological function, primarily as a transporter protein[64]. As a result, determining a drug's affinity for serum albumin is extremely important. Binding to HSA influences drug absorption, metabolism, dispersion and excretion by controlling the free, active concentration of a drug, providing a reservoir for a long period of activity, and finally influencing drug absorption, metabolism, dispersion, and excretion. Drugs usually bind to one or a few high-affinity sites, with association constants ranging from $l0^3$ to 10^6 M^{-1}.

1.2.2 Importance Of Transport Proteins

Transport proteins are important among the various types of proteins because they are involved in the transportation of substances across the membrane. Serum albumin is the most abundant transport protein in blood plasma, and it is primarily responsible for the transport and metabolism of various exogenous and endogenous molecules. These proteins, for example ,transport water-insoluble lipids in the bloodstream and are also involved in regulating osmotic blood pressure [65,66]. Hemoglobin, which transports oxygen from the lungs to the tissue, is a well-known example of a transport protein (**Figure 1.2-3**)[67,68]. Myoglobin serves a similar function in muscle tissue, absorbing oxygen from hemoglobin in the blood and storing or transporting it until the muscle cells require it. The cytochromes are a completely different type of carrier molecule[69].

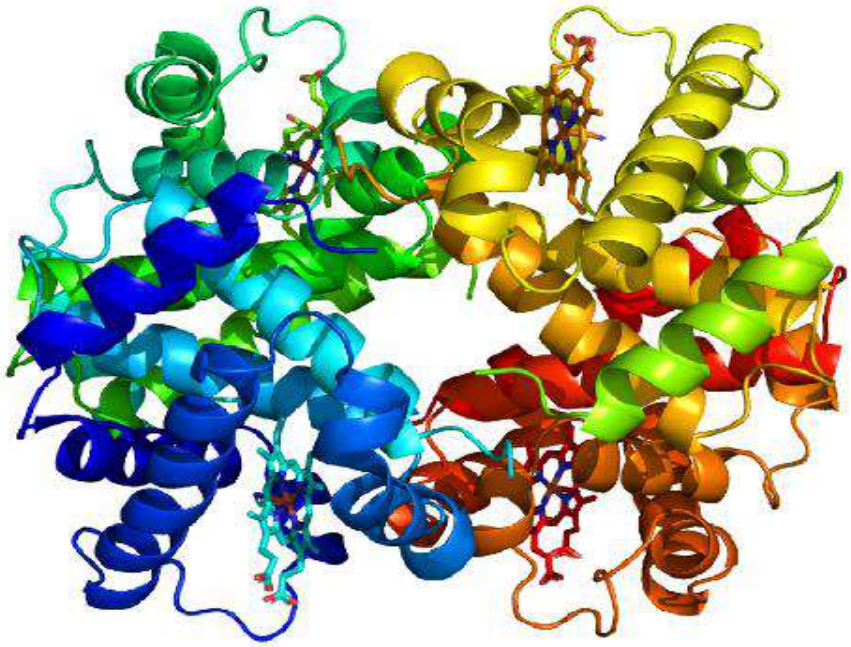

Figure 1.2-3: Structures of hemoglobin (code: 1GCW, Resolution: 2.00 Å)

The electron carrier proteins are involved in the electron transport chain which is a part of the respiratory process. Competitive inhibition affects the function and properties of these carrier proteins. Cyanide binding to cytochrome, for example, inhibits proteins that are essential to the electron transport system in respiration. Carbon monoxide binding to hemoglobin has a similar effect on organisms.

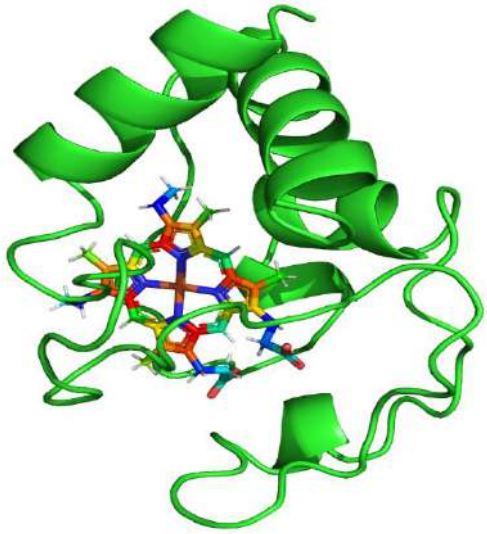

Figure 1.2-4: Structures of cytochrome c (code: 7MRI, Resolution: 2.46 Å)

1.3 bovine serum albumin

1.3.1 Crystal structure of BSA

The amino acid sequence of BSA reveals that it contains 583 amino acid residues, three homologous -helical domains (I, II, and III), and a heart-shaped crystal structure. BSA's crystal structure was just recently identified. There are two sub-domains (A and B) for each domain [70]. It has two tryptophan residues, which are found in the amino acid sequence of the protein at positions 134 and 213 [71]. Nine loops are also a part of the protein's basic structure, which is joined by 17 disulphide linkages. These connections enable the protein's structural flexibility, which is brought about by different experimental conditions [72].

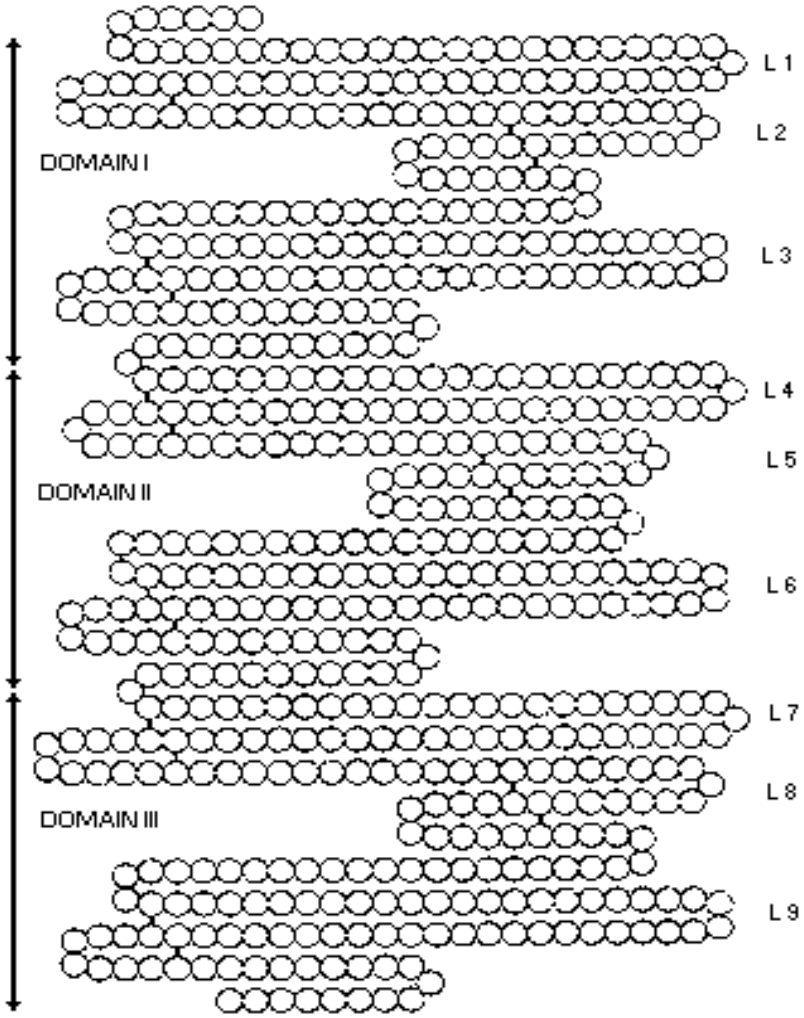

Figure 1.3-1: A graphic represents the three homologous domains and the nine loops connected by 17 disulphide linkages in serum albumins' amino acid sequence.

1.3.2 Binding site of BSA

Albumin in the blood has a strong preference for small and negatively charged hydrophobic molecules. The albumin structure's flexibility makes it easy to bind ligands, and its three-domain design provides a variety of binding sites. Albumin has two major and structurally selective binding sites for ligand molecules which can be referred to as site I and site II as a result of Sudlow and co-workers' pioneering work. [73,74]. Sudlow's site I is located in serum albumin subdomain IIA, whereas site II is located in serum albumin subdomain III A. Site I ligands are heterocyclic anions with the charge located in the molecule's centre. Site II ligands, on the other hand, are aromatic neutral molecules with a charge that is more concentrated on the ligand's periphery. Despite the fact that new research has revealed evidence supporting the existence of multiple subdomains, it is still widely

accepted that this protein contains two high affinities binding sites for small heterocyclic or aromatic compounds.

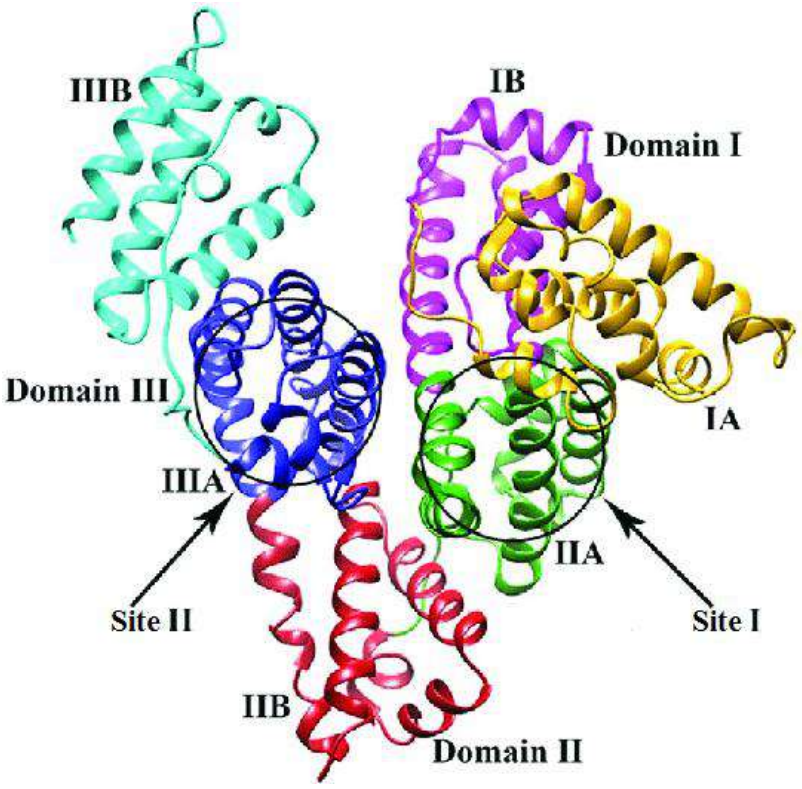

Figure 1.3-2: Major ligand binding sites in serum albumin.

1.3.3 Physicochemical Property

BSA's molecular weight has been estimated to be between 65,000 and 69,000 Da [75,76] . The highest absorbance of UV light is between 278.5 and 279 nm. The tryptophan residues in albumin dominate its fluorescence, having excitation and emission maxima of 282 nm and 343 nm, respectively. Albumin's rotation of polarized light is typical of globular proteins. At 233 nm, there is a strong negative Cotton effect. In the UV region, circular dichroism reveals minima at 209 and 222 nm and a high maximum near 195 nm. **Table 1.3-1** I summarize some of the physical properties of bovine serum albumin.

Table 1.3-1: physicochemical properties of bovine serum albumin

Property	Value
Molecular weight[77]	69 000 Da
Sedimentation constant $SD_{20,W}\times10^{13}$[76]	4.5
Diffusion constant $D_{20,W}\times10^{7}$[78]	5.9

Partial specific volume $\bar{V}_{20}$[79]	0.733
Intrinsic viscosity $[\eta]$[80]	0.041
Overall dimensions A°[81]	41.6×140.9
Isoelectric point [82]	4.7
Isoionic point [83]	5.3
Optical absorbance at 279nm , 1g L^{-1}[84]	0.677
Mean residue ellipticity × 10^{-3}[85]	
$(\theta)_{209nm}$	21.1
$(\theta)_{222nm}$	20.1
Helical content %[86]	54

1.4 Interactions of Ligands with Serum Albumins

The binding of ligands with proteins, which is reversible in nature, is revealed through means of various weak non-covalent intermolecular interactions that include electrostatic, hydrophobic, hydrogen bonding, van der Waals, cation-π, and π-π stacking type interactions. A short description about these interactions is given below.

1.4.1 Hydrogen Bonds

Hydrogen bonds have played a crucial role in the development of structural biology. They arise from a dipole-dipole interaction between an electronegative atom and a hydrogen atom that is covalently bonded to nitrogen, oxygen or fluorine [87]. The energy range of a hydrogen bond is relatively low, ranging from 5 to 30 kJ/mol, in comparison to covalent bonds, which have a range of 155 kJ/mol [88]. Nevertheless, hydrogen bonds are relatively strong compared to Van der Waals forces, yet weaker than covalent, ionic, and metallic bonds. These weak bonds can be rapidly formed or broken during binding events, conformational changes, or protein folding. Remarkably, thermal fluctuations in biological systems can also activate or deactivate hydrogen bonds in specific cases [89]. Hydrogen bonds are precise and directional due to their preferred orientations, lengths, and angles. These unique characteristics make hydrogen bonds crucial for controlling specific interactions during biological identification processes.

1.4.2 Hydrophobic interaction

These types of interactions are linked to the aggregation tendency of non-polar groups in order to minimize their unfavourable interactions with water molecules [90,91].These are leading driving elements in stabilizing the protein structure, biomembranes and micelles [92,93]. They are involved in various biomolecular recognition events like protein-DNA interactions, protein-ligand and host-guestbinding as well as in the formation of quaternary protein structure[90]. Hydrophobic interaction is a crucial non-covalent force in protein-ligand interaction[94].The interactions between ligands and the hydrophobic side chains of proteins also help significantly to the binding free energy. The hydrophobicity effect is considered as a dominant force in most of the drugs like zonisamide[95], etoricoxib[96], amoxicillin[97], halothane[98], due to hydrophobic nature of binding pockets of serum albumin.

1.4.3 Van der Waals Interactions

These interactions are essential in both proteins folding and biomacromolecule-ligand binding events. In fact, they are distance-dependent interactions that can be both attractive and repulsive. Because of the uneven distribution of electrons within them, these types of interactions appear between adjacent uncharged and non-bonded atoms[99]. They are classified into three main types:

1) Dipole-dipole interaction: the interaction between permanent dipoles.

2) Dipole-induced dipole interaction: the interaction between a permanent dipole and a temporary dipole (formed by the nearby permanent dipole).

3) London dispersion interaction: the interaction between induced dipoles.

Such interactions have been well documented in many protein-ligand binding events, such as niclosamide-serum proteins (human serum albumin (HSA), hemoglobin (Hb), and globulin)[100], malachite green-bovine serum[101].

1.4.4 Interactions Mediated by Aromatic Rings

Aromatic amino acid rings (Phe, Trp, and Tyr) and ligands can interact non-covalently. Electrostatic interactions can be used to describe these interactions[102]. For interactions between two aromatic systems, parallel geometry (two rings facing each other) and perpendicular geometry are the two most common geometries (two aromatic rings are face to edge arrangement). As the "side" atoms that are interacting become more acidic—for example, when a highly electron-removing replacement

interacts with the ortho- or para position perpendicular interactions take place. There are two different kinds of interactions in aromatic rings.

1.4.4.1 π-π Interaction

The non-covalent interactions between flat aromatic rings are known as π- stacking or π- π interactions, which contribute to the energy and directionality of entropy-driven stacking[103]. Aromatic amino acid residues contain π electrons that are distributed above and below the plane of the aromatic rings, resulting in a small net negative charge on the ring's face and a positive charge on the hydrogen atoms at its edge. This type of interaction plays a crucial role in the self-assembly process of amyloid formation and is targeted by many inhibitors containing aromatic rings [104,105], such as polyphenols. For example, in the amino glycoside phosphotransferase enzyme (APH (3-IIIa)), a π-stacking interaction occurs between Tyr42 and the adenine ring of the nucleotide, contributing 2 kcal/mol of binding energy [106].

1.4.4.2 Cation-π Interaction

The Cation- π-type interactions exist between the ligand's cations and the π electron cloud of the aryl rings of various amino acids in proteins. About 26% of all tryptophan in proteins is involved in the formation of cation-π type interactions with other amino acids such as lysine and arginine [107]. In protein, cationic lysine and arginine can form cation-interactions with the phenylalanine and tyrosine aryl rings [108]. Protein-ligand interactions, such as Cys-loop receptors (ligand-gated ion channels) with acetylcholine[109], tetrodotoxin binding to Na^+ channels[110], are notable examples of cation-interactions.

Chapter 2

Experimental

2.1 Chemicals, Reagents and Solvents

Bovine serum albumins (From Biochem Chemopharma) dichloromethane (From Biochem Chemopharma 99.99%), ethanol 99% (From Sigma Aldrich), toluene (From Honeywell), N, N-dimethyl formamide (DMF) (From sigma Aldrich), α-tocopherol (97 %) (From Alfa Aesa), tetrabutylammonium tetrafluoroborate (TBPP) (electrochemical grade Sigma-Aldrich 99%) was used as supporting electrolyte and its concentration was kept 0.1M. The rest of the reagents are of analytical grade. All air and water sensitive reactions were performed in oven dried glassware under a nitrogen atmosphere using typical manifold procedures. Nitrogen and oxygen gas were provided from the company Linde gas Algérie. (Research grade (99.99%) Compounds that are not described were synthesized according to the literature procedures.

2.2 Techniques

2.2.1 Cyclic voltammetry technique

Cyclic voltammetry is a technique used to investigate the electrochemical performance of a system, and it is equivalent to double potential step chronoamperometry [111]. Randles and Sevcik[112,113] published and described the theory of cyclic voltammetry for the first time in 1938. It is the most widely used technique for obtaining qualitative information about the reactions which take place in an electrochemical cell system and the potentials at which they actually occur. A cyclic voltammogram (CV) is created by applying a predetermined linear potential to an immersed, stationary electrode and sweeping between a starting potential (Emin) and a final value (Emax) that increases or decreases over time.(**Figure 2.2-1**)[114].

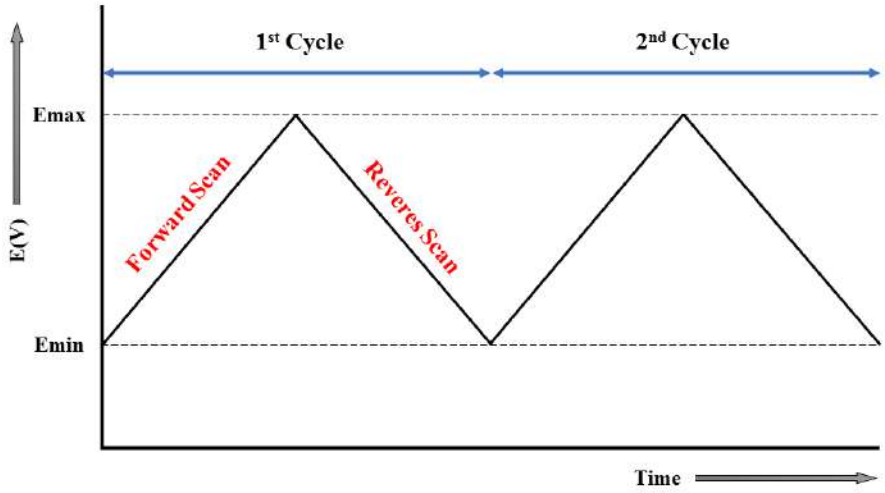

Figure 2.2-1: Potential scan from an initial value (Emin) to final value (Emax) with respect time

The applied potential causes current to flow through the electrode, either oxidizing or reducing the species, making cyclic voltammetry an ideal method for determining concentration. This analytical method shows the potential at which the redox process occurs, and the magnitude of this current is proportional to the analyte concentration in solution. [114]. The following are the two basic processes that occur at the electrode electrolyte surface:

(a) Capacitive Current:

Capacitive current is also known as "double-layer current." When an electrode is perturbed, current is the result of the assembly or removal of charge particles in the electrode electrolyte interface; it does not include any actual charge transfer. [115]. A concentration gradient is formed as a result of the depletion of the electro-active material at the electrode surface. According to Fick's Law [116] (equation *2.2-1)*), the diffusion of the reactant towards the electrode surface and the diffusion of the corresponding reaction product away from the electrode surface.

$$\frac{\partial A}{\partial t} = D\frac{\partial^2 A}{\partial x^2} \qquad 2.2\text{-}1)$$

(b) Faradaic Current:

Faradaic current is produced by non-adsorptive electrochemical reactions that take place at the electrode interface at the electrode surface. Faraday's Law (equation 2.8)[117], controls the redox reaction which states that the amount of charged species (oxidant) transferred is proportional to the number of moles of reactant converted.

$$\frac{[A]_0}{[B]_0} = e^{nF/RT} \qquad 2.2\text{-}2)$$

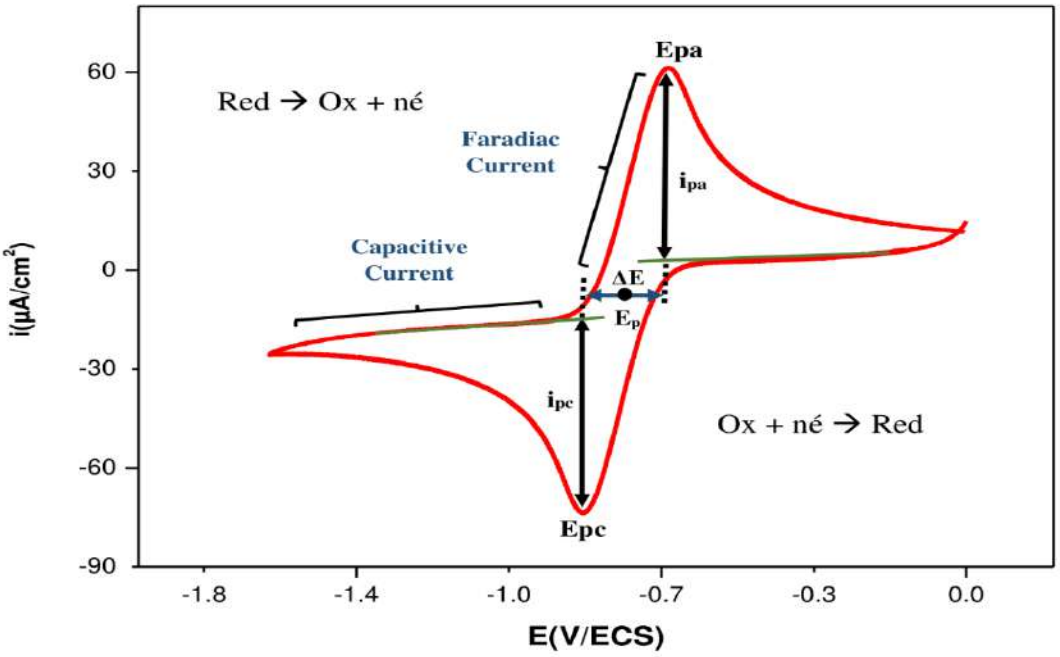

Figure 2.2-2: The cyclic voltammogram of a Nernstian electrochemical reaction.

Electron transfer is not rate dependent in an electrochemically reversible process, and the rate of electron transfer is fast enough to keep the oxidized and reduced forms of redox species in equilibrium at the electrode surface [118]. CV can be used to determine the parameters Ip (Ipa and Ipc), Ep (Epa and Epc), and Ep (Epa-Epc) for both oxidation and reduction reactions under a given experimental condition [119]. Understanding the electrode process and the reversibility of the electrochemical reactions provided by these parameters is critical [120,121] reversible reaction:

The ratio of peak currents at the anode (Ipa) to peak currents at the cathode (Ipc) is one:

$$\left|\frac{Ipa}{Ipc}\right| = 1 \qquad (2.2\text{-}3)$$

According to the Randles-Sevcik equation, peak currents are proportional to the square root of the scan rate $V^{1/2}$:

$$Ipa = 0.4463\, nFCA\left(\frac{zFvD}{RT}\right)^{1/2} \qquad 2.2\text{-}4)$$

Which is simplified in:

$$Ipa = 2.69 \times 10^{5} n^{3/2} CAD^{1/2} v^{1/2} \qquad (2.2\text{-}5)$$

Where n is the number of electron equivalent exchanged during the redox process, F is the Faraday's constant (96485 C/mol), C is the bulk concentration (mol/dm^3), A is the active area of the working electrode (dm^2), υ is the voltage scan rate (V/s), D is the diffusion coefficient (dm^2/s), R is the universal gas constant (8.314 J/mol. K), T is the temperature (K) and Ipa is the anodic peak current (A).

The redox couple potential Ep (against SHE) and the peak potential are related as follows:

$$Ep = (Epc + Epa)/2 \qquad (2.2\text{-}6)$$

The positions of peak potential are independent from the scan rate.

The voltage separation between the two peak potentials can be calculated as follows when n electrons are involved in the reaction:

$$\Delta E = Epc - Epa = \left(\frac{59}{n}\right) mV \qquad (2.2\text{-}7)$$

In the study of the BSA-Fc interaction, the peak currents at the anodic and cathodic zones in the voltammogram of the Fc are first traced. The shifted profiles were then monitored as BSA was gradually added. This interaction's titration is given by the equation[122,123]:

$$\log\frac{1}{[BSA]} = \log K_b + log\,\frac{ip}{ip_0 - ip} \qquad (2.2\text{-}8)$$

Where ip_0 and ip are currents in the absence and presence of BSA respectively and K_b is the binding constant and [BSA] signifies molar concentration of BSA. Therefore, the plot of log (1/ [BSA]) versus log(ip/(ip_0-ip)) gives a straight line and the value of K_b can be determined from the antilog of the intercept of the line on the Y-axis.

2.2.2 UV/VIS technique

Absorption of visible UV Spectroscopy is the most widely used spectroscopic tool for obtaining information about the formation of protein-ligand complexes. It determines how much radiation is absorbed as a function of frequency or wavelength when it interacts with a sample. Any change in the sample's environment alters the relative energy of the ground and excited states, resulting in spectral shifts. [124,125].

The absorbance (A) of an absorber (concentration C) having a molar extinction coefficient ε at a given wavelength λ is expressed by the equation (Beer's law) [126]:

$$Absorbance\ (A) = log\frac{I_0}{I} = \varepsilon lC \qquad (2.2\text{-}9)$$

Where A is absorbance (optical density), Io and I are the intensity of the incident and transmitted light, C is the concentration of the light absorbing species and l is the path length of the light absorbing medium.

Benesi and Hildebrand described a graphical method for determining the binding constant (K_b) and molar extinction coefficient (ε) of 1:1 electron donor-acceptor complexes formed between species donor (Fc) and acceptor (BSA)[127].The binding constant (K) and molar absorptivity (ε) of the (Fc-BSA) association complex were calculated using the equation below.

$$[\ BSA\ ] + [\ Fc\ ] \underset{}{\overset{Kb}{\rightleftharpoons}} [\ Fc\text{-}BSA\ ] \qquad (2.2\text{-}10)$$

The Benesi-Hildebrand analysis of K_b involves the measurement of the [Fc-BSA] absorbance. In plots of $A_0/(A-A_0)$ versus $1/[BSA]$ gave a slope of $\varepsilon_f/(\varepsilon_b-\varepsilon_f)$ is given by the ratio of the slope to the intercept. Values for K_b with a magnitude order of 10^5 M^{-1} are thought to indicate a relatively strong interaction between BSA and metal complexes. [128,129].

$$\frac{A_0}{A-A_0} = \frac{\varepsilon_f}{\varepsilon_b-\varepsilon_f} + \frac{\varepsilon_f}{\varepsilon_b-\varepsilon_f}\frac{1}{K_b[BSA]} \qquad (2.2\text{-}11)$$

Where A_0 and A are the absorbencies of the ligands and their adducts with BSA, respectively, $\varepsilon_f, \varepsilon_b$ are respectively their extinction coefficients.

2.2.3 Protein-drug Docking

Through the use of a computational tool, in silico methods can aid in the identification of drug targets and the visualization of interaction[130,131]. They can also be used to analyse target structures for potential binding or active sites, generate candidate molecules and test for drug likeness, which should be able to rank them, as well as identify the true binding mode for a given ligand and estimate its binding affinity. As a result, a scoring function should be capable of not only distinguishing and ranking various similar alternatives. Understanding the binding mode and affinity between interacting molecules requires an understanding of protein tertiary structure. Handling the flexibility of the protein receptor efficiently is currently regarded as one of the most difficult challenges in the field of docking. Protein flexibility can have a significant impact on binding-site location and orientation[132]. Protein-drug interactions are crucial in a wide range of biological processes and disease treatments. Studies in this area may provide information about the structural features of proteins, which may influence the therapeutic efficacy of drugs.

Molecular Docking

Molecular docking is a popular computational tool for studying molecular recognition, with the goal of predicting the binding mode and affinity of a complex formed by two or more constituent molecules with known structures. Protein-ligand docking, as shown in (**Figure 2.2-3**), is an important type of molecular docking because of its therapeutic applications in modern structure-based drug design. Many biological processes rely on the binding of small molecule ligands to large protein targets.

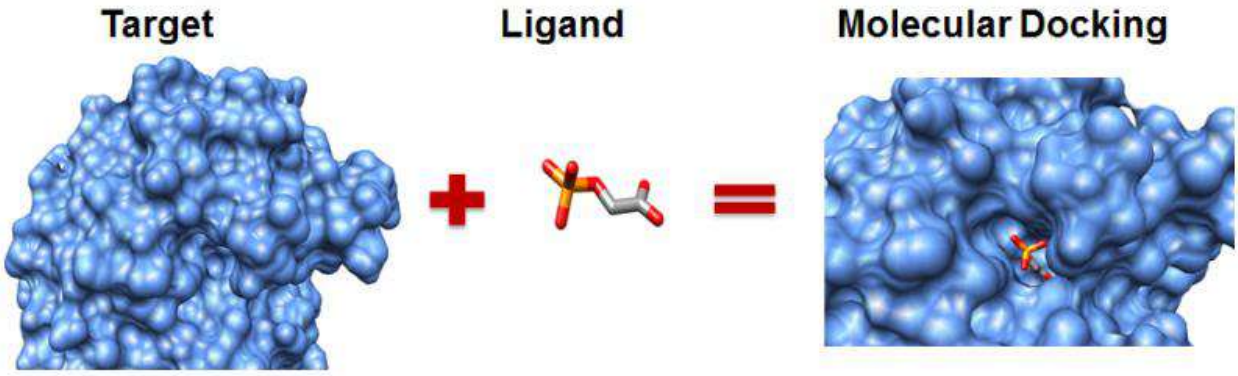

Figure 2.2-3: Elements in molecular docking[133].

Different experimental study methods, such as cyclic voltammetry and electron spectroscopy, generally allow for studying receptor-ligand interactions and determining binding energy, but

predictive methods using simulation, in addition to these experimental approaches, are required to understand how a receptor interacts with a ligand [108]. The most widely used predictive approach in medical and pharmaceutical research is molecular docking simulation. In the field of medical and pharmaceutical research, molecular docking simulation is the most widely used predictive method. Protein-ligand docking is a particularly important and well-established methodology in the field of molecular docking, and an important part of the current drug discovery process [132,134,135]. As shown in the illustration, recent advances in protein-ligand docking are based on two aspects rigid body docking and flexible docking[136](**Figure 2.2-3**)

AutoDock

AutoDock software, which is the latest version 4.0, applies molecular dynamics to anticipate the docking of a flexible ligand with a rigid protein binding site based on the protein region encompassing the binding site and the substrate[137] . It uses the AMBER force field in combination with free energy scoring functions and an extensive collection of protein-ligand complexes with established protein-ligand constants to attain the highest level of predictive accuracy and computational efficiency.

Pymol

PyMOL is an independent molecular visualization software that is widely adopted by protein crystallographers because of its flexibility, speed, and exceptional rendering quality. It is extensively utilized in creating figures for scientific publications that report fresh macromolecular structures [138,139]. The software was created by Warren DeLano and is proficiently operated using abbreviated menus and/or command scripting language [140], which requires a certain level of familiarity to use effectively.

Binding site prediction

Protein-ligand binding sites are the active regions present on the surface of proteins that perform crucial functions, and therefore, the detection of these sites is often the initial step in exploring protein activities and developing structure-based drugs. The analysis of the active sites, i.e., the ligand binding sites, of the receptor protein was carried out using Prank Web (http://prankweb.cz/). The binding sites are comprised of residues that are positioned within the active sites and act as catalytic residues [141,142].

2.3 Experimental

2.3.1 Cyclic Voltammetry Experiments

Cyclic voltammetry experiments were performed using a three-electrode electrochemical cell of a volume of 12 mL containing a glassy carbon (GC) working electrode with a geometric area of 0.013 cm^2, a platinum wire as counter (auxiliary), and a Hg/Hg_2Cl_2 paste covered wire as reference electrode on a PGZ301 potentiostat/galvanostat (Radiometer Analytical SAS, France).

For the cyclic voltammetry characterisation tests of the synthesized ferrocene derivatives, voltammograms of 10 mM solutions of each derivative in acetonitrile were initially acquired at a scan rate of potential equal to 100 $mV.s^{-1}$, and subsequently voltammograms were recorded at scan rates of potential equal to 200, 300, 400, and 500 $mV.s^{-1}$.

For BSA interaction study, voltammograms of 1 mM solutions of each ferrocene derivative were recorded in ethanol/PBS (90:10) solution at pH = 7.2 with supporting electrolyte 0.1 M TBFP in the absence of BSA after degassing the solution from oxygen for at least 10 minutes with bubbling nitrogen gas. The procedure was then repeated with increasing concentrations of BSA. After each electrochemical assay, the working electrode was polished.

2.3.2 UV-Vis Experiments

UV-Vis tests were carried out using a UV-Vis spectrometer (Shimadzu 1800) and a quartz voltametric cell with a volumetric capacity of 5 mL. Data was collected using a Pentium IV (4.0 GHz CPU and 4 Gb RAM) microcomputer with UV probe software version 2.34. (Shimadzu). OriginLab software version 2.0 was used for graphs plots, and calculations (Integral Software, France).

For UV-Vis characterization experiments of the synthesized ferrocene derivatives, the spectrum of 1 mM solution of each derivative in acetonitrile was obtained at room temperature.

For BSA interaction study, spectrums of 1 mM solution of each ferrocene derivative were recorded in ethanol/PBS (90:10) solution at pH = 7.2 in the absence of BSA, then repeated with increasing concentration of BSA.

In order to study HHb interactions, the electronic spectra of 0.1 mM HHb in ethanol/PBS (90:10) solution at pH = 7.2 was obtained in the absence of ferrocene derivatives. The spectroscopic response of the same quantity of HHB was then measured after the addition of a solution of each ferrocene derivative in the same solvent at gradually increasing concentrations.

2.3.3 Molecular Docking experiments

All docking studies were conducted on a Pentium 3.30 GHz with RAM 4.00 Go 256 MB memory running Windows 10. The AutoDock 4.2 program, which is based on the Lamarckian Genetic Algorithm (LGA) plus GA search, was utilized for docking calculations. Docking simulations were done using the default parameters, and the number of runs was set to 50 with 150 persons and 2,500,000 energy assessments. The search was carried out in a grid of 41 and 51 points per dimension, separated by 1.000 Å. The grid centres determined by (prankweb.cz) web servers and sizes for each ligand were $40\times40\times40Å^3$, with a step size of 0.375 centred on the binding site of BSA. The best conformation with the lowest docking energy was chosen. At the completion of the docking runs, several binding energies of the ligands with their corresponding conformations were acquired; the best energetically advantageous docked pose was utilized in the docking analysis.

Chapter 3

Synthesis and Characterization

3.1 General Procedure for the Synthesis of N-ferrocnylmethylanilines derivatives

Reaction of nitroaniline or aminobenzonitrile with the well-known quaternary salt trimethylferrocenylmethylammonium iodide produces the corresponding N-(ferrocenylmethyl)nitroaniline or N-(ferrocenylmethylamino) benzonitrile derivatives respectively (**Figure 3.1-1**). Experimental data and procedure of preparation for the obtained derivatives are reported in literature [143,144].

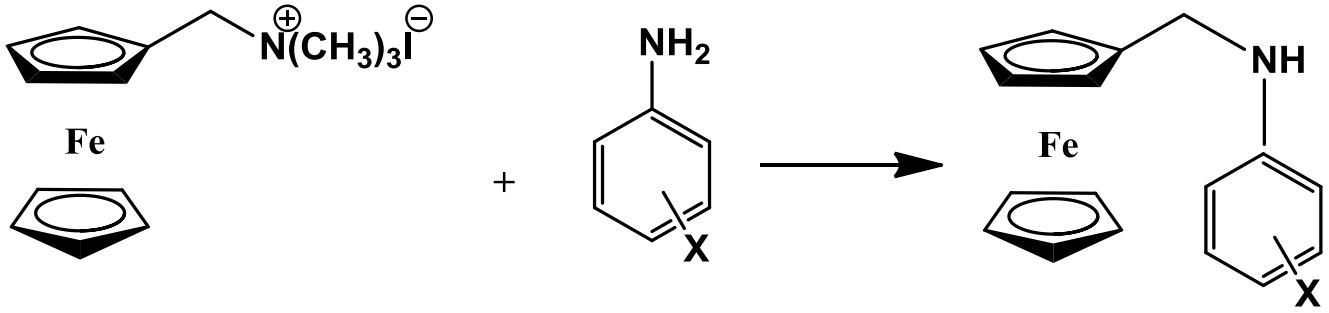

Figure 3.1-1: Synthesis of N-ferrocnylmethylanilines derivatives

X = H **X = 2-NO2** **X = 2-CN**

X = 3-NO2 **X = 3-CN**

X = 4-NO2 **X = 4-CN**

Table 3.1-1: Principal results obtained from the Synthesis of N-ferrocnylmethylanilines derivatives

Entry	Substrate	Product	Yield (%)	mp °C	Time (h)
1	Aniline	N-ferrocenylmethylaniline	85	110	5
2	2-nitroaniline	N-(ferrocenylmethyl)-2-nitroaniline	89 (92*)	112	7
3	3-nitroaniline	N-(ferrocenylmethyl)-3-nitroaniline	73 (95*)	117	6
4	4-nitroaniline	N-(ferrocenylmethyl)-4-nitroaniline	90 (94*)	114	6
5	2-aminobenzonitrile	2-(ferrocenylmethylamino)benzonitrile	92 (95.5*)	127	8
6	3-aminobenzonitrile	3-(ferrocenylmethylamino)benzonitrile	62 (47*)	128	7
7	4-aminobenzonitrile	4-(ferrocenylmethylamino)benzonitrile	65 (92.7*)	134	6

3.2 Acylation of N-ferrocnylmethylaniline derivatives

3.2.1 N-FERROCENYLMETHYL -N-PHENYLBENZAMIDE (FMAA)

3.2.1.1 Synthesis of N-ferrocenylmethyl-N-phenylbenzamide

In a 100 mL three-necked round-bottom flask, N-ferrocenylmethyl aniline (200 mg, 0.45 mmol) and 4-nitrobenzoyl chloride (116 mg, 0.68 mmol) were dissolved in 50 mL DCM in the presence of pyridine (37µl ,0.45 mmol), the obtained mixture is stirred under an atmosphere of nitrogen for one hour. The evolution of the reaction was followed by TLC. reaction mixture was extracted with a solution of hydrochloric acid (6M) to remove any trace of unreacted pyridine, washed with water, and dried over MgSO4. The solvent was removed under vacuum, and the obtained residue was purified on a silica gel column chromatography using a mixture of DCM and toluene (90:10) as eluent. Evaporation of the solvent gave an orange solid product which was recrystallized in 90% ethanol/water to offer a red crystalline plate (yield 54%, m.p. 152.5 °C)

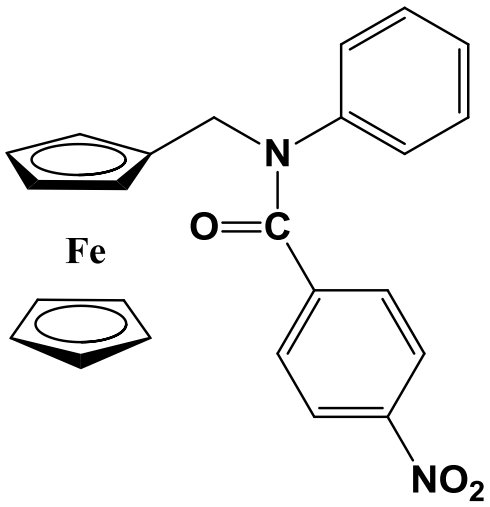

Figure 3.2-1: Chemical structure of N-ferrocenylmethyl-N-phenylbenzamide

3.2.1.2 **Cyclic voltametric characterization**

N-ferrocenylmethyl-N-phenylbenzamide was dissolved in DCM solution containing 0.1 M TBAP as a supporting electrolyte. Measurements were carried out in 2×10^{-3} M solution at room temperature in the potential range from 0 to 1 V for FMA and 0 to 0.9V for FMAA with scan rate $0.1Vs^{-1}$.

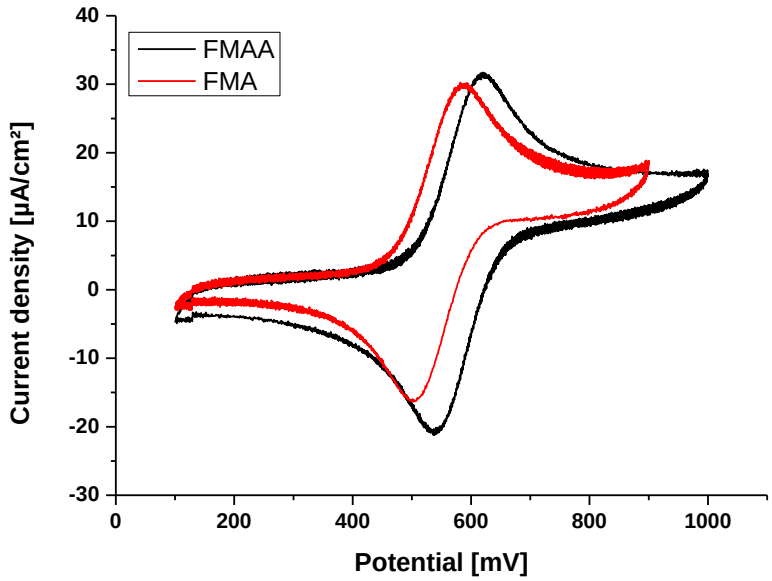

Figure 3.2-2*:* Cyclic voltammogram of FMA (red line) and FMAA (black line) recorded at 0.1V.s^{-1} potential sweep rate on a Pt disk electrode at 298K

the ratio ipa/ipc is equal to unity and the redox potential $E_{1/2}$ is found equal to 545 mV/SCE for FMA and 580 mV/SCE for FMAA. The shift of potential towards left can be attributed to the electron withdrawing nature of the substituted nitro groups. The ΔEp value for the peak-to-peak separation of the cathodic and anodic peak of the Fc^{3+}/Fc^{2+} couple was 72 mV, which is close to the ideal value of 60 mV for fully reversible one-electron processes [145,146].

Equation *(2.2-5)* is used to calculate the diffusion coefficient of FMAA based on the succession of cyclic voltammograms shown in **Figure 3.2-3**.

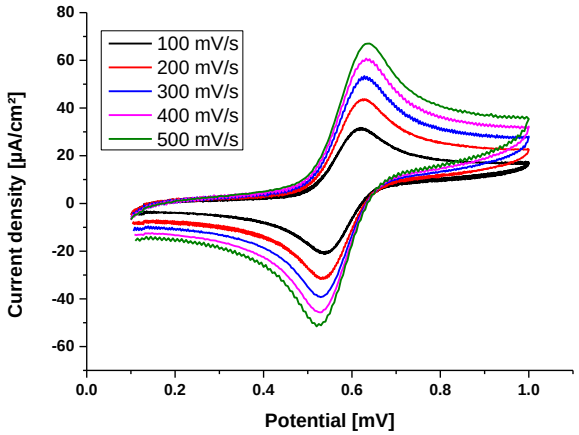

Figure 3.2-3: cyclic voltammograms of 100 µM of FMAA at different scan rates (0.1-0.2-0.3-0.4-0.5 $V.s^{-1}$) at 298 K on a Pt electrode

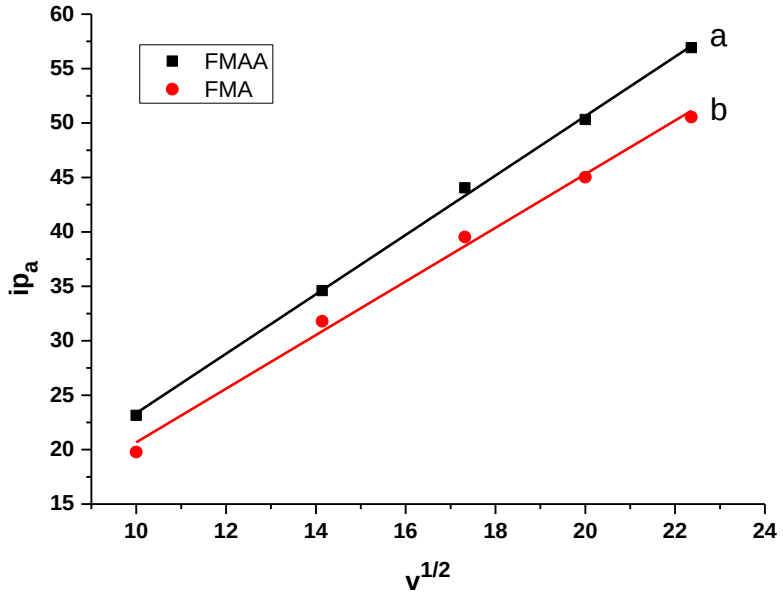

Figure 3.2-4: Anodic peak current vs. square root of scan rate for FMA(a) and FMAA(b)

The linearity of the relation between the square root of the scan rates and the anodic peak current density for both FMA(a) and FMAA(b) demonstrated that the redox process was controlled by the diffusion step. The diffusion coefficients were calculated using the slopes of Randles–Sevcik plots. Obtained electrochemical parameters are shown in the **Table 3.2-1**.

Table 3.2-1: The electrochemical parameters of FMA and FMAA

Adduct	Formal potential (Ea-Ec) (mV)	Half wave potential $E_{1/2}$ (mV)	Current ratio ipa/ipc	Diffusion coefficient D ($cm^2.s^{-1}$)
FMA	77	545	1.00	1.524×10^{7}
FMAA	72	580	0.99	1.237×10^{7}

3.2.1.3 **Spectroscopy Characterization**

3.2.1.3.1 UV-visible Spectroscopic characterization

The UV/Vis spectra of DCM solutions of FMAA are shown in **Figure 3.2-5**. Spectrum has absorption bands at 267 nm that corresponds to $\pi\rightarrow\pi^*$. So, electronic transitions can be described by ligand-center transition.

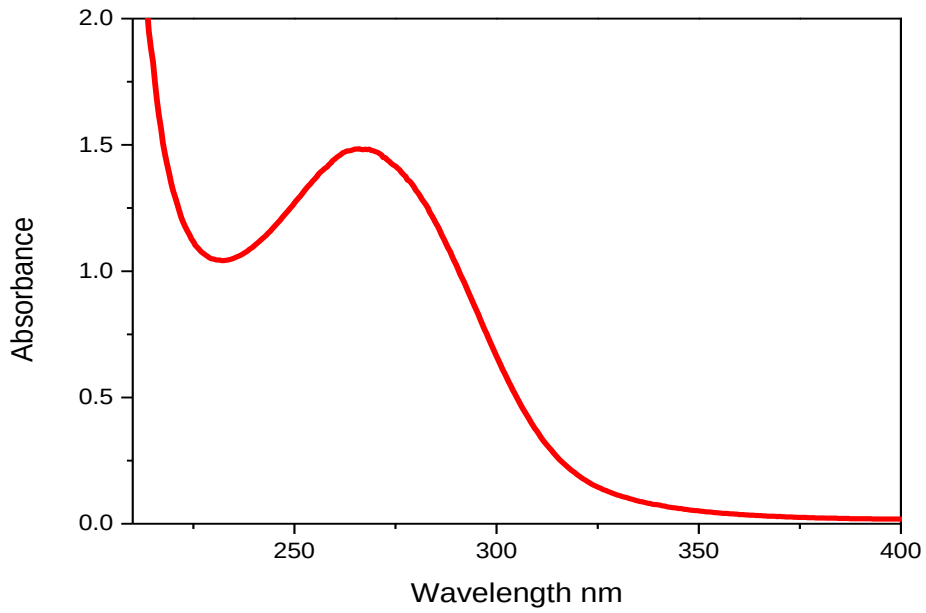

Figure 3.2-5: Electronic spectra of FMAA in DCM, concentration: 10^{-4} M.

3.2.1.3.2 IR characterization

The FTIR spectrum of the product is shown in **Figure 3.2-6**. The figure shows a characteristic absorption peak due to the N-H of amine group at 1656 cm^{-1} disappeared, C=O stretching vibration appeared at 1645.21 cm^{-1}. The main characteristic bands 3105.91 cm^{-1} correspond to C–H bond stretch. The stretching band of C-N is at 1287.09 cm^{-1}, the C=C stretch of the aromatic carbons is at 1593.70 cm^{-1}. The bands at 1517.66 and 1344.73 cm^{-1} correspond to N-O bond stretch, while the

ferrocene cyclopentadienyl ring and C-H bending vibration appeared respectively at 1108.03 and 1008.69 cm^{-1} indicating that the product is monosubstituted.

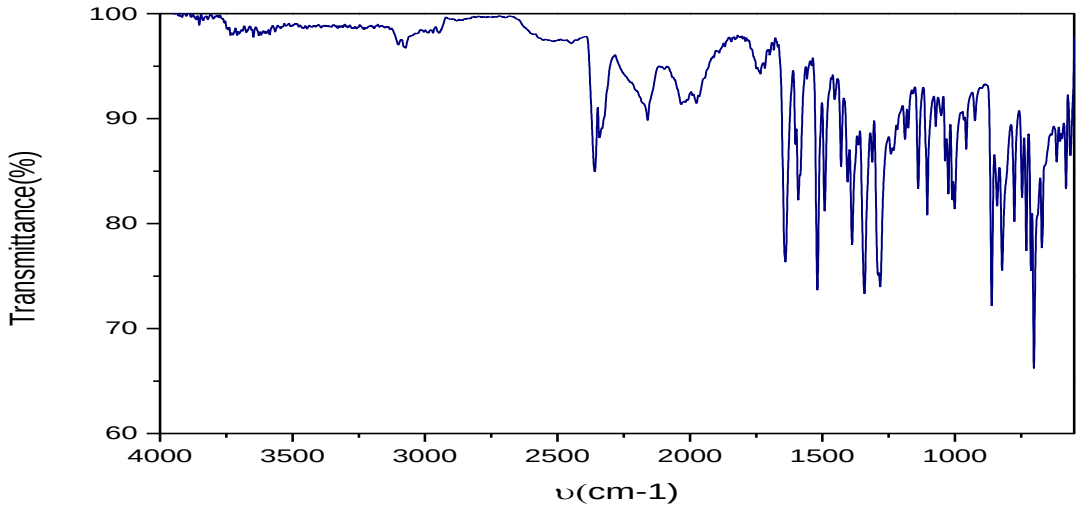

Figure 3.2-6: IR spectrum of N-ferrocenylmethyl-N-phenylbenzamide

3.2.1.3.3 Proton NMR characterization

The ^{1}H, NMR spectrum of N-ferrocenylmethylaniline, **Figure 3.2-7** shows all the expected peaks for the nineteen protons of AN. The 9 protons of the α and β protons of the substituted cyclopentadienyl ring of ferrocene and unsubstituted cyclopentadienyl ring resonated at δ = 4.09 ppm. The two protons of the methylene group are shifted at δ = 4.30 ppm, this shift is attributed to the electron donor effect of the nitrogen atom. The nine aromatic protons of the two phenyl groups resonated respectively at δ = 7.05 (2H, H8), 7.16 (1H, H9), 7.22 (2H, H7), 7.48 (2H, H12) and δ =8.03 (2H, H13) ppm.

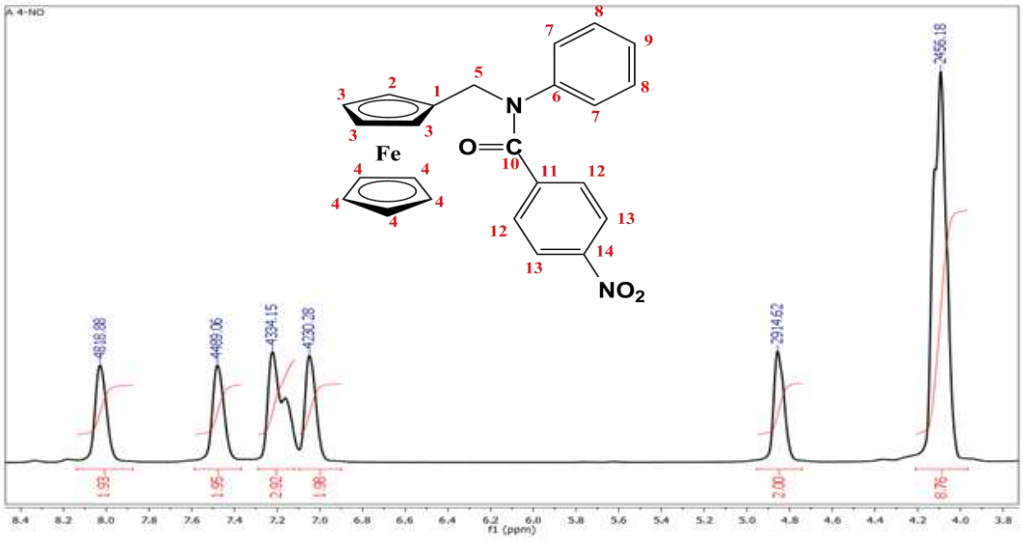

Figure 3.2-7: 1H NMR spectrum of N-ferrocenylmethyl-N-phenylbenzamide

3.2.2 N-ferrocenylméthyl-3-nitro-N-(4-nitrophenyl)benzamide (FM3NA)

3.2.2.1 Synthesis of N-ferrocenylméthyl-3-nitro-N-(4-nitrophenyl)benzamide

In a 100 mL three-necked round-bottom flask, N-ferrocenylmethyl-3-ntroaniline (200 mg, 0.41 mmol) and 4-nitrobenzoyl chloride (166 mg, 0.62 mmol) were dissolved in 50 mL DCM in the presence of pyridine (33µl ,0.41 mmol), the obtained mixture is stirred under an atmosphere of nitrogen for 1.5 hour. The evolution of the reaction was followed by TLC. reaction mixture was extracted with a solution of hydrochloric acid (6M) to remove any trace of unreacted pyridine, washed with water, and dried over MgSO4. The solvent was removed under vacuum, and the obtained residue was purified on a silica gel column chromatography using a mixture of DCM and toluene (95:05) as eluent. Evaporation of the solvent gave an orange solid product which was recrystallized in 90% ethanol/water to offer a red orange needle (yield 48%, m.p. 124.4 °C).

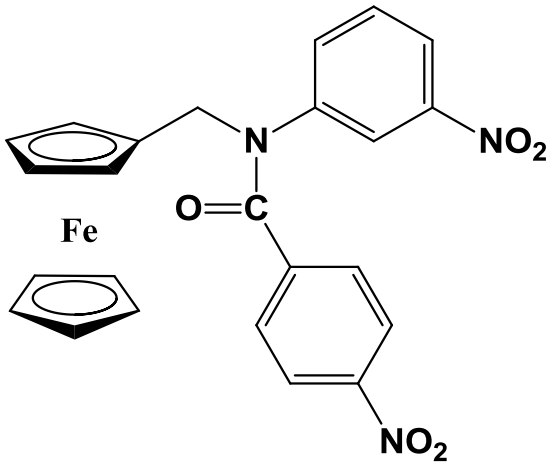

Figure 3.2-8: Chemical structure of N-ferrocenylméthyl-3-nitro-N-(4-nitrophenyl)benzamide

3.2.2.2 **Cyclic voltametric characterization**

N-ferrocenylméthyl-3-nitro-N-(4-nitrophenyl)benzamide was dissolved in DCM solution containing 0.1 M TBAP as a supporting electrolyte. Measurements were carried out in 2×10^{-3} M solution at room temperature in the potential range from 0 to 1 V for FM3N and FM3NA with scan rate $0.1Vs^{-1}$.

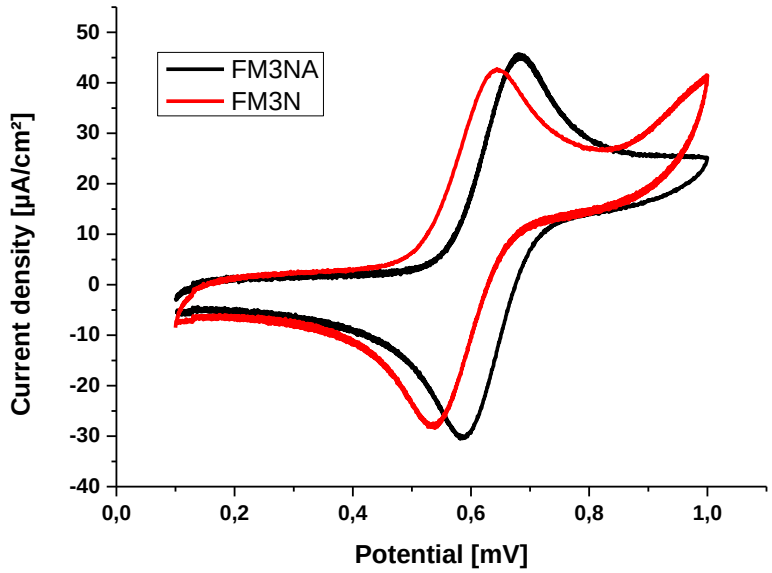

Figure 3.2-9: Cyclic voltammogram of FM3N (red line) and FM3NA (black line) was recorded at $0.1V\ s^{-1}$ potential sweep rate on Pt disk electrode at 298K

Cyclic voltammograms of solutions containing FM3N and FM3NA are shown in **Figure 3.2-9**. the ratio ipa/ipc is equal to unity and the redox potential $E_{1/2}$ is found equal to 591 mV/SCE for FM3N

and 633 mV/SCE for FM3NA. The shift of potential towards left can be attributed to the electron withdrawing nature of the substituted nitro groups. The ΔEp value for the peak-to-peak separation of the cathodic and anodic peak of the Fc^{3+}/Fc^{2+} couple was 90 mV, which is close to the ideal value of 60 mV for fully reversible one-electron processes

Equation (2.2-5) is used to calculate the diffusion coefficient of FM3NA based on the succession of cyclic voltammograms shown in **Figure 3.2-10**.

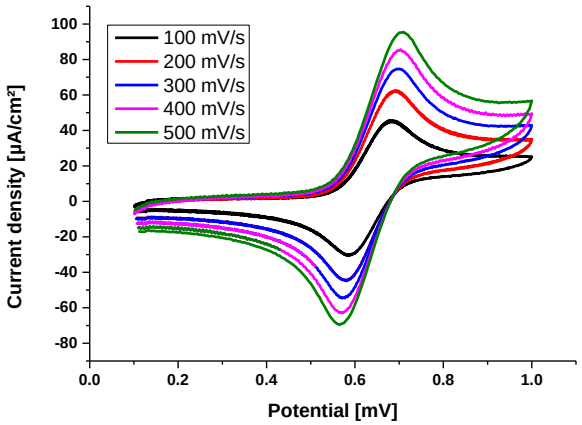

Figure 3.2-10: cyclic voltammograms of 100 µM of FM3NA at different scan rates (0.1-0.2-0.3-0.4-0.5 $V.s^{-1}$) at 298 K on Pt electrode

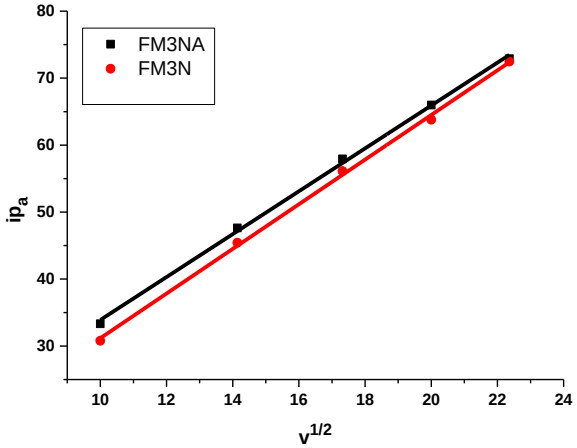

Figure 3.2-11 Anodic peak current vs. square root of scan rate for FM3N (a) and FM3NA (b)

The linearity of the relation between the square root of the scan rates and the anodic peak current density for both FM3N (a) and FM3NA (b) demonstrated that the redox process was controlled by the

diffusion step. The diffusion coefficients were calculated using the slopes of Randles–Sevcik plots. The electrochemical parameters are shown in the **Table 3.2-2**.

Table 3.2-2: The electrochemical parameters of FM3N and FM3NA

Adduct	Formal potential (Ea-Ec) (mV)	Half wave potential $E_{1/2}$ (mV)	Current ratio ipa/ipc	Diffusion coefficient D ($cm^2.s^{-1}$)
FM3N	103	591	1	2.67×10^{7}
FM3NA	90	633	1	2.09×10^{7}

3.2.2.3 **Spectroscopy Characterization**

3.2.2.3.1 UV-visible Spectroscopic characterization

The UV/Vis spectra of DCM solutions of FM3NA are shown in **Figure 3.2-12**. Spectrum has absorption bands at 258 nm that corresponds to $\pi\rightarrow\pi^*$. So, electronic transitions can be described by ligand-centre transition.

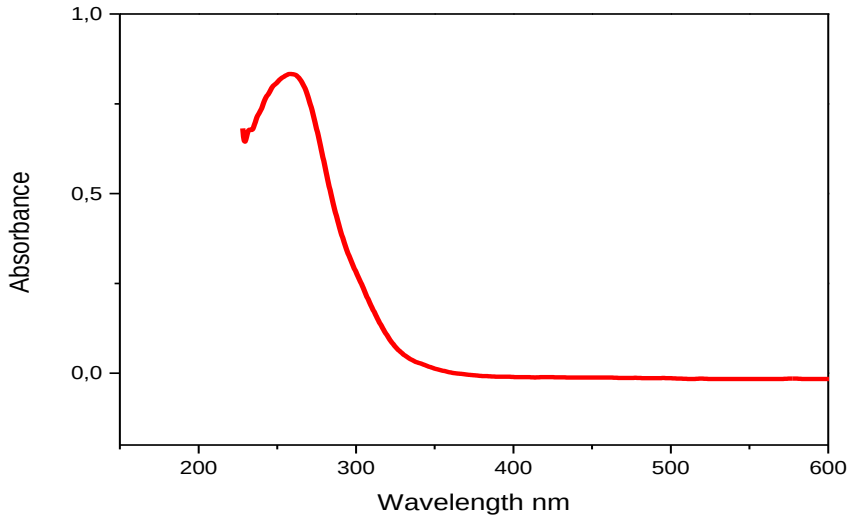

Figure 3.2-12 : Electronic spectra of FM3NA in DCM, Concentration: 10^{-4} M.

3.2.2.3.2 IR characterization

The FTIR spectrum of the product is shown in **Figure 3.2-13**.The figure shows a characteristic absorption peak due to the N-H of amine group at 1616.49 cm^{-1} disappeared, C=O stretching vibration appeared at 1647.92 cm^{-1}. The main characteristic bands 3112.83 cm^{-1} correspond to C–H bond stretch. The stretching band of C-N is at 1263.56 cm^{-1}, the C=C stretch of the aromatic carbons is at 1607.40 cm^{-1}. The bands at 1528.26 and 1338.49 cm^{-1} correspond to N-O bond stretch, while the

ferrocene cyclopentadienyl ring and C-H bending vibration appeared respectively at 1105.22 and 1004.90 cm^{-1} indicating that the product is monosubstituted.

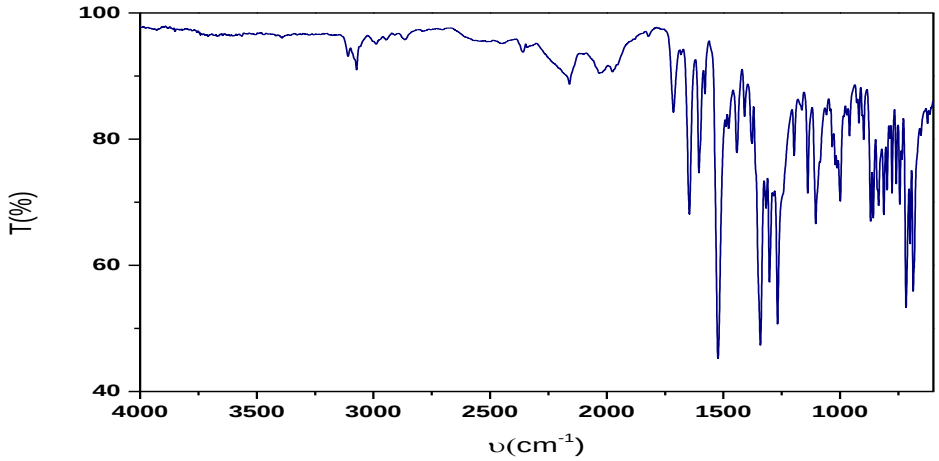

Figure 3.2-13: IR spectrum of FM3NA

3.2.2.3.3 Proton NMR characterization

The 1H, NMR spectrum of N-ferrocenylméthyl-3-nitro-N-(4-nitrophenyl)benzamide, **Figure 3.2-14**, shows all the expected peaks for the nineteen protons of FM3NA. The 9 protons of the α and β protons of the substituted cyclopentadienyl ring of ferrocene and unsubstituted cyclopentadienyl ring resonated at δ = 4.12 ppm. The two protons of the methylene group are shifted at δ = 4.90 ppm, this shift is attributed to electron donor effect of the nitrogen atom. The eight aromatic protons of the phenyl groups resonated respectively at δ = 7.40 (1H, H8), 7.45 (1H, H7), 7.69 (1H, H9), 7.58 (2H, H13), 8.01 (1H, H10) and δ =8.07 (2H, H14) ppm.

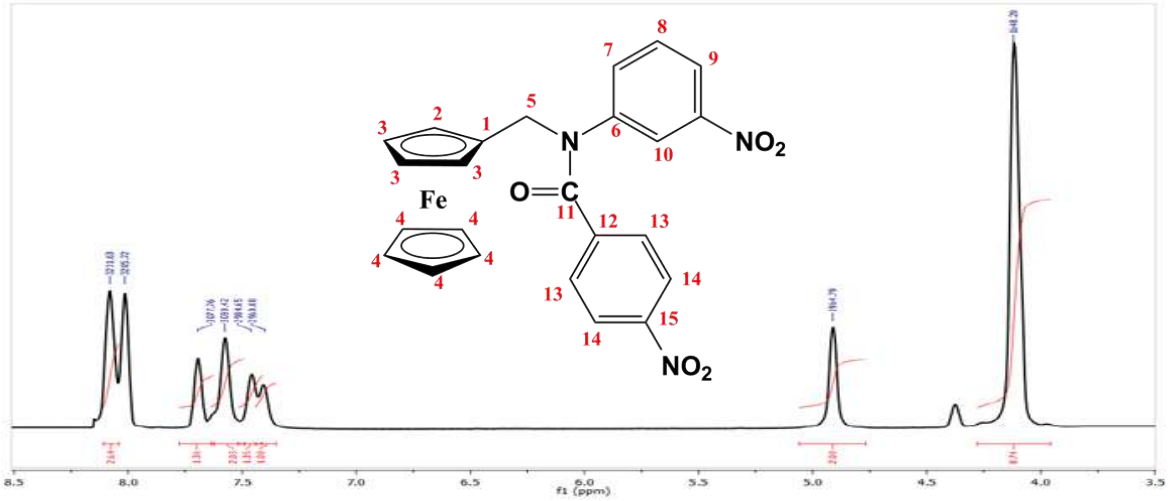

Figure 3.2-14: 1H NMR spectrum of FM3NA

3.2.3 N-ferrocenylméthyl-4-nitro-N-(4-nitrophenyl)benzamide (FM4NA)

3.2.3.1 Synthesis of N-ferrocenylméthyl-4-nitro-N-(4-nitrophenyl)benzamide

In a 100 mL three-necked round-bottom flask, N-ferrocenylmethyl-4-ntroaniline (180 mg, 0.37 mmol) and 4-nitrobenzoyl chloride (94 mg, 0.56 mmol) were dissolved in 50 mL DCM in the presence of pyridine (30µl ,0.37 mmol), the obtained mixture is stirred under an atmosphere of nitrogen for two hours. The evolution of the reaction was followed by TLC. reaction mixture was extracted with a solution of hydrochloric acid (6M) to remove any trace of unreacted pyridine, washed with water, and dried over MgSO4. The solvent was removed under vacuum, and the obtained residue was purified on a silica gel column chromatography using a mixture of DCM and petroleum ether (90:10) as eluent. Evaporation of the solvent gave a red-orange solid product which was recrystallized in 90% ethanol/water to offer a red needle (yield 52%, m.p. 140.5 °C).

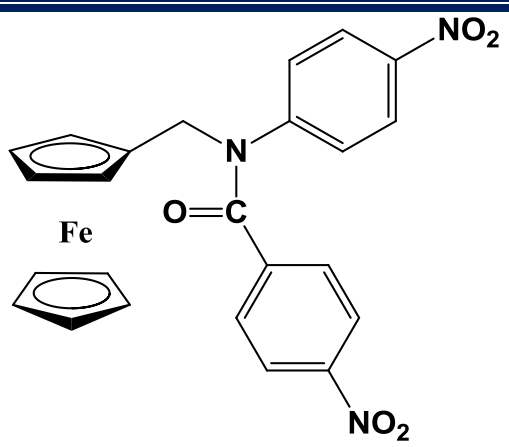

Figure 3.2-15: Chemical structure of N-ferrocenylméthyl-4-nitro-N-(4-nitrophenyl)benzamide

3.2.3.2 **Cyclic voltametric characterization**

N-ferrocenylméthyl-4-nitro-N-(4-nitrophenyl)benzamide was dissolved in DCM solution containing 0.1 M TBAP as a supporting electrolyte. Measurements were carried out in 2×10^{-3} M solution at room temperature in the potential range from 0 to 1 V for FM4N and 0 to 0.9V for FM4NA with scan rate $0.1Vs^{-1}$.

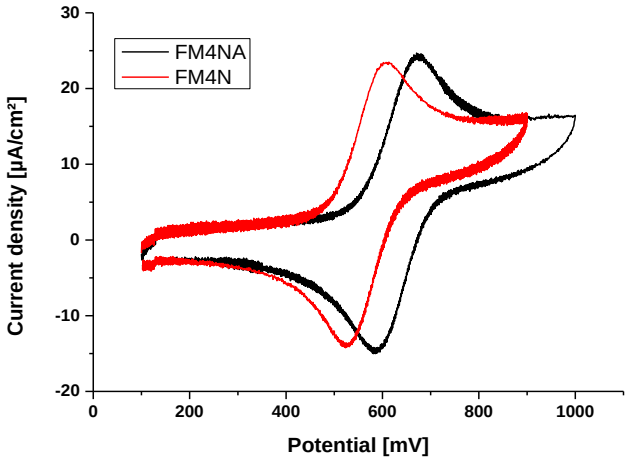

Figure 3.2-16: Cyclic voltammogram of FM4N (red line) and FM4NA (black line) was recorded at 0.1V s^{-1} potential sweep rate on Pt disk electrode at 298K

Cyclic voltammograms of solutions containing FM4N and FM4NA shown in **Figure 3.2-16**. the ratio ipa/ipc is equal to unity and the redox potential $E_{1/2}$ is found equal to 566 mV/SCE for FM4N and 631 mV/SCE for FM4NA. The shift of potential towards left can be attributed to the electron withdrawing nature of the substituted nitro groups. The ΔEp value for the peak-to-peak separation of

the cathodic and anodic peak of the Fc^{3+}/Fc^{2+} couple was 81 mV, which is close to the ideal value of 60 mV for fully reversible one-electron processes

Equation (2.2-5) is used to calculate the diffusion coefficient of FM4NA based on the succession of cyclic voltammograms shown in **Figure 3.2-18**.

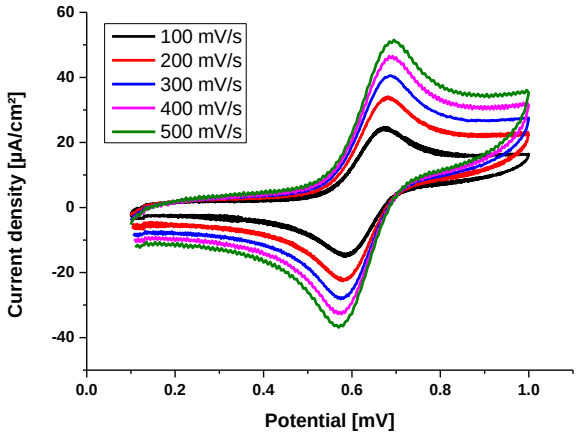

Figure 3.2-17 : cyclic voltammograms of 100 µM of FM4NA at different scan rates (0.1-0.2-0.3-0.4-0.5 $V.s^{-1}$) at 298 K on Pt electrode

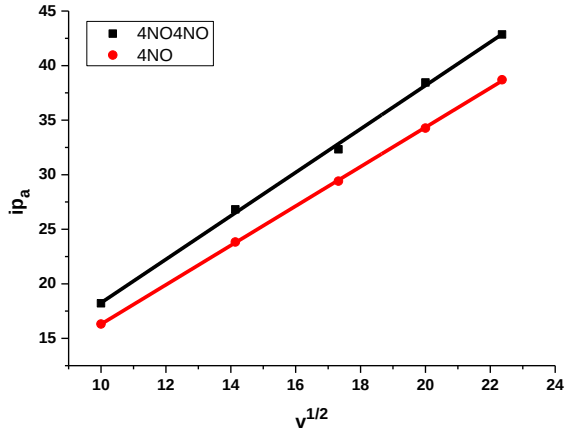

Figure 3.2-18 : Anodic peak current vs. square root of scan rate for FM4N (a) and FM4NA (b)

The linearity of the relation between the square root of the scan rates and the anodic peak current density for both FM4N (a) and FM4NA (b) demonstrated that the redox process was controlled by the diffusion step. The diffusion coefficients were calculated using the slopes of Randles–Sevcik plots. Obtained electrochemical parameters are shown in the **Table 3.2-3**.

Table 3.2-3: The electrochemical parameters of FM4N and FM4NA

Adduct	Formal potential (Ea-Ec) (mV)	Half wave potential $E_{1/2}$ (mV)	Current ratio ipa/ipc	Diffusion coefficient D ($cm^2.s^{-1}$)
FM4N	76	566	1	8.10×10^{8}
FM4NA	81	631	1	6.62×10^{8}

3.2.3.3 **Spectroscopy Characterization**

3.2.3.3.1 UV-visible Spectroscopic characterization

The UV/Vis spectra of DCM solutions of FM4NA are shown in **Figure 3.2-19**. Spectrum has absorption bands at 269 nm that corresponds to $\pi\rightarrow\pi^*$. So, electronic transitions can be described by ligand-centre transition.

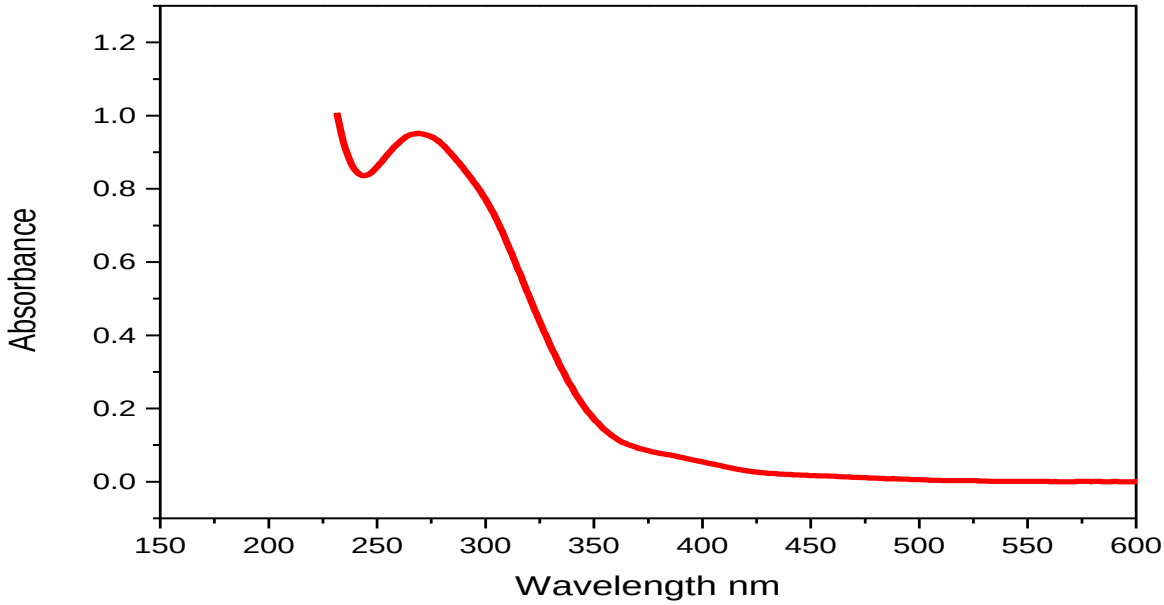

Figure 3.2-19 : Electronic spectra of FM4NA in DCM, Concentration: 10^{-4} M.

3.2.3.3.2 IR characterization

The FTIR spectrum of the product is shown in **Figure 3.2-20**.The figure shows a characteristic absorption peak due to the N-H of amine group at 1628.58 cm^{-1} disappeared, C=O stretching vibration appeared at 1670 cm^{-1} . The main characteristic bands 3112.05 cm^{-1} correspond to C–H bond stretch. The stretching band of C-N is at 1273.60 cm^{-1}, the C=C stretch of the aromatic carbons is at 1593.70 cm^{-1}. The bands at 1108.03 and 1024.63 cm^{-1} correspond to N-O bond stretch, while the

ferrocene cyclopentadienyl ring and C-H bending vibration appeared respectively at 1108.03 and 1024.63 cm^{-1} indicating that the product is monosubstituted

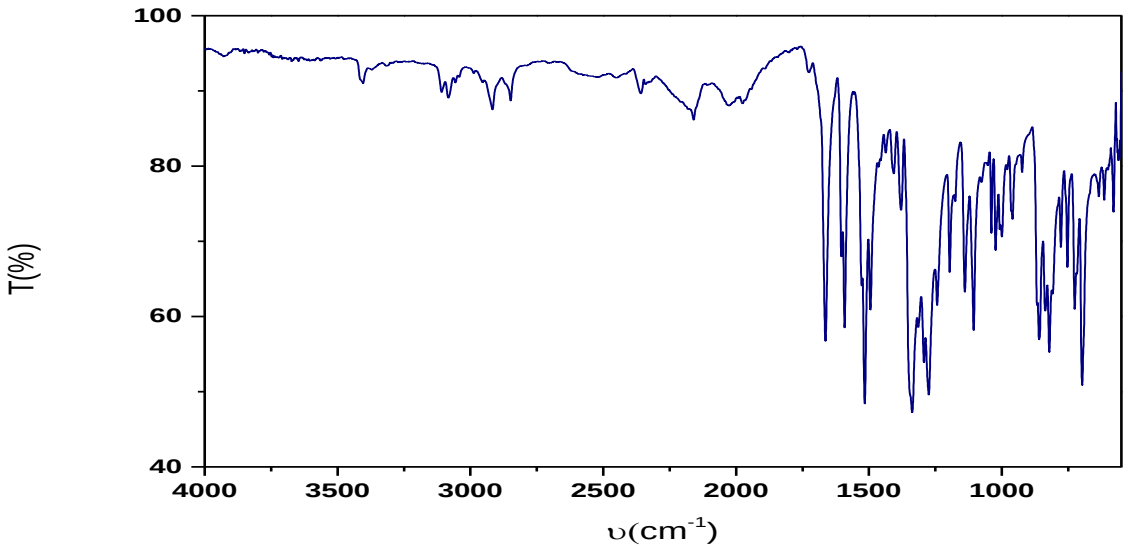

Figure 3.2-20: IR spectrum of FM4NA

3.2.3.3.3 Proton NMR characterization

The 1H, NMR spectrum of N-ferrocenylméthyl-4-nitro-N-(4-nitrophenyl)benzamide, **Figure 3.2-21**, shows all the expected peaks for the nineteen protons of FM4NA. The 9 protons of the α and β protons of the substituted cyclopentadienyl ring of ferrocene and unsubstituted cyclopentadienyl ring resonated at δ = 4.10 ppm. The two protons of the methylene group are shifted at δ = 4.90 ppm, this shift is attributed to electron donor effect of the nitrogen atom. The eight aromatic protons of the phenyl groups resonated respectively at δ = 7.36 (2H, H7), 7.55 (2H, H12) and δ =8.07 (4H, H8 and H13) ppm

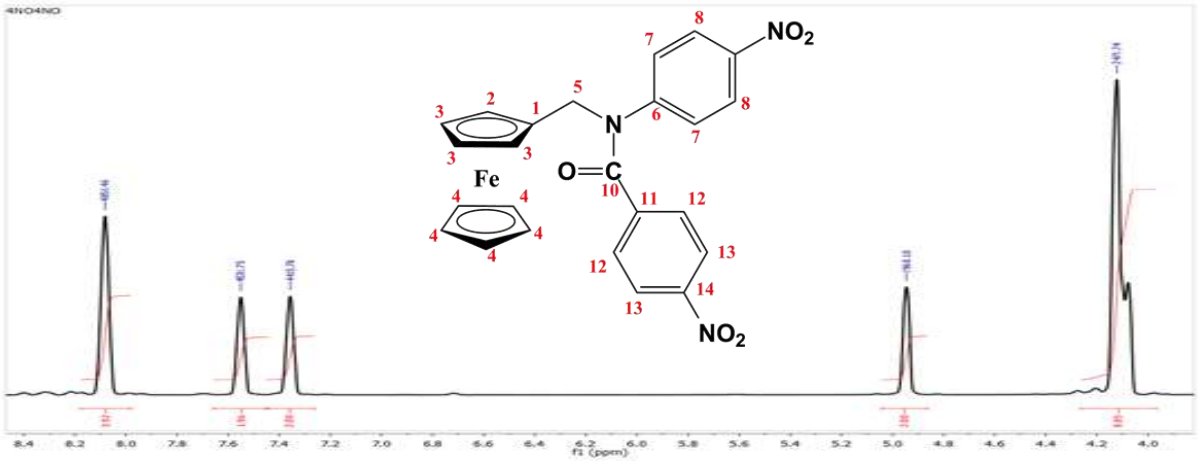

Figure 3.2-21: 1H NMR spectrum of FM4NA

3.2.4 N-ferrocenylmethyl-N-(3-cyanophenyl)-4-nitrobenzamide (FM3CA)

3.2.4.1 Synthesis of N-ferrocenylmethyl-N-(3-cyanophenyl)-4-nitrobenzamide

In a 100 mL three-necked round-bottom flask, N-ferrocenylmethyl-3-ntroaniline (150 mg , 0.32 mmol) and 4-nitrobenzoyl chloride (82 mg, 0.48 mmol) were dissolved in 50 mL DCM in the presence of pyridine (26µl ,0.32 mmol), the obtained mixture is stirred under an atmosphere of nitrogen for 50 minutes . The evolution of the reaction was followed by TLC. reaction mixture was extracted with a solution of hydrochloric acid (6M) to remove any trace of unreacted pyridine, washed with water, and dried over $MgSO_4$. The solvent was removed under vacuum, and the obtained residue was purified on a silica gel column chromatography using a mixture of DCM and toluene (80:20) as eluent. Evaporation of the solvent gave a brown solid product which was recrystallized in 90% ethanol/water to offer a golden needle (yield 59% , m.p. 139.1 °C).

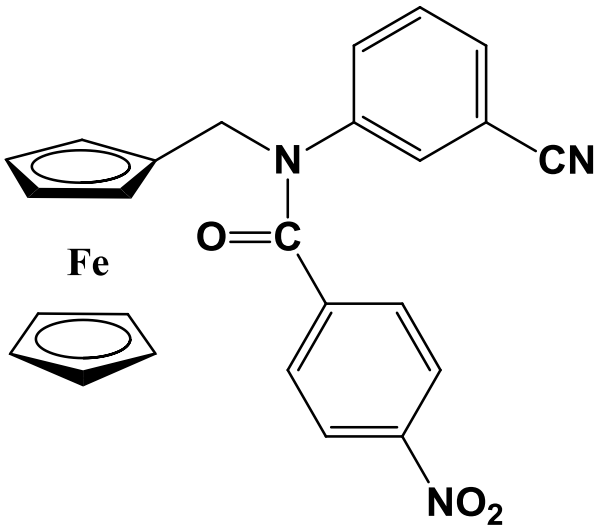

Figure 3.2-22: Chemical structure of N-ferrocenylmethyl-N-(3-cyanophenyl)-4-nitrobenzamide

3.2.4.2 **Cyclic voltametric characterization**

N-ferrocenylmethyl-N-(3-cyanophenyl)-4-nitrobenzamide was dissolved in DCM solution containing 0.1 M TBAP as a supporting electrolyte. Measurements were carried out in 2×10^{-3} M solution at room temperature in the potential range from 0 to 1 V for FM3C and FM3CA with scan rate $0.1Vs^{-1}$.

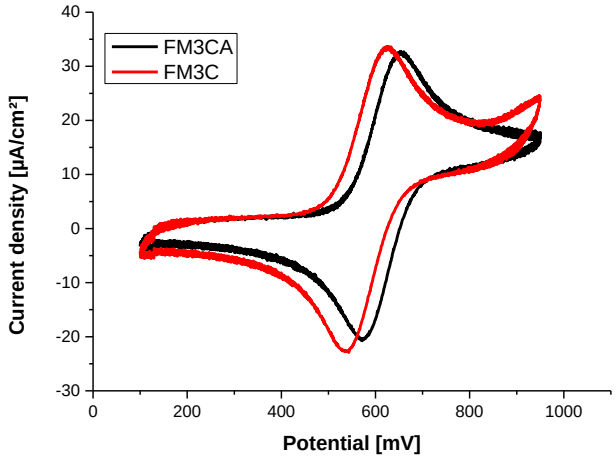

Figure 3.2-23: Cyclic voltammogram of FM3C (red line) and FM3CA (black line) was recorded at 0.1V s−1 potential sweep rate on Pt disk electrode at 298K

Cyclic voltammograms of solutions containing FM2N and FM2NA shown in **Figure 3.2-23**. the ratio ipa/ipc is equal to unity and the redox potential $E_{1/2}$ is found equal to 581 mV/SCE for FM3C

and 613 mV/SCE for FM3CA. The shift of potential towards left can be attributed to the electron withdrawing nature of the substituted nitro groups. The ΔEp value for the peak-to-peak separation of the cathodic and anodic peak of the Fc^{3+}/Fc^{2+} couple was 75 mV, which is close to the ideal value of 60 mV for fully reversible one-electron processes

Equation (2.2-5) is used to calculate the diffusion coefficient of FM3CA based on the succession of cyclic voltammograms shown in **Figure 3.2-24**.

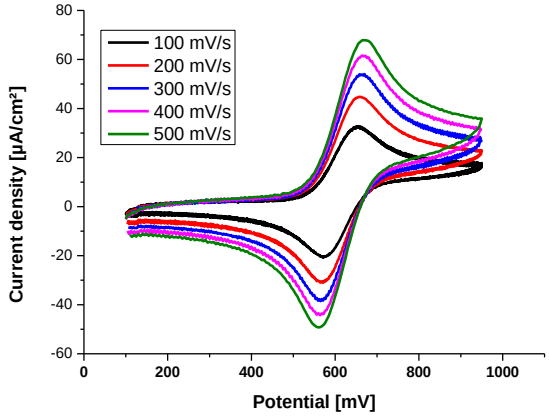

Figure 3.2-24: cyclic voltammograms of 100 µM of FM3CA at different scan rates (0.1-0.2-0.3-0.4-0.5 $V.s^{-1}$) at 298 K on Pt electrode

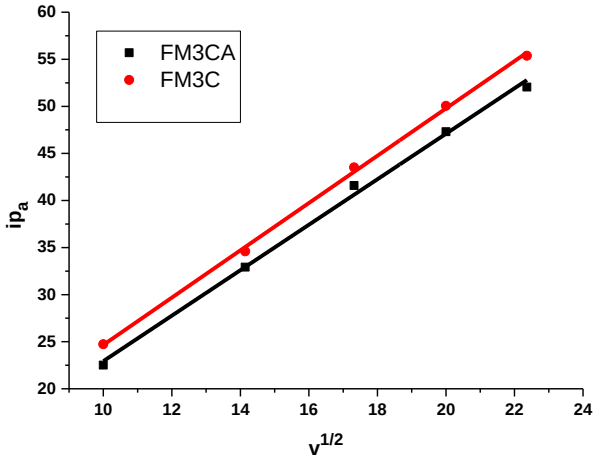

Figure 3.2-25: Anodic peak current vs. square root of scan rate for FM3C (a) and FM3CA (b)

The linearity of the relation between the square root of the scan rates and the anodic peak current density for both FM3C (a) and FM3CA (b) demonstrated that the redox process was controlled by the

diffusion step. The diffusion coefficients were calculated using the slopes of Randles–Sevcik plots. Obtained electrochemical parameters are shown in the **Figure 3.2-4**

Table 3.2-4: The electrochemical parameters of FM3C and FM3CA

Adduct	Formal potential (Ea-Ec) (mV)	Half wave potential $E_{1/2}$ (mV)	Current ratio ipa/ipc	Diffusion coefficient D ($cm^2.s^{-1}$)
FM3C	79	581	0.96	1.28×10^{7}
FM3CA	75	613	0.99	1.19×10^{7}

3.2.4.3 **Spectroscopy Characterization**

3.2.4.3.1 UV-visible Spectroscopic characterization

The UV/Vis spectra of DCM solutions of FM3CA are shown in **Figure 3.2-27**. Spectrum has absorption bands at 302 nm that corresponds to $\pi\rightarrow\pi^*$. So, electronic transitions can be described by ligand-centre transition.

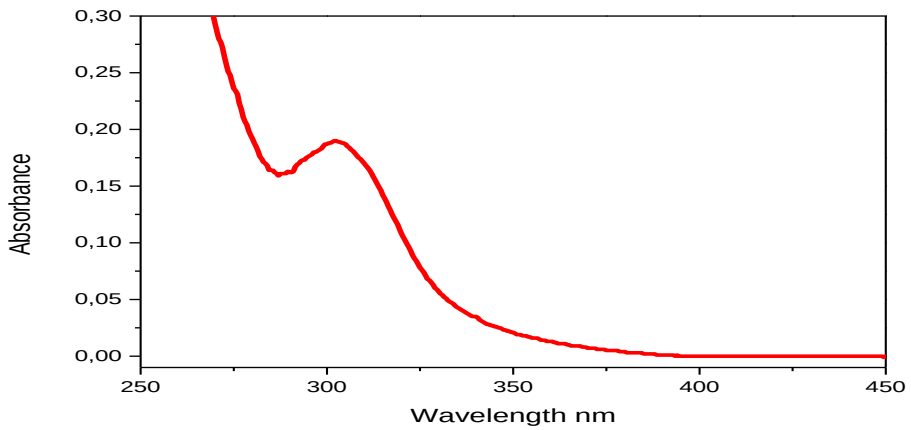

Figure 3.2-26: Electronic spectra of FM3CA in DCM, Concentration: 10^{-5} M.

3.2.4.3.2 IR characterization

The FTIR spectrum of the product is shown in **Figure 3.2-27**. The figure shows a characteristic absorption peak due to the N-H of amine group at 1606.82 cm^{-1} disappeared, C=O stretching vibration appeared at 1647.24 cm-1 . The main characteristic bands 3112.49 cm^{-1} correspond to C–H bond stretch. The stretching band of C-N is at 1268.81 cm^{-1}, the C=C stretch of the aromatic carbons is at 1589.77 cm^{-1}. The bands at 1518.86 and 1345.69 cm^{-1} correspond to N-O bond stretch, while the ferrocene cyclopentadienyl ring and C-H bending vibration appeared respectively at 1108.33 and 1002.33 cm^{-1} indicating that the product is monosubstituted

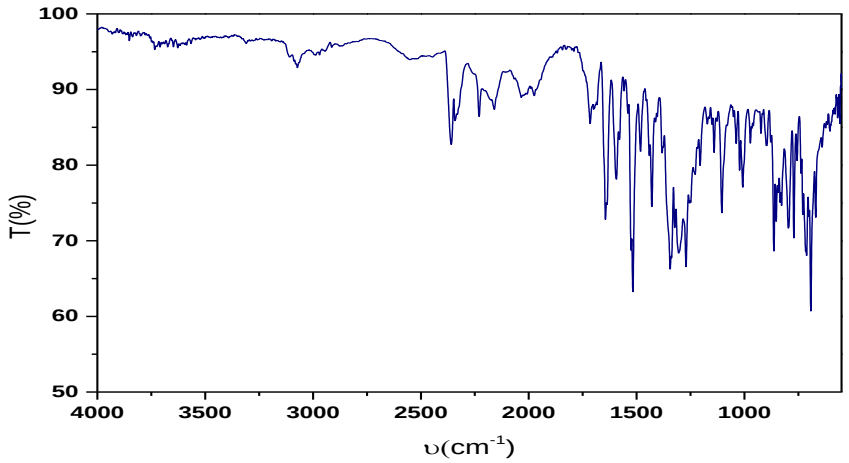

Figure 3.2-27: IR spectrum of FM3CA

3.2.4.3.3 Proton NMR characterization

The 1H, NMR spectrum of N-ferrocenylmethyl-N-(3-cyanophenyl)-4-nitrobenzamide, Figure 3.2-28, shows all the expected peaks for the nineteen protons of FM3CA. The 9 protons of the α and β protons of the substituted cyclopentadienyl ring of ferrocene and unsubstituted cyclopentadienyl ring resonated at δ = 4.10 ppm. The two protons of the methylene group are shifted at δ = 4.88 ppm, this shift is attributed to electron donor effect of the nitrogen atom. The eight aromatic protons of the phenyl groups resonated respectively at δ = 7.29 (1H, H8), 7.37 (1H, H9), 7.54 (2H, H13), 7.63 (1H, H7), 7.78 (1H, H10) and δ =8.08 (2H, H14) ppm.

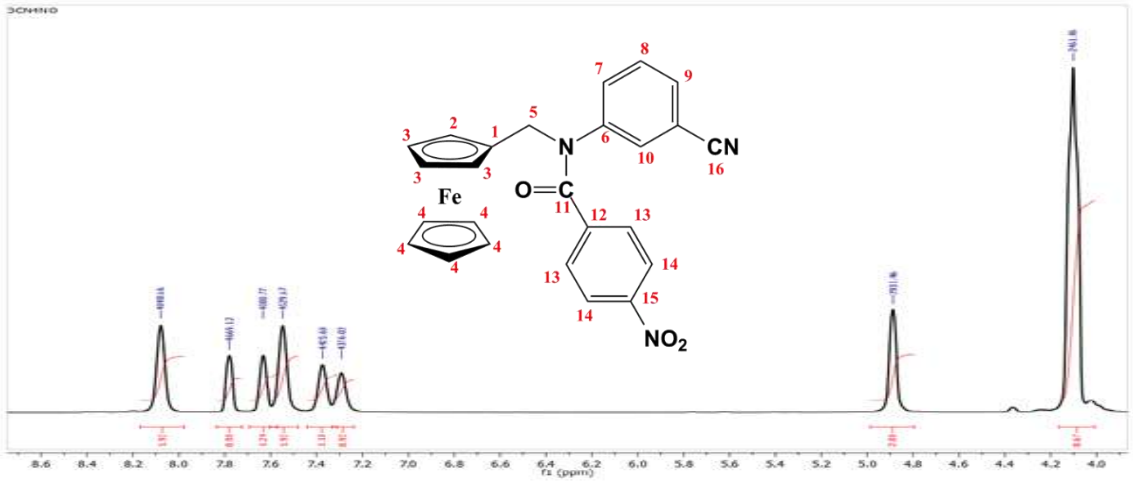

Figure 3.2-28: 1H NMR spectrum of FM3CA

3.2.5 N-ferrocenylmethyl-N-(4-cyanophenyl)-4-nitrobenzamide (FM4CA)

3.2.5.1 Synthesis of N-ferrocenylmethyl-N-(4-cyanophenyl)-4-nitrobenzamide

In a 100 mL three-necked round-bottom flask, N-ferrocenylmethyl-4-ntroaniline (150 mg , 0.32 mmol) and 4-nitrobenzoyl chloride (82 mg, 0.48 mmol) were dissolved in 50 mL DCM in the presence of pyridine (26µl ,0.32 mmol), the obtained mixture is stirred under an atmosphere of nitrogen for 50 minutes . The evolution of the reaction was followed by TLC. reaction mixture was extracted with a solution of hydrochloric acid (6M) to remove any trace of unreacted pyridine, washed with water, and dried over $MgSO_4$. The solvent was removed under vacuum, and the obtained residue was purified on a silica gel column chromatography using a mixture of DCM and toluene (90:10) as eluent. Evaporation of the solvent gave a yellow solid product which was recrystallized in 90% ethanol/water to offer a golden yellow cubic (yield 57% , m.p. 128.7 °C)

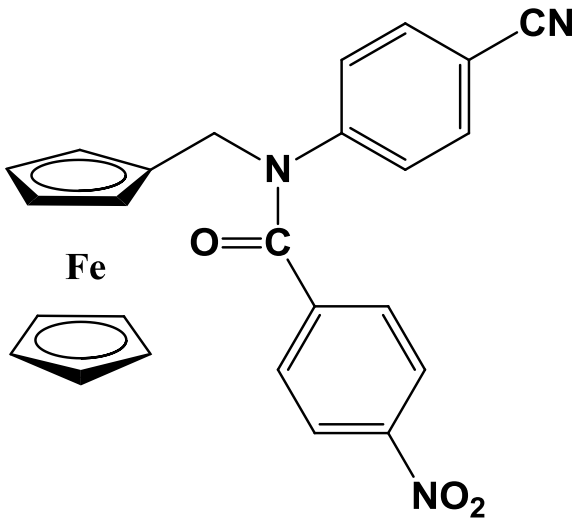

Figure 3.2-29: Chemical structure of N-ferrocenylmethyl-N-phenylbenzamide

3.2.5.2 **Cyclic voltametric characterization**

N-ferrocenylmethyl-N-(4-cyanophenyl)-4-nitrobenzamide was dissolved in DCM solution containing 0.1 M TBAP as a supporting electrolyte. Measurements were carried out in 2×10^{-3} M solution at room temperature in the potential range from 0 to 1 V for FM4C and FM4CA with scan rate $0.1Vs^{-1}$.

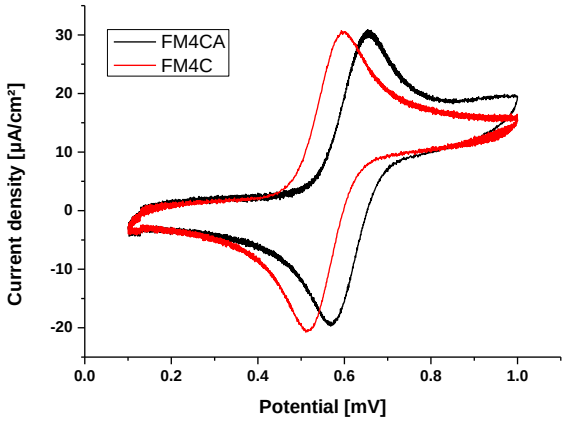

Figure 3.2-30: Cyclic voltammogram of FM4C (red line) and FM4CA (black line) was recorded at 0.1V s^{-1} potential sweep rate on Pt disk electrode at 298K

Cyclic voltammograms of solutions containing FM4C and FM4CA shown in **Figure 3.2-30**. the ratio ipa/ipc is equal to unity and the redox potential $E_{1/2}$ is found equal to 557 mV/SCE for FM4C and 612 mV/SCE for FM4CA. The shift of potential towards left can be attributed to the electron withdrawing nature of the substituted nitro groups. The ΔEp value for the peak-to-peak separation of the cathodic and anodic peak of the Fc^{3+}/Fc^{2+} couple was 76 mV, which is close to the ideal value of 60 mV for fully reversible one-electron processes

Equation (2.2-5) is used to calculate the diffusion coefficient of FM4CA based on the succession of cyclic voltammograms shown in **Figure 3.2-31**.

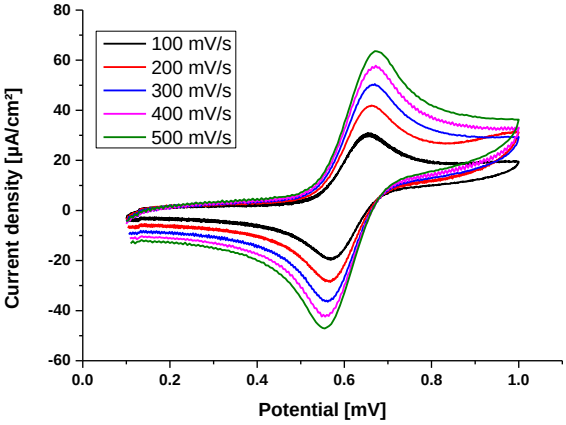

Figure 3.2-31: cyclic voltammograms of 100 µM of FM4CA at different scan rates (0.1-0.2-0.3-0.4-0.5 V.s^{-1}) at 298 K on Pt electrode

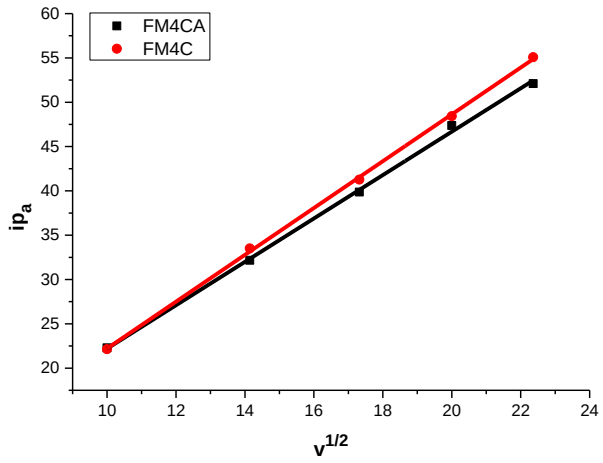

Figure 3.2-32: Anodic peak current vs. square root of scan rate for FM4C (a) and FM4CA (b)

The linearity of the relation between the square root of the scan rates and the anodic peak current density for both FM4C (a) and FM4CA (b) demonstrated that the redox process was controlled by the diffusion step. The diffusion coefficients were calculated using the slopes of Randles–Sevcik plots. Obtained electrochemical parameters are shown in the **Table 3.2-5**.

Table 3.2-5: The electrochemical parameters of FM4C and FM4CA

Adduct	Formal potential (Ea-Ec) (mV)	Half wave potential $E_{1/2}$ (mV)	Current ratio ipa/ipc	Diffusion coefficient D ($cm^2.s^{-1}$)
FM4C	75	557	0.97	1.42×10^{7}
FM4CA	76	612	0.99	1.21×10^{7}

3.2.5.3 Spectroscopy Characterization

3.2.5.3.1 UV-visible Spectroscopic characterization

The UV/Vis spectra of DCM solutions of FM4CA are shown in **Figure 3.2-33**. Spectrum has absorption bands at 259 nm that corresponds to $\pi\rightarrow\pi^*$. So, electronic transitions can be described by ligand-centre transition.

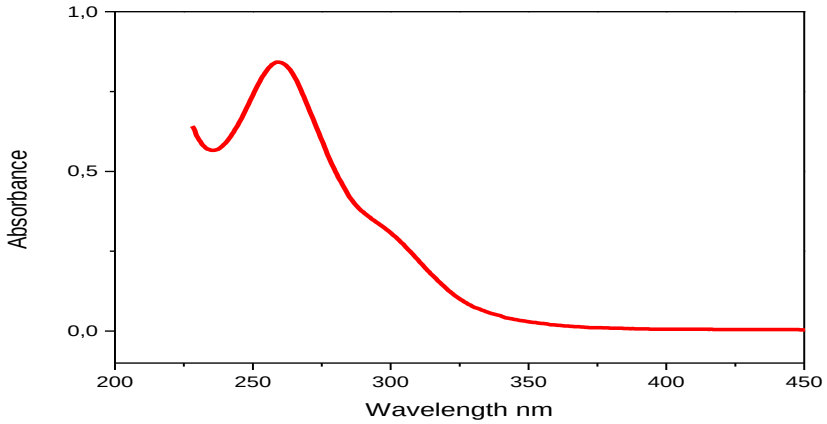

Figure 3.2-33: Electronic spectra of FM4CA

3.2.5.3.2 IR characterization

The FTIR spectrum of the product is shown in **Figure 3.2-34**. The figure shows a characteristic absorption peak due to the N-H of amine group at 1604.41 cm^{-1} disappeared, C=O stretching vibration appeared at 1640.21 cm-1 . The main characteristic bands 3102.23 cm^{-1} correspond to C–H bond stretch. The stretching band of C-N is at 1273.60 cm^{-1}, the C=C stretch of the aromatic carbons is at 1601.01 cm^{-1}. The bands at 1517.66 and 1344.73 cm^{-1} correspond to N-O bond stretch, while the ferrocene cyclopentadienyl ring and C-H bending vibration appeared respectively at 1100.67 and 1008.69 cm^{-1} indicating that the product is monosubstituted

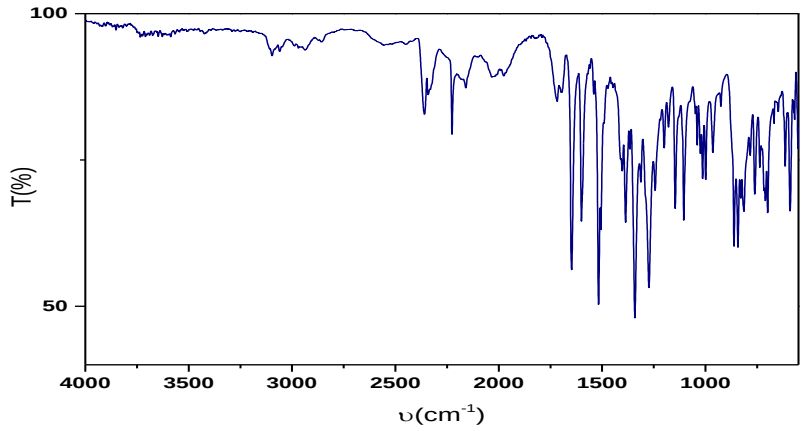

Figure 3.2-34: IR spectrum of FM4CA

3.2.5.3.3 Proton NMR characterization

The 1H, NMR spectrum of N-ferrocenylmethyl-N-(4-cyanophenyl)-4-nitrobenzamide, **Figure 3.2-35**, shows all the expected peaks for the nineteen protons of ANC4. The 9 protons of the α and β protons of the substituted cyclopentadienyl ring of ferrocene and unsubstituted cyclopentadienyl ring resonated at δ = 4.10 ppm. The two protons of the methylene group are shifted at δ = 4.91 ppm, this shift is attributed to electron donor effect of the nitrogen atom. The eight aromatic protons of the phenyl groups resonated respectively at δ = 7.28 (2H, H8), 7.71 (2H, H7), 7.52 (2H, H12) and δ =8.07 (2H, H13) ppm.

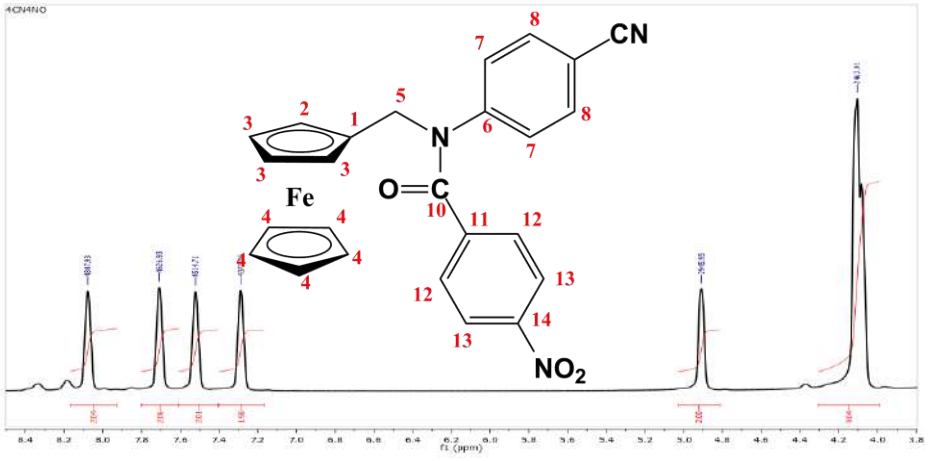

Figure 3.2-35: 1H NMR spectrum of FM4CA

Chapter 4

BSA interaction study

4.1 the study of the interaction of FcDB-BSA

4.1.1 Electrochemical BSA interaction study

Cyclic voltammetry was employed to investigate the interactions between synthesised ferrocenylmethylaniline derivatives and BSA in physiological pH using phosphate buffer solution at pH=7.2 [147]. BSA. Stock solutions were prepared by dissolving known amounts of BSA in 10 mL of double-distilled water, The concentration of the substance was evaluated based on the extinction coefficient of 44,300 $M^{-1}.cm^{-1}$ at 280 nm. The stock solutions were used within a period of 5 days post-preparation and were stored at a temperature of 4 °C until their usage. The method involves the registration of voltammograms for each derivative's 1 mM solution in ethanol/PBS (90:10) solution with 0.1 M TBFP as the supporting electrolyte. The voltammograms are recorded both in the presence and absence of BSA, while maintaining a pH value of 7.2.

After every electrochemical assay the working electrode was polished and the solution was degassed from oxygen by bubbling nitrogen gas for at least 15 minutes[148,149].

4.1.1.1 Binding constants

The interaction between FcDB and bovine serum albumin (BSA) was assessed by evaluating the shift in peak potential and reduction in peak height [150]. A decline in peak height and shift in peak negativity was observed when FcDB was titrated with BSA, up to an addition of approximately 5 µM BSA.

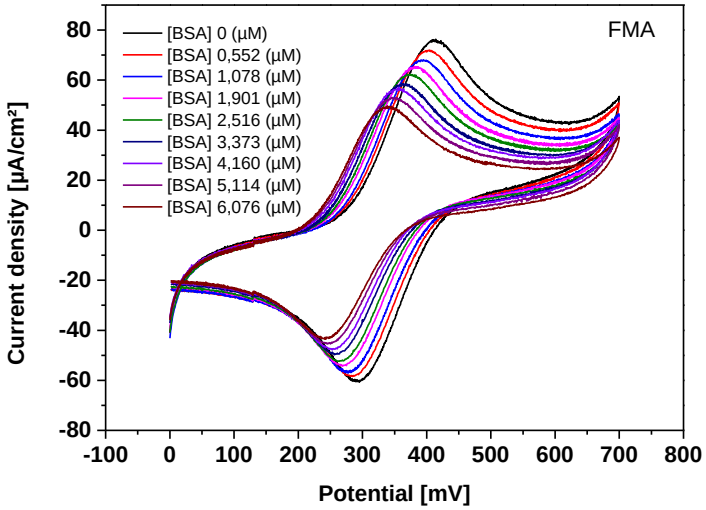
FMA
[BSA] 0 (µM)
[BSA] 0,552 (µM)
[BSA] 1,078 (µM)
[BSA] 1,901 (µM)
[BSA] 2,516 (µM)
[BSA] 3,373 (µM)
[BSA] 4,160 (µM)
[BSA] 5,114 (µM)
[BSA] 6,076 (µM)
Current density [µA/cm²]
Potential [mV]

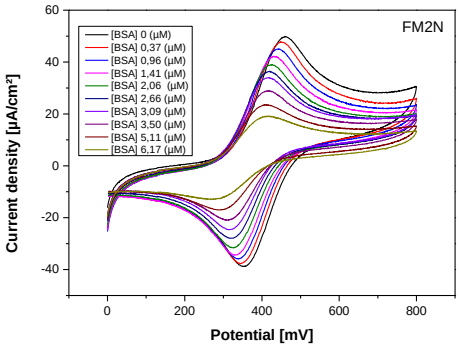
FM2N
[BSA] 0 (µM)
[BSA] 0,37 (µM)
[BSA] 0,96 (µM)
[BSA] 1,41 (µM)
[BSA] 2,06 (µM)
[BSA] 2,66 (µM)
[BSA] 3,09 (µM)
[BSA] 3,50 (µM)
[BSA] 5,11 (µM)
[BSA] 6,17 (µM)
Current density [µA/cm²]
Potential [mV]

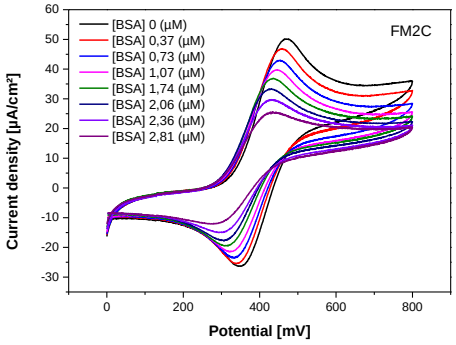
FM2C
[BSA] 0 (µM)
[BSA] 0,37 (µM)
[BSA] 0,73 (µM)
[BSA] 1,07 (µM)
[BSA] 1,74 (µM)
[BSA] 2,06 (µM)
[BSA] 2,36 (µM)
[BSA] 2,81 (µM)
Current density [µA/cm²]
Potential [mV]

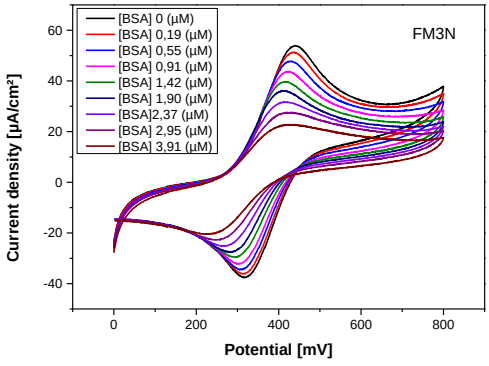
FM3N
[BSA] 0 (µM)
[BSA] 0,19 (µM)
[BSA] 0,55 (µM)
[BSA] 0,91 (µM)
[BSA] 1,42 (µM)
[BSA] 1,90 (µM)
[BSA]2,37 (µM)
[BSA] 2,95 (µM)
[BSA] 3,91 (µM)
Current density [µA/cm²]
Potential [mV]

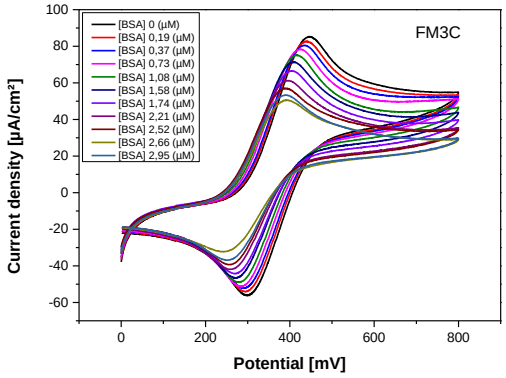
FM3C
[BSA] 0 (µM)
[BSA] 0,19 (µM)
[BSA] 0,37 (µM)
[BSA] 0,73 (µM)
[BSA] 1,08 (µM)
[BSA] 1,58 (µM)
[BSA] 1,74 (µM)
[BSA] 2,21 (µM)
[BSA] 2,52 (µM)
[BSA] 2,66 (µM)
[BSA] 2,95 (µM)
Current density [µA/cm²]
Potential [mV]

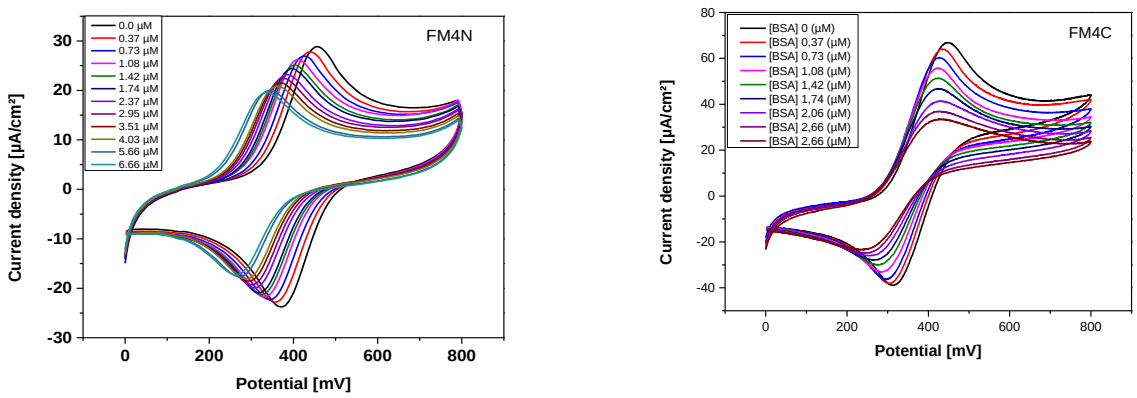

Figure 4.1-1: The cyclic voltammograms of 1 mM FcDB were obtained by performing a potential sweep rate of 0.1V s^{-1} on a GC disk electrode at 298K. The measurements were taken in the presence and absence of increasing concentrations of BSA in ethanol/PBS (90:10) solution with a pH of 7.2, using 0.1 M TBFP as a supporting electrolyte.

The association of FcDB with BSA leads to the formation of a complex, the thermodynamic properties of which can provide valuable insights into the binding or formation constant, expressed in units of M^{-1}. The K_b values of the FcDB-BSA complexes were calculated by utilizing the peak current values according to the given equation.(4.1-1).

$$\log \frac{1}{[BSA]} = log\, K_b + log \frac{i}{i_0 - i} \qquad (4.1\text{-}1)$$

Where [BSA] is the BSA concentration, K_b represents the binding constant, and i_0 and i indicate the anodic peak current density of the free and BSA-bound ligands respectively

The linear form of the $f(1/C) = i/(i_0-i)$ extracted from the above voltammogram are shown below

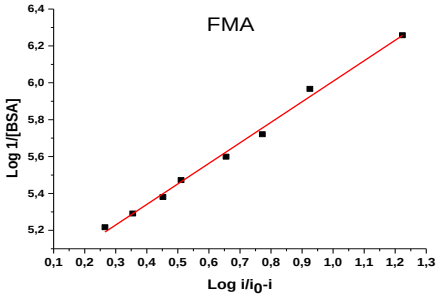

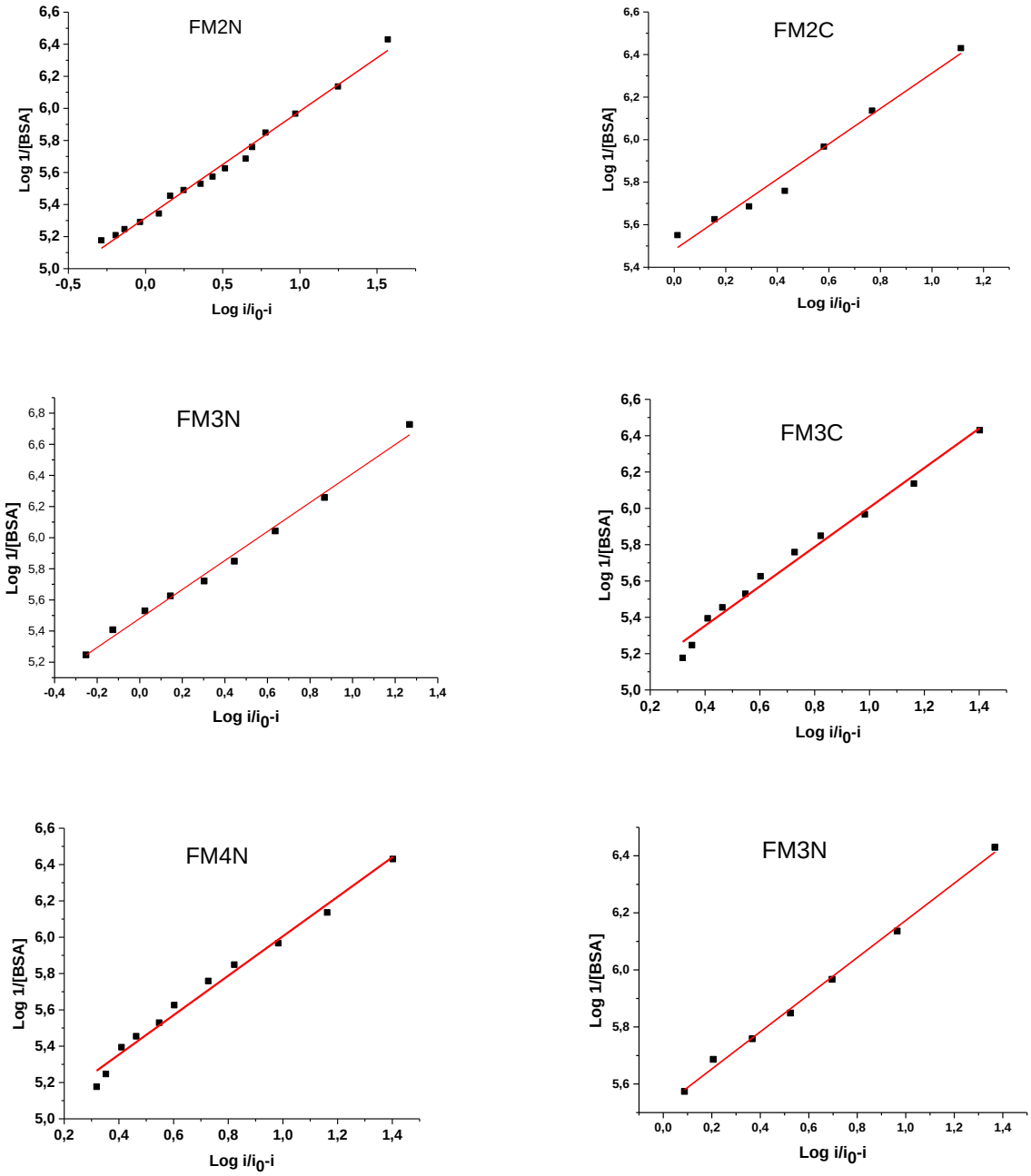

Figure 4.1-2: Log/ (1/[BSA]) versus log i/(i0-i) for FcDB with varying concentration of BSA used to calculate the binding constant of BSA- FcDB product.

The Gibbs free energy equation (4.1-2) and formation constant data were used to determine ΔG, the obtained values are given in **Table 4.1-1** .

$$\mathbf{\Delta}G\ (kJmol.1^{-1}) = RTlnK_b \qquad 4.1\text{-}2)$$

Where ΔG represents the free binding energy in $KJmol^{-1}$, R represents the gas constant, 8.32 $Jmol^{-1}K^{-1}$ while, T represents the absolute temperature, 298 K

Table 4.1-1: Binding constant and binding free energy values

Adduct	Equation	R^2	Kb (M^{-1})	ΔG ($KJ.mol^{-1}$)
BSA –**FMA**	y = 1,113x + 4,895	0.994	7.85×10^4	-27.95
BSA – **FM2N**	y = 0,664x + 5,317	0.989	2.07×10^5	-30.35
BSA – **FM3N**	y = 0,931x + 5,480	0.991	2.512×10^5	-30.82
BSA – **FM4N**	y = 1.087x + 4.919	0.983	8.297×10^4	-28.08
BSA – **FM2C**	y = 0,830x + 5,482	0.975	3.034×10^5	-31.29
BSA – **FM3C**	y = 1.086x + 4.919	0.983	1.621×10^5	-29.74
BSA – **FM4C**	y = 0,651x + 5,522	0.996	3.326×10^5	-31.52

The binding free energy obtained indicates the magnitude and sign of the interaction between the investigated ligands and BSA, with the former being indicative of the electrostatic mode and the latter indicating the spontaneity of the interaction [151].

4.1.1.2 Ratio of binding constants

The voltammograms depicted in **Figure 4.1-3**, which illustrate the cyclic voltammograms of a 1 mM FcDB solution in the absence and presence of BSA, can be utilized to determine the ratio of binding constants between the reduced form of FcDB and BSA and its oxidized form, $[FcDB]^+$. The addition of BSA leads to a shift in the anodic and cathodic peak potential values, which can be employed to calculate the binding constant ratio [152].

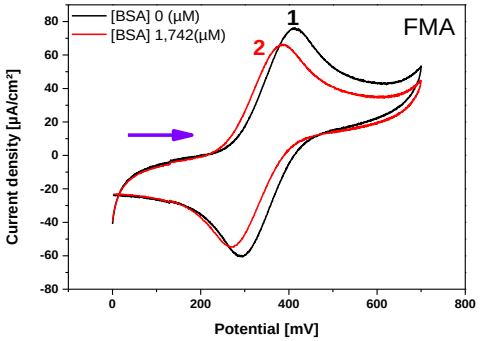

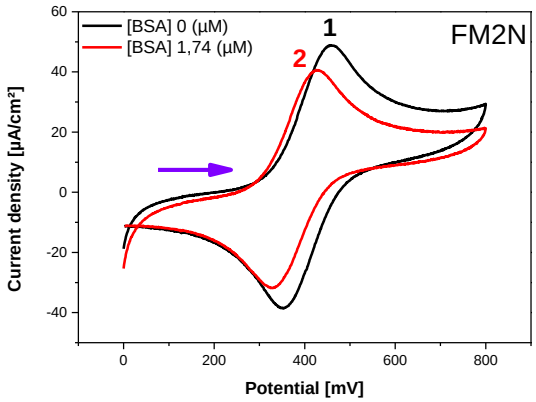
[BSA] 0 (µM)
[BSA] 1,74 (µM)
1
2
FM2N
Current density [µA/cm²]
Potential [mV]

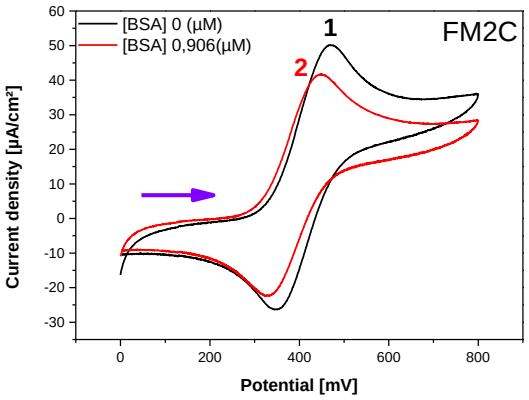
[BSA] 0 (µM)
[BSA] 0,906(µM)
1
2
FM2C
Current density [µA/cm²]
Potential [mV]

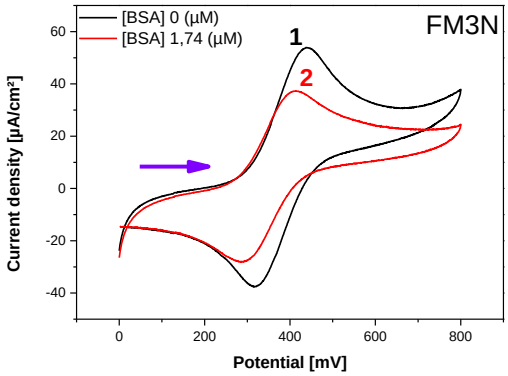
[BSA] 0 (µM)
[BSA] 1,74 (µM)
1
2
FM3N
Current density [µA/cm²]
Potential [mV]

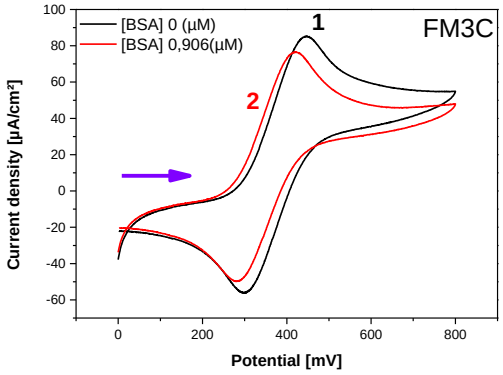
[BSA] 0 (µM)
[BSA] 0,906(µM)
1
2
FM3C
Current density [µA/cm²]
Potential [mV]

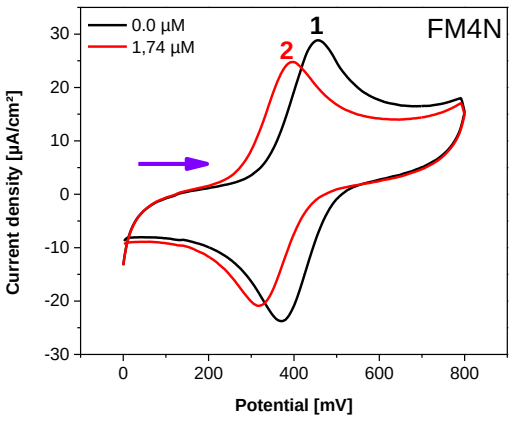
0.0 µM
1,74 µM
1
2
FM4N
Current density [µA/cm²]
Potential [mV]

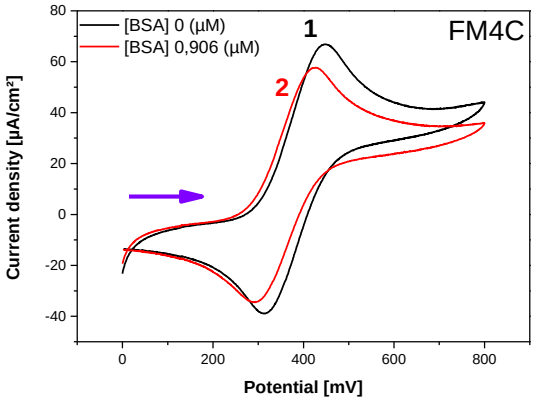
[BSA] 0 (µM)
[BSA] 0,906 (µM)
1
2
FM4C
Current density [µA/cm²]
Potential [mV]

Figure 4.1-3: The cyclic voltammograms were recorded for a 1 mM concentration of the investigated FcDB compounds, both in the presence (indicated by the red line) and absence (indicated by the black line) of BSA, at a scan rate of 100 $mV.s^{-1}$

In instances where the introduction of BSA causes a shift in the values of both anodic and cathodic peak potentials, the equilibrium principles outlined below may be employed [153],

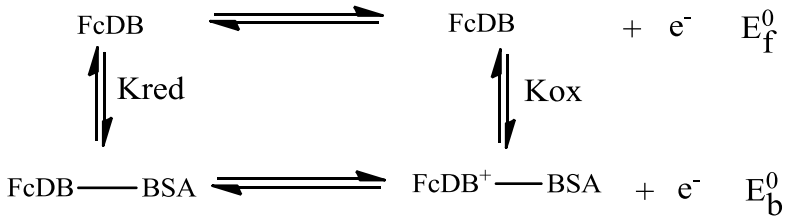

Figure 4.1-4: Redox process of the free and BSA bounded FcDB

By utilizing the Nernst relation to the equilibriums presented in **Figure 4.1-3**, the ensuing equation (4.1-3) is derived.

$$\Delta E^0 = E_b^0 - E_f^0 = E^0(\text{FcDB} - \text{BSA}) - E^0(\text{BSA}) = 0.061\frac{k_{ox}}{k_{red}} \qquad (4.1\text{-}3)$$

The formal potentials of the FcDB+/FcDB couple for both free and BSA-bound compounds are represented as E_f^0 and E_b^0, respectively. The voltammograms presented in **Figure 4.1-3** were used to calculate the formal potential shift, which is summarized in **Table 4.1-2**. Additionally, the ratios of binding constants were determined using equation (4.1-3) with appropriate replacements.

Table 4.1-2: The information obtained from the FcDB in its free form and when bound to BSA was utilized in the computation of the ratio of binding constants.

Entry	Epa	Epc	E°(V)	ΔE°(mV)	Kred/Kox
FMA	0.411	0.292	0.352	-24	2.3
BSA-FMA	0.388	0.268	0.328		
FM2N	0.458	0.424	0.350	-28.5	3.08
BSA- FM2N	0.353	0.330	0.342		
FM3N	0.439	0.318	0.379	-19	2.14
BSA- FM3N	0.412	0.278	0.345		
FM4N	0.495	0.368	0.432	-73.25	17.44
BSA- FM4N	0.397	0.319	0.358		

FM2C	0.470	0.353	0.412	-23	2.50
BSA- FM2C	0.448	0.328	0.408		
FM3C	0.448	0.293	0.371	-19	2.09
BSA- FM3C	0.421	0.282	0.352		
FM4C	0.450	0.314	0.382	-23	2.45
BSA- FM4C	0.425	0.293	0.359		

Based on the ratios of binding constants obtained, it can be inferred that the reduced form of FcDB exhibits stronger binding affinity towards BSA when compared to its oxidized forms [$FcDB^+$].

4.1.1.3 Diffusion coefficients

The electrochemical behavior of the free and BSA-bound FcDB was utilized to obtain their respective diffusion coefficients, as illustrated in **Figure 4.1-5**. Cyclic voltammograms were recorded for 1 mM of FcDB in both the absence and presence of BSA while varying the potential scan rates. These voltammograms demonstrated well-defined and stable redox peaks, which were associated with the redox process of FcDB.

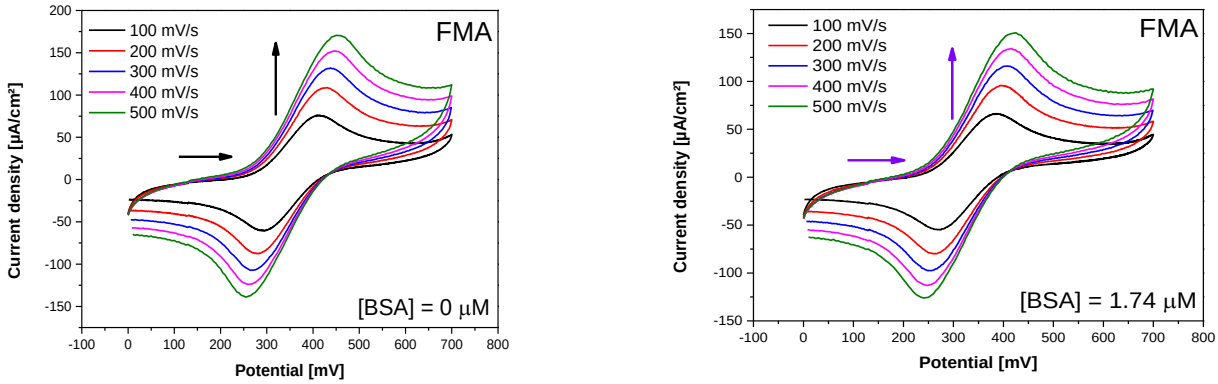

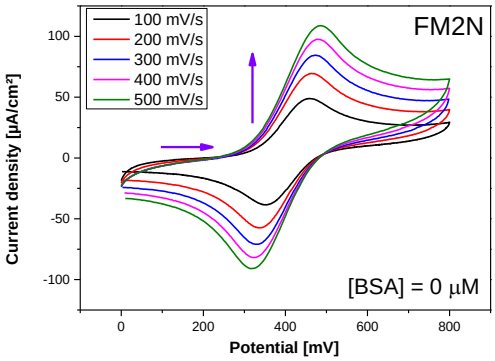
FM2N
100 mV/s
200 mV/s
300 mV/s
400 mV/s
500 mV/s
[BSA] = 0 μM
Current density [μA/cm²]
Potential [mV]

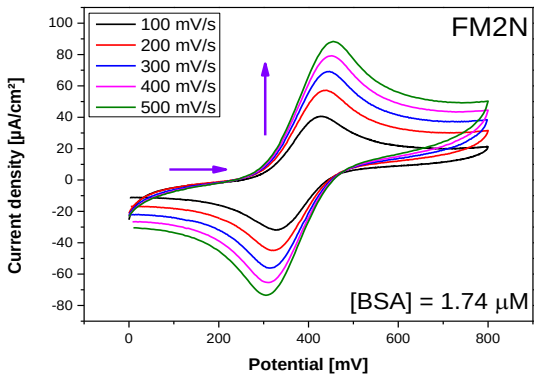
FM2N
100 mV/s
200 mV/s
300 mV/s
400 mV/s
500 mV/s
[BSA] = 1.74 μM
Current density [μA/cm²]
Potential [mV]

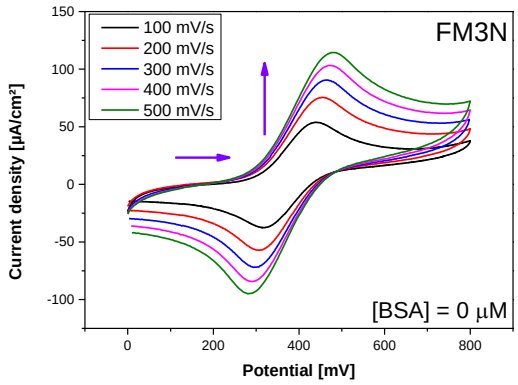
FM3N
100 mV/s
200 mV/s
300 mV/s
400 mV/s
500 mV/s
[BSA] = 0 μM
Current density [μA/cm²]
Potential [mV]

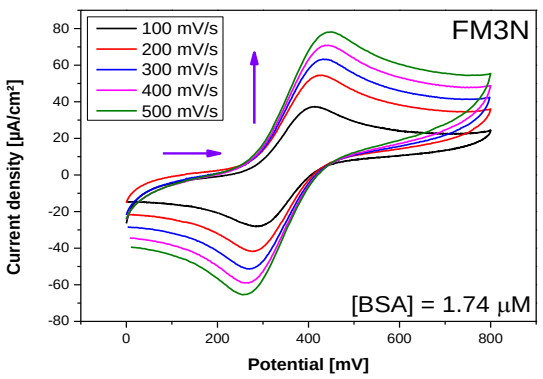
FM3N
100 mV/s
200 mV/s
300 mV/s
400 mV/s
500 mV/s
[BSA] = 1.74 μM
Current density [μA/cm²]
Potential [mV]

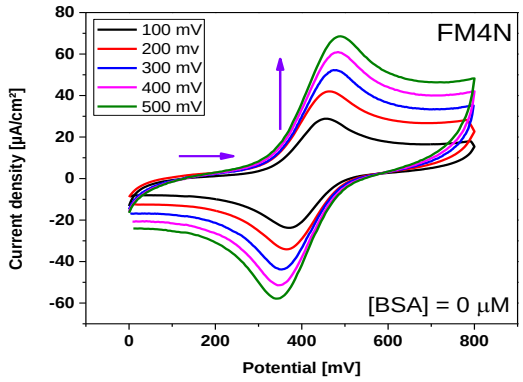
FM4N
100 mV
200 mv
300 mV
400 mV
500 mV
[BSA] = 0 μM
Current density [μA/cm²]
Potential [mV]

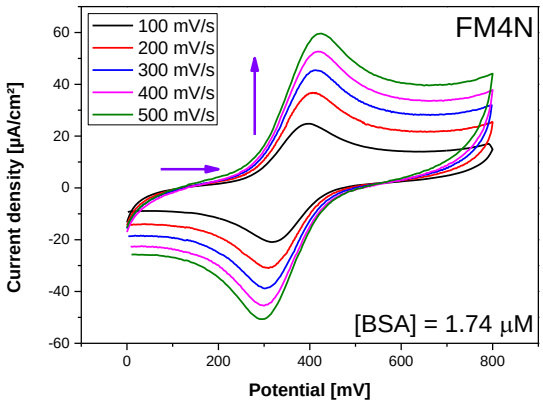
FM4N
100 mV/s
200 mV/s
300 mV/s
400 mV/s
500 mV/s
[BSA] = 1.74 μM
Current density [μA/cm²]
Potential [mV]

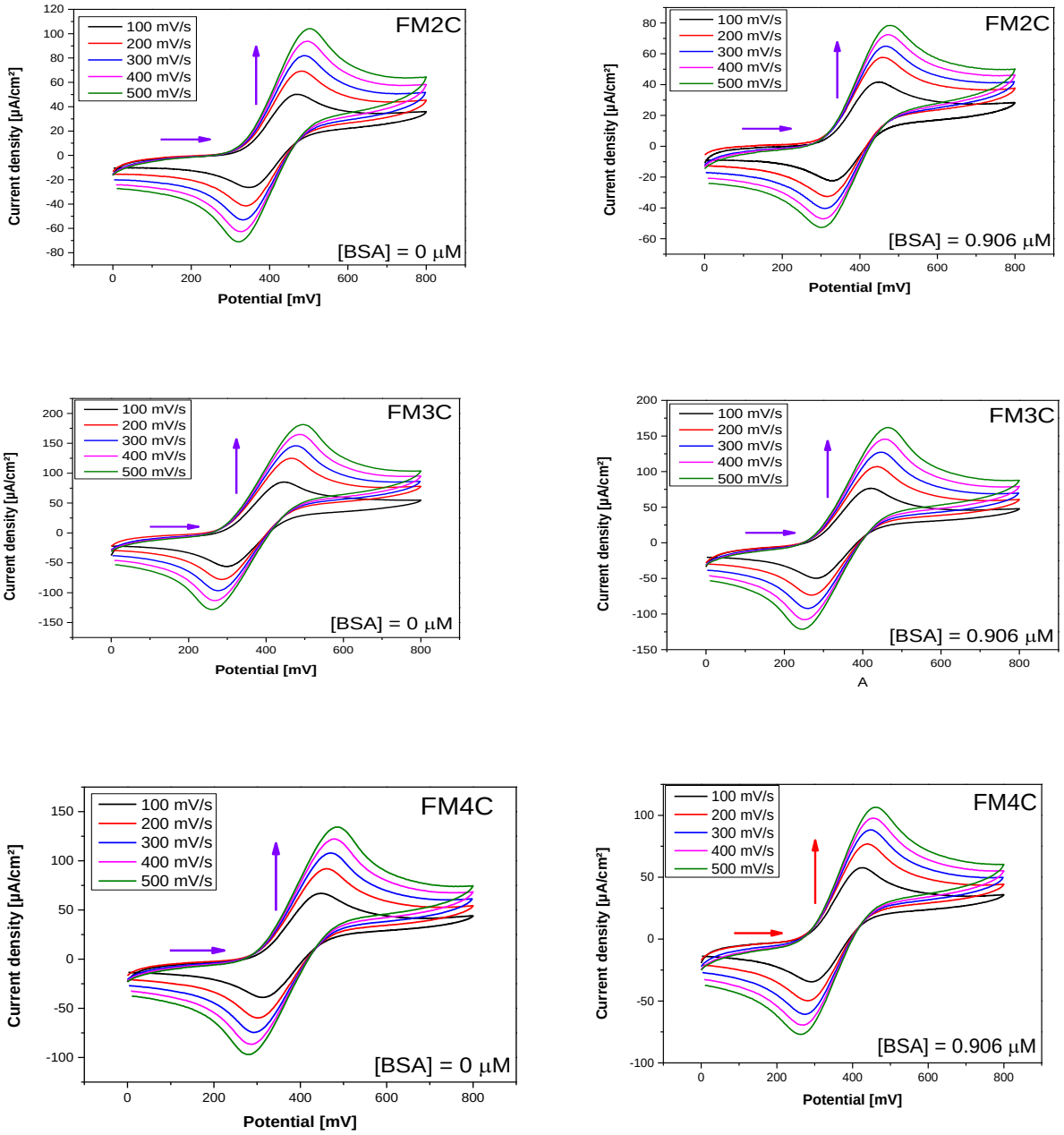

Figure 4.1-5: Cyclic voltammetry was performed on 1 mM of FcDB in a solution of ethanol/PBS (90:10) with various scan rates (0.1 , 0.2 ,0.3 ,0.4 and 0.5 $V \cdot s^{-1}$) in both the absence and presence of BSA.

The Randles–Sevcik equation was used to determinate the coefficient of diffusion of the free form of the FcDB and the bound form FcDB -BSA

$$i = 2.69 \times 10^5 n^{3/2} A C D^{1/2} v^{1/2} \qquad (4.1\text{-}4)$$

where i is the peak current (A), A is the surface area of the electrode (cm^2), C is the bulk concentration ($mol.cm^{-3}$) of the electro active species, D is the diffusion coefficient ($cm^2.s^{-1}$) and v is the scan rate ($V.s^{-1}$)

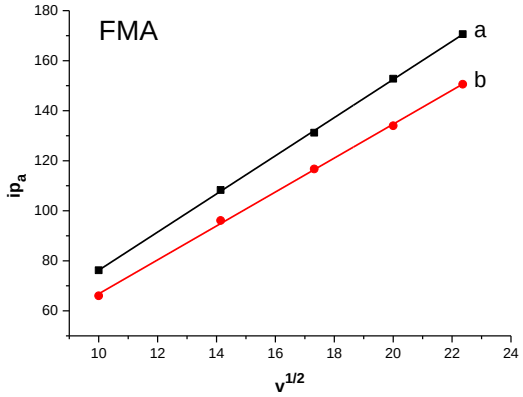
FMA
a
b
ip_a
$v^{1/2}$

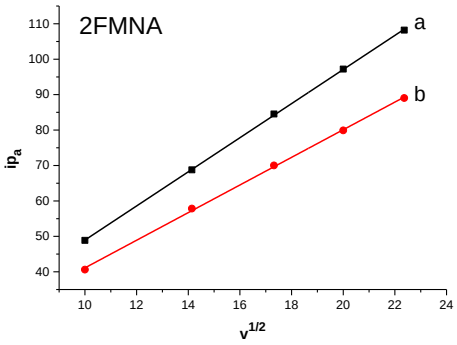
2FMNA
a
b
ip_a
$v^{1/2}$

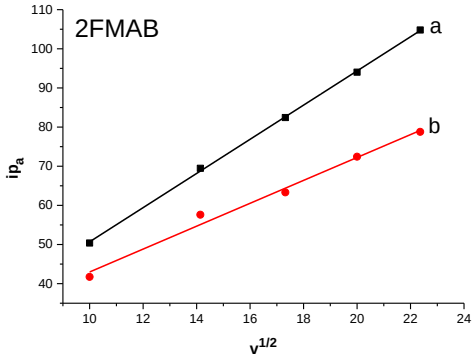
2FMAB
a
b
ip_a
$v^{1/2}$

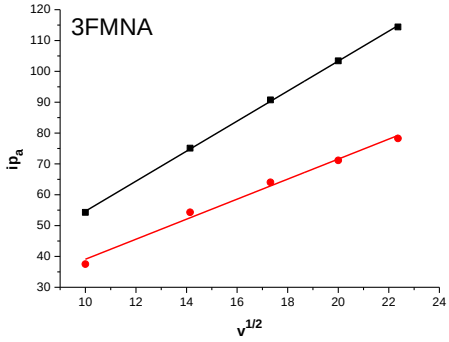
3FMNA
ip_a
$v^{1/2}$

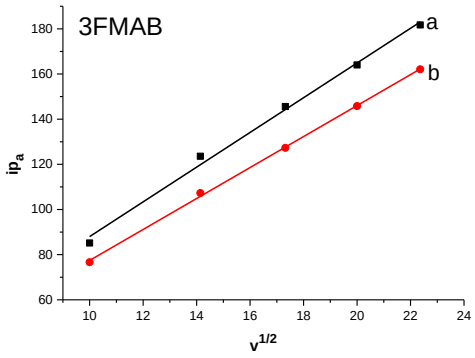
3FMAB
a
b
ip_a
$v^{1/2}$

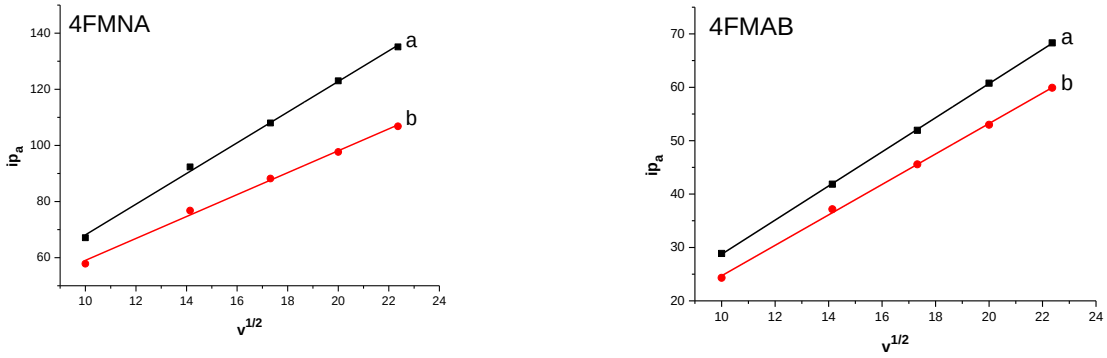

Figure 4.1-6: ia =f ($v^{1/2}$) plots of FcDB (1 mM) in the absence of BSA (a) and presence BSA (b) at scan rates ranging from 0.1 to 0.5 $V.s^{-1}$ in a solution of ethanol/PBS (90:10)

The correlation between FcDB-BSA, as illustrated in equation (4.1-4), implies that the redox process is kinetically regulated by the diffusion step. The diffusion coefficients were calculated using the slopes of the Randles-Sevcik plots and are presented in **Table 4.1-3**. Notably, the diffusion coefficient of FcDB bound to BSA was considerably lower than that of free FcDB.

Table 4.1-3: Values of diffusion constants were obtained for both the free and BSA-bound forms of FcDB.

Compound	Equation	R^2	$D(cm^2.s^{-1})$
FMA	7.626x – 0.025	0.999	11.886×10^{-7}
BSA-FMA	6.783x – 1.021	0.999	9.402×10^{-7}
FM2N	y = 4.813x + 0.829	0.999	4.736×10^{-7}
BSA- FM2N	y = 1.637x + 0.527	0.999	3.107×10^{-7}
FM3N	y = 4.886x + 6.004	0.999	4.880×10^{-7}
BSA- FM3N	y = 2.005x + 0.946	0.998	2.154×10^{-7}
FM4N	y = 3.196x - 3.221	0.999	8.351×10^{-7}
BSA- FM4N	y = 1.968x + 0.397	0.995	6.649×10^{-7}
FM2C	y = 4.37x + 7.04	0.999	3.895×10^{-7}
BSA- FM2C	y = 2.92x + 13.729	0.985	1.749×10^{-7}
FM3C	y = 7.68x + 11.13	0.993	12.081×10^{-7}
BSA- FM3C	y = 6.86x + 8.85	0.999	9.615×10^{-7}
FM4C	y = 5.47x + 13.456	0.998	6.109×10^{-7}

BSA- FM4C	y = 3.905x + 19.99	0.995	3.118×10^{-7}

The reduced diffusion coefficient observed for FcDB-BSA when compared to FcDB can be attributed to the larger molecular weight of the FcDB-BSA complex.

4.1.2 Electronic spectroscopy BSA interaction study

UV-Vis spectroscopy was utilized as a straightforward technique to explore the interaction between BSA and FcDB. **Figure 4.1-7** displays the electronic absorption spectra of 0.5 M in a solution of ethanol/PBS (90:10) with a pH of 7.2 in the presence of varying concentrations of BSA, as well as in its absence. The absorbance of FcDB was detected around 400 nm, which is attributed to the $\pi \rightarrow \pi*$ transition in the conjugated ring of the ferrocene moiety [154]. Any modification in the UV-Vis absorption spectra of metal complexes due to the addition of BSA was considered as proof of the existence of an interaction between them. The maximum absorption of FcDB at this wavelength exhibited a slight hypochromic and bathochromic shift with the incremental addition of BSA.

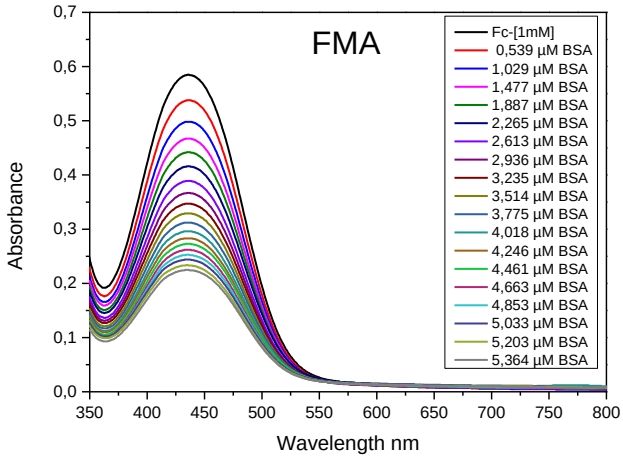

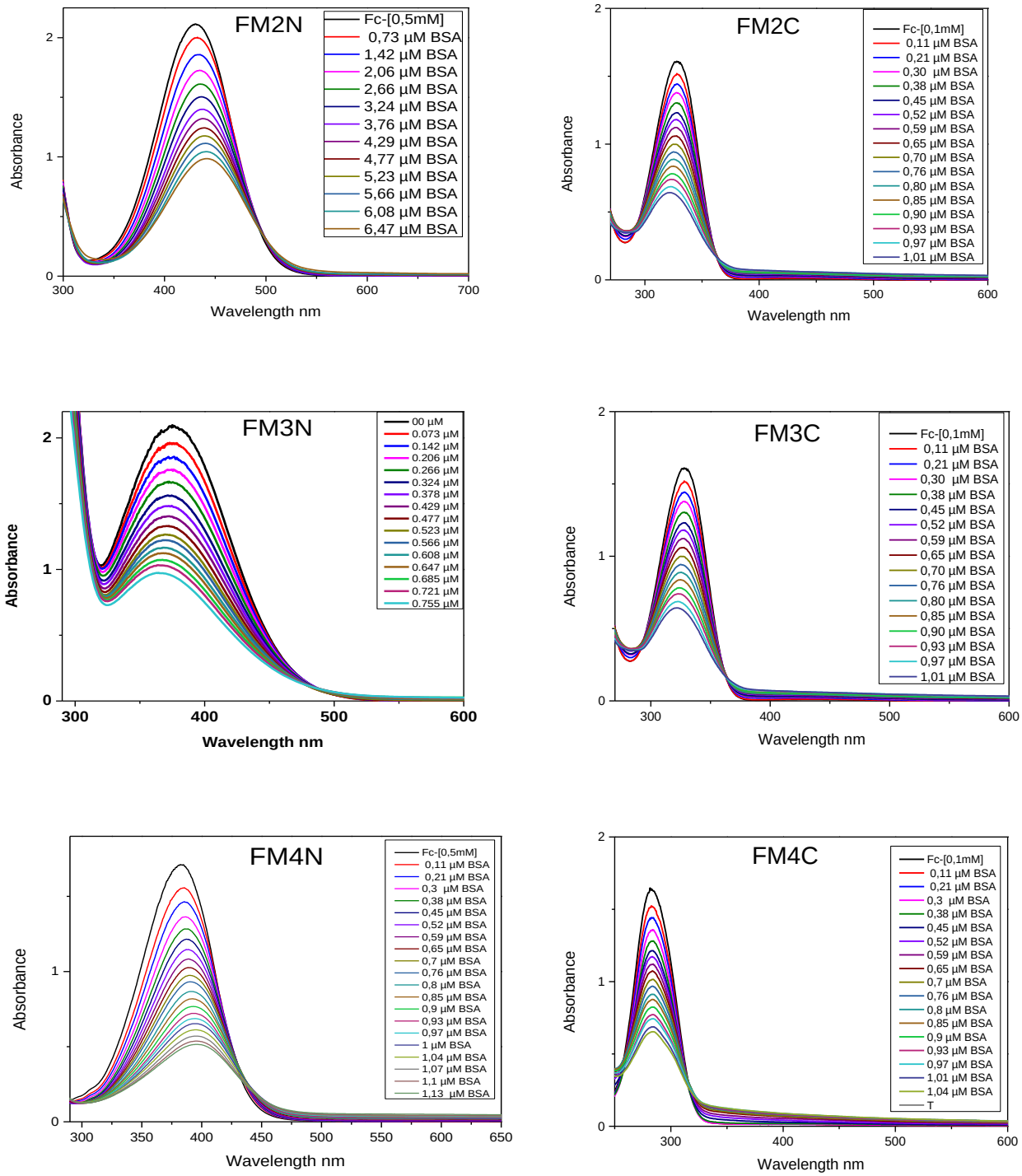

Figure 4.1-7: Absorbance spectra of FcDB, with increasing concentrations of BSA (0–22.5 µM).The concentration of FcDB was fixed at 1 mM at physiological pH 7.2

$$\frac{A_0}{A - A_0} = \frac{\varepsilon}{\varepsilon - \varepsilon_0} + \frac{\varepsilon}{\varepsilon - \varepsilon_0} \frac{1}{K_b[BSA]} \qquad (4.1\text{-}5)$$

Based upon the increase in absorbance, the binding constant (K_b) was calculated according to Benesi-Hildebrand equation (4.1-5)

Where, A_0 and A are the absorbance of FcDB and FcDB -BSA respectively, ε_0 and ε are the absorption coefficients of FcDB and FcDB -BSA respectively

The slope to intercept ratio of the plot between $A_0/(A- A_0)$ vs. 1 / [BSA] yielded the binding constant

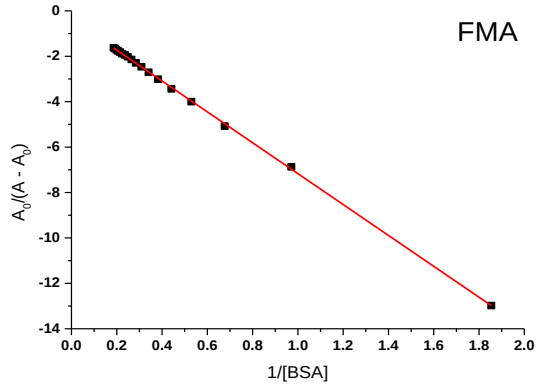

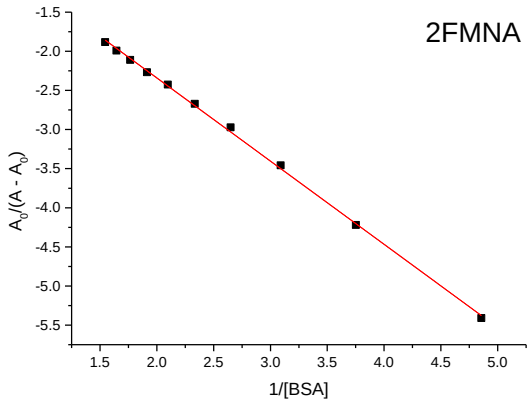

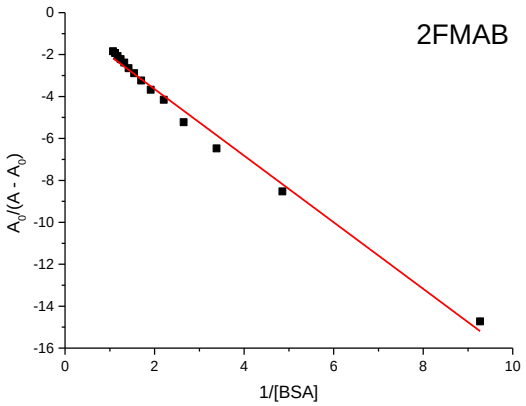

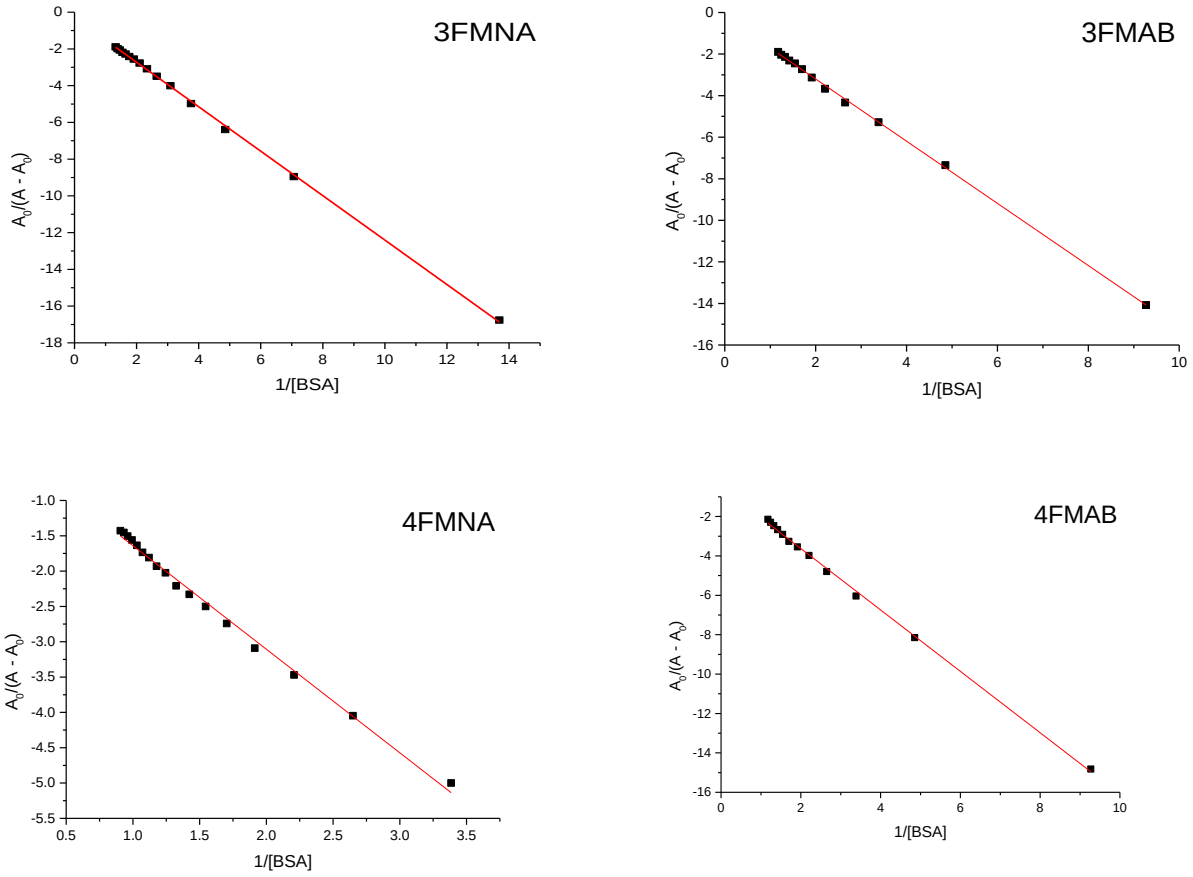

Figure 4.1-8: The plot of (A_0 / (A-A_0)) versus 1 / [BSA] was used to calculate the binding constants

Table 4.1-4 contains the computed values of binding constants and their corresponding free binding energies, which were determined using equation (4.1-5).

Table 4.1-4: Binding constant and binding free energy values

Adduct	Equation	R^2	Kb (M^{-1})	ΔG ($KJ.mol^{-1}$)
BSA –**FMA**	y = -6.802x – 0.366	0.999	5.381×10^4	-27.01
BSA –**FM2N**	y = -1,063x - 0,213	0.999	2.01×10^4	-30.27
BSA – **FM3N**	y = -1,210x - 0,306	0.999	$2,53 \times 10^4$	-30.84
BSA – **FM4N**	y = -1,466x - 0,173	0.994	1.18×10^5	-28.96
BSA –**FM2C**	y = -1,587x - 0,473	0.990	2.98×10^4	-31.25
BSA – **FM3C**	y = -1,495x - 0,208	0.999	1.39×10^4	-29.36
BSA – **FM4C**	y = -1,558x -0,509	0.998	3.26×10^4	-31.47

4.1.3 Molecular docking BSA interaction study

To further understand the binding mode and direction of the studied compounds with BSA, molecular docking was utilized. The purpose of this was to confirm and interpret the results obtained from the voltametric and spectroscopic measurements, as well as explore additional information on the preferred binding site and mode. Through molecular docking, the interactions between the ligands and BSA were simulated and visualized, allowing for a more comprehensive analysis of the binding mode and the interactions established between the compounds and BSA in the active site of the receptor

4.1.3.1 Structural optimization

In this study, Density Functional Theory (DFT) was utilized to optimize the molecular structures of the compounds without any symmetry constraints, using the Gaussian 09 package. The B3LYP exchange functional of Becke and the Lee-Yang-Parr correlation functional were utilized, and the 6-311++G(d,p) basis set was employed for the calculations. The optimized structures of the compounds are presented in **Figure 4.1-9**.

FMA

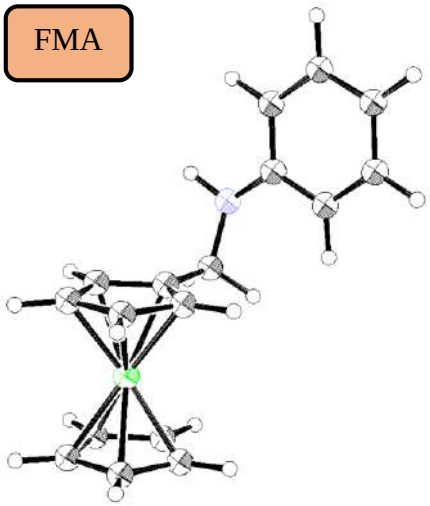

FM2N

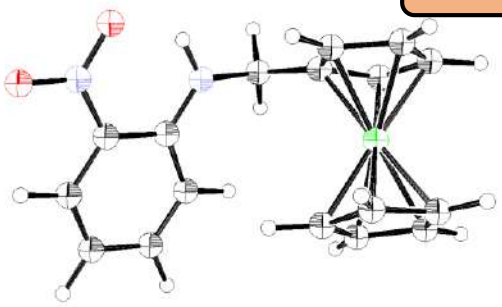

FM2C

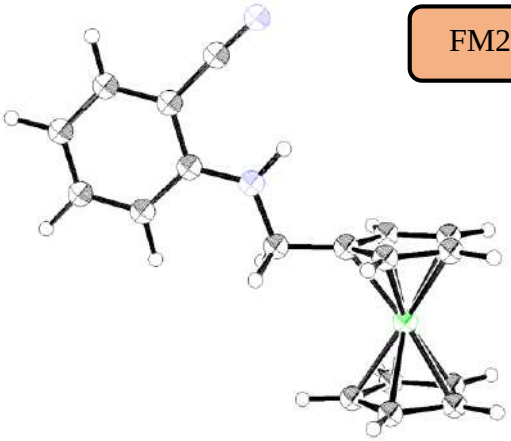

FM3N

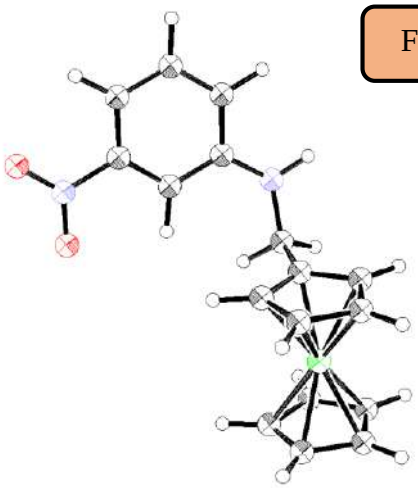

FM3C

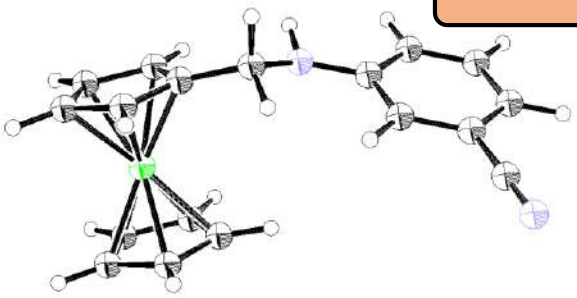

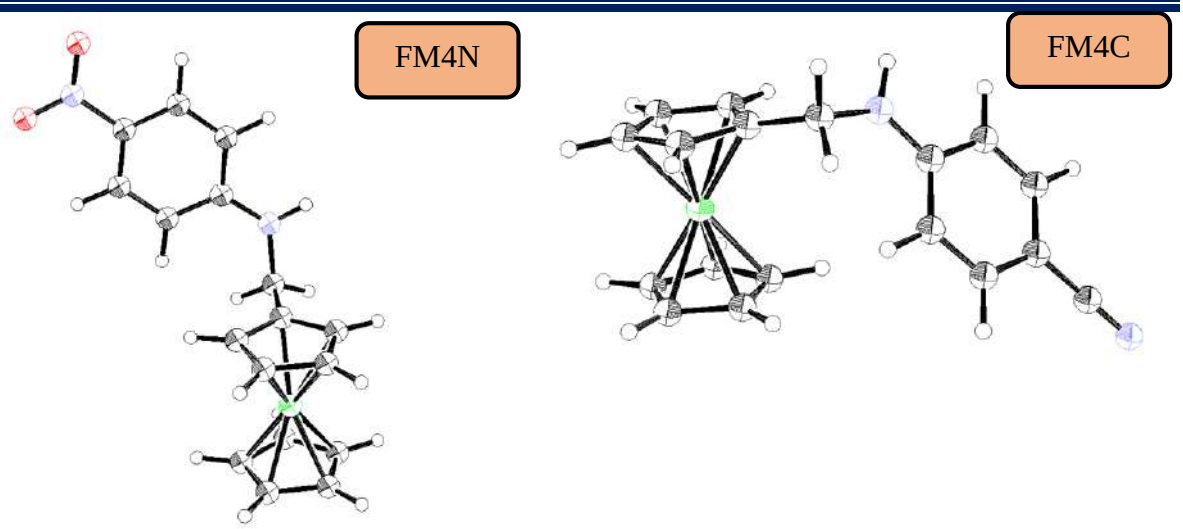

Figure 4.1-9: The optimized structures of FcDB have been depicted using ORTEP View 03, V1.08, where hydrogen is indicated by white, carbon by grey, iron by green, and nitrogen by blue color codes.

4.1.3.2 Binding site determination

The Prank Web server analysis showed that there were 9 potential binding sites, which can be seen in **Figure 4.1-10**. Additionally, the Proteins BSA (RCSB, PDB code: 4f5u) server research identified four potential binding sites (**Table 4.1-5**), with the more highly-scored pockets being considered more likely to be druggable. The druggability of a target refers to the ability of a binding site to accommodate small molecules in terms of their physicochemical properties such as size, shape, electrostatics, and hydrophobicity, allowing them to bind with high affinity. Furthermore, it also involves the ability to bind small molecules that possess certain physicochemical properties, which place them in the "drug-like" property space, indicating that the binding site is suitable for interaction.

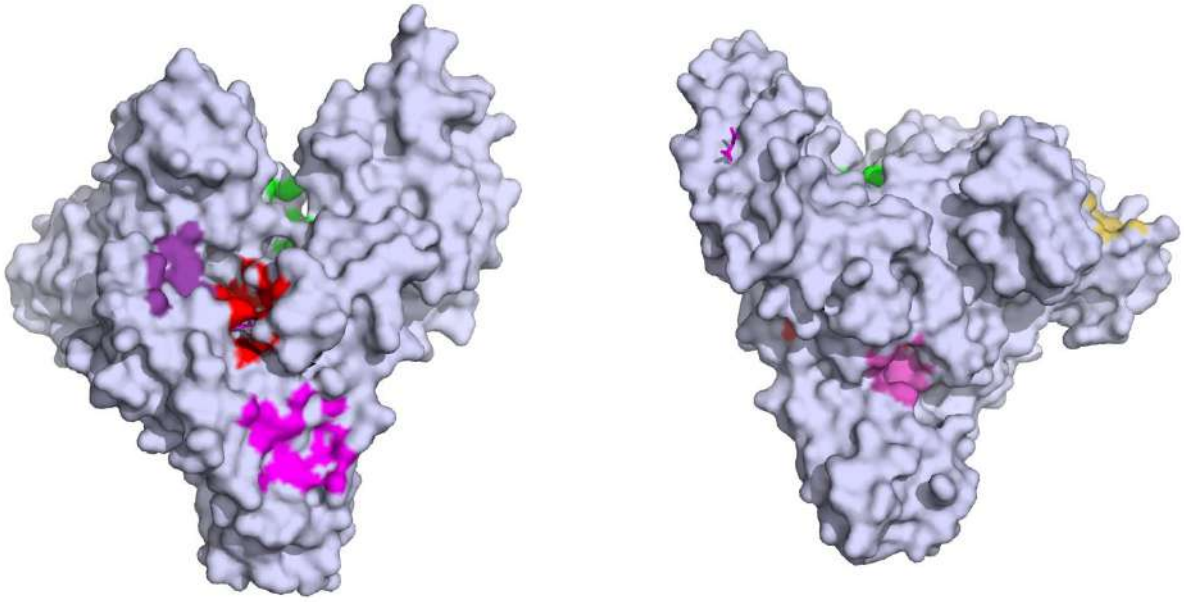

Figure 4.1-10: Predicted binding pockets: surface view of BSA (code: 4f5u)

All coloured spaces represent the active site. Data related to it is mentioned in the following **Table 4.1-5**

Table 4.1-5: The active sites on BSA from Prankweb server

Name	Rank	Score	Probability	Grid Canter		
				X	Y	Z
pocket1	1	13.46	0.705	12.89	42.94	72.51
pocket2	2	3.38	0.125	3.91	45.61	55.35
pocket3	3	3.07	0.104	22.27	30.41	85.66
pocket4	4	2.04	0.044	14.32	56.02	71.57
pocket5	5	2.03	0.043	4.29	31.81	77.37
pocket6	6	1.82	0.034	18.14	33.23	63.77
pocket7	7	1.36	0.016	14.07	27.55	63.25
pocket8	8	1.21	0.012	7.22	33.88	73.60
pocket9	9	0.78	0.003	-22.22	59.25	69.40

The first binding site has the highest pocket score, value of 13.46, which contained the following residues A_149 A_190 A_194 A_198 A_213 A_217 A_218 A_221 A_237 A_241 A_290.

Pocket 9 has the smallest cavity 7 amino acids (number A_45 A_46 A_49 A_61 A_64 A_69 A_72 A_73) and the lowest affinity binding 0.78.

4.1.3.3 Molecular docking studies

The docking studies of the FcDB ligand into BSA were achieved using AutoDock 4.2. The crystal structure of BSA, with a resolution of 2.04 A°, was downloaded from the protein data bank (RCSB, PDB code: 4f5u). For the program and all analysed derivatives, the size of the grid map in the focus docking calculations for ligands compounds was set to 40×40×40 A3 in the x, y, and z directions with a grid point spacing of 0.375 A. Docking analysis was performed on the stable conformation with the lowest binding energy [155]. The interaction was generated with PLIP webservice and visualizer by PyMOL software., which was represented in **Figure 4.1-11**

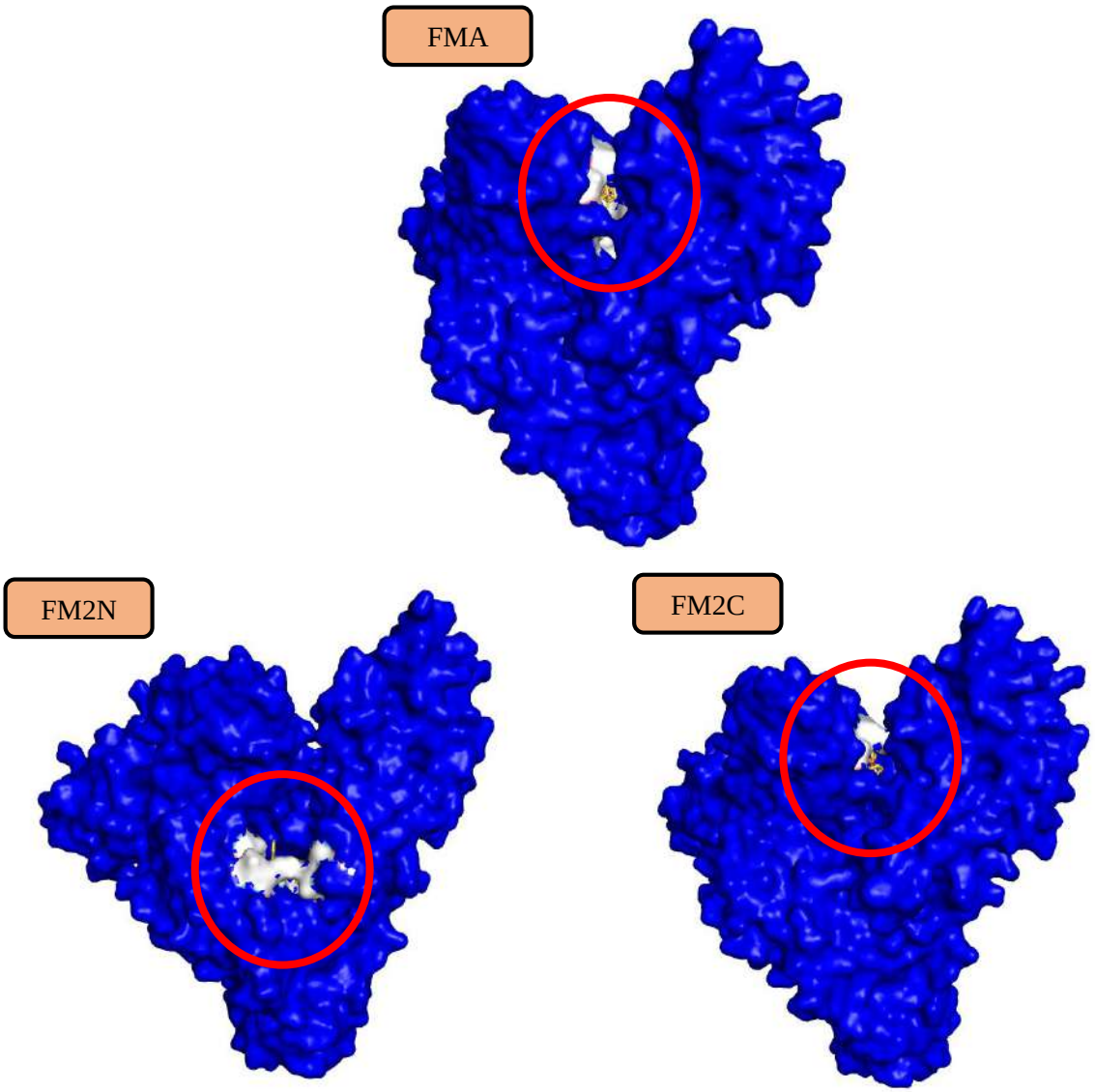

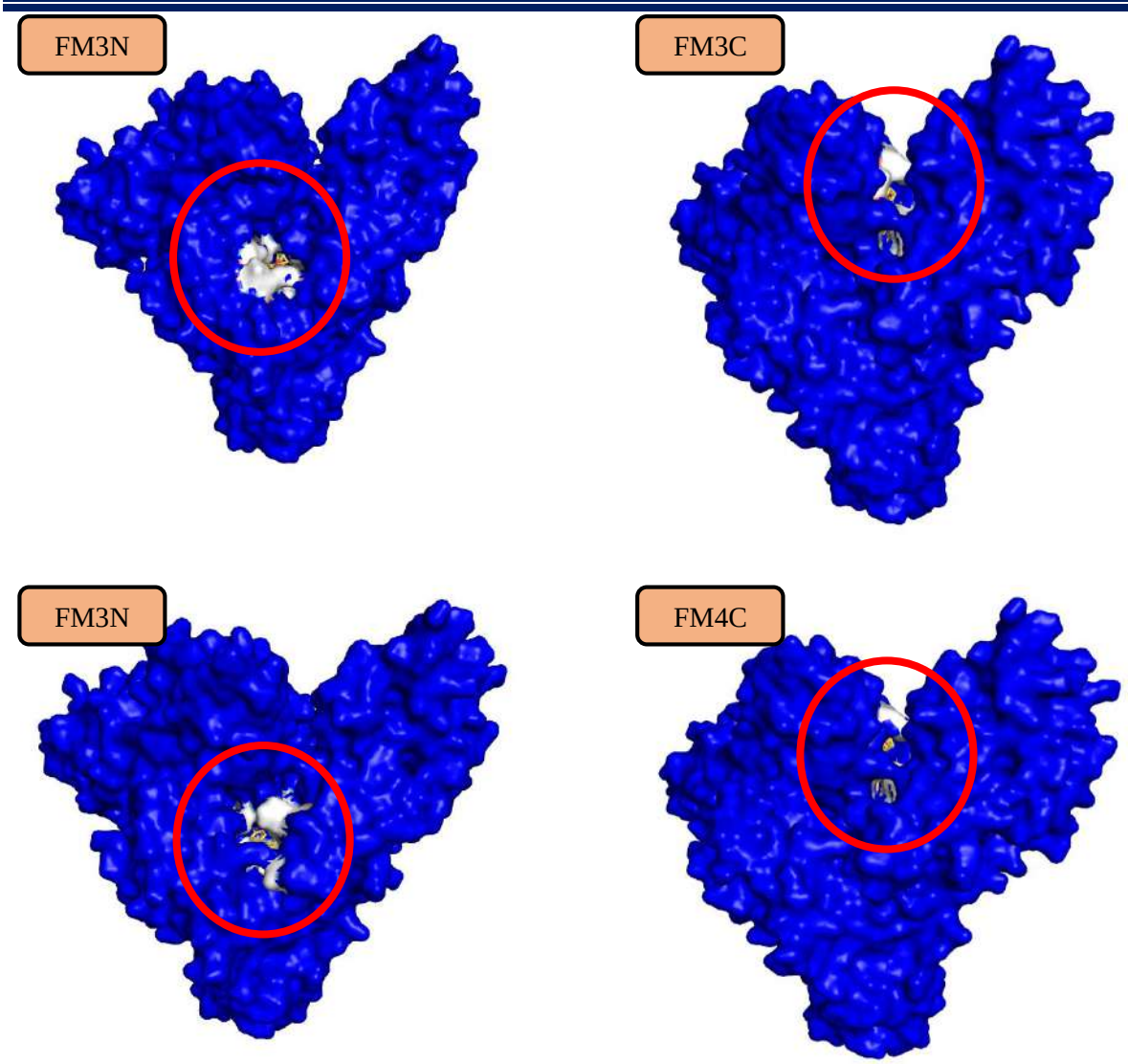

Figure 4.1-11: Representation 3D Structures of BSA (PDB code:4f5u)

All data related to BSA-FcDB interactions in the best active site is explained in the following table

Table 4.1-6: Binding constant and binding free energy values

Complex	K (M^{-1})	ΔG ($KJ.mol^{-1}$)	The number of runs	pocket
BSA –**FMA**	7.50×10^{4}	-27.83	36	2
BSA –**FM2N**	2.52×10^{5}	-30.84	48	1
BSA – **FM3N**	2.29×10^{5}	-30.60	48	1
BSA – **FM4N**	9.82×10^{4}	-28.50	40	1
BSA –**FM2C**	3.0×10^{5}	-31.27	28	2

BSA – **FM3C**	1.65×10^5	-29.80	46	2
BSA – **FM4C**	3.42×10^5	-31.60	1	2

Results from molecular docking analysis revealed that all designed compounds have acquired the binding site region with better binding energy, the energy which represent affinities range from -27 KJ/mol to -31 KJ/mol. Based on the docking results, FcDB has the lowest energy , whereas 4FMBA has the highest binding affinity. FMA and FMN derivative ligands are located in pocket 1 , and it formed strong inter-molecular interactions with BSA . FMC derivative ligands are located in pocket 2. The results of the docking study are in accordance with cyclic voltammetry and spectroscopic approaches techniques, which provide important information on the mechanism of binding of the FcDB complex to BSA.

According to the findings of molecular docking analysis, the binding process between FcDB and BSA involves hydrogen bonding, hydrophobic forces, and π-cation interaction. The interaction between FcDB and the nearby residues in the active site of BSA is demonstrated in **Figure 4.1-12**. Additionally, the Protein-Ligand Interaction, an automated web service for identifying relevant non-covalent protein-ligand contacts in 3-D structures, was employed to detect the interactions between each FcDB molecule and the surrounding amino acid residues. The interactions were then examined and visualized using PyMOL software.

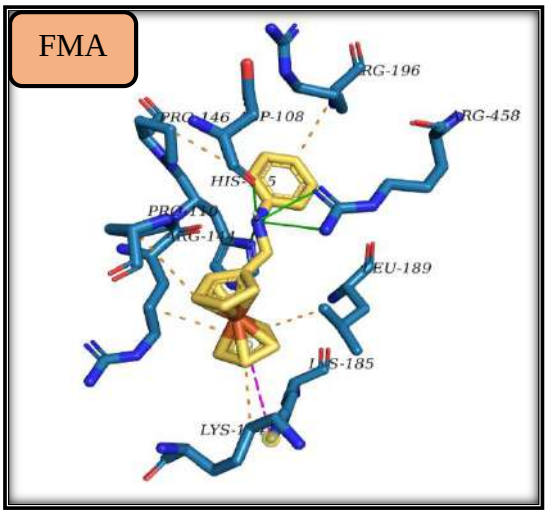

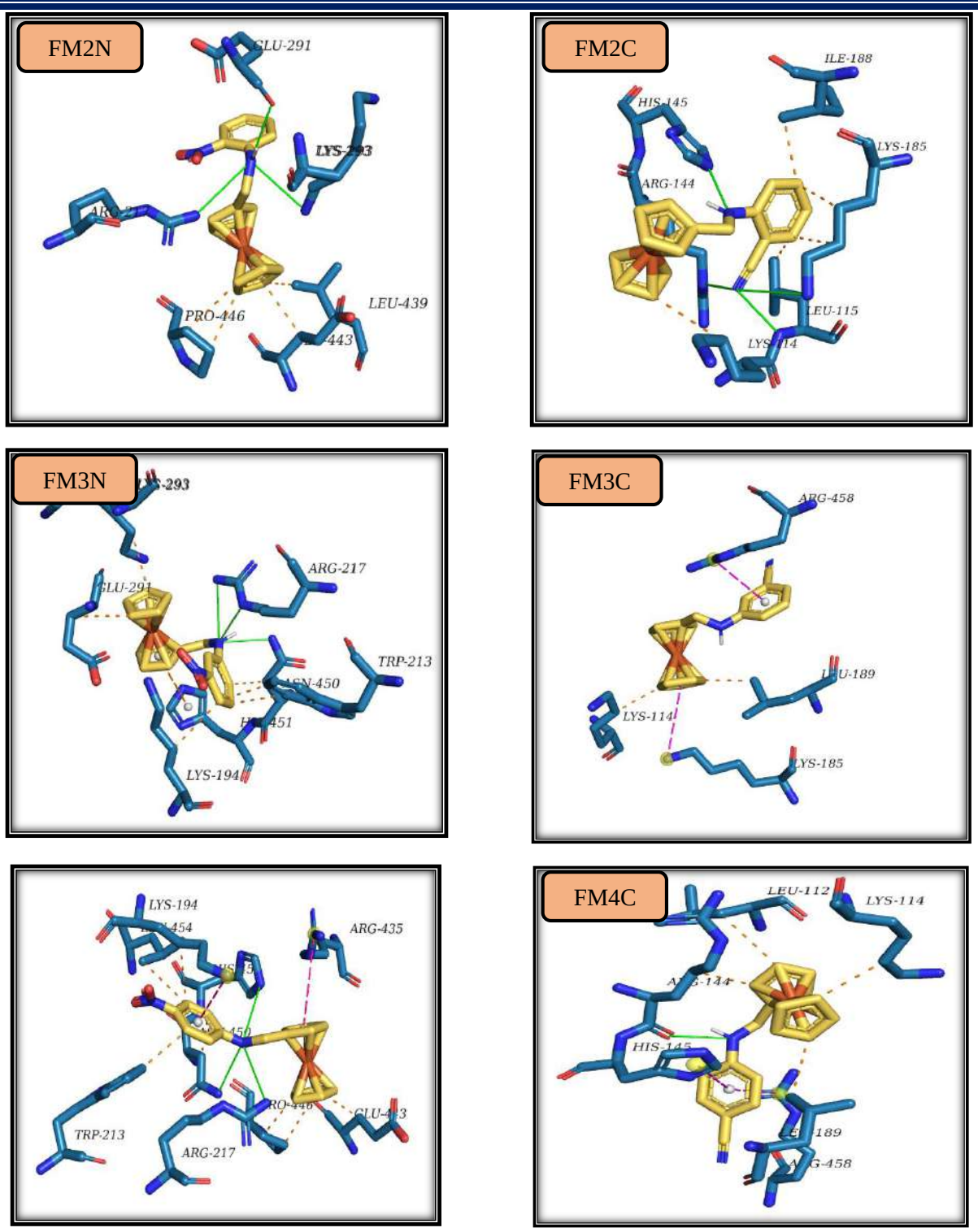

Figure 4.1-12: The PLIP web service generated the optimal docking poses for BSA-FcDB, highlighting the hydrophobic and hydrogen bond interactions. In the resulting image, the elements are color-coded: white represents hydrogen, red represents oxygen, blue represents nitrogen, and

brown represents iron. The interactions are identified by their respective colors: hydrogen bonds are represented in blue, hydrophobic forces in silver, π-stacking in green, and π-cation in orange.

The tables presented below summarize the type of interactions, distances, and the residues involved in the interactions.

Table 4.1-7: The hydrophobic interactions occurring between the ligands FcDB and BSA are being examined.

Sample code	Residue	Amino acid	Distance (Å)
FMA	110A	PRO	3.80
	114A	LYS	3.09
	144A	ARG	3.60
	146A	PRO	3.98
	189A	LEU	3.53
	196A	ARG	3.52
FM2N	439A	LEU	3.31
	443A	GLU	3.28
	446A	PRO	3.66
	446A	PRO	3.24
FM3N	194A	LYS	3.66
	213A	TRP	3.14
	213A	TRP	3.63
	291A	GLU	3.80
	293A	LYS	3.41
	450A	ASN	3.21
FM4N	194A	LYS	3.49
	213A	TRP	3.13
	443A	GLU	3.50
	446A	PRO	3.31
	446A	PRO	3.97
	450A	ASN	3.20

	454A	LEU	3.66
FM2C	114A	LYS	3.71
	115A	LEU	3.06
	185A	ARG	3.24
	185A	LYS	3.61
	185A	IYS	3.05
FM3C	114A	LYS	3.15
	189A	LEU	3.51
FM4C	112A	LEU	3.65
	114A	LYS	3.24
	144A	ARG	3.22
	189A	LEU	3.59

Table 4.1-8: Hydrogen bonding the ligands FcDB and BSA

Sample code	Residue	Amino acid	H-A	D-A
FMA	108A	ASP	1.77	2.68
	145A	HIS	2.97	3.54
	458A	ARG	2.43	3.13
	458A	ARG	3.32	3.87
FM2N	217A	ARG	3.33	4.04
	291A	GLU	3.05	3.63
	293A	LYS	3.05	3.63
FM3N	217A	ARG	2.85	3.46
	217A	ARG	2.89	3.46
	450A	ASN	2.33	3.18
FM4N	217A	ARG	3.31	4.00
	450A	ASN	2.55	3.46
	451A	HIS	3.57	4.10

FM2C	115A	LEU	1.99	2.96
	144A	ARG	2.59	3.27
	145A	HIS	2.40	3.08
	185A	LYS	3.43	3.78
FM4C	144A	ARG	1.81	2.66

Table 4.1-9: π-stacking interactions between ligands

Sample code	Residue	Amino acid	Distance (Å)
FMA	185A	LYS	4.95
FM2N	451A	HIS	4.30
FM4N	194A	LYS	4.24
	435A	ARG	5.06
FM3C	185A	LYS	4.56
	458A	ARG	3.92
FM4C	145A	HIS	3.95
	458A	ARG	3.53

The aforementioned Tables provide evidence that the ligand FcDB interacted with BSA via hydrogen bonding and hydrophobic forces. **Table 4.2-6** lists the specific residues and amino acids that participated in these interactions. Additionally, **Table 4.2-7** presents the measured distances between the hydrogen atoms and the receptor atoms (H-A), as well as between the donor and receptor atoms (H-D). Furthermore, the results of molecular docking simulations suggest a π-π stacking interaction between the positively charged amino acid residue and the phenyl cycle of the ligand.

FMA was found to have strong binding to BSA with hydrophobic interactions at PRO110, LYS114, ARG144, PRO146, LEU189 and ARG196 residues and forms a series of hydrogen bonds with ASP108, HIS145, ARG458 residue and π-cation interaction with LYS185 of distance 4.95 angstroms of BSA protein.

Docking study shows that FM2N attaches to LEU439, GLU443, PRO446 and PRO446 residues via hydrophobic interactions and creates three hydrogen bonds with LEU439, GLU443 and PRO446 residues.

Figure 4.1-12 depicts the binding conformation and binding site residues of FM3N. 5 hydrogen LYS194, TRP213, GLU291, LYS293 and ASN450 bonds are formed with FM3N, whilst other BSA hydrophobic residues are distributed between FM3N (LYS194, TRP213, GLU291, LYS293 and ASN450) and pi-cation interaction with LYS194, ARG435 of distance 4.24, 5.06 angstroms of BSA protein respectively.

Figure 4.1-12 shows the interaction of FM4N with BSA. Six hydrogen bonds were observed between the ligand and the amino acid residues LYS194, TRP213, GLU443, PRO446, ASN450, and LEU454. Also, a series hydrophobic interaction with LYS194, TRP213, GLU443, PRO446, PRO446, PRO446, ASN450 and LEU454 residues were formed.

FM2C binds strongly to BSA, having hydrophobic contacts at LYS114, LEU115, ARG185, LYS185, and IYS185 residues and hydrogen bonds with LYS114, LEU115, ARG185, LYS185, and IYS185 residues.

Figure 4.1-12 represents the hydrogen bond interaction FM3C with LYS114 and LEU189.Also bind by hydrophobic interactions at LYS114 and LEU189 residues. two electrostatic interactions were also seen between the π electron cloud of fused aromatic ring and LYS185 and ARG458 residues.

FM4C was discovered to have strong binding to BSA, with hydrophobic contacts at LEU112, LYS114, ARG144, and LEU189 residues, four hydrogen bonds with LEU112, LYS114, ARG144, and LEU189 residues, and a pi-cation interaction with HIS145, AGR458 of 3.95, 3.53 angstroms.

In terms of molecular interaction and mechanism, the molecular docking results have well validated the experimental data. which were validated by in silico results.

Table 4.1-10: Binding parameters (k and ΔG) of FcDB compounds obtained from CV, UV-vis and docking methods.

Method	**CV**		**Uv-vis**		**Docking**	
Complex	**K (M^{-1})**	ΔG ($KJ.mol^{-1}$)	**K (M^{-1})**	ΔG ($KJ.mol^{-1}$)	**K (M^{-1})**	ΔG ($KJ.mol^{-1}$)
BSA –**FMA**	7.85×10^{4}	-27.95	5.381×10^{4}	-27.01	7.50×10^{4}	-27.83
BSA –**FM2N**	2.07×10^{5}	-30.35	2.01×10^{4}	-30.27	2.52×10^{5}	-30.84
BSA – **FM3N**	2.51×10^{5}	-30.82	$2{,}53 \times 10^{4}$	-30.84	2.29×10^{5}	-30.60
BSA – **FM4N**	8.30×10^{4}	-28.08	1.18×10^{5}	-28.96	9.82×10^{4}	-28.50

BSA –**FM2C**	3.03×10^5	-31.29	2.98×10^4	-31.25	3.0×10^5	-31.27
BSA – **FM3C**	1.62×10^5	-29.74	1.39×10^4	-29.36	1.65×10^5	-29.80
BSA – **FM4C**	3.33×10^5	-31.52	3.26×10^4	-31.47	3.42×10^5	-31.60

4.2 The study of the interaction of FcDA-BSA

4.2.1 Electrochemical BSA interaction study

4.2.1.1 Binding constants

By observing the shift in peak potential and the reduction in peak height, it can be inferred that there was an interaction between the sample and BSA. The experimental results indicate a negative shift in peak potential and a decrease in peak height upon titration with BSA.

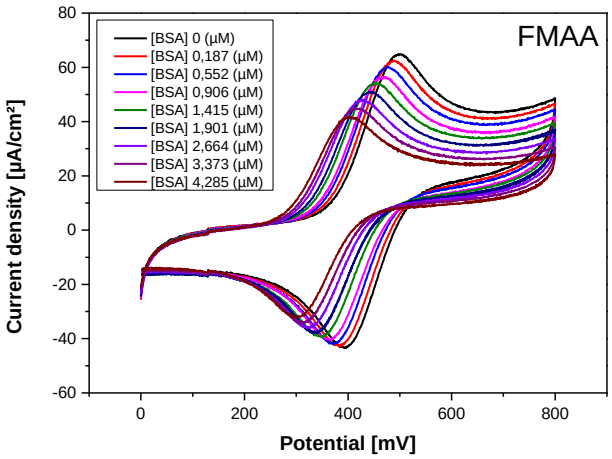

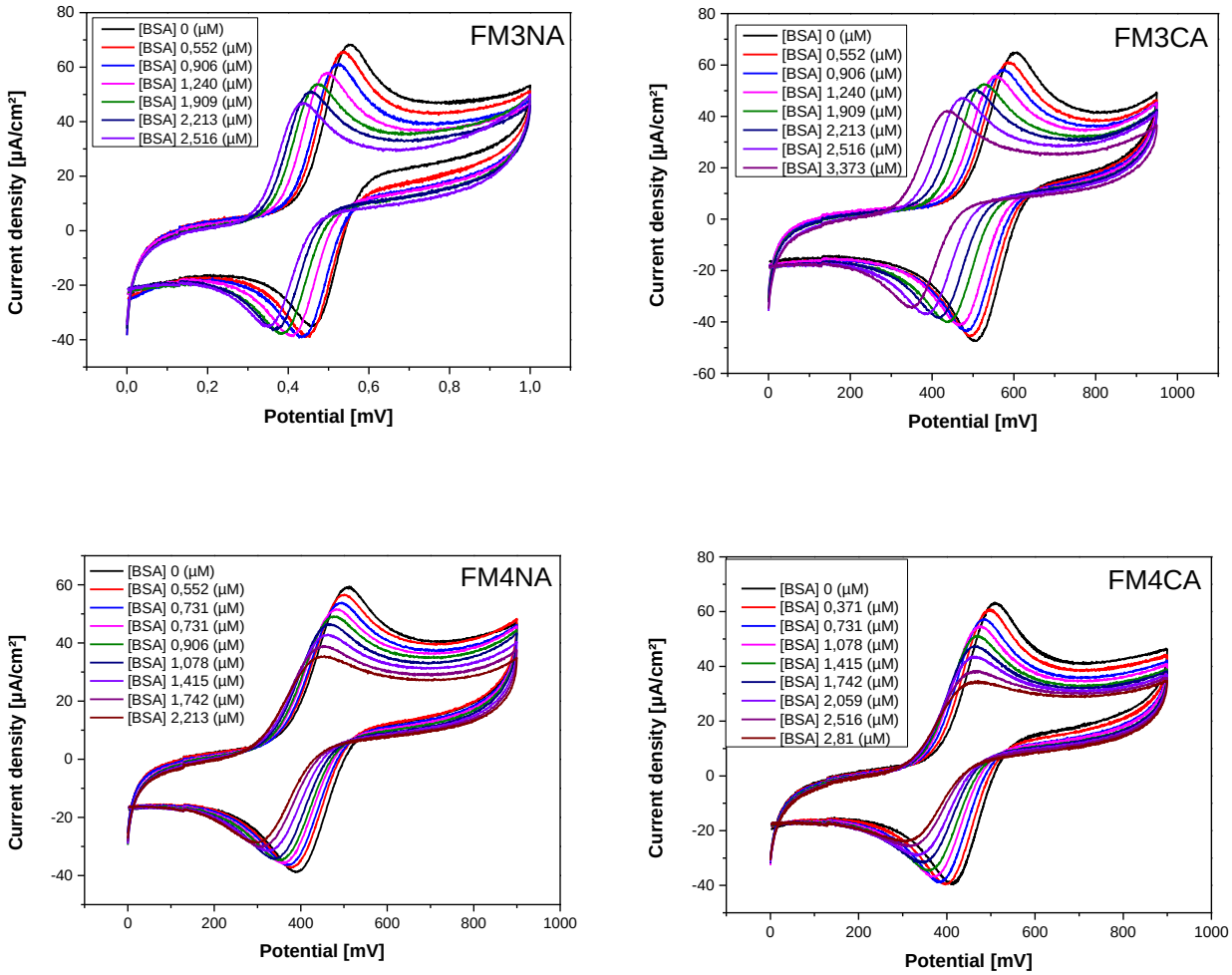

Figure 4.2-1: The cyclic voltammograms of 1 mM FcDA were obtained by performing a potential sweep rate of 0.1V s−1 on a GC disk electrode at 298K. The measurements were taken in the presence and absence of increasing concentrations of BSA in ethanol/PBS (90:10) solution with a pH of 7.2, using 0.1 M TBFP as a supporting electrolyte.

The interaction of FcDA with a BSA results in complex and the thermodynamic of this complex can yield the information about binding or formation constant K_b (M^{-1}). K_b values of FcDA –BSA complexes were determined using the peak current values and following equation (4.1-1)

The linear form of the f(1/C)=i/(i0-i)extracted from the above voltammogram

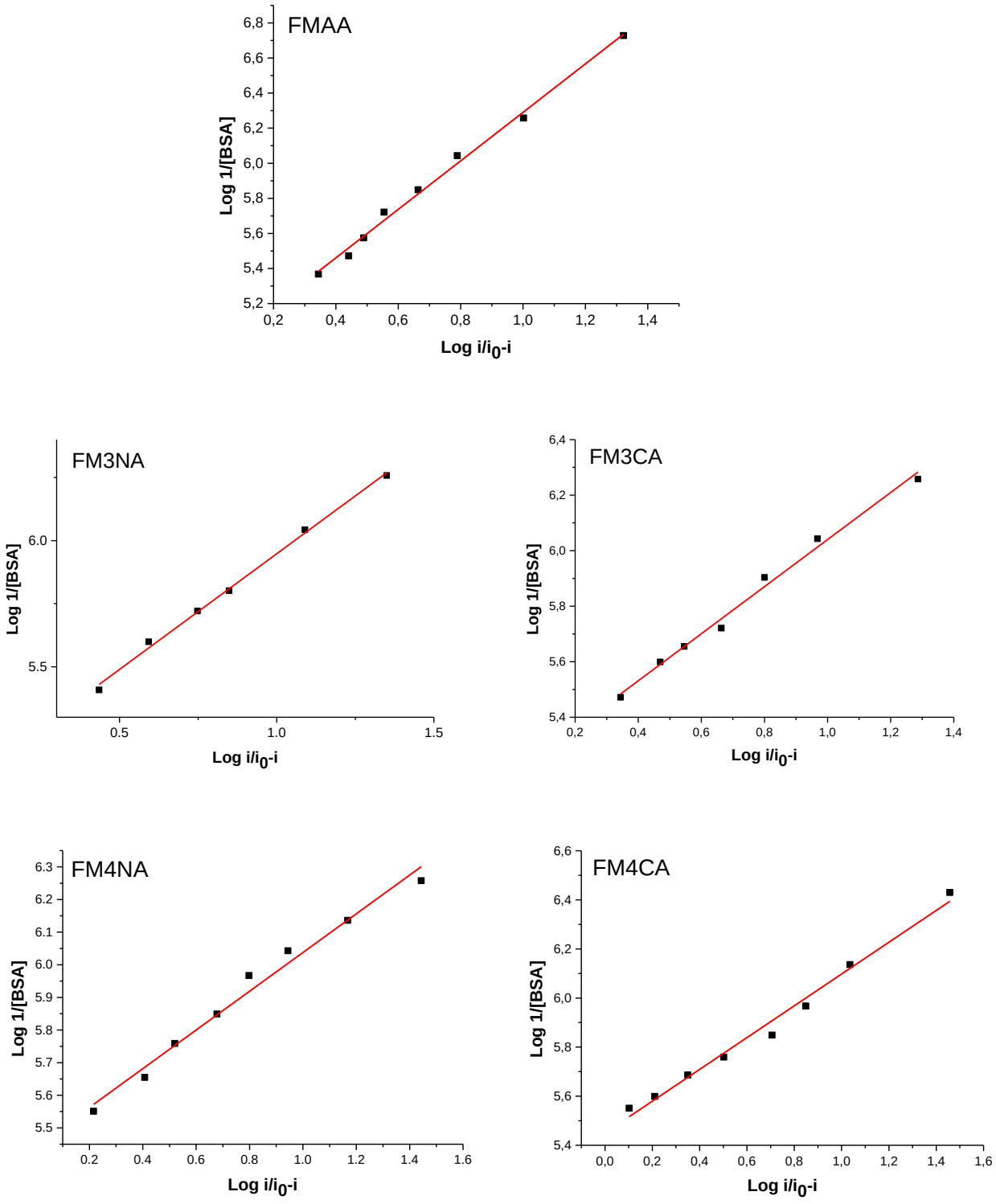

Figure 4.2-2: Log/ (1/[BSA]) versus log i/(i_0-i) for FcDA with varying concentration of BSA used to calculate the binding constant of BSA- FcDA product.

The Gibbs free energy equation (4.1-2) and formation constant data were used to evaluate ΔG and the obtained values are given in **Table 4.1-1** .

Table 4.2-1: Binding constant and binding free energy values

Adduct	Equation	R^2	Kb (M^{-1})	ΔG ($KJ.mol^{-1}$)
BSA –**FMAA**	y = 1,382x + 4,908	0,993	7.94×10^4	-27.97
BSA –**FM3NA**	y = 0,916x + 5,031	0.996	1.07×10^5	-28.71
BSA –**FM4NA**	y = 0.593x + 5.444	0.991	2.75×10^5	-31.06
BSA –**FM3CA**	y = 0,847x + 5,192	0.989	1.55×10^5	-29.62
BSA –**FM4CA**	y = 0.647x + 5.450	0.993	2.82×10^5	-31.11

The obtained binding free energy, in terms of both its order of magnitude and sign, provides insights into the nature of the interactions between the ligands and BSA. Specifically, the electrostatic mode of the interactions can be determined from the order of magnitude of the binding free energy, while the spontaneity of the interactions can be inferred from the sign of the binding free energy.

4.2.1.2 Ratio of binding constants

The voltammograms depicted in **Figure 4.2-3**, which illustrate the cyclic voltammograms of a 2 mM FcDA solution in the absence and presence of BSA, can be utilized to determine the ratio of binding constants between the reduced form of FcDA and BSA and its oxidized form, $[FcDA]^+$. The addition of BSA leads to a shift in the anodic and cathodic peak potential values, which can be employed to calculate the binding constant ratio [152].

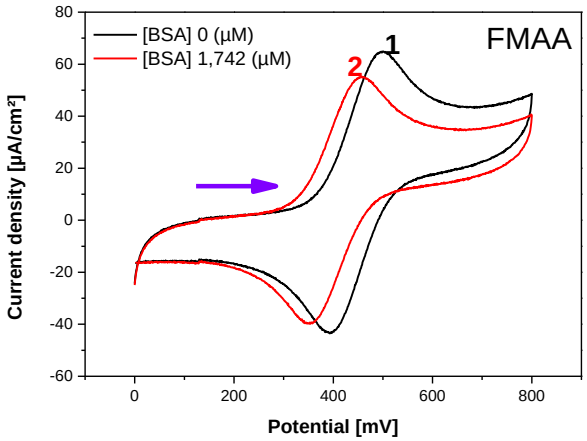

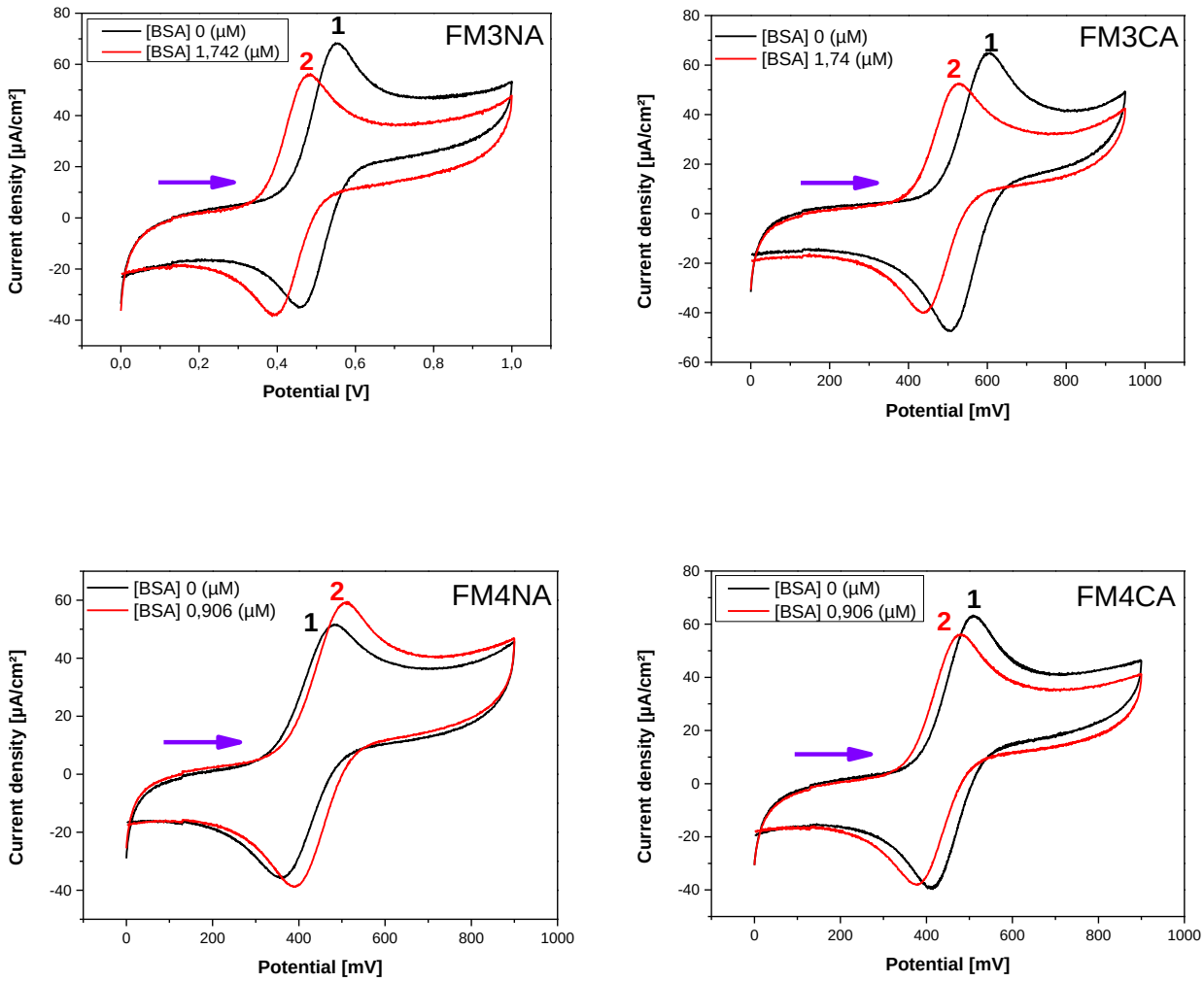

Figure 4.2-3: The cyclic voltammograms were recorded for a 2 mM concentration of the investigated FcDA compounds, both in the presence (indicated by the red line) and absence (indicated by the black line) of BSA, at a scan rate of 100 $mV.s^{-1}$

In instances where the introduction of BSA causes a shift in the values of both anodic and cathodic peak potentials, the equilibrium principles outlined below may be employed [153],

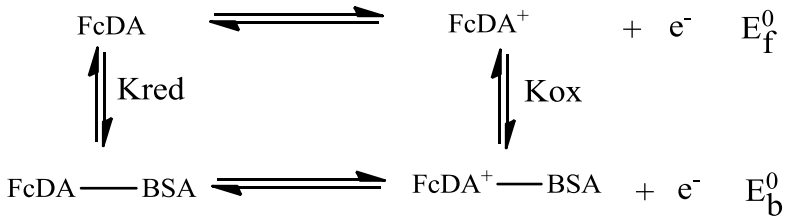

Figure 4.2-4: Redox process of the studied compounds with BSA and FcDA

By utilizing the Nernst relation to the equilibriums presented in **Figure 4.1-4**, the ensuing equation (4.1-3) is derived

The formal potential shift ΔE^0 calculated based on the voltammograms of **Figure 4.2-4**, are summarized in **Table 4.2-2**. The ratios of the binding constants were calculated from equation (4.1-3) by replacing ΔE^0

The formal potentials of the $FcDA^+$/FcDA couple for both free and BSA-bound compounds are represented as and , respectively. The voltammograms presented in **Figure 4.2-4** were used to calculate the formal potential shift, which is summarized in **Table 4.2-2**. Additionally, the ratios of binding constants were determined using equation (4.1-3) with appropriate replacements.

Table 4.2-2: The information obtained from the FcDA in its free form and when bound to BSA was utilized in the computation of the ratio of binding constants.

Entry	Epa	Epc	E°(V)	ΔE°(mV)	Kred/Kox
FMAA	0.498	0.393	0.446	70	15.36
BSA- FMAA	0.428	0.323	0.376		
FA3NA	0.552	0.457	0.505	67	13.66
BSA- FA3NA	0.482	0.393	0.438		
FA4NA	0.510	0.390	0.450	29	3.04
BSA- FA4NA	0.484	0.359	0.422		
FA3CA	0.603	0.506	0.555	72	16.61
BSA- FA3CA	0.527	0.438	0.483		
FA4CA	0.509	0.412	0.461	32	3.49
BSA- FA4CA	0.480	0.377	0.429		

Based on the obtained ratios of the binding constants, it can be concluded that the reduced form of the ligands exhibits stronger binding affinity towards BSA compared to the oxidised form.

4.2.1.3 Diffusion coefficients

The electrochemical behavior of the free and BSA-bound FcDA was utilized to obtain their respective diffusion coefficients, as illustrated in **Figure 4.2-5**. Cyclic voltammograms were recorded for 2 mM of FcDA in both the absence and presence of BSA while varying the potential scan rates. These voltammograms demonstrated well-defined and stable redox peaks, which were associated with the redox process of FcDA

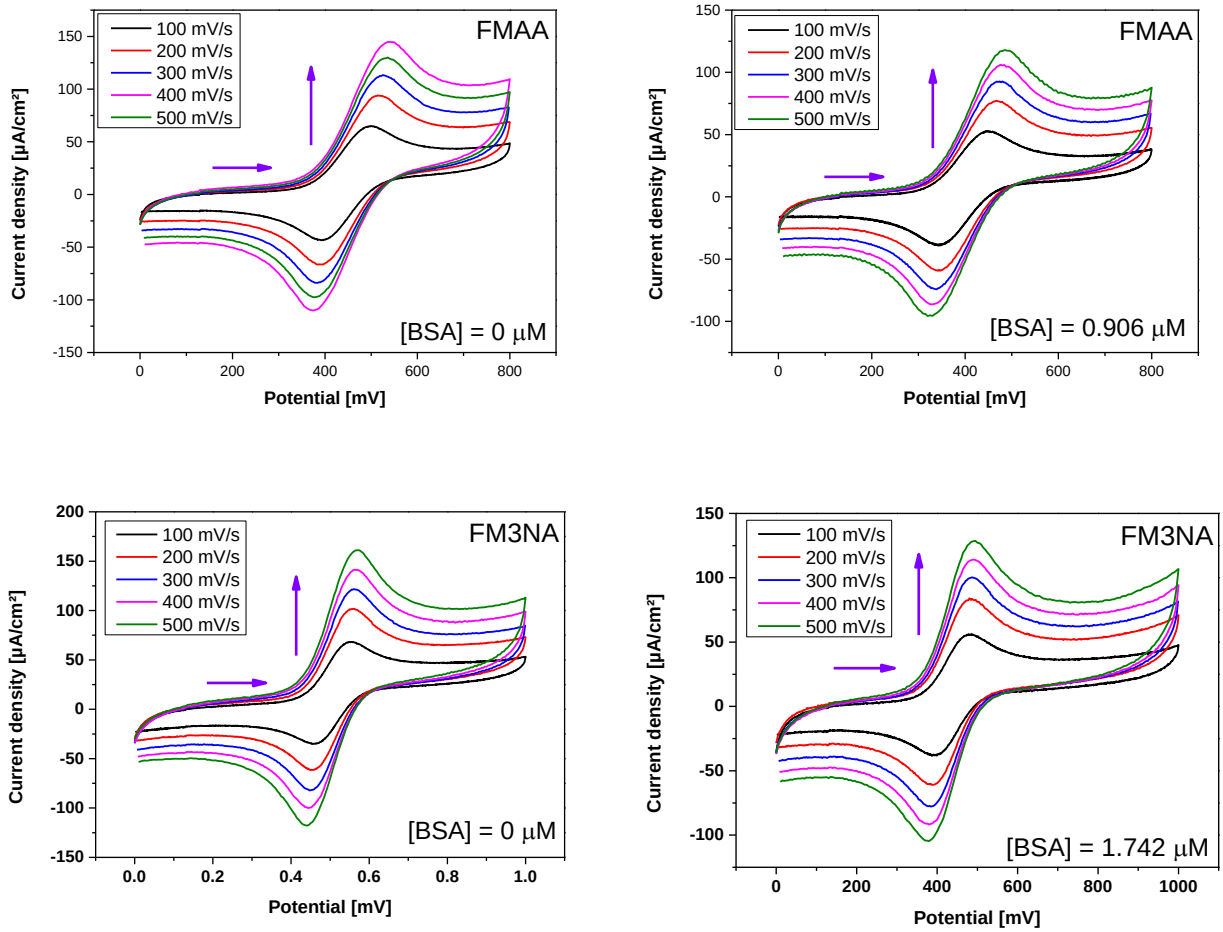

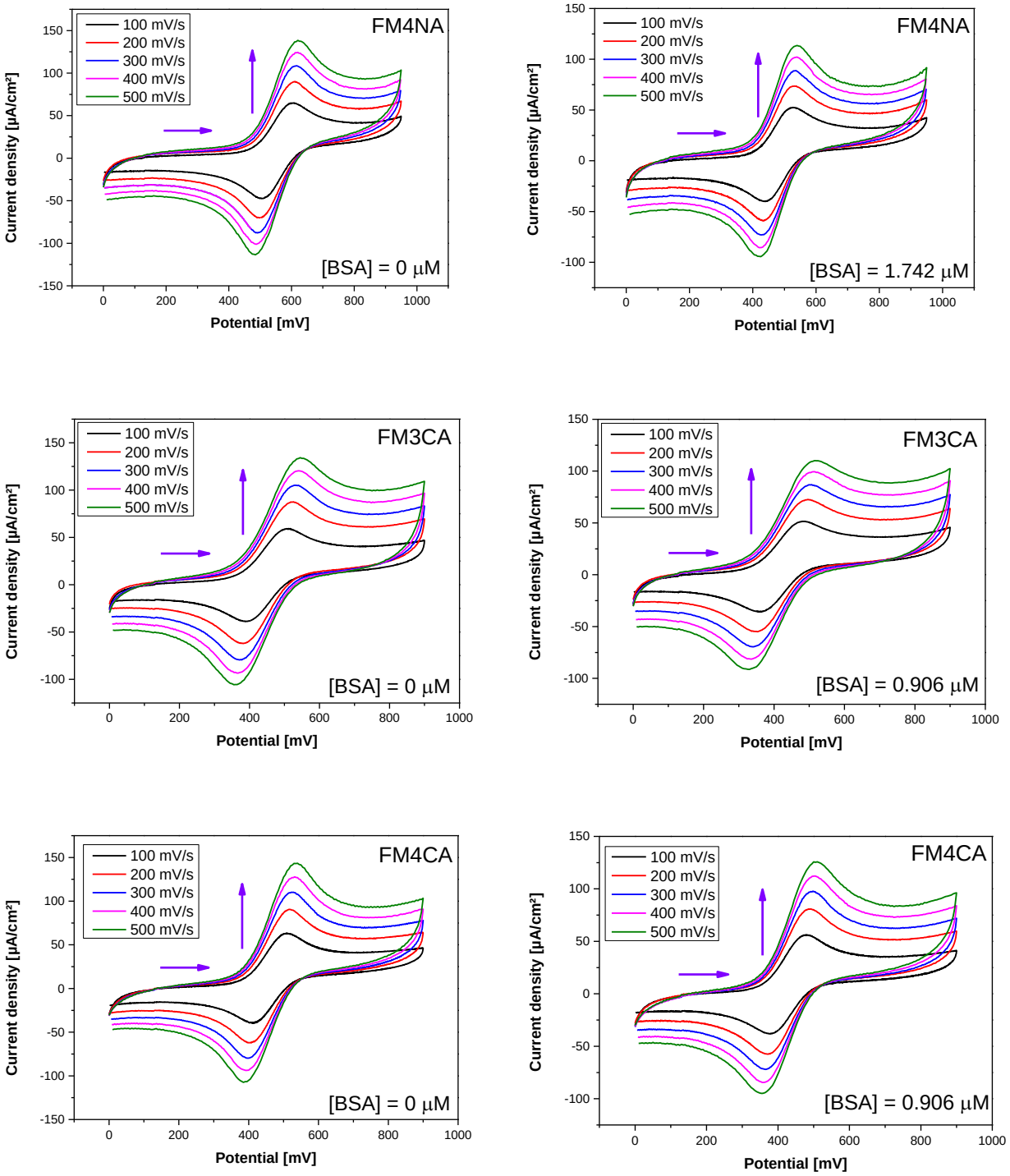

Figure 4.2-5: Cyclic voltammetry was performed on 2 mM of FcDA in a solution of ethanol/PBS (90:10) with various scan rates (0.1 , 0.2 ,0.3 ,0.4 and 0.5 $V \cdot s^{-1}$) in both the absence and presence of BSA.

The Randles–Sevcik equation (4.1-4) was used to determinate the coefficient of diffusion of the free form of the FMA and the bound form of FMA-BSA

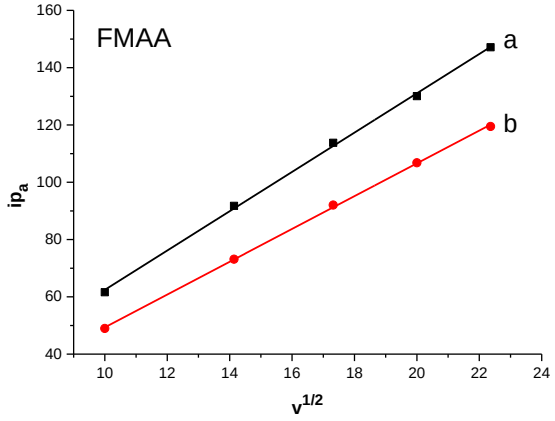

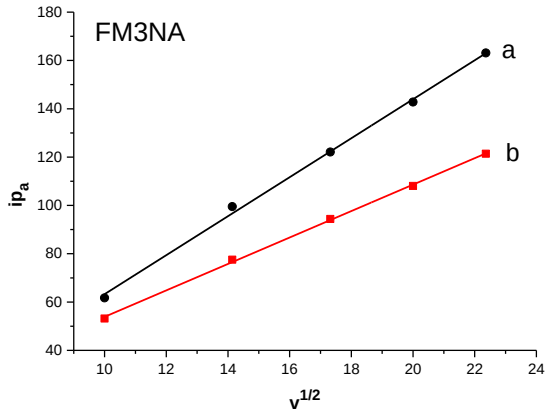

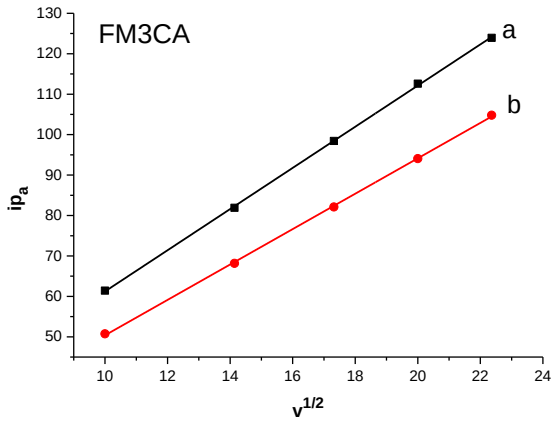

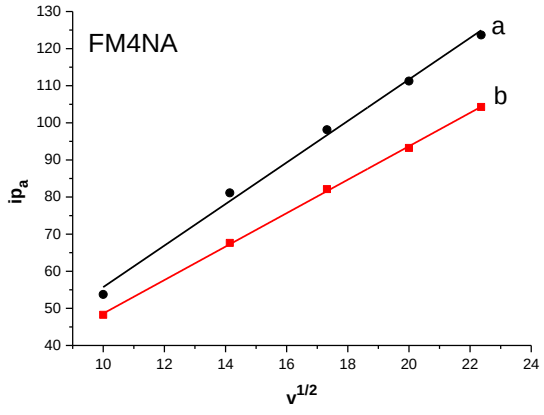

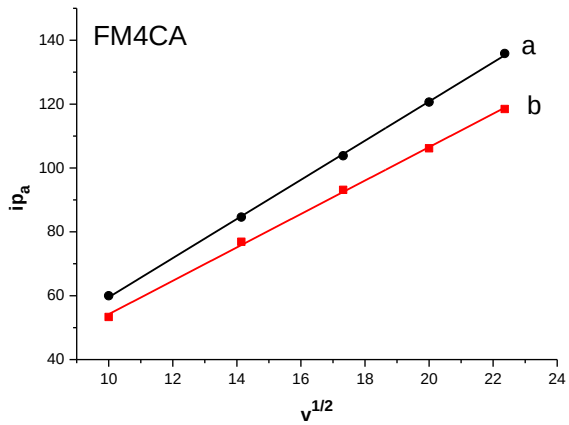

Figure 4.2-6: ia =f ($v^{1/2}$) plots of FcDA (2 mM) in the absence of BSA (a) and presence BSA (b) at scan rates ranging from 0.1 to 0.5 V.s-1 in a solution of ethanol/PBS (90:10)

The linearity of the relation for FcDA-BSA suggests that the redox process is kinetically controlled by the diffusion step. The diffusion coefficients were determined from the slopes of Randles–Sevcik plots. Values are given in Table 4.1-3. It can be seen that the diffusion coefficient of FcDA bound BSA is remarkably lower than that of the free FcDA

The correlation between FcDA-BSA, as illustrated in equation (4.2-1), implies that the redox process is kinetically regulated by the diffusion step. The diffusion coefficients were calculated using the slopes of the Randles-Sevcik plots and are presented in Table 4.1-3. Notably, the diffusion coefficient of FcDA bound to BSA was considerably lower than that of free FcDA.

Table 4.2-3: Diffusion constants values of the free and BSA bound form of FMA

Entry	Equation	R^2	$D(cm^2.s^{-1})$
FMAA	6.687 x – 3.259	1	9.14×10^{-7}
BSA-FMAA	5.725 x -7.912	0.999	6.70×10^{-7}
FM3NA	8.067 x – 17.399	0.999	1.33×10^{-6}
BSA- FM3NA	5.472 x – 0.839	0.999	6.12×10^{-7}
FM4NA	5.597 x - 0.249	0.997	6.40×10^{-7}
BSA- FM4NA	4.507 x – 3.536	0.999	4.15×10^{-7}
FM3CA	5.090 x – 10.329	0.999	5.29×10^{-7}
BSA- FM3CA	4.376 x -6.616	0.999	3.90×10^{-7}
FM4CA	6.129 x – 1.773	0.999	7.68×10^{-7}
BSA- FM4CA	5.232 x + 1.886	0.999	5.59×10^{-7}

The reduced diffusion coefficient observed for FcDA-BSA when compared to FcDA can be attributed to the larger molecular weight of the FcDA-BSA complex.

4.2.2 Electronic spectroscopy BSA interaction study

ligand binding interactions were studied using UV-visible spectroscopy [39]. Serum albumins exhibit a UV absorption peak at 280 nm, where three amino acids, in particular tryptophan,

phenylalanine, and tyrosine, absorb the most. UV-visible adsorption spectrum measurements show the interaction of ligand-serum albumin complexes. The rise in drug concentration causes an increase in absorbance, which verifies the change in polarity around the tryptophan residue and the change in peptide strand of serum albumins, and hence the change in hydrophobicity. As a result, drug binding to the protein molecule result in a change in the peptide bond, as shown in **Figure 4.2-7**, which is responsible for the change in protein conformation[156–159].

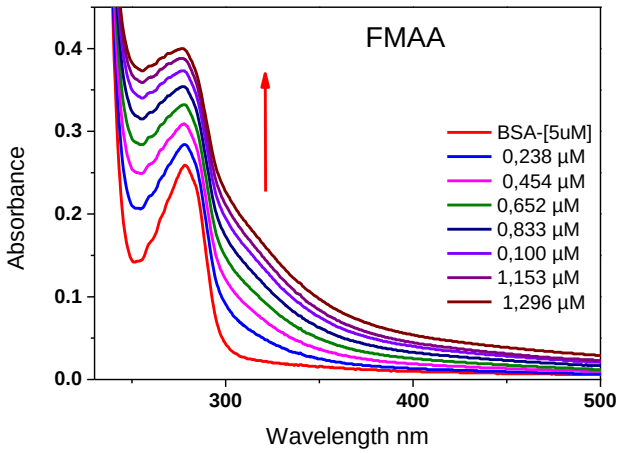

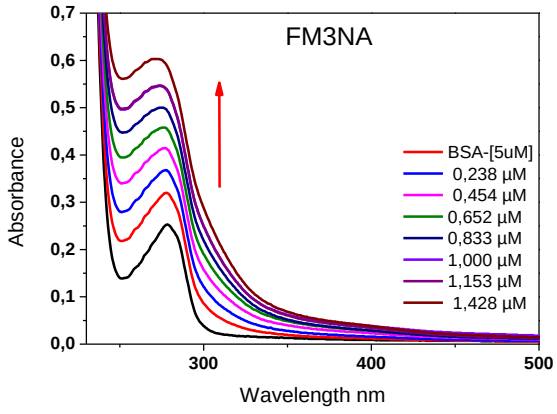

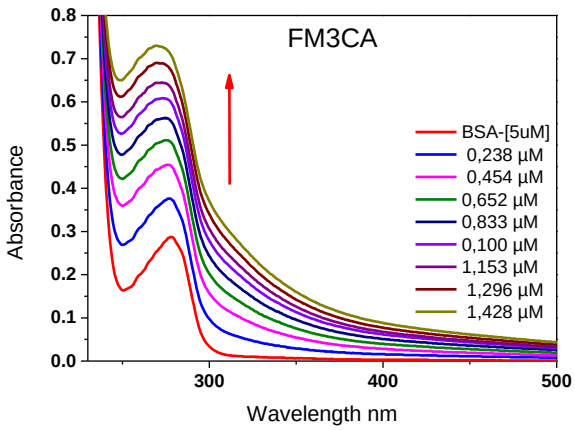

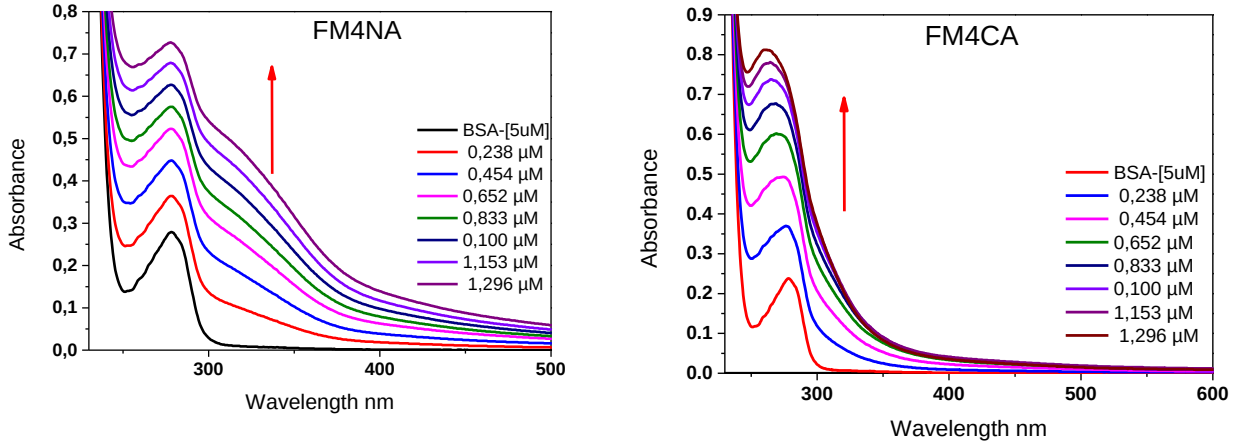

Figure 4.2-7: Absorbance spectra of FcDA, with increasing concentrations of BSA (0–22.5 µM). The concentration of FcDA was fixed at 1 mM at physiological pH 7.2

$$\frac{1}{A - A_0} = \frac{1}{A_{max} - A} + \frac{1}{A_{max} - A_0}\,\frac{1}{K_b[FcDA]} \qquad (4.2\text{-}2)$$

Based upon the increase in absorbance, the binding constant (K_b) was calculated according to Benesi-Hildebrand equation (4.2-2)

Where, A_0 and A are the absorbance of FcDA and their complexes with BSA, A_{max} is the obtained absorbance at saturation and [FcDA] is the concentration of deriver study.

The slope to intercept ratio of the plot between $1/(A - A_0)$ vs. 1 / [FcDA] yielded the binding constant

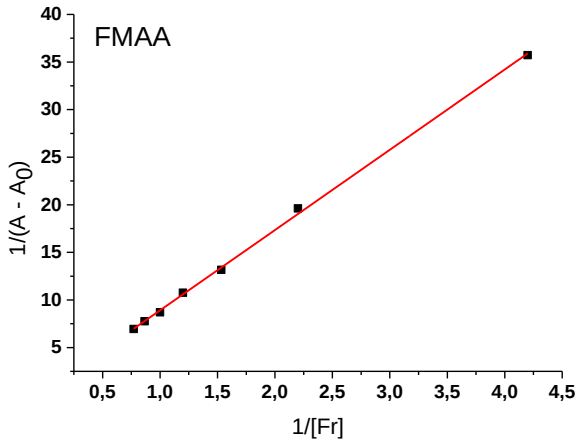

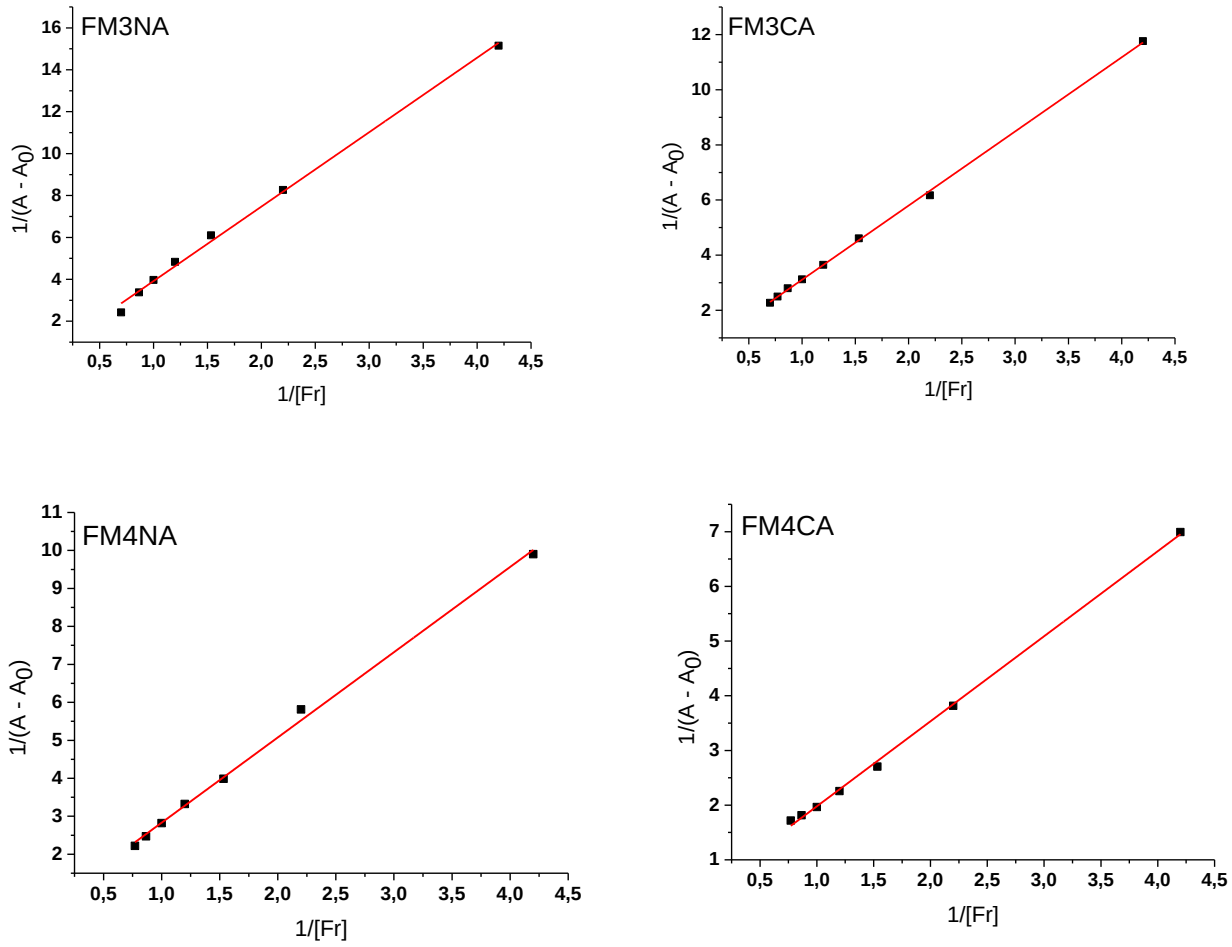

Figure 4.2-8: The plot of (A_0 / (A-A_0) versus 1 / [BSA] was used to calculate the binding constants

The obtained values of binding constants and their corresponding free binding energies was calculated using the equation (4.1-2) are presented in **Table 4.2-4**

Table 4.2-4: Binding constant and binding free energy values

Adduct	Equation	R^2	Kb (M^{-1})	ΔG ($KJ.mol^{-1}$)
BSA –**FMAA**	y = 8,434x +0,476	0.999	5.643×10^4	-27.12
BSA –**FM3NA**	y = 3,553x +0,362	0.996	1.018×10^5	-28.59
BSA –**FM4NA**	y = 2,245x +0,585	0.996	2.605×10^5	-30.91
BSA –**FM3CA**	y = 2,689x +0,419	0.999	1.558×10^5	-29.64
BSA –**FM4CA**	y = 1,555x +0,423	0.998	2.720×10^5	-31.01

4.2.3 Molecular docking BSA interaction study

4.2.3.1 Structural optimization

The ligands are optimised following the same steps as mentioned in the previous section, results are shown in figure 4.2-9.

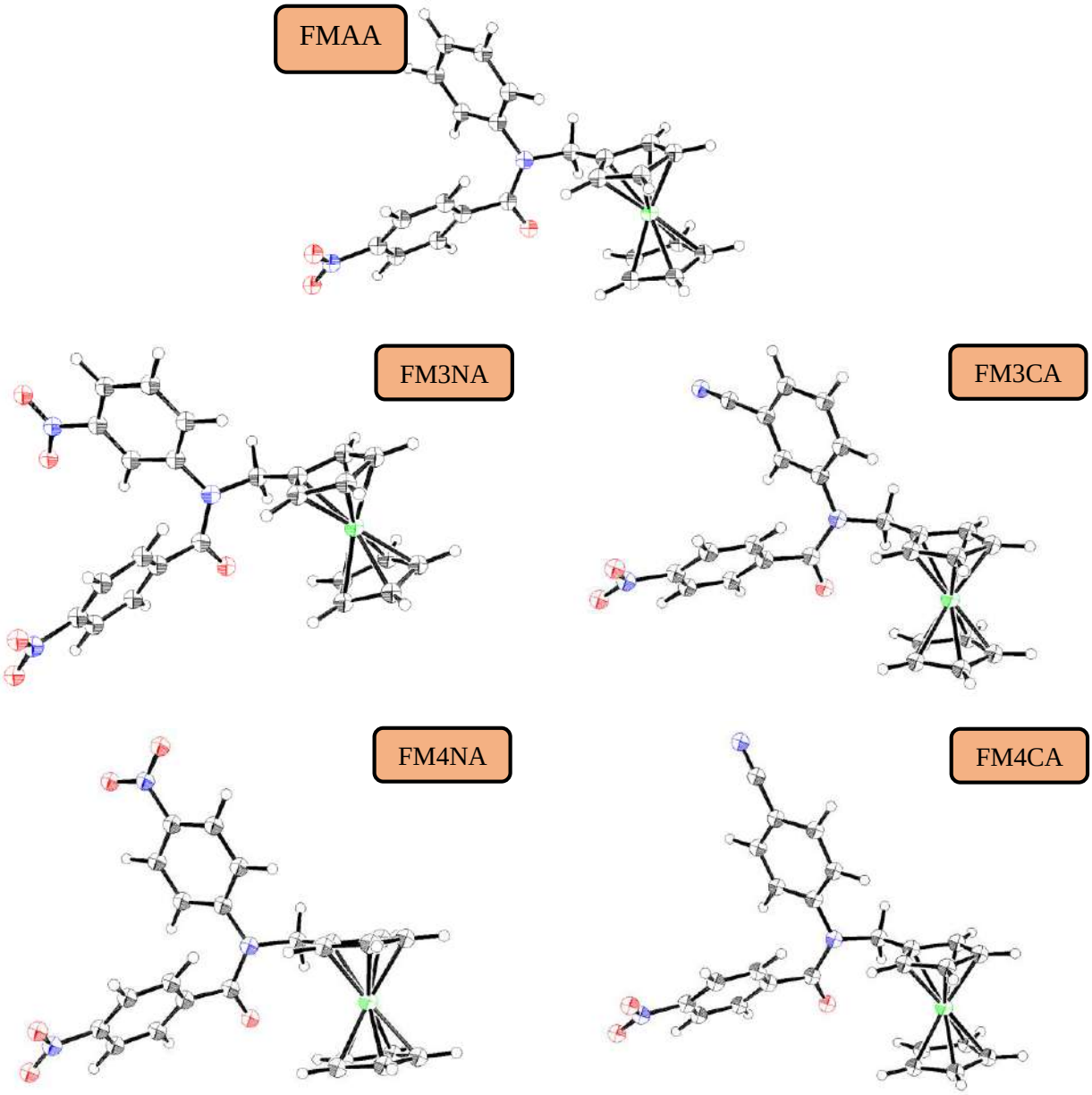

Figure 4.2-9: The optimized structures of FcDA represented by ORTEP View 03, V1.08 ; color codes are hydrogen (white), carbon (grey), iron (green), nitrogen (blue).

4.2.3.2 Molecular docking studies

The docking studies of the FcDA ligand into BSA were achieved using AutoDock 4.2. The crystal structure of BSA, with a resolution of 2.04 A°, was downloaded from the protein data bank (RCSB, PDB code: 4f5u). For the program and all analysed derivatives, the size of the grid map in the focus docking calculations for ligands compounds was set to 40×40×40 A^3 in the x, y, and z directions with a grid point spacing of 0.375 A. Docking study was performed on the stable conformation with the lowest binding energy. The interaction was generated with PLIP webservice and visualizer by PyMOL software., which was represented in figure .

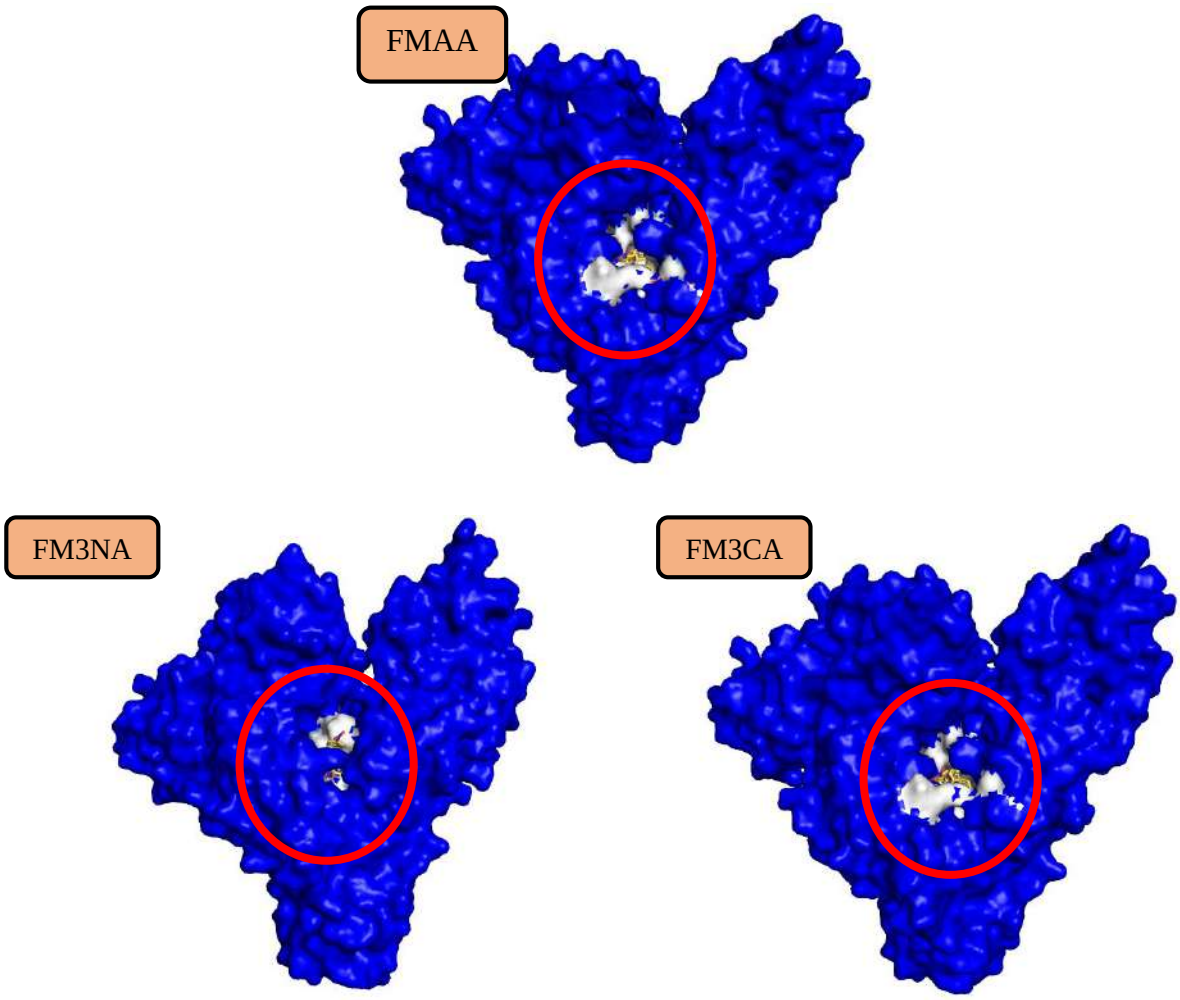

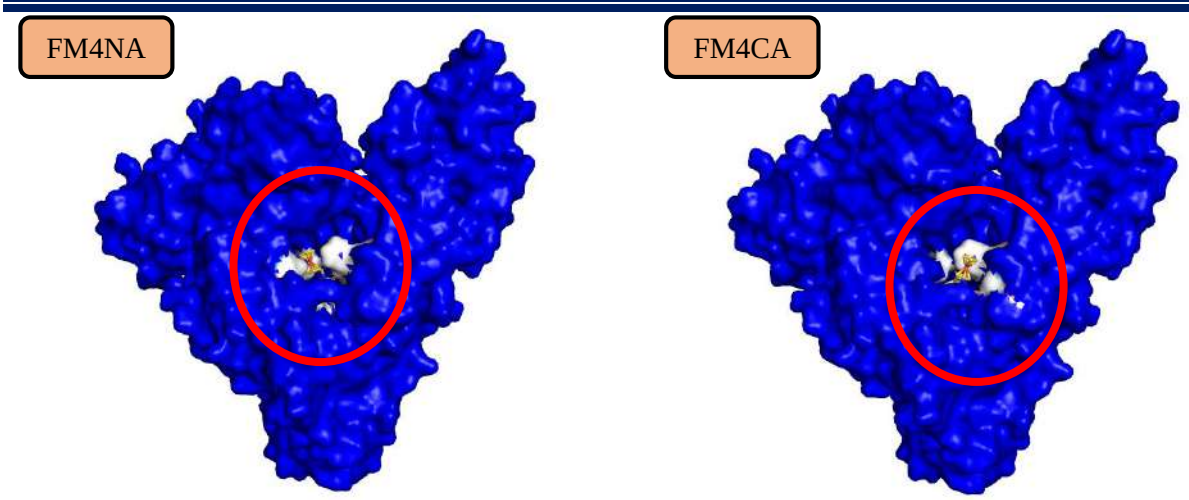

Figure 4.2-10: Representation 3D Structures of BSA (PDB code:4f5u)

All data related to BSA-FcDA interactions in the best active site is explained in the following table

Table 4.2-5: Binding constant and binding free energy values

Complex	K (M^{-1})	ΔG ($KJ.mol^{-1}$)	The number of runs	pocket
BSA –**FMAA**	6.91×10^{4}	-27.63	8	1
BSA –**FM3NA**	1.09×10^{5}	-28.76	47	1
BSA –**FM4NA**	2.25×10^{5}	-30.56	10	1
BSA –**FM3CA**	1.43×10^{5}	-29.43	8	1
BSA –**FM4CA**	2.94×10^{5}	-31.22	9	1

Results from molecular docking suggest that hydrogen bonding, hydrophobic forces and π-cation interaction are involved in the binding process. **Figure 4.2-11** illustrates the interaction of FcDA with the nearby residues in the active site of BSA. The visualization of the interaction was generated with PLIP web server (protein Ligand Interaction Profiler). Lastly, the better docked protein–ligand complexes were modified and analysed using the visualizer PyMOL.

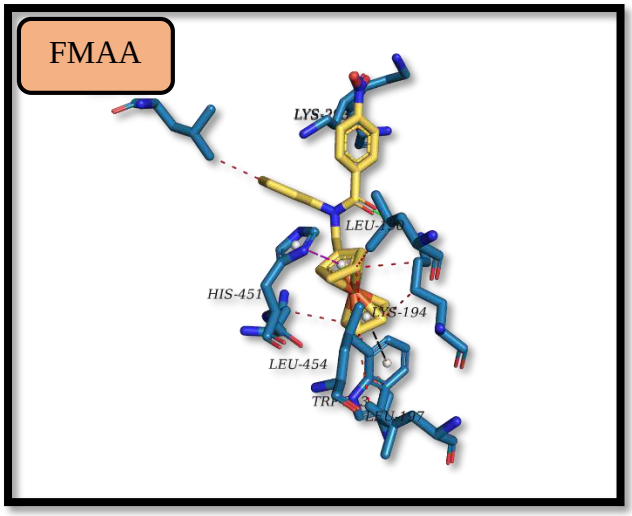
FMAA
HIS-451
LYS-194
LEU-454

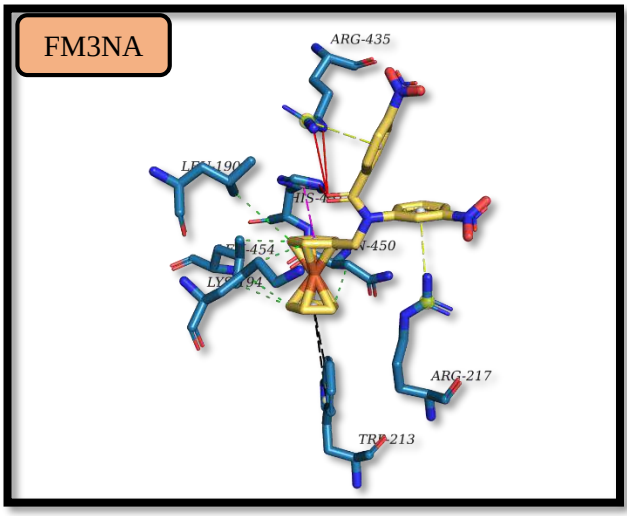
FM3NA
ARG-435
ARG-217
TRP-213

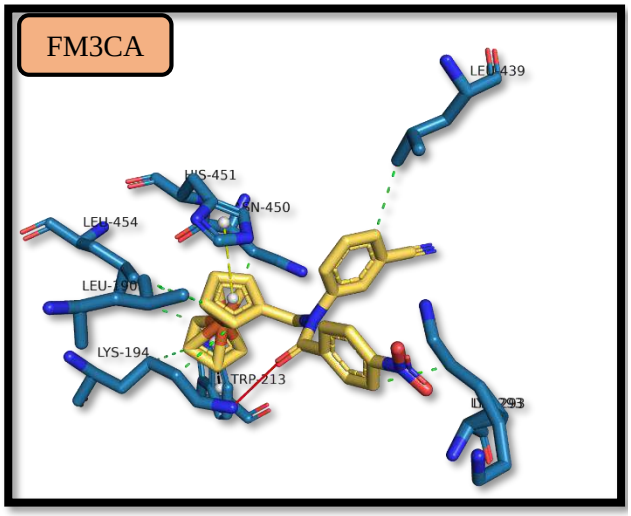
FM3CA
LEU-439
HIS-451
LEU-454
LEU-460
LYS-194
TRP-213

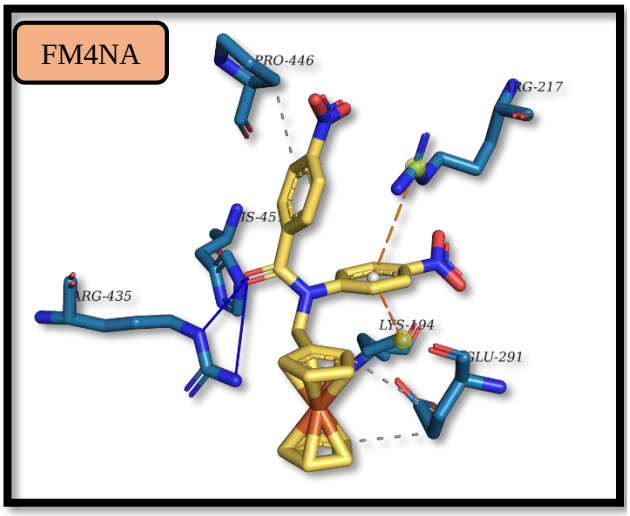
FM4NA
PRO-446
ARG-435
LYS-194

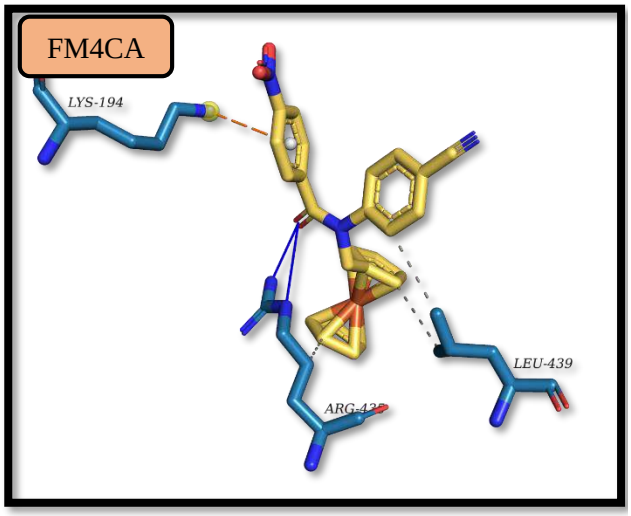
FM4CA
LYS-194
LEU-439

Figure 4.2-11: Best docking poses for BSA-FcDA generated with PLIP web service illustrating the hydrophobic and H-bons interactions. Elements colors: hydrogen, oxygen, nitrogen, and iron are represented in white, red, blue and brown, respectively

Hydrogen bonds (blue**)**, hydrophobic forces (silver**),** π-stacking (green), π-cation (orange)

The tables presented below summarize the type of interactions, distances, and the residues involved in the interactions

Table 4.2-6: Hydrophobic forces between the ligands FMA and BSA

Sample code	Residue	Amino acid	Distance (Å)
FMAA	190A	LEU	3.76
	194A	LYS	3.08
	194A	LYS	3.13
	197A	LEU	3.94
	293A	LYS	3.80
	439A	LEU	3.50
	450A	ASN	3.18
	454A	LEU	3.29
	454A	LEU	3.13
FM3NA	190A	LEU	3.98
	194A	LYS	3.65
	194A	LYS	3.08
	450A	ASN	3.21
	454A	LEU	3.47
	454A	LEU	2.93
FM4NA	291A	GLU	3.31
	291A	GLU	3.92
	446A	PRO	3.46
FM3CA	190A	LEU	3.79
	194A	LYS	3.15
	194A	LYS	3.16

	293A	LYS	3.47
	439A	LEU	3.08
	450A	ASN	3.27
	454A	LEU	3.58
	454A	LEU	3.08
FM4CA	435A	ARG	3.78
	439A	LEU	3.53
	439A	LEU	3.77

Table 4.2-7: Hydrogen bonding between the ligands FcDA and BSA

Sample code	Residue	Amino acid	H-A	D-A
FMAA	194A	LYS	1.86	2.82
FM3NA	435A	ARG	3.42	3.95
	435A	ARG	2.97	3.54
	451A	HIS	2.59	3.25
FM4NA	435A	ARG	2.01	3.02
	435A	ARG	3.10	3.83
	451A	HIS	2.27	3.20
FM3CA	194A	LYS	1.70	2.62
FM4CA	435A	ARG	3.11	3.70
	435A	ARG	1.61	2.55

Table 4.2-8: π-stacking interactions between ligands

Sample code	Residue	Amino acid	Distance (Å)
FMAA	213A	TRP	4.33
	451A	HIS	3.44
FM3NA	213A	TRP	5.43
	213A	TRP	4.16
	451A	HIS	3.43

FM3CA	213A	TRP	4.27
	451A	HIS	3.42

Table 4.2-9: π-Cation interactions between ligands

Sample code	Residue	Amino acid	Distance (Å)
FM3NA	217A	ARG	4.56
	435A	ARG	3.94
FM4NA	194A	LYS	3.17
	217A	ARG	1.87
FM3CA	194A	LYS	3.60

The ligand FcDA interacted with BSA via hydrogen bonding and hydrophobic forces, as shown in **Table 4.2-6** show the residues and amino acids involved in these interactions. The distance between hydrogen and the receptor atoms (H-A) and between donor and receptor atoms (D-R) are also shown in **Table 4.2-7**. (H-D). Furthermore, molecular docking data for the complex BSA-FcDA revealed π-stacking and π-cation interactions between the positively charged amino acid residue and the ligand's phenyl cycle.

FMAA binds strongly to BSA, having hydrophobic contacts at LEU190, LYS194, LEU197, LYS293, LEU439, ASN450 and LEU454 residues and one hydrogen bond at LYS194 residues. π-stacking interaction with TRP213, HIS451 of distance 4.24, 5.06 angstroms of BSA protein respectively.

Docking study shows that FM3NA attaches to LEU439, GLU443, PRO446 and PRO446 residues via hydrophobic interactions and forms three hydrogen bonds with LEU439, GLU443 and PRO446 residues. Two electrostatic interactions were also seen between the π electron cloud of fused aromatic ring and the ring of LYS185 and ARG458 residues.

FM4NA was discovered to have strong binding to BSA, with hydrophobic contacts at GLU291 and PRO446 residues, two hydrogen bonds at ARG435 and HIS451 residues, and a π-cation interaction with LYS194 and AGR217 of 3.17 and 1.87 angstroms respectively.

Figure 4.2-11 illustrated the binding conformation and binding site residues of FM3CA. one hydrogen LYS194 bonds are formed with FM3CA, whilst other BSA hydrophobic residues are

distributed between FM3CA (LEU190, LYS194, LYS293, LEU439, ASN450 and LEU454) and π-cation interaction with TRP213 and HIS451 and other one π-Cation LYS194 residues of BSA protein respectively.

The investigated ligand FM4CA forms a hydrogen bond with BSA via the residue ARG435.Furthermore, hydrophobic interactions linked FM4CA to charged residues ARG435 and LEU439.

Table 4.2-10: Binding parameters (k and ΔG) of FcDA compounds obtained from CV, UV-vis and docking methods.

Method	CV		Uv-vis		Docking	
Complex	K (M^{-1})	ΔG ($KJ.mol^{-1}$)	K (M^{-1})	ΔG ($KJ.mol^{-1}$)	K (M^{-1})	ΔG ($KJ.mol^{-1}$)
BSA –**FMAA**	7.94×10^{4}	-27.97	5.64×10^{4}	-27.12	6.91×10^{4}	-27.63
BSA –**FM3NA**	1.07×10^{5}	-28.71	1.02×10^{5}	-28.59	1.09×10^{5}	-28.76
BSA –**FM4NA**	2.75×10^{5}	-31.06	2.61×10^{5}	-30.91	2.25×10^{5}	-30.56
BSA –**FM3CA**	1.55×10^{5}	-29.62	1.56×10^{5}	-29.64	1.43×10^{5}	-29.43
BSA –**FM4CA**	2.82×10^{5}	-31.11	2.72×10^{5}	-31.01	2.94×10^{5}	-31.22

Table 4.4-6 clearly shows that the molecular docking results are in good agreement with those obtained from experimental assays

Chapter 5

HHb interaction study

5.1 Hemoglobin preparation

Fresh blood (5 ml) was obtained from the EL MAJDE laboratory's blood bank and put into a violet vial containing EDTA as an anticoagulant. This was centrifuged at 4000 rpm for 15 minutes, separating the RBCs from the WBCs, platelets (as a grey buffy coat), and plasma (yellow–green liquid). The supernatant was discarded with the exception of the RBCs (approximately 2 ml). According to Parpart et al [160]. RBC samples were produced by saline water dilution. This was utilized as a test sample.

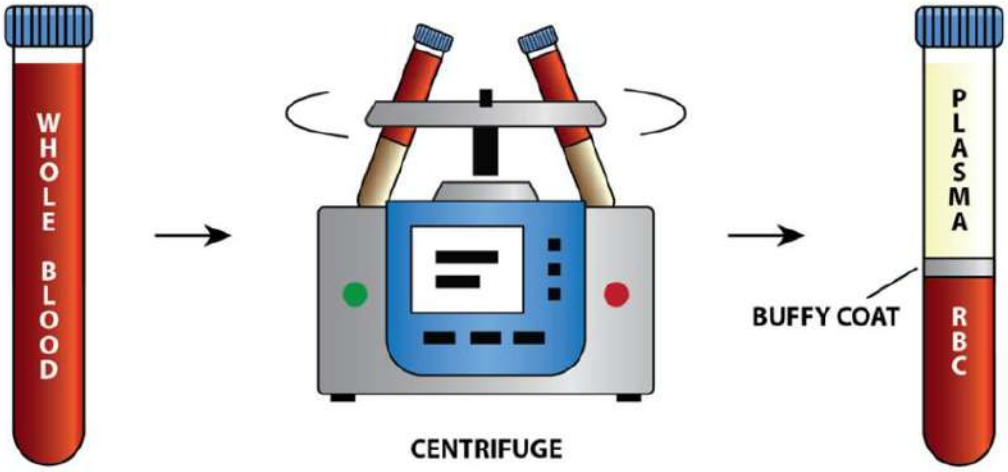

Figure 5.1-1: Red blood cell preparation [161]

5.2 Hemoglobin UV-visible Spectroscopic characterization

A UV-Vis spectrophotometer was used to characterize the sample, which resulted in peak absorption to identify electronic transitions of a molecule. The **Figure 5.2-1** depicts five blood peaks that describe the hemoglobin (Hb) [162,163]. The first peak at 275 nm is attributed to the π-π* transitions of the carbonyl (C═O) groups of the aromatic amino acid residues (Trp, Tyr, and Phe) [164], the second peak at 342 nm corresponds to the globin-heme interaction, the third peak at 415 nm corresponds to the heme, the fourth peak at 540 nm corresponds to the heme-heme interaction, and the fifth peak at 574nm . The absorbance of hemoglobin at 415 nm (ε= 125 $mol^{-1}cm^{-1}$) was used to calculate its molar concentration[165].

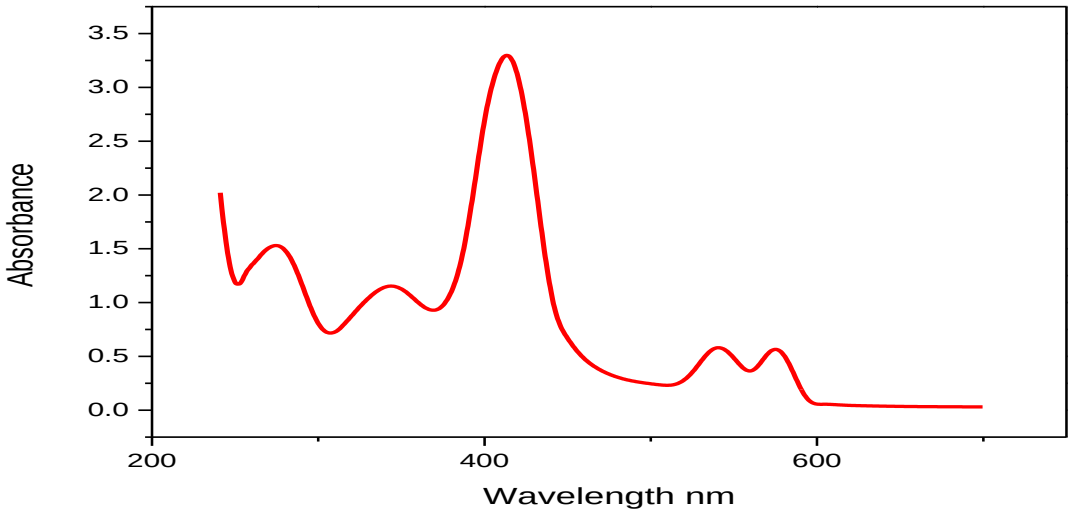

Figure 5.2-1: Absorbance spectra of Hemoglobin concentration 2.6×10^{-5} M at physiological pH 7.2

Hemoglobin interaction studies using electronic spectroscopy

5.3 The study of the interaction of FcDB-HHb

5.3.1 Hemoglobin interaction studies using UV-Visible Spectroscopy

Figure 5.3-1 depicts the effect of gradually increasing concentration of FcDB on a hemoglobin solution.

.

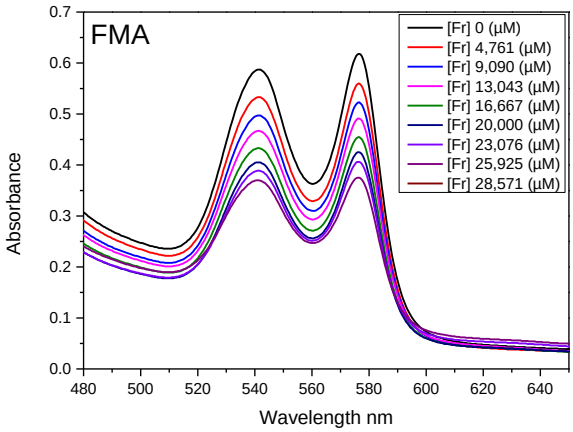

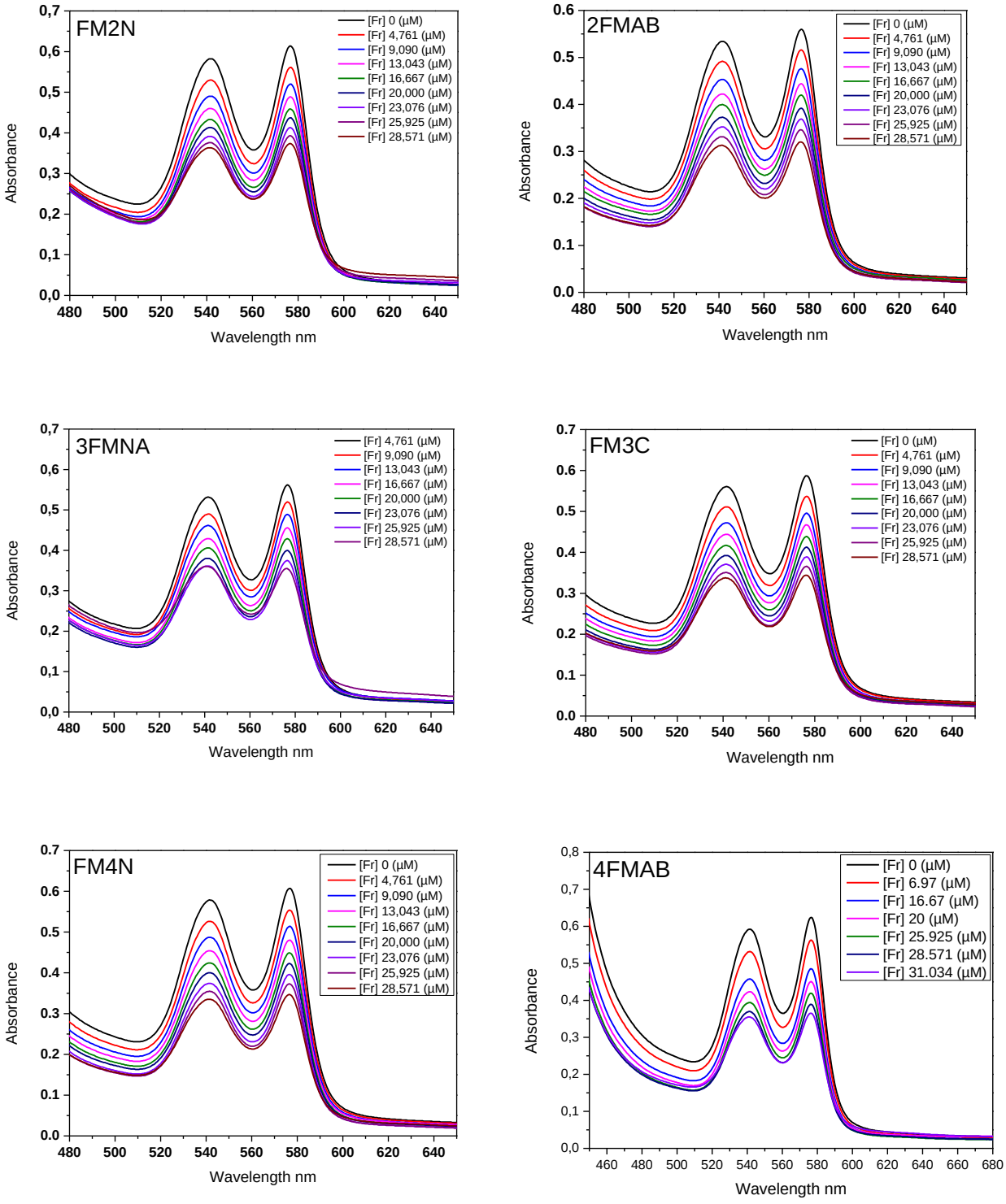

Figure 5.3-1: UV-visible absorption spectra of HHb were examined in the presence of varying concentrations of FcDB in a solution consisting of ethanol and PBS in a ratio of 90:10.

Binding constant and binding free energy

The intrinsic binding constant was determined by utilizing an equation (5.3-1) that employed the alteration in absorbance values induced by the incremental addition of FcDB concentrations.

$$\frac{A_0}{A - A_0} = \frac{\varepsilon}{\varepsilon - \varepsilon_0} + \frac{\varepsilon}{\varepsilon - \varepsilon_0}\frac{1}{K_b[FcD]} \qquad 5.3\text{-}1)$$

The determination of the binding constant (Kb) involves the calculation of the ratio of the intercept to the slope of the graph depicting the relationship between $A_0/(A\text{-}A_0)$ and 1/[FcDB]. This graph is illustrated in **Figure 5.3-2** .

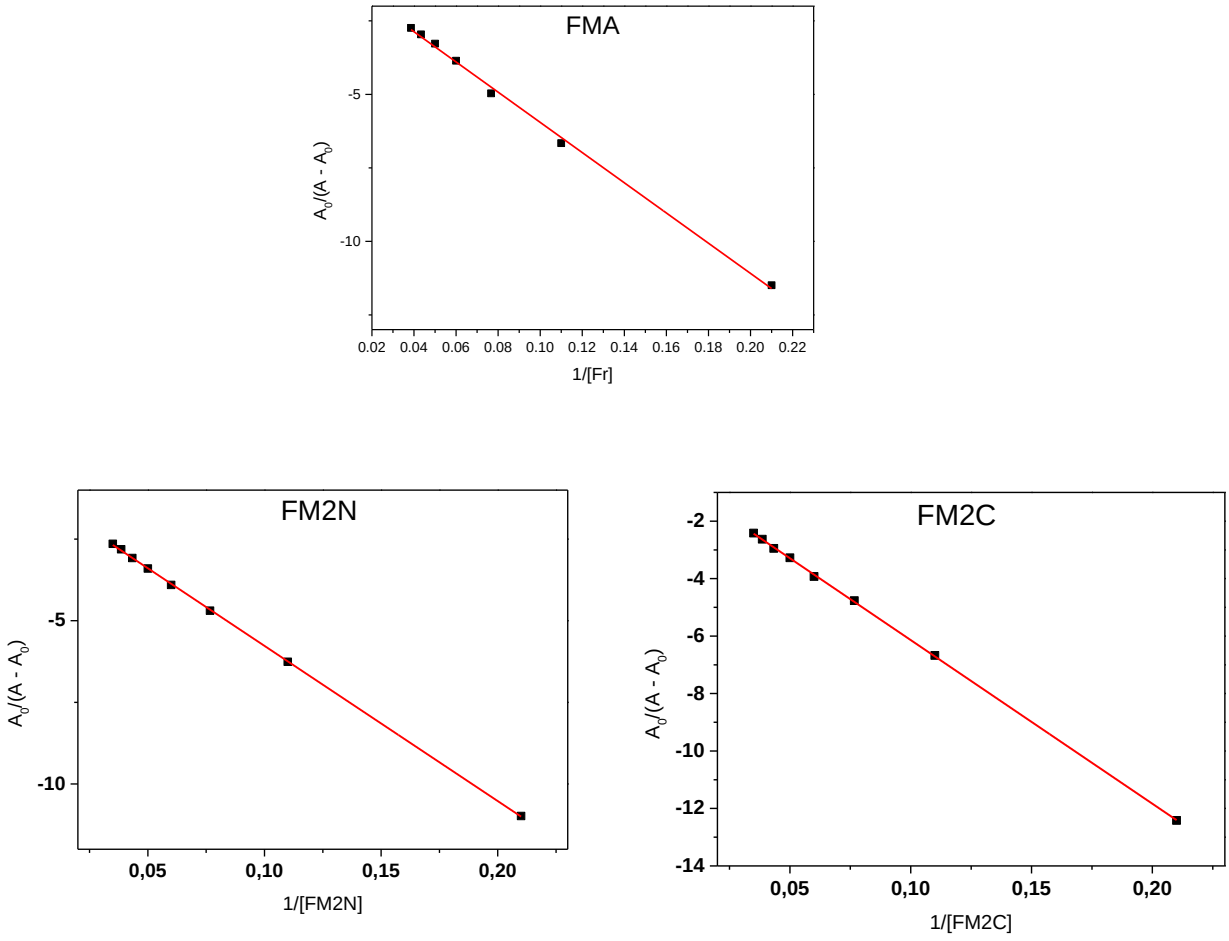

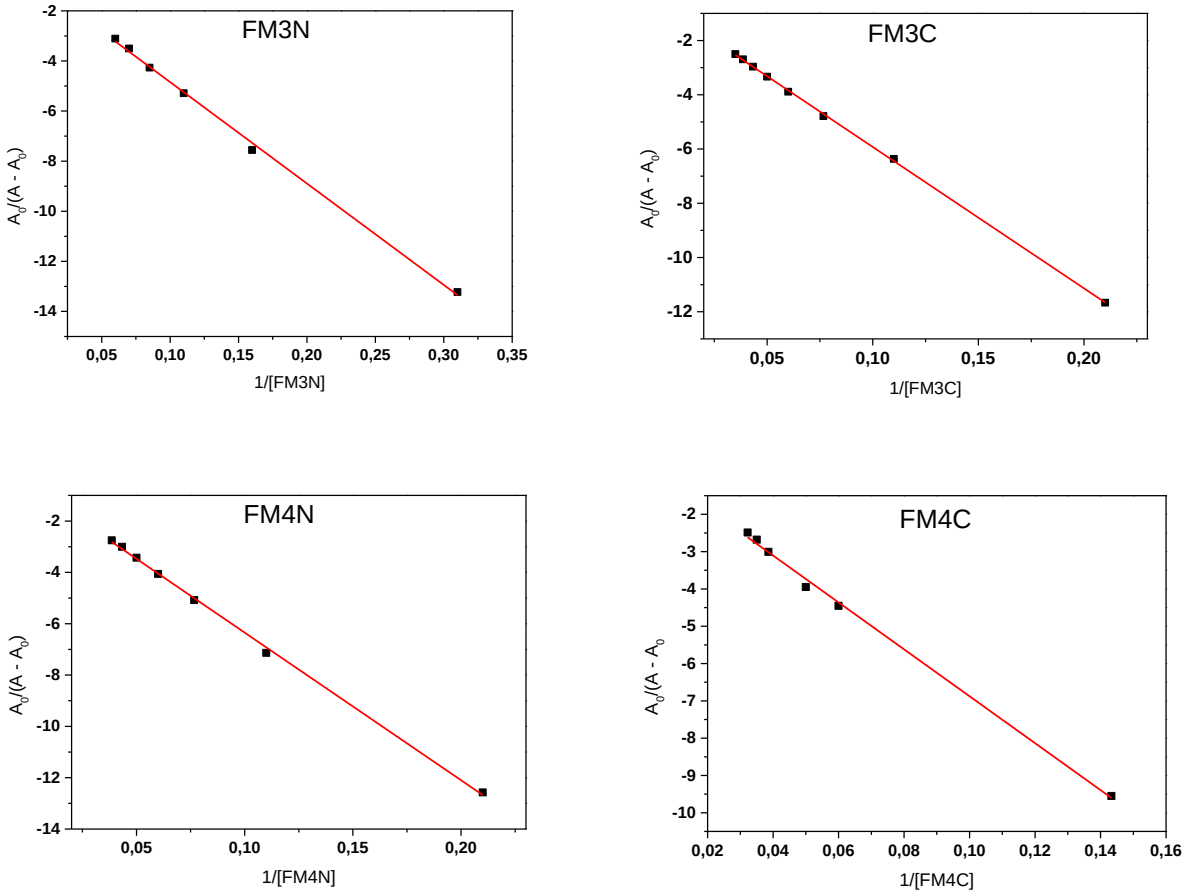

Figure 5.3-2: The binding constants between HHb and FcDB molecules were determined by plotting $A_0/(A-A_0)$ against 1/[FcDB]. These plots were employed in the calculation of the binding constants.

The changes in binding free energy were estimated following the same method as described for HHb, the obtained results are summarized in **Table 5.3-1**

Table 5.3-1: Binding constant and binding free energy estimates for FcDB ligands with HHb calculated from UV measurements at 298 K

Adduct	Equation	R^2	Kb (M^{-1})	ΔG ($KJ.mol^{-1}$)
HHb –**FMA**	y = -51.369x – 0.998	0.998	1.59×10^4	-23.98
HHb – **FM2N**	y = -47,533x - 1,017	0.999	2.14×10^4	-24.72
HHb – **FM3N**	y = - 40,487x - 0,794	0.999	1.95×10^4	-24.49
HHb – **FM4N**	y = - 57,501x - 0,597	0.998	1.03×10^4	-22.92
HHb – **FM2C**	y = -56,958x - 0,442	0.999	7.78×10^3	-22.21

HHb – **FM3C**	y = - 52,128x - 0,711	0.999	1.36×10^4	-23.61
HHb – **FM4C**	y = -62.872x - 0.859	0.996	9.36×10^3	-22.67

The results indicate that **FM3N** is more strongly attached to haemoglobin than the other studied derivatives.

5.3.2 Hemoglobin interaction studies using molecular docking analysis

The synthesized ligands FcDB were docked into HHb structure to determine the complexes possible binding mode with HHb and to further visualize the interactions.

5.3.2.1 Binding site determination

The analysis results on the prank Web server revealed 16 possible binding sites, as shown in **Figure 5.3-3**. The results of the Proteins HHb (RCSB, PDB code: 1gcw) server research revealed four potential binding sites (**Table 5.3-2**

Table 5.3-2)

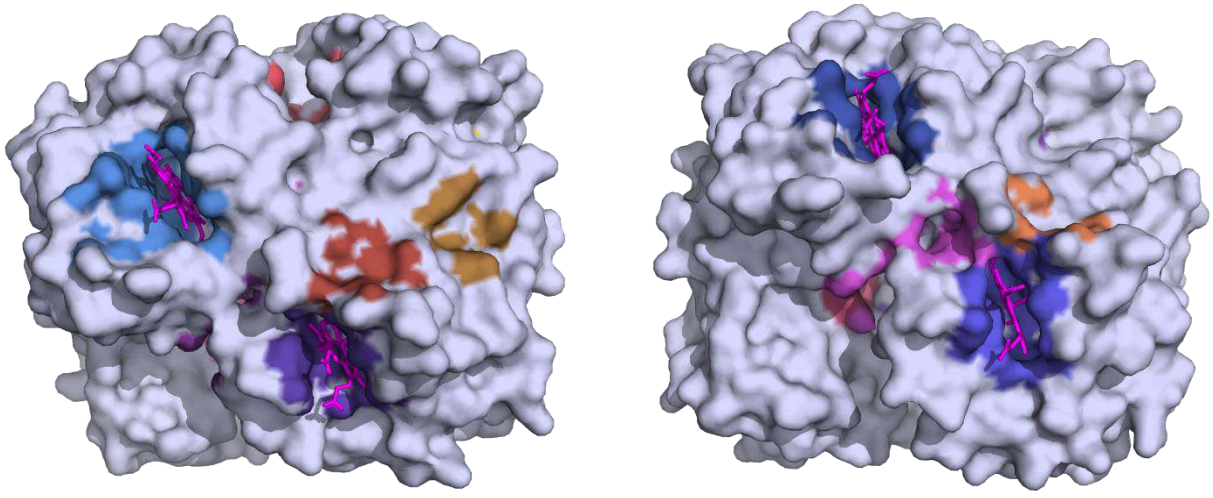

Figure 5.3-3: surface view of HHb (code: 1gcw) and predicted binding pockets in different color

All coloured spaces represent the active site. Data related to it is mentioned in the following **Table 5.3-2**

Table 5.3-2: The best 10 active sites on HHb from Prankweb server

name	rank	score	probability	Grid centre		
				x	y	z
pocket1	1	56.94	0.984	31.19	37.03	27.93
pocket2	2	56.87	0.984	18.40	46.40	57.30
pocket3	3	51.32	0.978	17.63	21.31	52.75
pocket4	4	49.1	0.975	5.46	39.60	28.52
pocket5	5	9.73	0.564	26.47	33.83	46.00
pocket6	6	9.73	0.564	17.34	32.15	29.43
pocket7	7	9.28	0.542	13.41	34.12	53.83
pocket8	8	8.85	0.521	18.25	44.52	38.59
pocket9	9	4.71	0.218	21.54	26.73	37.68
Pocket10	10	3.73	0.149	8.35	41.80	44.90

5.3.2.2 Molecular docking studies

The docking studies of the FcDB ligand into HHb were achieved using AutoDock 4.2. The crystal structure of HHb, with a resolution of 2.00 A°, was downloaded from the protein data bank (RCSB, PDB code: 1gcw). For all analysed derivatives, the size of the grid map in the focus docking calculations for ligands compounds was set to 40×40×40 A^3 in the x, y, and z directions with a grid point spacing of 0.375 A. Docking analysis was performed on the stable conformation with the lowest binding energy[166]. The interaction was generated with PLIP webservice and visualizer by PyMOL software., the results are presented in **Figure 5.3-4**

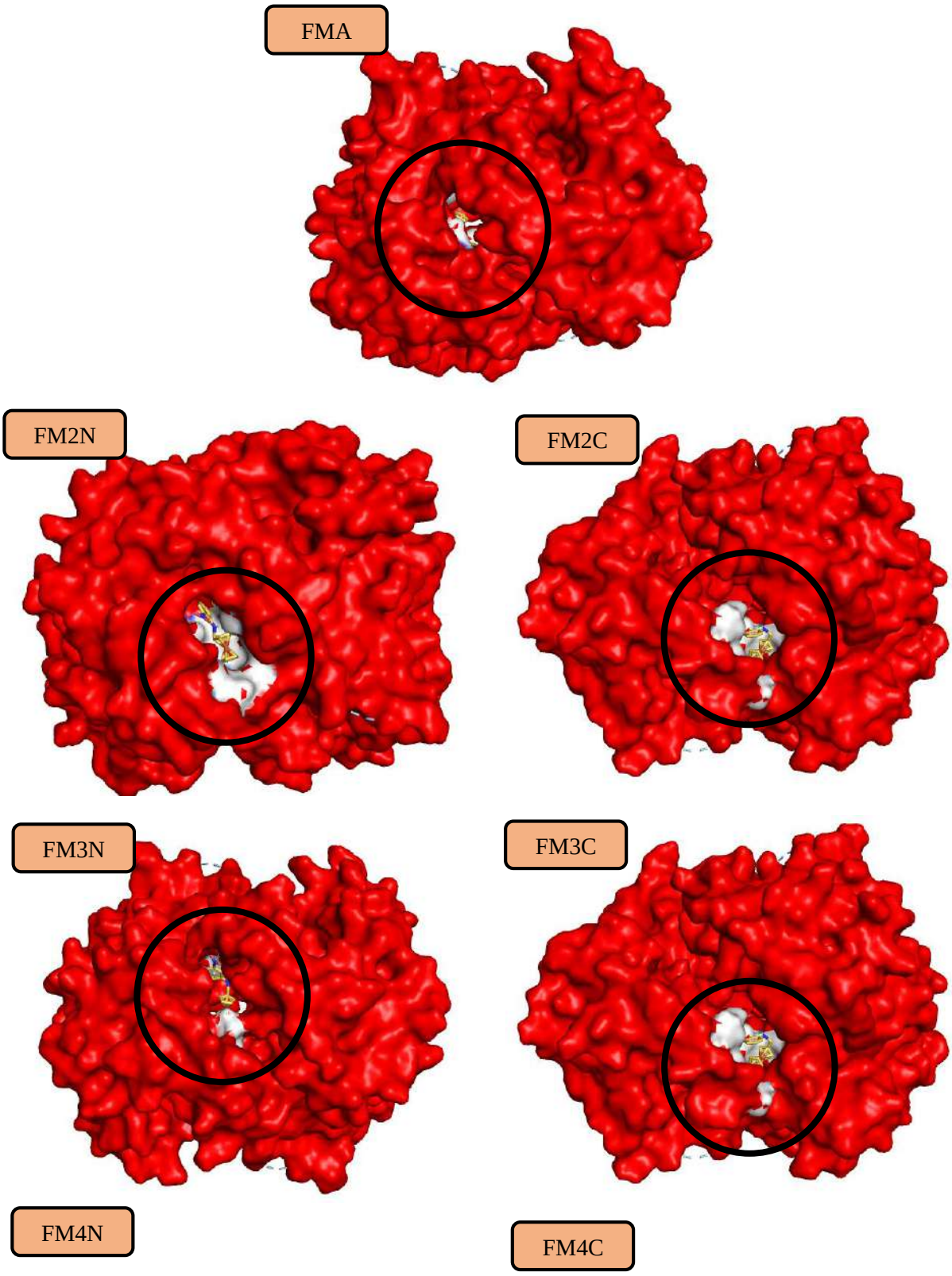
FMA
FM2N
FM2C
FM3N
FM3C
FM4N
FM4C

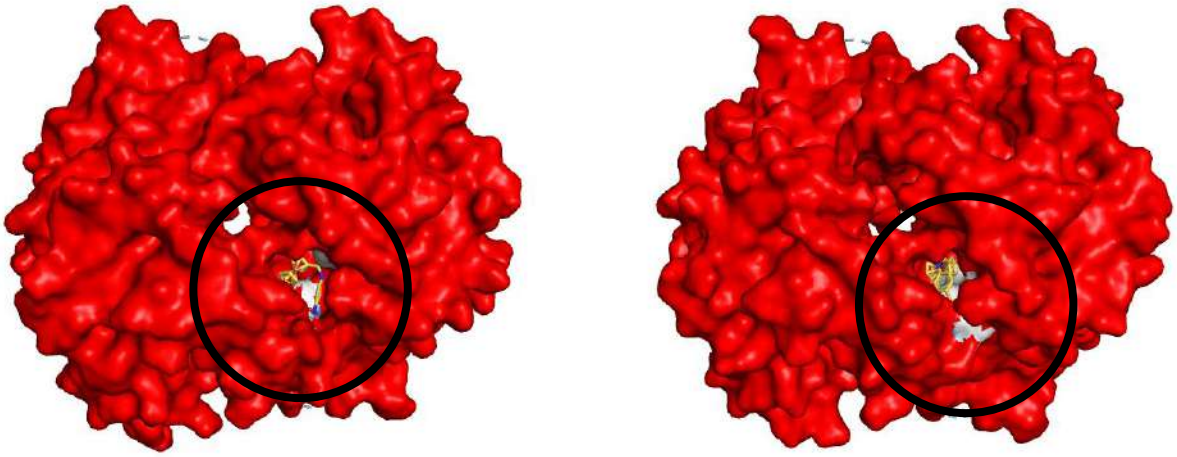

Figure 5.3-4: 3D Structures representation of HHb (PDB code:1gcw)

All data related to HHb-FcDA interactions in the best active site is explained in the following table

Table 5.3-3: Binding constant and binding free energy values

Complex	K (M^{-1})	ΔG ($KJ.mol^{-1}$)	The number of runs	pocket
HHb –FMA	1.54×10^{4}	-23.91	2	5
HHb – FM2N	2.51×10^{4}	-25.12	49	1
HHb – FM3N	1.96×10^{4}	-24.50	50	5
HHb – FM4N	1.04×10^{4}	-22.94	43	5
HHb – FM2C	7.83×10^{3}	-22.23	46	8
HHb –FM3C	1.38×10^{4}	-23.65	45	6
HHb –FM4C	9.77×10^{3}	-22.78	45	8

According to the molecular docking analysis, the binding process between FcDB and HHb is influenced by hydrogen bonding, hydrophobic forces, and π-cation interactions. The interaction between FcDB and the active site residues of HHb is depicted in **Figure 5.3-5** , which was generated using the PLIP web server. The visualizer PyMOL was used to modify and analyze the protein-ligand complexes that exhibited the best docking results.

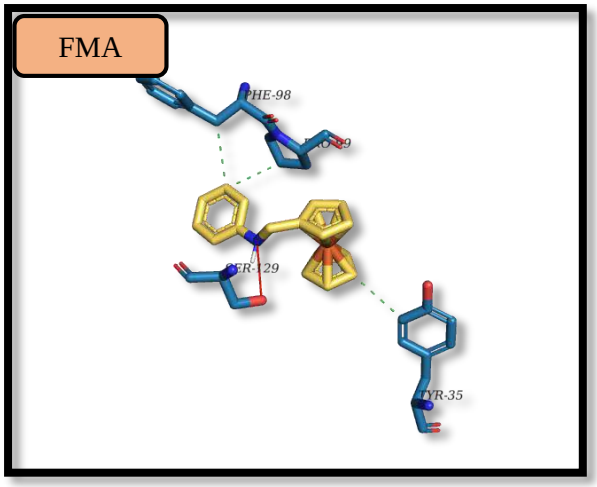
FMA
PHE-98
SER-129
TYR-35

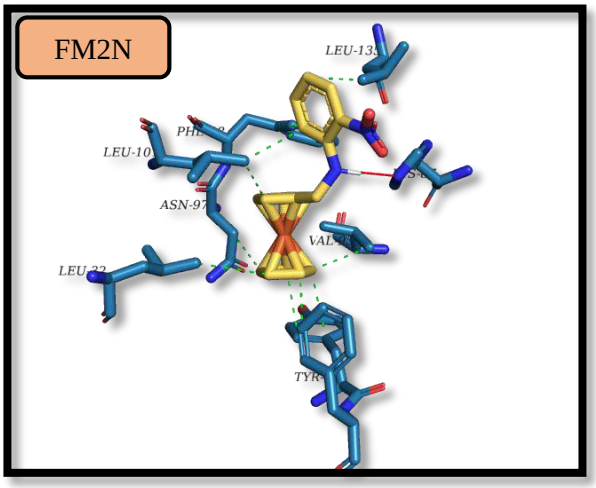
FM2N
LEU-13
LEU-10
ASN-97
LEU-32

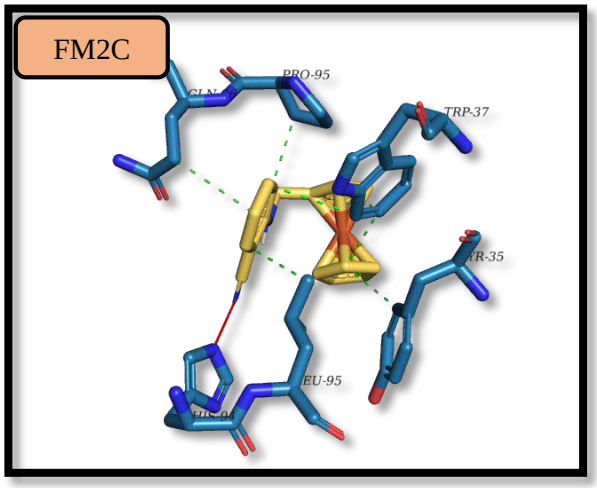
FM2C
PRO-95
TRP-37
TYR-35
LEU-95

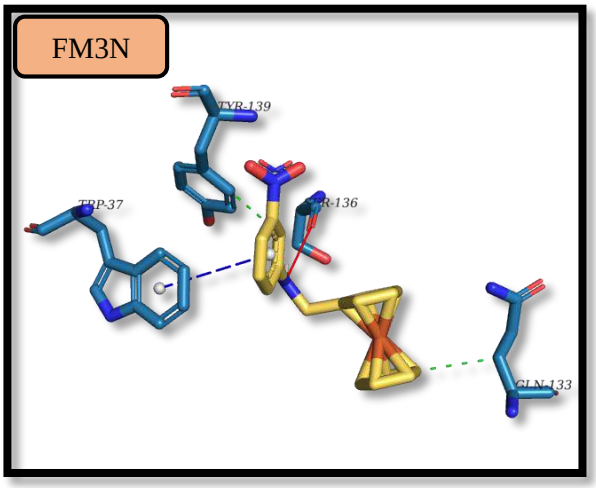
FM3N
TYR-139
TRP-37
GLN-133

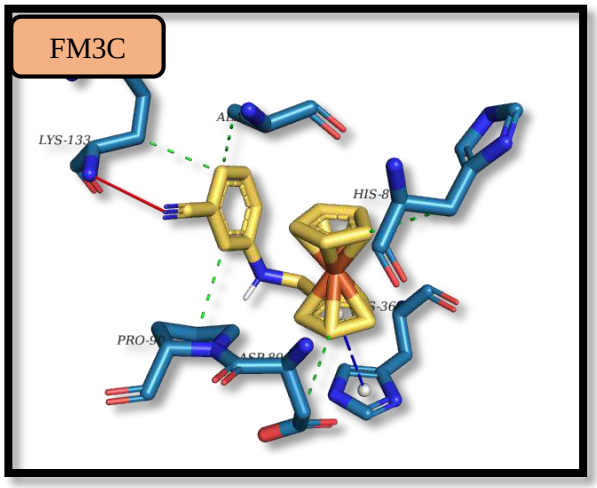
FM3C
LYS-133
HIS-8

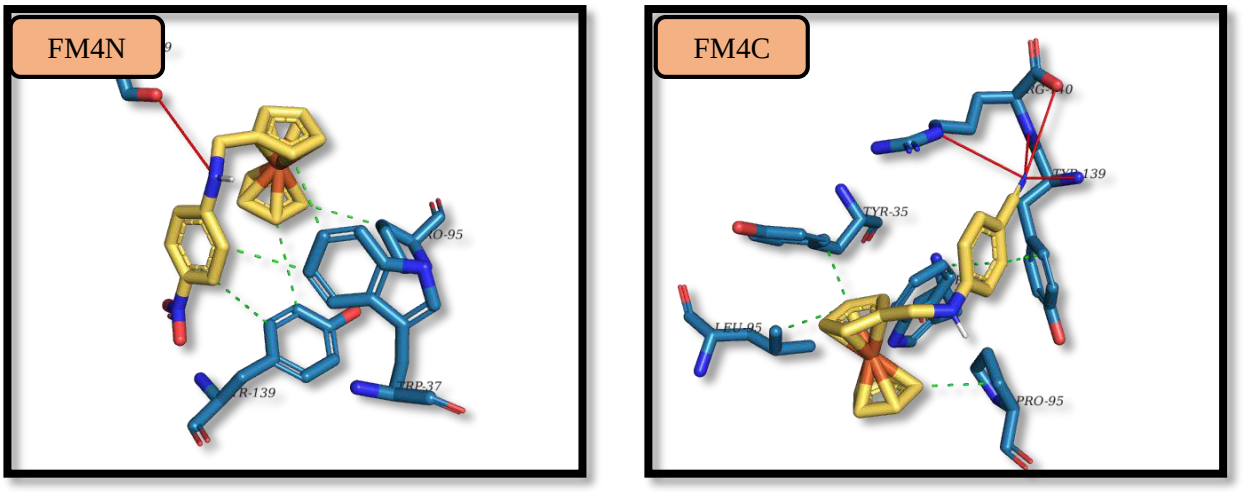

Figure 5.3-5: The PLIP web service generated the optimal docking poses for HHb-FcDB, highlighting the hydrophobic and hydrogen bond interactions. In the resulting image, the elements are color-coded: white represents hydrogen, red represents oxygen, blue represents nitrogen, and brown represents iron. The interactions are identified by their respective colors: hydrogen bonds are represented in blue, hydrophobic forces in silver, π-stacking in green, and π-cation in orange.

The tables presented below summarize the type of interactions, distances, and the residues involved in the interactions

Table 5.3-4: Hydrophobic interaction between the ligands FcDB and HHb

Sample code	Residue	Amino acid	Distance (Å)
FMA	35B	TYR	3.37
	98A	PHE	3.43
	99A	PRO	3.48
FM2N	32A	LEU	3.74
	42A	TYR	3.33
	42A	TYR	3.54
	43A	PHE	3.25
	93A	VAL	3.57
	97A	ASN	3.36
	98A	PHE	3.61
	101A	LEU	3.24
	101A	LEU	3.52
	135A	LEU	3.5
FM3N	133A	GLN	3.43
	139A	TYR	3.15

Sample code	Residue	Amino acid	Distance (Å)
FM4N	37B	TRP	3.25
	37B	TRP	3.25
	95C	PRO	2.28
	139C	TYR	3.76
	139C	TYR	3.96
FM2C	35D	TYR	3.5
	37D	TRP	3.05
	37D	TRP	3.51
	37D	TRP	3.13
	95D	PRO	3.19
	95D	LEU	3.44
	96A	GLN	3.62
FM3C	83D	ALA	3.58
	87D	HIS	3.85
	89D	ASP	3.78
	90D	PRO	3.35
	133D	LYS	3.07
FM4C	35D	TYR	3.41
	37D	TRP	3.51
	95A	PRO	3.46
	95D	LEU	3.49
	139A	TYR	3.24

Table 5.3-5: Hydrogen bonding between the ligands FcDB and HHb

Sample code	Residue	Amino acid	H-A	D-A
FMA	129A	SER	2.13	3.04
FM2N	87A	HIS	2.07	3.00
FM3N	136C	SER	1.99	2.84
FM4N	129A	SER	3.21	4.05
FM2C	94D	HIS	2.07	2.95
FM3C	133D	LYS	2.08	2.99
FM4C	139A	TYR	2.48	3.23
	140A	ARG	2.22	3.18
	140A	ARG	3.30	3.85
	140A	ARG	3.03	3.87

Table 5.3-6: π-stacking interactions between ligands

Sample code	Residue	Amino acid	Distance (Å)
FM3N	37B	TRP	5.06
FM3C	36A	HIS	3.53

Docking analysis shows that FMA binds to TYR35B, PHE98A, PRO99A and PRO446 residues via hydrophobic interactions and forms one hydrogen bond with SER129A residues.

Figure 5.3-5 shows the interaction of molecule FM2N with HHb the molecule showed one hydrogen bond interactions with amino acid residues HIS136C. and forms a series hydrophobic interaction to LEU32A, TYR42A, PHE43A, VAL93A, ASN97A, PHE98A, LEU101A and LEU135A residues.

FM3N was found to have strong binding to HHb with hydrophobic interactions to GLN133A and TYR139A residues and forms a hydrogen bond with SER136C residue and π-stacking interaction with TRP37B of a distance equal to 5.06Å .

FM4N also have strong binding affinity to HHb with hydrophobic interactions to TRP37B, PRO95C and TYP139C residues and one hydrogen bond to SER129A residue.

The binding conformation and binding site residues for FM2C are shown in **Figure 5.3-5** ligand is formed a hydrogen HIS94D bonds , whereas hydrophobic residues of the HHb are interacted (TYR35D, POR95C, TYR139C).

FM3C was found to bind strongly to HHb with hydrophobic interactions to ALA83A, HIS87D, ASP89D, PRO90D , LYS133D residues and one hydrogen bond LYS133D residue and π-stacking interaction with HIS36A of a distance equal to 3.53Å

Docking analysis shows that FM4C binds to TYR35D, TRP37D, PRO95A, LEU95D and TYR139A residues via hydrophobic interactions and forms four hydrogen bonds with TYR139A and ARG140A residues.

5.4 The study of the interaction of FcDA-HHb

5.4.1 Hemoglobin interaction studies using UV-Visible Spectroscopy

The UV-vis spectroscopy methods were utilized to investigate the interaction of FcDA-HHb with increasing concentrations of FcDA

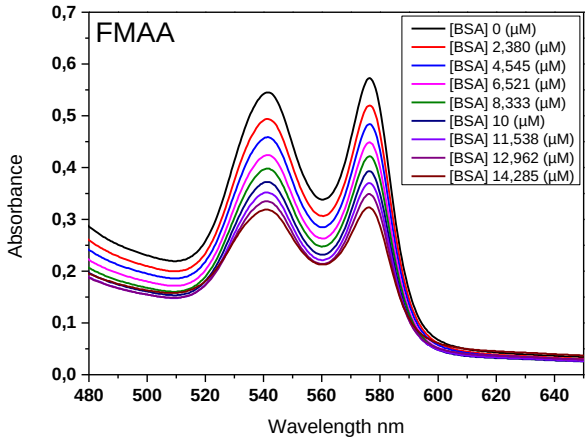

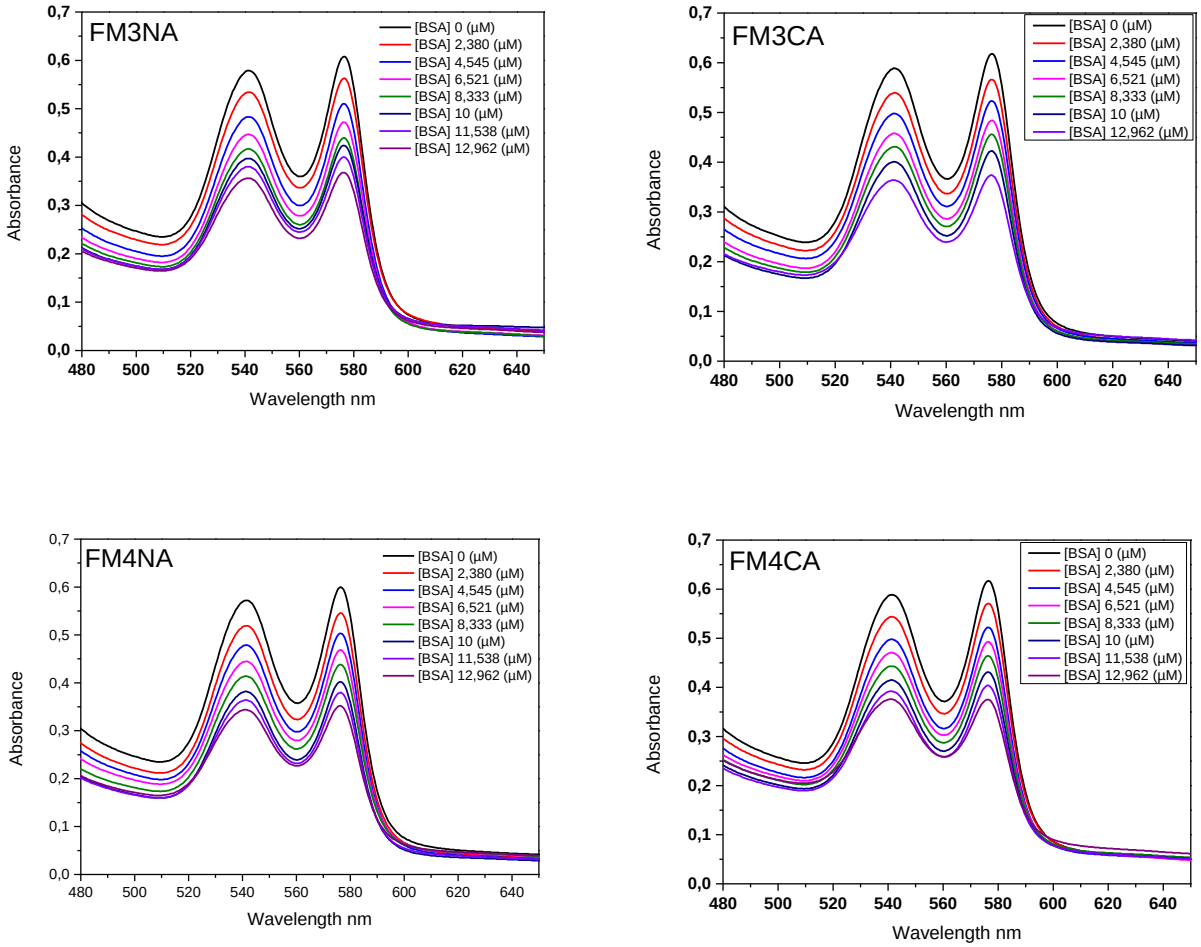

Figure 5.4-1: UV-visible absorption spectra of HHb were examined in the presence of varying concentrations of FcDA in a solution consisting of ethanol and PBS in a ratio of 90:10.

Binding constant and binding free energy

The intrinsic binding constant was determined by utilizing an equation (5.3 1) that employed the alteration in absorbance values induced by the incremental addition of FcDA concentrations.

The determination of the binding constant (K_b) involves the calculation of the ratio of the intercept to the slope of the graph depicting the relationship between $A_0/(A-A_0)$ and 1/[FcDB]. This graph is illustrated in **Figure 5.4-2**

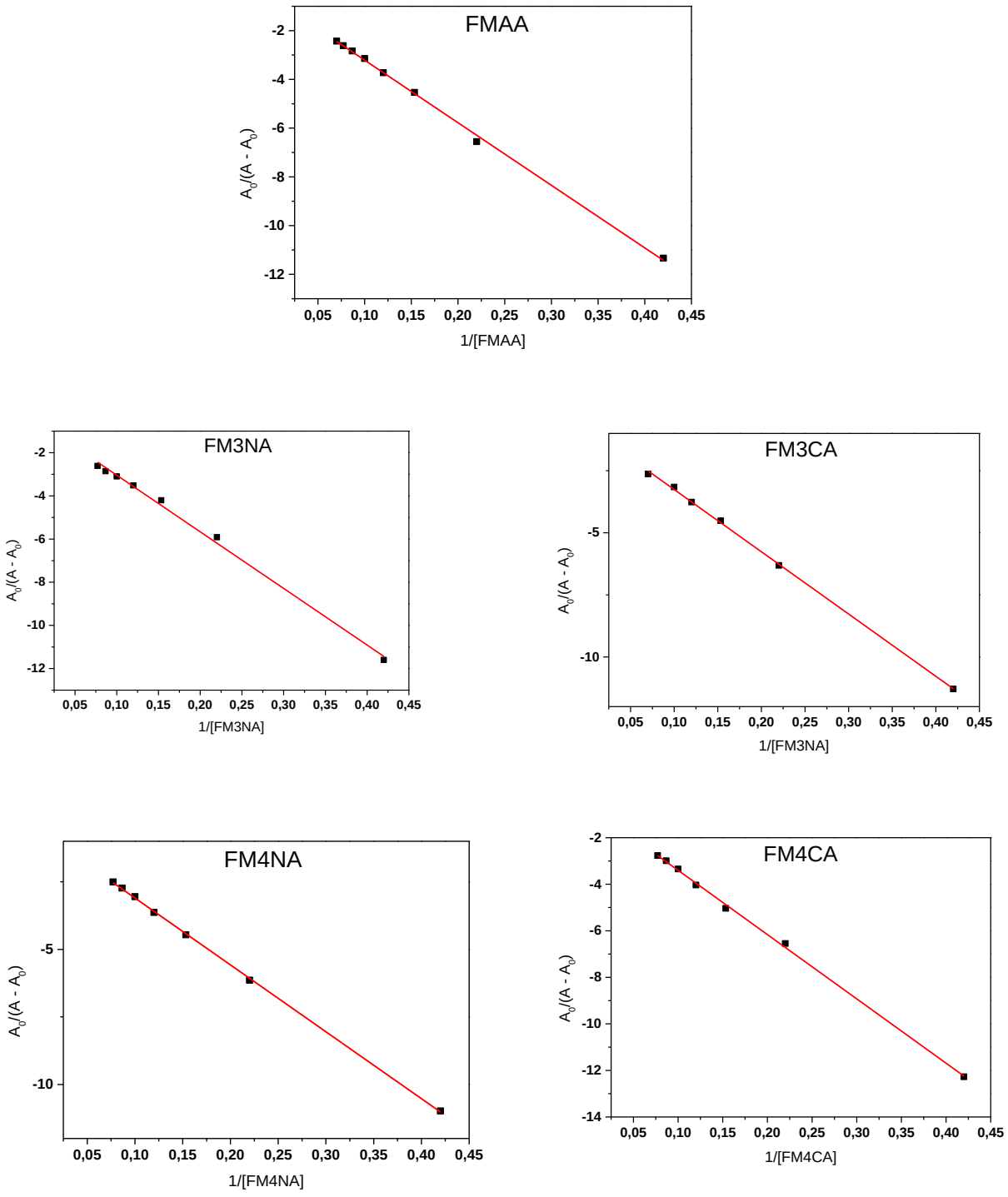

Figure 5.4-2: The binding constants between HHb and FcDB molecules were determined by plotting A0/(A-A0) against 1/[FcDB]. These plots were employed in the calculation of the binding constants.

The changes in binding free energy were estimated as described for HHb, the obtained results are summarized in **Table 5.4-1**.

Table 5.4-1: Binding constant and binding free energy estimates for FcDA ligands with HHb calculated from UV measurements at 298 K

Adduct	Equation	R^2	Kb (M^{-1})	ΔG ($KJ.mol^{-1}$)
HHb –**FMAA**	y = - 25,675x - 0,643	0.998	2.505×10^4	-25.11
HHb –**FM3NA**	y = - 26,234x - 0,418	0.995	1.593×10^4	-23.99
HHb– **FM4NA**	y = - 24,751x - 0,624	0.999	2.521×10^4	-25.13
HHb – **FM3CA**	y = - 25,069x - 0,751	0.999	2.995×10^4	-25.56
HHb – **FM4CA**	y = - 27,624x - 0,638	0.998	2.310×10^4	-24.91

5.4.2 Hemoglobin interaction studies using molecular docking

Molecular docking analysis of the produced ferrocene derivatives FcDA was carried out using human haemoglobin retrieved from the Protein Data Bank at http://www.pdb.org (PDB ID: 1gcw), **Figure 5.3-4**..

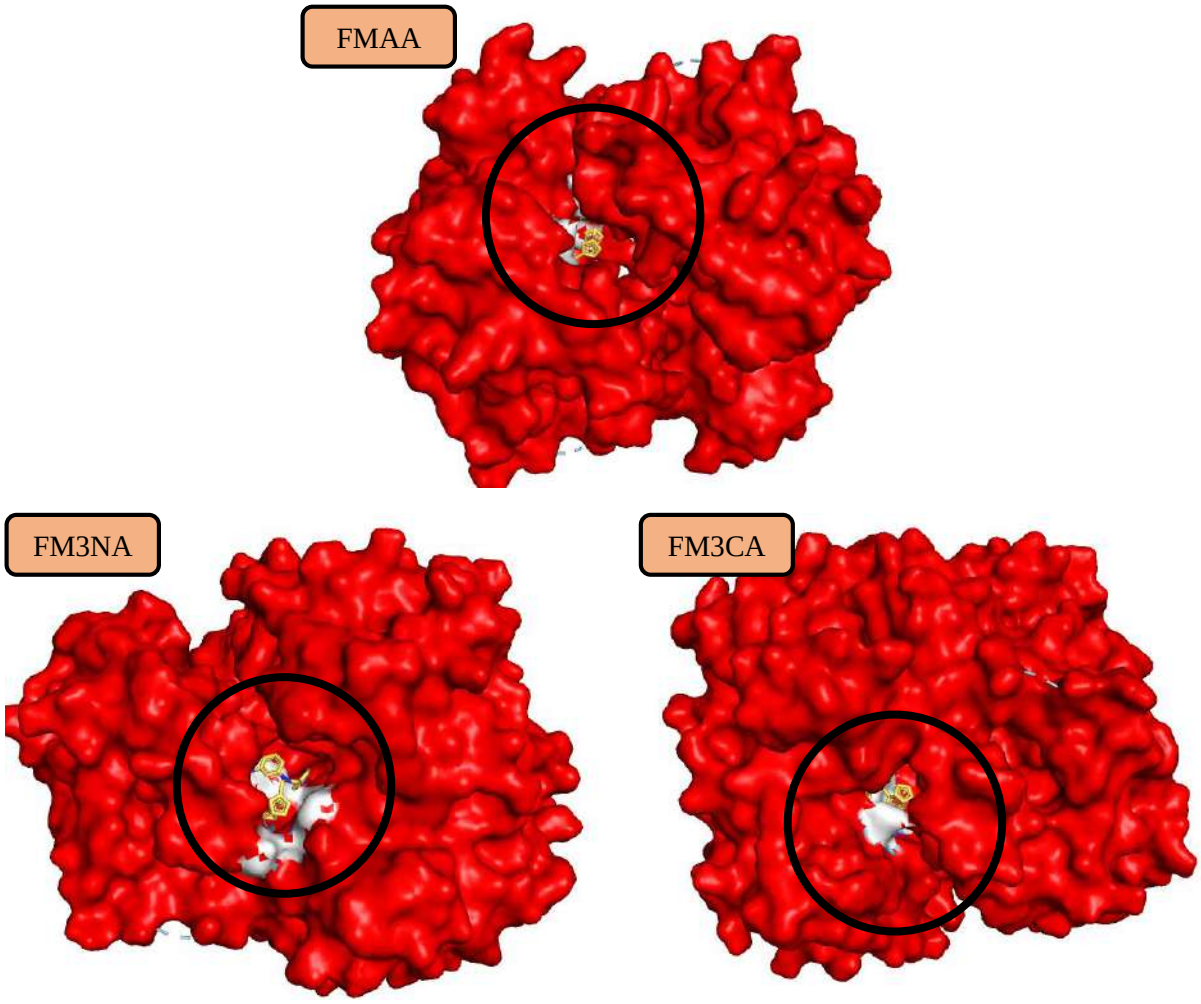

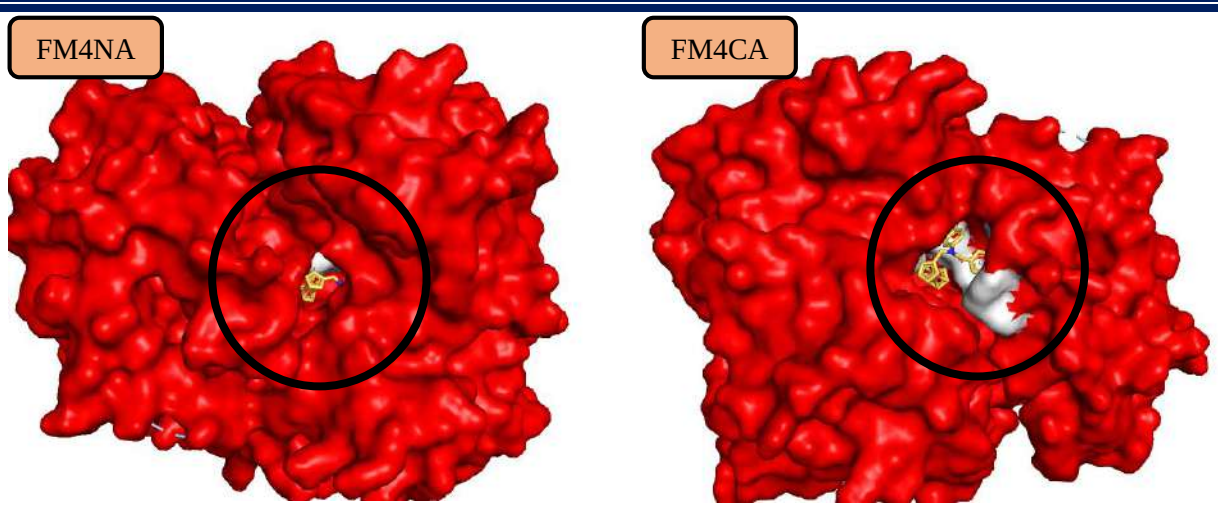

Figure 5.4-3: 3D Structures Representation of HHb (PDB code:1gcw)

All data related to HHb-FcDA interactions in the best active site is explained in the following table

Table 5.4-2: Binding constant and binding free energy values

Complex	K (M^{-1})	ΔG ($KJ.mol^{-1}$)	The number of runs	pocket
HHb –**FMAA**	2.50×10^{4}	-25.11	18	10
HHb –**FM3NA**	1.54×10^{4}	-23.90	6	2
HHb– **FM4NA**	2.29×10^{4}	-25.21	46	8
HHb – **FM3CA**	1.29×10^{4}	-23.48	37	9
HHb – **FM4CA**	2.22×10^{4}	-25.16	50	7

According to the molecular docking analysis, the binding process between FcDA and HHb is influenced by hydrogen bonding, hydrophobic forces, and π-cation interactions. The interaction between FcDB and the active site residues of HHb is depicted in **Figure 5.4-4**, which was generated using the PLIP web server. The visualizer PyMOL was used to modify and analyze the protein-ligand complexes that exhibited the best docking results.

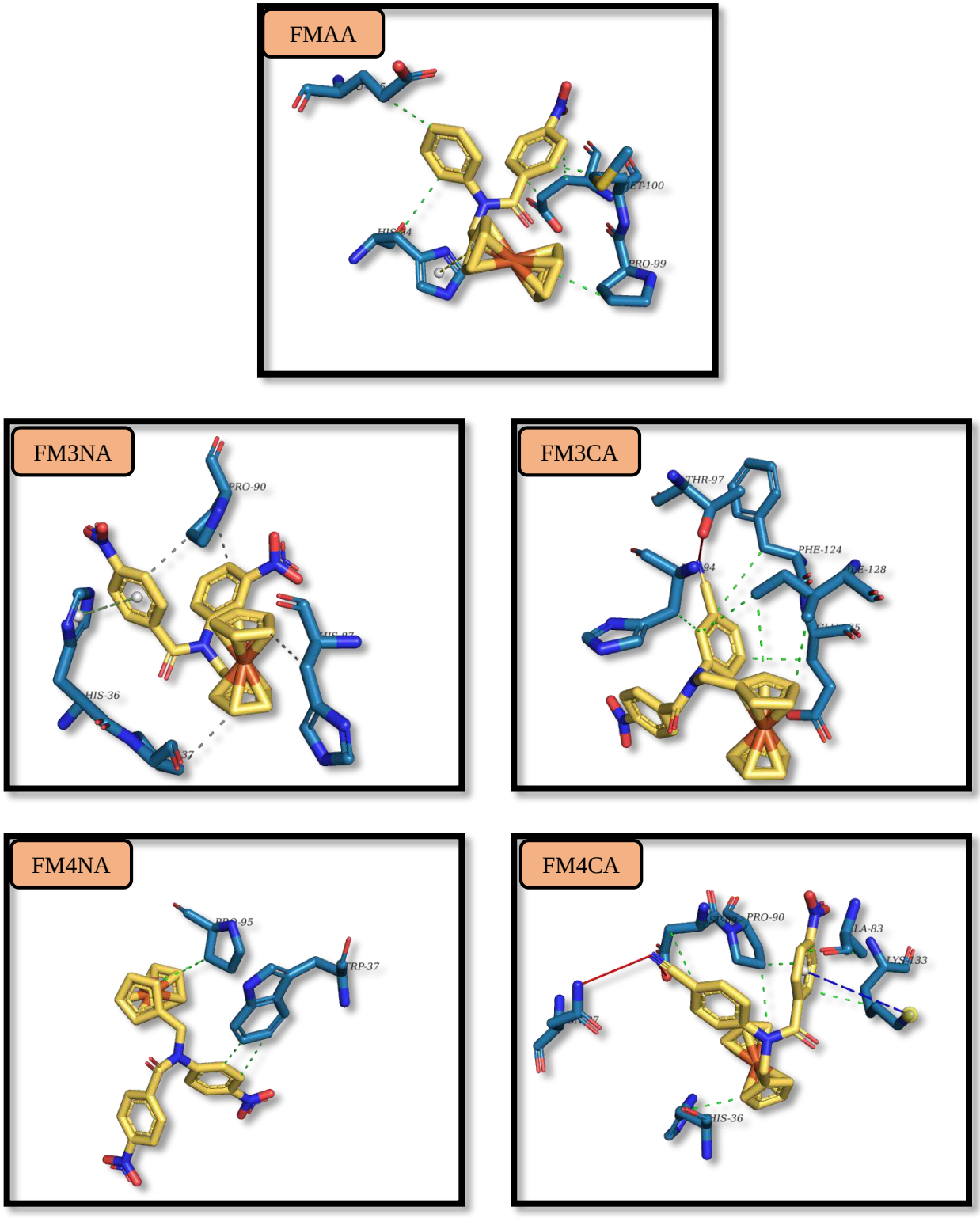

Figure 5.4-4: The PLIP web service generated the optimal docking poses for HHb-FcDB, highlighting the hydrophobic and hydrogen bond interactions. In the resulting image, the elements are color-coded: white represents hydrogen, red represents oxygen, blue represents nitrogen, and

brown represents iron. The interactions are identified by their respective colors: hydrogen bonds are represented in blue, hydrophobic forces in silver, π-stacking in green, and π-cation in orange.

The tables presented below summarize the type of interactions, distances, and the residues involved in the interactions

Table 5.4-3: hydrophobic interactions between ligands HHb

Sample code	Residue	Amino acid	Distance (Å)
FMAA	94D	HIS	3.72
	99C	PRO	3.37
	100C	MET	3.75
	103C	GLU	3.57
	103C	GLU	3.66
	125C	GLU	3.73
FM3NA	37A	PRO	3.30
	87D	HIS	3.83
	90D	PRO	3.39
	90D	PRO	2.97
FM4NA	37D	TRP	3.01
	37D	TRP	3.81
	95A	PRO	3.11
	95A	PRO	3.19
FM3CA	94B	HIS	3.95
	124B	PHE	3.99
	125B	GLU	3.24
	128B	ILE	3.53
	128B	ILE	3.57
	128B	ILE	3.71
FM4CA	36C	HIS	3.59

	83C	ALA	2.95
	89B	ASP	3.98
	90B	PRO	3.18
	90B	PRO	3.09
	133B	LYS	3.59

Table 5.4-4: Hydrogen bonding between the ligands FcDA and HHb

Sample code	Residue	Amino acid	H-A	D-A
ANC3	97B	THR	2.54	2.99
ANC4	89B	ASP	2.91	3.61
	97C	ASN	2.77	3.71

Table 5.4-5: π-stacking and π-cation interactions between ligands FcDA and HHb

Sample code	Residue	Amino acid	Distance (Å)
π-stacking			
FMAA	94D	HIS	5.22
FM3NA	36A	HIS	4.18
π-cation			
FM4CA	133B	LYS	5.45

FMAA was discovered to have strong binding to HHb, with hydrophobic contacts to HIS94D, PRO99C, MET100C, GLU103C and GLU125C residues, π-stacking interaction with HIS94D of 5.22Å respectively.

Figure illustrated the binding conformation and binding site residues of FM3NA. One hydrogen bond is formed with amino acid THR97B, whilst other HHb hydrophobic residues are distributed between FM3NA (PRO37A, HIS87D and PRO90D) and pi-stacking interaction with HIS36A .

The investigated ligand FM4NA forms only hydrophobic interactions bond with HHb to the TRP37D and PRO95A residues

Docking study shows that FM3CA attaches to HIS94B, PHE124B, GLU125B and ILE128B residues via hydrophobic interactions and one hydrogen bond to THR97B residue.

FM4CA binds strongly to HHb, having hydrophobic contacts at HIS36C, ALA83C, ASP89B, PRO90B and LYS133B residues and two hydrogen bonds to ASP89B and ASN97C residues. π- cation interaction with LYS133B.

Chapter 6

antioxidants study

The study of the interaction of FMAA- $O_2^{-\cdot}$

The superoxide anion radical $O_2^{-\cdot}$ scavenging activity of FcDA was measured using an assay. In this assay, $O_2^{-\cdot}$ was generated electrochemically by the one-electron reduction of molecular oxygen in DMF with 0.1 M TBFP as the supporting electrolyte. The assay involved the addition of increasing concentrations of the studied molecules to an electrochemical cell containing $O_2^{-\cdot}$ solution. Cyclic voltammograms were recorded after each addition of the test molecules with a scan rate of 0.1 V s^{-1}, from 0.0 to -1.4 V. **Figure 6.1-1** illustrates the voltammograms obtained in oxygen-saturated DMF containing 0.1 M of TBFB in the absence and presence of rising quantities of FcDA in the same solvent.[167,168].

6.1 Binding constants

Figure 6.1-1 demonstrates that adding different concentrations of FcDA in DMF to a solution of commercial oxygen-saturated DMF leads to a noteworthy reduction in peak current density. This decrease in peak current density is attributed to the formation of FcDA-$O_2^{-\cdot}$ product, which results in a decrease in the concentration of free $O_2^{-\cdot}$ radicals. [169].

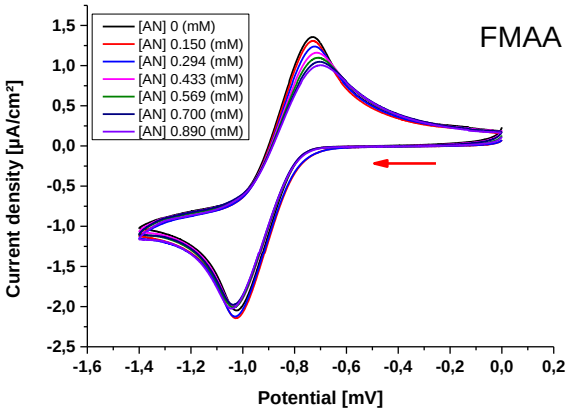

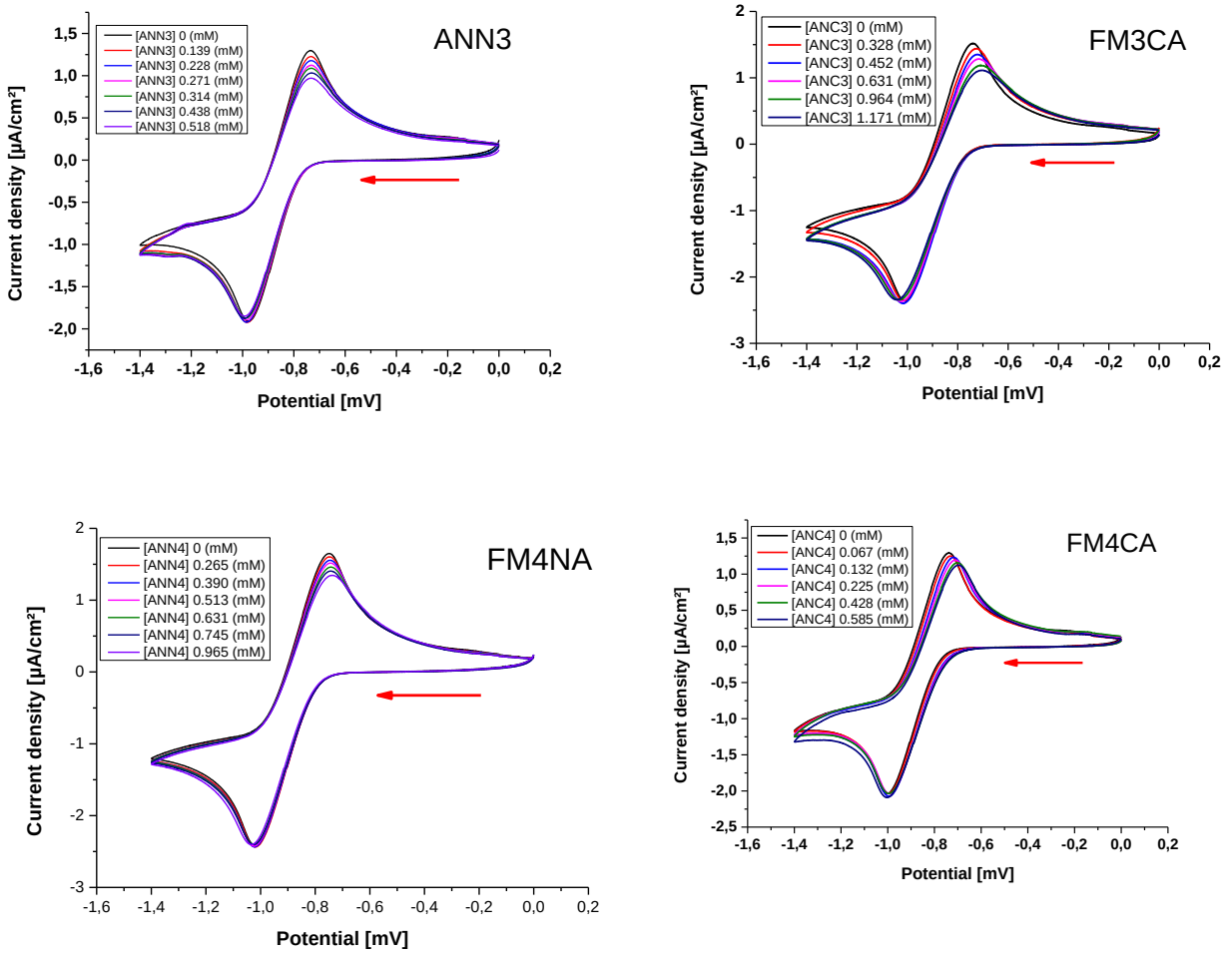

Figure 6.1-1: The cyclic voltammograms were recorded for oxygen-saturated DMF in the presence of increasing concentrations of FcDA and in its absence.

The binding constant can be calculated from equation (6.1-1) [170].

$$log\frac{1}{[FcDA]} = logk + log\frac{i}{i_0 - i} \qquad (6.1\text{-}1)$$

Where C is the concentration of FcDA, Kb is the binding constant, and i_0 indicate the anodic peak current density of the free $O_2^{-\cdot}$ and i indicate $O_2^{-\cdot}$- FcDA bound ligands respectively

The linear form of the f(1/[$FcDA$]) = logi/(i_0-i)extracted from the above voltammogram

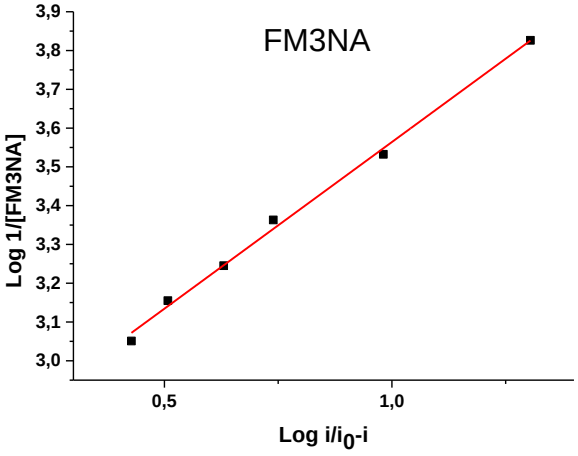
FM3NA
Log 1/[FM3NA]
Log i/i0-i
3,9
3,8
3,7
3,6
3,5
3,4
3,3
3,2
3,1
3,0
0,5
1,0

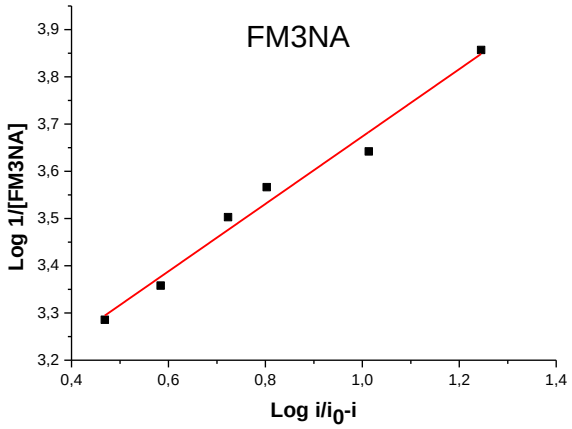
FM3NA
Log 1/[FM3NA]
Log i/i0-i
3,9
3,8
3,7
3,6
3,5
3,4
3,3
3,2
0,4
0,6
0,8
1,0
1,2
1,4

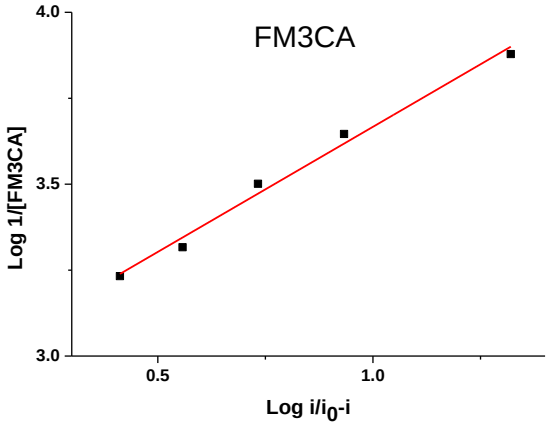
FM3CA
Log 1/[FM3CA]
Log i/i0-i
4.0
3.5
3.0
0.5
1.0

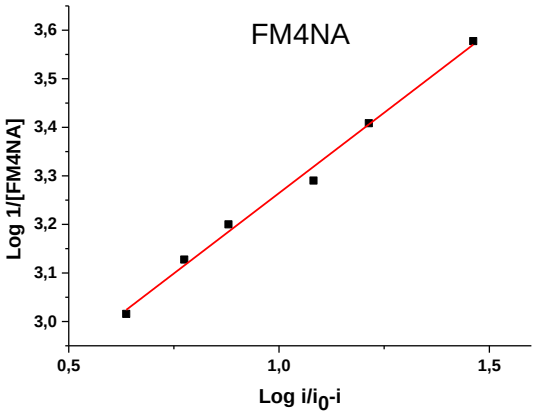
FM4NA
Log 1/[FM4NA]
Log i/i0-i
3,6
3,5
3,4
3,3
3,2
3,1
3,0
0,5
1,0
1,5

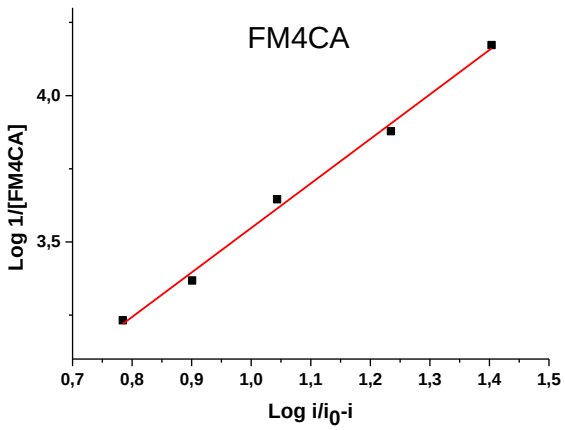
FM4CA
Log 1/[FM4CA]
Log i/i0-i
4,0
3,5
0,7
0,8
0,9
1,0
1,1
1,2
1,3
1,4
1,5

Figure 6.1-2: The binding constant of the $O_2^{-\cdot}$- FcBA product was calculated by plotting log (1/[FcBA]) against log i/(i0-i) for $O_2^{-\cdot}$ with varying concentrations of FcBA. Similarly, the binding constants of $O_2^{-\cdot}$- FcDA products were determined using DMF/0.1M TBFB.

The Gibbs free energy equation **(6.1-2)** was used to calculate ΔG, obtained values are given in

$$\Delta G = -RT\ln K_b \qquad (6.1\text{-}2)$$

Where ΔG represents the free binding energy in $KJmol^{-1}$, R represents the gas constant, 8.32 $Jmol^{-1}K^{-1}$ while, T represents the absolute temperature, 298K.

Table 6.1-1: Binding constant and binding free energy values

Adduct	Equation	R^2	Kb (M^{-1})	ΔG ($KJ.mol^{-1}$)
FMAA – $O_2^{-\cdot}$	y = 0.859x + 2.704	0,995	5.06×10^2	-15.44
FM3NA - $O_2^{-\cdot}$	y = 0.713x + 2.960	0.990	9.12×10^2	-16.89
FM4NA - $O_2^{-\cdot}$	y = 0.662x + 2.602	0.996	4×10^2	-14.85
FM3CA - $O_2^{-\cdot}$	y = 0.728x + 2.939	0.995	8.68×10^2	-16.79
FM4CA - $O_2^{-\cdot}$	y = 1.520x + 2.027	0.997	1.06×10^2	-11.57

The magnitude of ΔG reflects the weak binding character between $O_2^{-\cdot}$ and FcDA , whereas the negative sign suggests the spontaneity of the $O_2^{-\cdot}$-FcDA interactions.

6.2 Diffusion Coefficients

The diffusion coefficients were determined from the voltammograms shown in **Figure 6.2-1**. These voltammograms were generated by altering the potential scan rates of the free radical $O_2^{-\cdot}$ and its bound forms FcDA-$O_2^{-\cdot}$. All of the voltammograms exhibited stable redox peaks that could be attributed to the $O_2^{-\cdot}/O_2$ couple redox process.

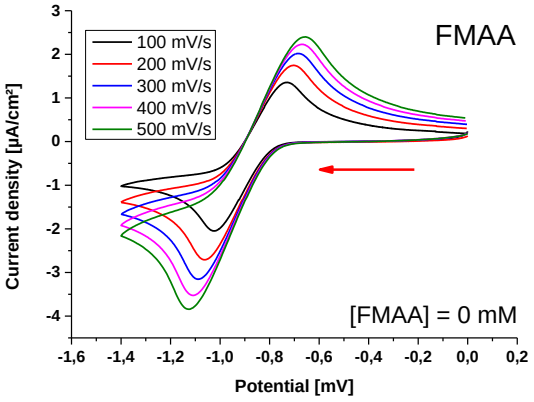
FMAA
100 mV/s
200 mV/s
300 mV/s
400 mV/s
500 mV/s
[FMAA] = 0 mM
Current density [µA/cm²]
Potential [mV]

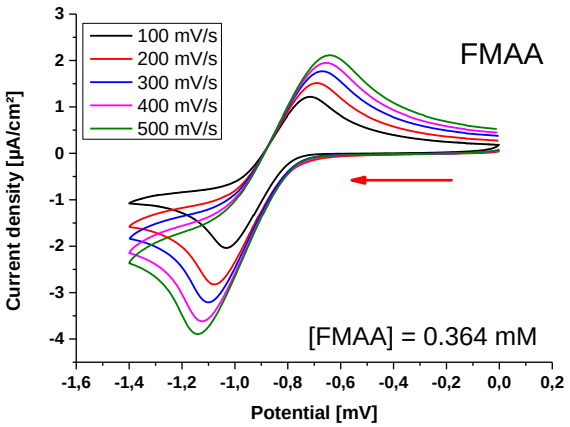
FMAA
100 mV/s
200 mV/s
300 mV/s
400 mV/s
500 mV/s
[FMAA] = 0.364 mM
Current density [µA/cm²]
Potential [mV]

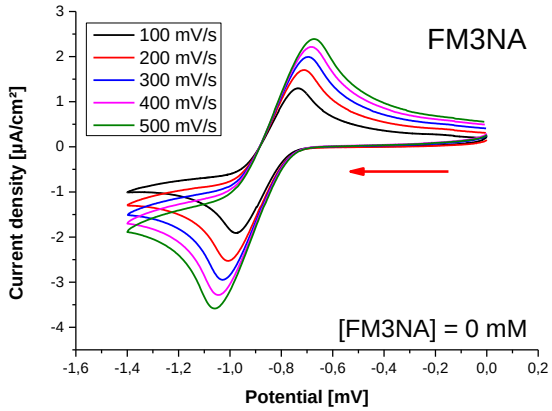
FM3NA
100 mV/s
200 mV/s
300 mV/s
400 mV/s
500 mV/s
[FM3NA] = 0 mM
Current density [µA/cm²]
Potential [mV]

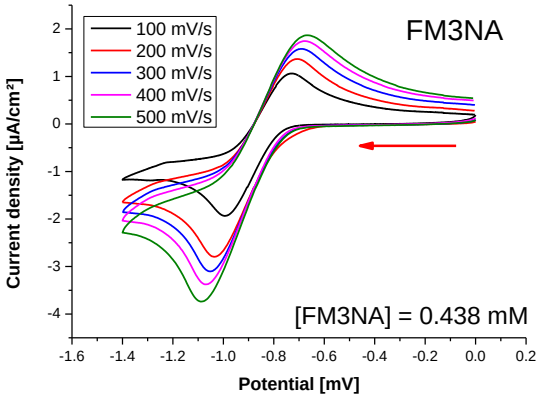
FM3NA
100 mV/s
200 mV/s
300 mV/s
400 mV/s
500 mV/s
[FM3NA] = 0.438 mM
Current density [µA/cm²]
Potential [mV]

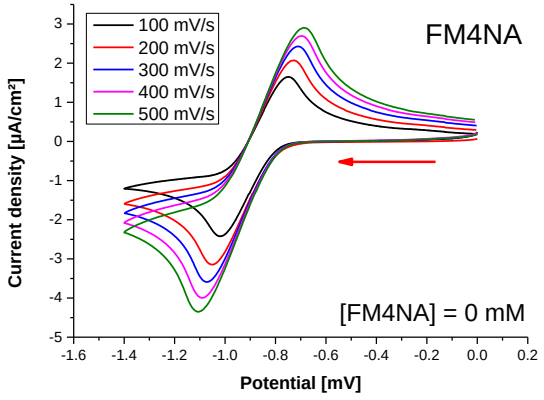
FM4NA
100 mV/s
200 mV/s
300 mV/s
400 mV/s
500 mV/s
[FM4NA] = 0 mM
Current density [µA/cm²]
Potential [mV]

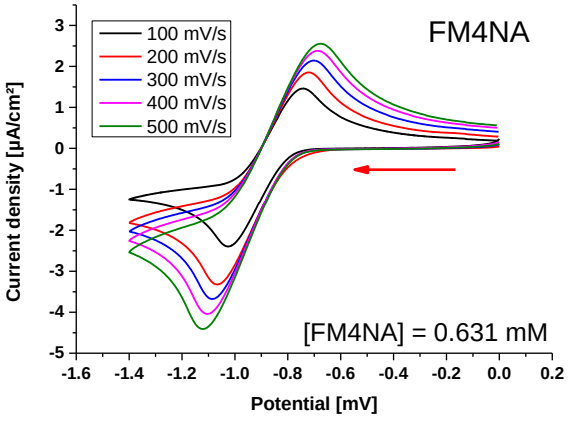
FM4NA
100 mV/s
200 mV/s
300 mV/s
400 mV/s
500 mV/s
[FM4NA] = 0.631 mM
Current density [µA/cm²]
Potential [mV]

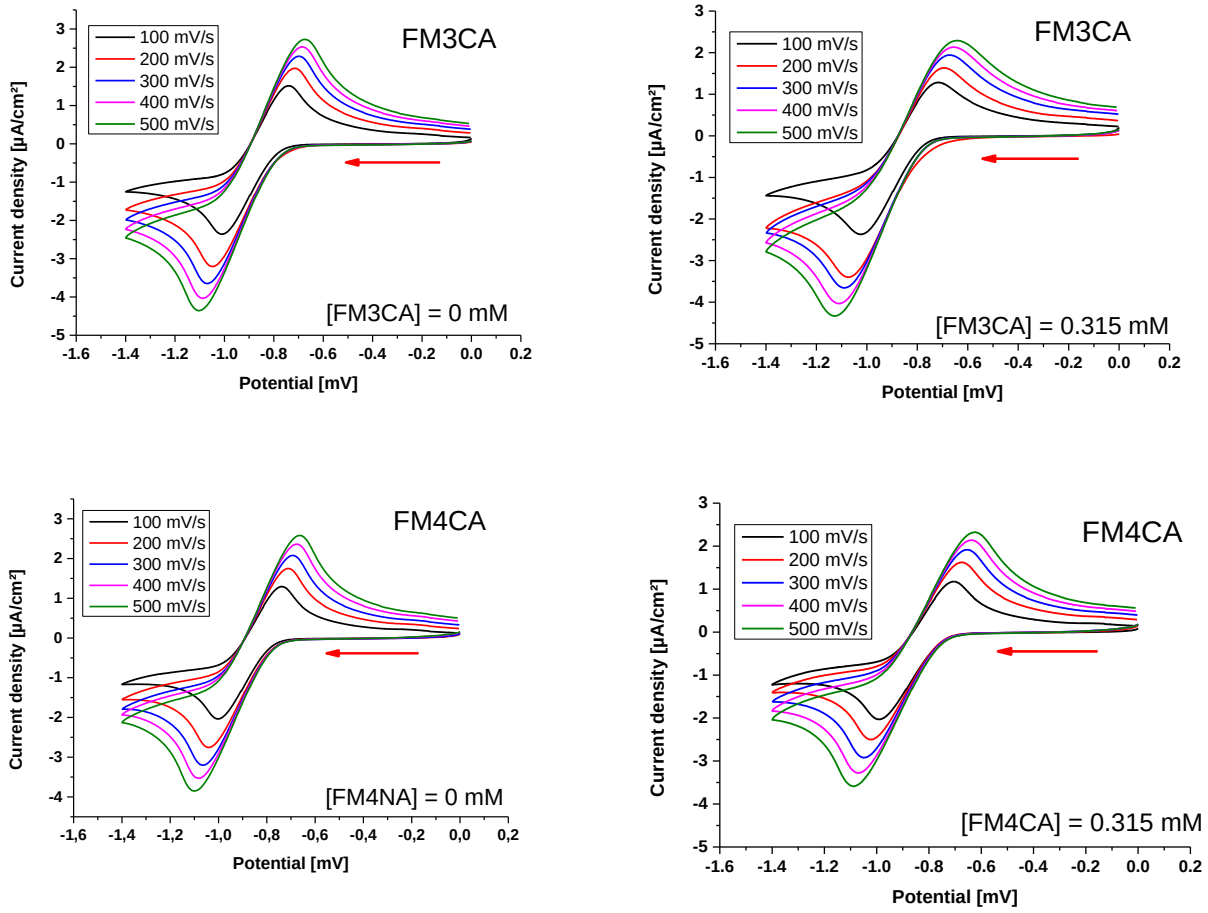

Figure 6.2-1: The cyclic voltammograms were recorded at scan rates of 0.1, 0.2, 0.3, 0.4, and 0.5 V/s for $O_2^{-\cdot}$ in DMF in the presence of rising concentrations of FcDA, as well as in its absence.

The Randles–Sevcik equation 6.2-1) was used to determinate the coefficient of diffusion of the free form of the FcDA and its bound form FcDA-$O_2^{-\cdot}$ [170–172].

$$i = 2.69 \times 10^5 n^{3/2} A C D^{1/2} v^{1/2} \qquad 6.2\text{-}1)$$

where i is the peak current (A), A is the surface area of the electrode (cm^2), C is the bulk concentration ($mol.cm^{-3}$) of the electroactive species, D is the diffusion coefficient ($cm^2.s^{-1}$) and v is the scan rate ($V.s^{-1}$)

Figure 6.2-2 shows that the square root of the potential scan rates is linearly correlated with the peak current density of both $O_2^{-\cdot}$ and its bound form FcDA-$O_2^{-\cdot}$, indicating that the redox process is governed by the diffusion step.

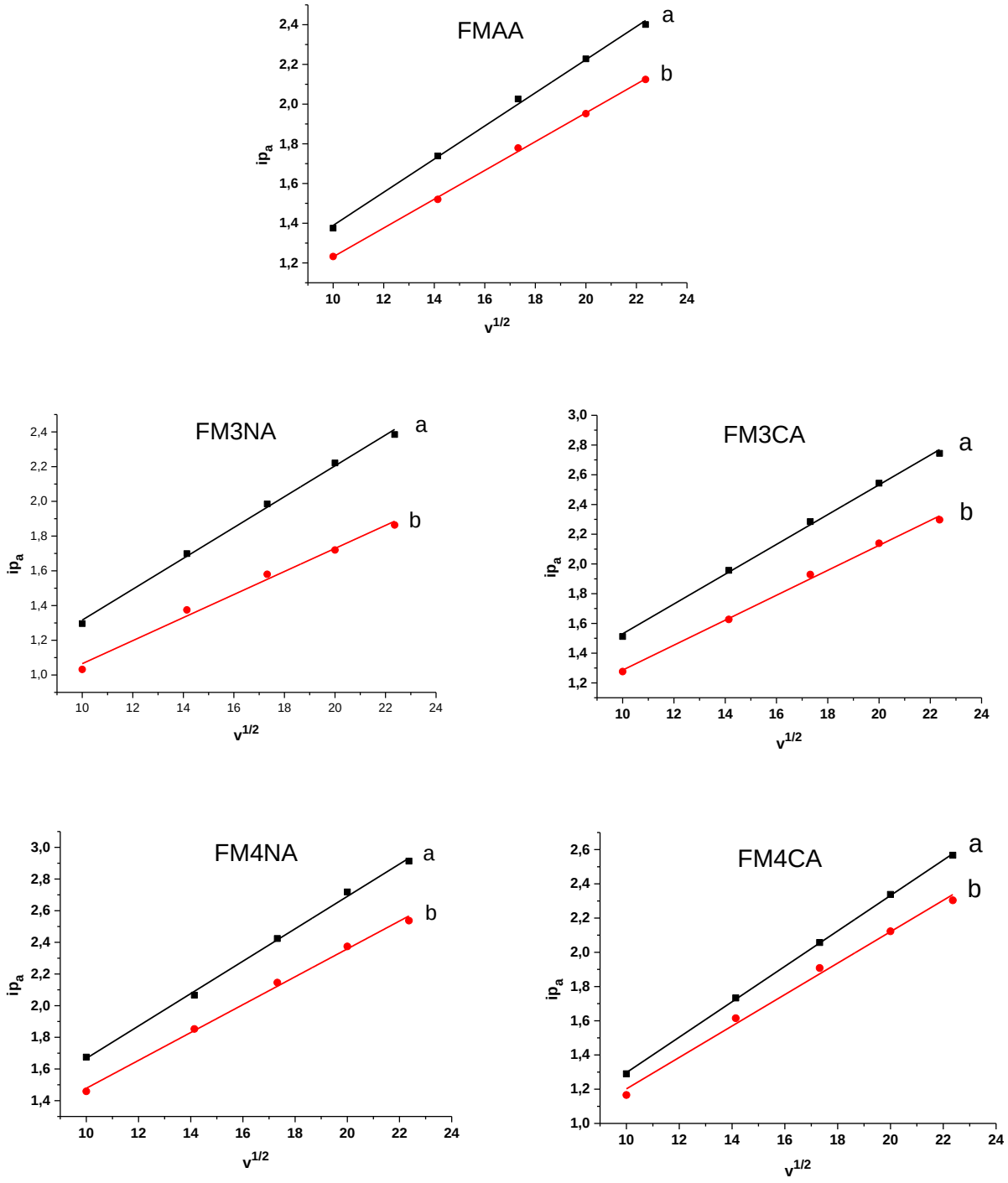

Figure 6.2-2: The plots of ia=f($v^{1/2}$) for $O_2^{-\cdot}$ in the absence (represented by black lines) and presence of FcDA (represented by red lines) were generated at different scan rates of 0.1, 0.2, 0.3, 0.4, and 0.5 $V \cdot s^{-1}$.

The Randles-Sevcik plots were used to determine the diffusion coefficients of both free and FcDA-bound $O_2^{-\cdot}$. The calculated values are presented in the results. **Table 6.2-1**.

Table 6.2-1: Values of the diffusion coefficients of the free and $O_2^{-\cdot}$ bound FcDA.

Entry	Equation	R^2	$D(cm^2.s^{-1})$
$O_2^{-\cdot}$	y= 0.0834 x + 0.554	0.999	6.87×10^{-6}
FMAA – $O_2^{-\cdot}$	y = 0.072 x + 0.505	0.998	5.19×10^{-6}
$O_2^{-\cdot}$	y = 0.088 x + 0.428	0.998	4.61×10^{-4}
FM3NA – $O_2^{-\cdot}$	y = 0.066 x + 0.401	0.995	1.11×10^{-5}
$O_2^{-\cdot}$	y = 0.102 x + 0.643	0.999	1.27×10^{-5}
FM4NA – $O_2^{-\cdot}$	y = 0.088 x + 0.597	0.998	9.42×10^{-6}
$O_2^{-\cdot}$	y = 0.447 x + 0.083	0.998	3.771×10^{-5}
FM3CA – $O_2^{-\cdot}$	y = 0.100 x + 0.529	0.999	5.092×10^{-5}
$O_2^{-\cdot}$	y = 0.103 x + 0.262	0.999	5.20×10^{-5}
FM4CA – $O_2^{-\cdot}$	y = 0.092 x + 0.284	0.918	4.01×10^{-5}

The diffusion coefficients of restricted FcDA-$O_2^{-\cdot}$ are minimal when compared to free $O_2^{-\cdot}$, indicating the formation of FcDA-$O_2^{-\cdot}$ products. The increased molecular weight of the produced product accounts for the decrease in the apparent diffusion coefficient of $O_2^{-\cdot}$ in the presence of FcDA.

6.3 Ratio of binding constants

In the presence of $O_2^{-\cdot}$, a decrease in the shift anodic current peak (ipa) of FcDA is accompanied by a shift in the anodic potential peak (Epa) to higher negative potential values (**Figure 6.3-1**) This electrochemical behaviour was used to calculate the constant binding ratio [173].

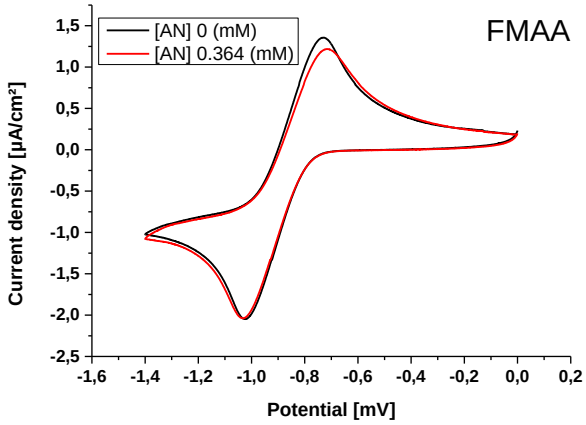
FMAA
[AN] 0 (mM)
[AN] 0.364 (mM)
Current density [µA/cm²]
Potential [mV]

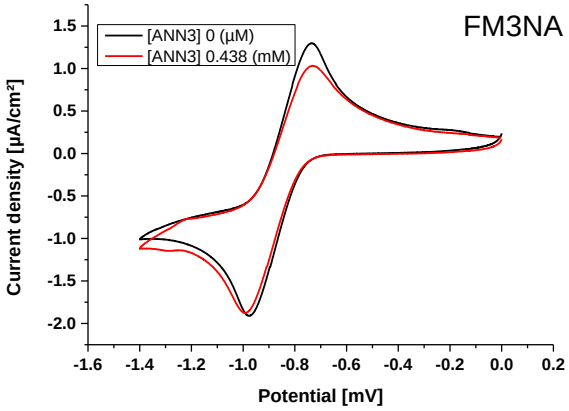
FM3NA
[ANN3] 0 (µM)
[ANN3] 0.438 (mM)
Current density [µA/cm²]
Potential [mV]

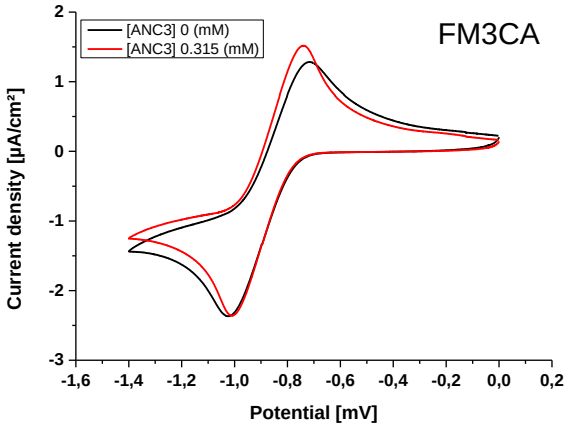
FM3CA
[ANC3] 0 (mM)
[ANC3] 0.315 (mM)
Current density [µA/cm²]
Potential [mV]

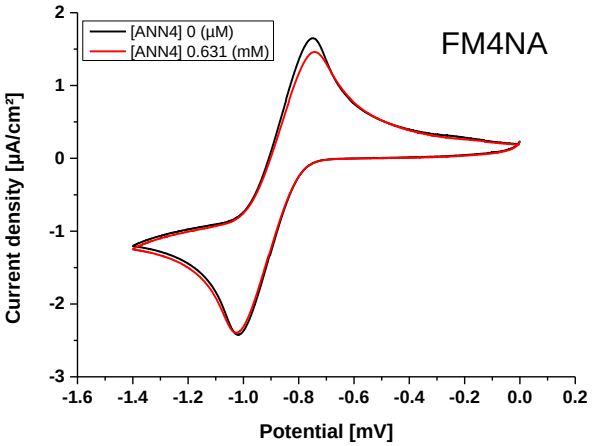
FM4NA
[ANN4] 0 (µM)
[ANN4] 0.631 (mM)
Current density [µA/cm²]
Potential [mV]

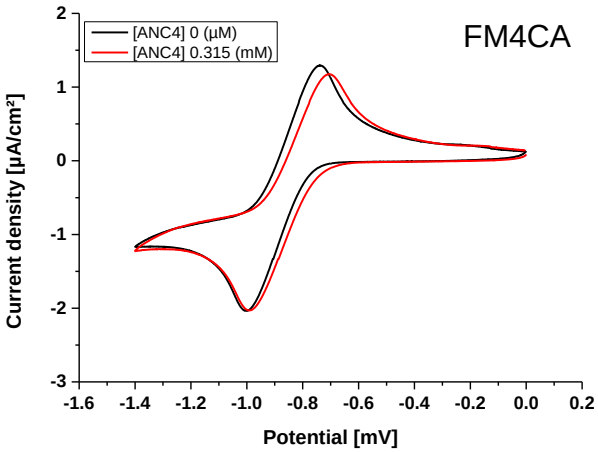
FM4CA
[ANC4] 0 (µM)
[ANC4] 0.315 (mM)
Current density [µA/cm²]
Potential [mV]

Figure 6.3-1: Cyclic voltammograms were recorded for $O_2^{-\cdot}$ in a DMF solution with a scan rate of 100 mV.s^{-1} on a glass carbon electrode using 0.1 M TBFP as a supporting electrolyte. The voltammograms were obtained in the absence (black line) and presence (red line) of FcDA.

When FcDA is introduced to an oxygen-saturated DMF solution, there is a shift in the peak potential values, indicating changes in equilibrium. This shift can be described using the following equilibriums [152]:

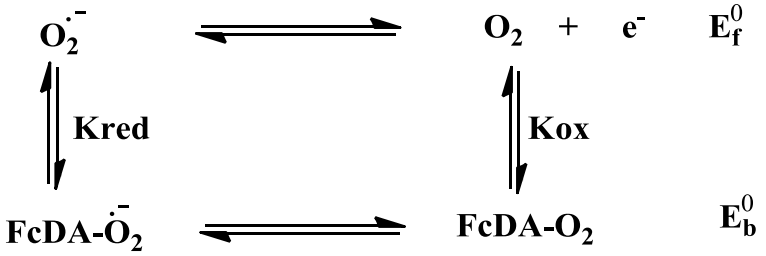

Figure 6.3-2: Redox process of the studied compounds with $O_2^{-\cdot}$ and FMA

The Nernst relation 6.3-1) was applied to the equilibriums represented in **Figure 6.3-2**, this gives the following equations:

$$\Delta E^0 = E_f^0 - E_b^0 = E^0(O_2^{-\cdot}) - E^0(O_2^{-\cdot} - FcDA) = 0.061\frac{k_{ox}}{k_{red}} \qquad 6.3\text{-}1)$$

The formal potentials of the $O_2^{-\cdot}$ / O_2 couple in the free and bound forms, respectively, are E_f^0 and E_b^0. The peak potential shift E_0 and the decreasing rate of the anodic peak current density ipa percent are represented in **Table 6.3-1**. The ratio of the binding constants is obtained by replacing ΔE_0 from **Table 6.3-1** in equation **Error! Reference source not found.**

Table 6.3-1: Electrochemical data of the free and $O_2^{-\cdot}$ bound forms of FcDA used to calculate the ratio of the binding constants

Entry	Epa	Epc	E°(V)	ΔE°(mV)	Kred/Kox
$\mathbf{O_2^{-\cdot}}$	-0.736	-1.016	-0.876	-0.5	1.019
FMAA – $\mathbf{O_2^{-\cdot}}$	-0.720	-1.033	-0.877		
$\mathbf{O_2^{-\cdot}}$	-0.735	-0.975	-0.863	8.5	1.393
FM3NA – $\mathbf{O_2^{-\cdot}}$	-0.731	-0.996	-0.863		
$\mathbf{O_2^{-\cdot}}$	-0.750	-1.021	-0.885	-5.5	1.239

FM4NA – $O_2^{-\cdot}$	-0.754	-1.028	-0.891		
$O_2^{-\cdot}$	-0.737	-1.006	-0.872	-1	1.039
FM3CA – $O_2^{-\cdot}$	-0.720	-1.025	-0.873		
$O_2^{-\cdot}$	-0.739	-1.005	-0.815	24	0.399
FM4CA – $O_2^{-\cdot}$	-0.706	-0.990	-0.848		

The obtained values of the binding constant ratios show that the reduced form $O_2^{-\cdot}$ of the couple $O_2^{-\cdot}$ / O_2 interacts with FcDA stronger than the oxidized form O_2 . however, the only exception FM4NA demonstrated that the reduced form of oxygen is bound stronger.

6.4 half-maximal inhibitory concentration (IC_{50})

The following equation (6.4-1) was used to determine $O_2^{-\cdot}$ inhibition [17,37,38].

$$\%\, O_2^{-\cdot} radical\ scavenging\ activity = \frac{i_{pa_0} - i_{pa}}{i_{pa_0}} x100 \qquad 6.4\text{-}1)$$

Where $i_{pa_0} and\ i_{pa}$ are the anodic current peaks of active oxygen in the absence and presence of increasing concentrations of studied ligands, respectively.

The plot of $O_2^{-\cdot}$ scavenging activity against different compound concentrations gives accesses to the half-maximal inhibitory concentration (IC_{50}) values (inset plots of **Figure 6.4-1**). The antioxidant activity was reported as IC_{50} value. The IC50 value represents the concentration of the substance that inhibits the production of $O_2^{-\cdot}$ by 50%.

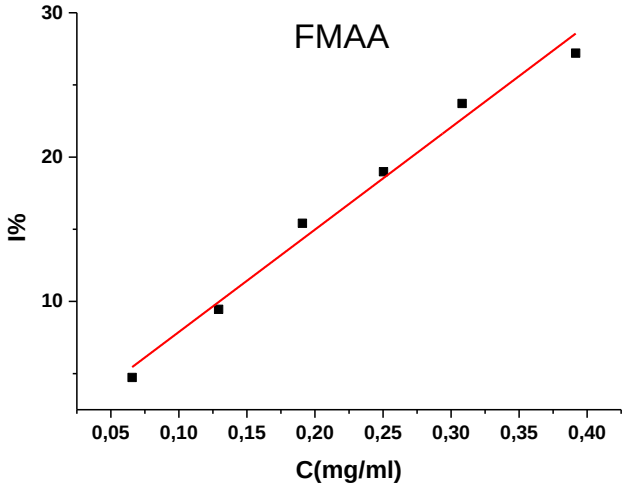
FMAA
I%
C(mg/ml)
30
20
10
0,05
0,10
0,15
0,20
0,25
0,30
0,35
0,40

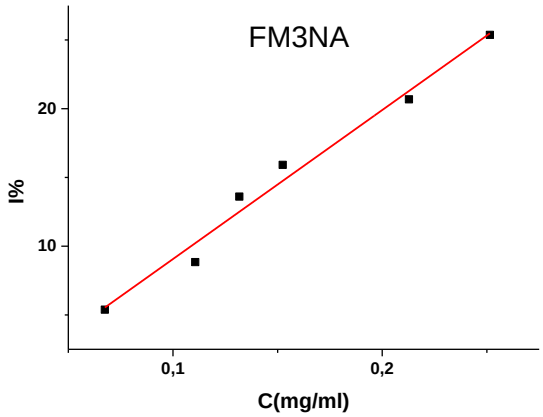
FM3NA
I%
C(mg/ml)
20
10
0,1
0,2

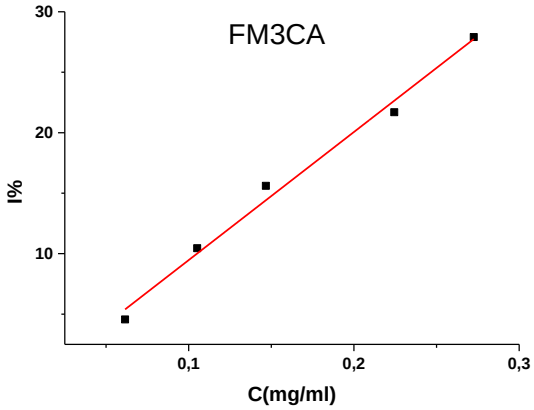
FM3CA
I%
C(mg/ml)
30
20
10
0,1
0,2
0,3

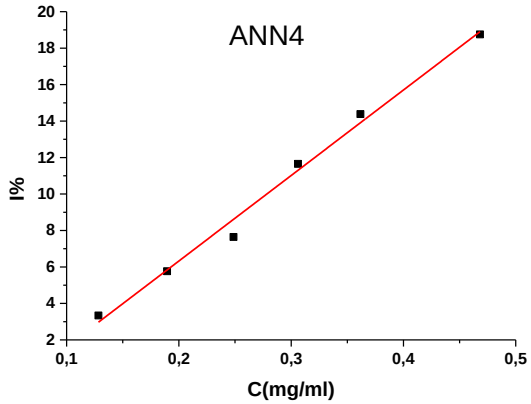
ANN4
I%
C(mg/ml)
20
18
16
14
12
10
8
6
4
2
0,1
0,2
0,3
0,4
0,5

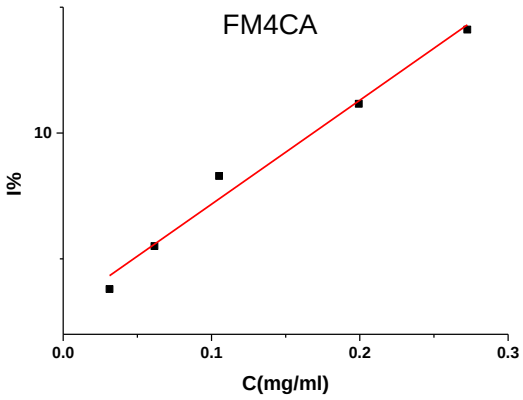
FM4CA
I%
C(mg/ml)
10
0.0
0.1
0.2
0.3

Figure 6.4-1: Typical plots of I% as a function of C (mg/ml) used for calculation the **IC_{50}** values of ligands FcDA with $O_2^{-\cdot}$

Table 6.4-1: IC50 values of the studied compounds

Adduct	Equation	R^2	IC_{50} (mM)
FMAA – $O_2^{-\cdot}$	y = 70.890 x + 0.799	0,992	1.63
FM3NA - $O_2^{-\cdot}$	y = 108.38 x – 1.773	0.991	0.98
FM4NA - $O_2^{-\cdot}$	y = 48.89 x – 3.049	0.999	2.33
FM3CA - $O_2^{-\cdot}$	y = 105.90 x – 1.119	0.995	1.04
FM4CA - $O_2^{-\cdot}$	y = 41.328 x + 3.037	0.991	2.76
α-Tocopherol*	y = 15.99x + 1.37	0.950	3.04

The scavenging activity of all FcDA compounds against $O_2^{-\cdot}$ radicals was found to be promising based on the IC50 values. Comparison of the results with the standard α-tocopherol indicates that all of the complexes exhibit significant scavenging activity [167] .

Conclusion

The main objective of the research work presented in this thesis was to study the binding mode of a series of ferrocene derives with BSA and HHb using experimental and theoretical techniques such as voltametric, spectroscopic assays and molecular docking simulations. We have successfully synthesised seven N-ferrocenylmethylanline and their acylated forms , the obtained derivatives were characterized by spectroscopy (UV-Vis, NMR (^{1}H), and IR) and electrochemical (CV) techniques. Then the interaction of the synthesized derivatives with BSA and HHb was also investigated, finally, the antioxidant activity of all derivatives was evaluated.

The negative values of the obtained free binding energy of the adduct BSA-Fc indicate that the interaction is a spontaneous process.

In addition, the binding properties of ferrocene derivatives towards human hemoglobin was also studied using electronic spectroscopy techniques and molecular modelling simulations. The hydrogen bonding and hydrophobic interactions in the adducts HHb-Fc play a crucial role in complex stabilization (HHb-Fc). Molecular docking calculations indicated that Van der Waal and electrostatic forces occur in this type of interaction, however, hydrophobic forces play a significant role in the binding of ferrocene derivatives to BSA and HHb.

Cyclic voltammetry experiments were used to evaluate the antioxidant activity and the interaction of the superoxide anion radical with the synthesised ferrocene derivatives. The electrostatic interaction mode and spontaneity of the interaction between the free superoxide anion radical and all investigated compounds were indicated by the negative sign and order of magnitude of the obtained binding free energy. Other binding parameters such as binding constant and ratio of binding constant were also determined from cyclic voltametric data.

References

[1] U. Kragh-Hansen, Molecular aspects of ligand binding to serum albumin., Pharmacol. Rev. 33 (1981) 17–53.

[2] W.J. Jusko, M. Gretch, Plasma and Tissue Protein Binding of Drugs in Pharmacokinetics, Drug Metab. Rev. 5 (1976) 43–140. https://doi.org/10.3109/03602537608995839.

[3] X. Qu, T. Komatsu, T. Sato, O. Glatter, H. Horinouchi, K. Kobayashi, E. Tsuchida, Structure, Photophysical Property, and Cytotoxicity of Human Serum Albumin Complexed with Tris(dicarboxymethylene)[60]fullerene, Bioconjug. Chem. 19 (2008) 1556–1560. https://doi.org/10.1021/bc800207j.

[4] M.-G. Wen, X.-B. Zhang, J.-N. Tian, S.-H. Ni, H.-D. Bian, Y.-L. Huang, H. Liang, Binding interaction of xanthoxylin with bovine serum albumin, J. Solution Chem. 38 (2009) 391–401.

[5] X.M. He, D.C. Carter, Atomic structure and chemistry of human serum albumin, Nature. 358 (1992) 209–215.

[6] T. Topală, A. Bodoki, L. Oprean, R. Oprean, Bovine Serum Albumin Interactions with Metal Complexes, Clujul Med. 87 (2014) 215–219. https://doi.org/10.15386/cjmed-357.

[7] Y. Rahman, S. Afrin, M. Tabish, Interaction of pirenzepine with bovine serum albumin and effect of β-cyclodextrin on binding: A biophysical and molecular docking approach, Arch. Biochem. Biophys. 652 (2018) 27–37. https://doi.org/10.1016/j.abb.2018.06.005.

[8] C. Ràfols, S. Amézqueta, E. Fuguet, E. Bosch, Molecular interactions between warfarin and human (HSA) or bovine (BSA) serum albumin evaluated by isothermal titration calorimetry (ITC), fluorescence spectrometry (FS) and frontal analysis capillary electrophoresis (FA/CE), J. Pharm. Biomed. Anal. 150 (2018) 452–459. https://doi.org/10.1016/j.jpba.2017.12.008.

[9] Å. Frostell-Karlsson, A. Remaeus, H. Roos, K. Andersson, P. Borg, M. Hämäläinen, R. Karlsson, Biosensor Analysis of the Interaction between Immobilized Human Serum Albumin and Drug Compounds for Prediction of Human Serum Albumin Binding Levels, J. Med. Chem. 43 (2000) 1986–1992. https://doi.org/10.1021/jm991174y.

[10] H. Monirinasab, M. Zakariazadeh, H. Kohestani, M. Kouhestani, F. Fathi, Study of β-lactam-based drug interaction with albumin protein using optical, sensing, and docking methods, J. Biol. Phys. 48 (2022) 177–194.

[11] N.J. Mukta, S. Mahbub, M.J. Abedin, M.E. Hossain, D. Kumar, M.A. Hoque, M.A. Khan, M.T. Rehman, N. Azum, M. Akram, H.M. Marwani, Effect of Temperature and Additives on the Interaction of Ciprofloxacin Hydrochloride Drug with Polyvinylpyrrolidone and Bovine Serum Albumin: Spectroscopic and Molecular Docking Study, J. Oleo Sci. 70 (2021) 397–407. https://doi.org/10.5650/jos.ess20306.

[12] T. Lanez, H. Hemmami, Antioxidant Activities of N-ferrocenylmethyl-2- and -3-nitroaniline and Determination of their Binding Parameters with Superoxide Anion Radicals, Curr. Pharm. Anal. 13 (2017) 110–116. https://doi.org/10.2174/1573412912666160831145524.

[13] C. Ornelas, Application of ferrocene and its derivatives in cancer research, New J. Chem. 35 (2011) 1973. https://doi.org/10.1039/c1nj20172g.

[14] M. Patra, G. Gasser, N. Metzler-Nolte, Small organometallic compounds as antibacterial agents, Dalt. Trans. 41 (2012) 6350. https://doi.org/10.1039/c2dt12460b.

[15] C. Biot, G. Glorian, L.A. Maciejewski, J.S. Brocard, O. Domarle, G. Blampain, P. Millet, A.J. Georges, H. Abessolo, D. Dive, Synthesis and antimalarial activity in vitro and in vivo of a new ferrocene− chloroquine analogue, J. Med. Chem. 40 (1997) 3715–3718.

[16] E.G. Ferrer, A. Bosch, O. Yantorno, E.J. Baran, A spectroscopy approach for the study of the interactions of bioactive vanadium species with bovine serum albumin, Bioorg. Med. Chem. 16 (2008) 3878–3886.

[17] A.C. Fick, U.M. Reinscheid, Characterization of the binding epitope of ciprofloxacin bound to human serum albumin, J. Pharm. Biomed. Anal. 41 (2006) 1025–1028.

[18] H. Yoshitsugu, T. Fukuhara, M. Ishibashi, T. Nanbo, N. Kagi, Key fragments for identification of positional isomer pair in glucuronides from the hydroxylated metabolites of RT-3003 (Vintoperol) by liquid chromatography/electrospray ionization mass spectrometry, J. Mass Spectrom. 34 (1999) 1063–1068.

[19] T.J. KEALY, P.L. PAUSON, A New Type of Organo-Iron Compound, Nature. 168 (1951) 1039–1040. https://doi.org/10.1038/1681039b0.

[20] S.A. Miller, J.A. Tebboth, J.F. Tremaine, 114. Dicyclopentadienyliron, J. Chem. Soc. (1952) 632–635. https://doi.org/10.1039/JR9520000632.

[21] G. Wilkinson, M. Rosenblum, M.C. Whiting, R.B. Woodward, THE STRUCTURE OF IRON BIS-CYCLOPENTADIENYL, J. Am. Chem. Soc. 74 (1952) 2125–2126. https://doi.org/10.1021/ja01128a527.

[22] J.A. Page, G. Wilkinson, The Polarographic Chemistry of Ferrocene, Ruthenocene and the Metal Hydrocarbon Ions, J. Am. Chem. Soc. 74 (1952) 6149–6150. https://doi.org/10.1021/ja01143a540.

[23] E.O. Fischer, W. Pfab, Cyclopentadien-Metallkomplexe, ein neuer Typ metallorganischer Verbindungen, Zeitschrift Für Naturforsch. B. 7 (1952) 377–379. https://doi.org/10.1515/znb-1952-0701.

[24] R.B. Woodward, M. Rosenblum, M.C. Whiting, A NEW AROMATIC SYSTEM, J. Am. Chem. Soc. 74 (1952) 3458–3459. https://doi.org/10.1021/ja01133a543.

[25] F.A. Cotton, G. Wilkinson, Bioinorganic chemistry, _____. Adv. Inorg. Chem. 5th Ed. New York John Wiley Sons. (1988) 1335–1376.

[26] N. Mohammadi, A. Ganesan, C.T. Chantler, F. Wang, Differentiation of ferrocene D 5d and D 5h conformers using IR spectroscopy, J. Organomet. Chem. 713 (2012) 51–59. https://doi.org/10.1016/j.jorganchem.2012.04.009.

[27] File:Ferrocen MO-Scheme.svg - Wikimedia Commons, (n.d.). https://commons.wikimedia.org/wiki/File:Ferrocen_MO-Scheme.svg (accessed July 2, 2022).

[28] A.N. Nesmeyanov, V.A. Sazonova, V.N. Drozd, Hydroxyferrocene, Tetrahedron Lett. 1 (1959) 13–15. https://doi.org/https://doi.org/10.1016/S0040-4039(00)91032-3.

[29] G.D. Broadhead, J.M. Osgerby, P.L. Pauson, 127. Ferrocene derivatives. Part V. Ferrocenealdehyde, J. Chem. Soc. (1958) 650–656. https://doi.org/10.1039/JR9580000650.

[30] J.M. Osgerby, P.L. Pauson, 128. Ferrocene derivatives. Part VI. DL-ferrocenylalanine, J. Chem. Soc. (1958) 656–660. https://doi.org/10.1039/JR9580000656.

[31] P. Meunier, I. Ouattara, B. Gautheron, J. Tirouflet, D. Camboli, J. Besançon, Synthèe, caractérisation et propriétés cytotoxiques des premiers 'métallocénonucléosides,' Eur. J. Med. Chem. 26 (1991) 351–362. https://doi.org/https://doi.org/10.1016/0223-5234(91)90070-4.

[32] M.F.R. Fouda, M.M. Abd-Elzaher, R.A. Abdelsamaia, A.A. Labib, On the medicinal chemistry of ferrocene, Appl. Organomet. Chem. 21 (2007) 613–625.

[33] P. Köpf-Maier, H. Köpf, E.W. Neuse, Ferrocenium Salts—The First Antineoplastic Iron Compounds, Angew. Chemie Int. Ed. English. 23 (1984) 456–457. https://doi.org/10.1002/anie.198404561.

[34] C. Biot, N. François, L. Maciejewski, J. Brocard, D. Poulain, Synthesis and antifungal activity of a ferrocene–fluconazole analogue, Bioorg. Med. Chem. Lett. 10 (2000) 839–841. https://doi.org/10.1016/S0960-894X(00)00120-7.

[35] T. Itoh, S. Shirakami, N. Ishida, Y. Yamashita, T. Yoshida, H.-S. Kim, Y. Wataya, Synthesis of novel ferrocenyl sugars and their antimalarial activities, Bioorg. Med. Chem. Lett. 10 (2000) 1657–1659. https://doi.org/10.1016/S0960-894X(00)00313-9.

[36] C. Baldoli, S. Maiorana, E. Licandro, G. Zinzalla, D. Perdicchia, Synthesis of Chiral Chromium Tricarbonyl Labeled Thymine PNA Monomers via the Ugi Reaction, Org. Lett. 4 (2002) 4341–4344. https://doi.org/10.1021/ol026994a.

[37] W. Liu, Y. Tang, Y. Guo, B. Sun, H. Zhu, Y. Xiao, D. Dong, C. Yang, Synthesis, characterization and bioactivity determination of ferrocenyl urea derivatives, Appl. Organomet. Chem. 26 (2012) 189–193. https://doi.org/10.1002/aoc.2837.

[38] B.E. Maryanoff, S.L. Keeley, F.J. Persico, Replacement of aromatic or heteroaromatic groups in nonsteroidal antiinflammatory agents with the ferrocene group, J. Med. Chem. 26 (1983) 226–229. https://doi.org/10.1021/jm00356a020.

[39] D. Scutaru, L. Tătaru, I. Mazilu, E. Diaconu, T. Lixandru, C. Simionescu, Monosubstituted derivatives of ferrocene. Ferrocene-containing penicillins and cephalosporins, J. Organomet. Chem. 401 (1991) 81–85. https://doi.org/10.1016/0022-328X(91)86197-X.

[40] D. Scutaru, I. Mazilu, L. Tătaru, M. Văţă, T. Lixandru, Synthesis and characterization of some new ferrocene-containing rifamycins, J. Organomet. Chem. 406 (1991) 183–187. https://doi.org/10.1016/0022-328X(91)83185-7.

[41] H. Parveen, R.A.S. Alatawi, N.H. El Sayed, S. Hasan, S. Mukhtar, A.U. Khan, Synthesis, characterization and biological evaluation of some novel nitrogen and sulphur containing organometallic heterocycles, Arab. J. Chem. 10 (2017) 1098–1106. https://doi.org/https://doi.org/10.1016/j.arabjc.2015.05.002.

[42] D. Dive, C. Biot, Ferrocene Conjugates of Chloroquine and other Antimalarials: the Development of Ferroquine, a New Antimalarial, ChemMedChem. 3 (2008) 383–391. https://doi.org/10.1002/cmdc.200700127.

[43] G. Gasser, I. Ott, N. Metzler-Nolte, Organometallic Anticancer Compounds, J. Med. Chem. 54 (2011) 3–25. https://doi.org/10.1021/jm100020w.

[44] T. Lanez, M. Henni, Antioxidant activity and superoxide anion radical interaction with 2-(ferrocenylmethylamino) benzonitrile and 3-(ferrocenylmethylamino) benzonitrile, J. Iran. Chem. Soc. 13 (2016) 1741–1748. https://doi.org/10.1007/s13738-016-0891-1.

[45] T. Lanez, H. Hemmami, Antioxidant Activities of N-ferrocenylmethyl-2- and -3-nitroaniline and Determination of their Binding Parameters with Superoxide Anion Radicals, Curr. Pharm. Anal. 13 (2016) 110–116. https://doi.org/10.2174/1573412912666160831145524.

[46] A. Kedadra, T. Lanez, E. Lanez, H. Hemmami, M. Henni, Synthesis and antioxidant activity of six novel N-ferrocenylmethyl-N-(nitrophenyl)and-N-(cyanophenyl)-acetamides: Cyclic voltammetry and molecular docking studies, J. Electrochem. Sci. Eng. 12 (2022) 293–304. https://doi.org/10.5599/jese.1162.

[47] T. Lanez, E. Lanez, A Molecular Docking Study of N-Ferrocenylmethylnitroanilines as Potential Anticancer Drugs, Int. J. Pharmacol. Phytochem. Ethnomedicine. 2 (2016) 5–12. https://doi.org/10.18052/www.scipress.com/IJPPE.2.5.

[48] Z. Nadjiba, B. Chérifa, T. Lanez, E. Lanez, In Silico Study on N-Ferrocenylmethyl-N-Phenylpropionohydrazide and N-Ferrocenylmethyl-N-Pheylbenzohydrazide as Anticancer Drugs for Breast and Prostate Cancer, Int. J. Pharmacol. Phytochem. Ethnomedicine. 11 (2018) 17–25. https://doi.org/10.18052/www.scipress.com/ijppe.11.17.

[49] O. Bernardo, S. González-Pelayo, L.A. López, Synthesis and Applications of Ferrocene-Fused Nitrogen Heterocycles, Eur. J. Inorg. Chem. 2022 (2022) e202100911.

[50] M. Patra, G. Gasser, The medicinal chemistry of ferrocene and its derivatives, Nat. Rev. Chem. 1 (2017) 0066. https://doi.org/10.1038/s41570-017-0066.

[51] S. Peter, B.A. Aderibigbe, Ferrocene-Based Compounds with Antimalaria/Anticancer Activity, Molecules. 24 (2019) 3604. https://doi.org/10.3390/molecules24193604.

[52] D. Whitford, Proteins: Structure and Function, Wiley, 2013. https://books.google.fr/books?id=AnodNhuMAdkC.

[53] L.G. Closs, Principles of biochemistry (Fourth Edition), 1983. https://doi.org/10.1016/0016-7037(83)90289-2.

[54] J.M. Berg, J.L. Tymoczko, L. Stryer, Biochemistry, (2002).

[55] D. Voet, J.G. Voet, Biochemistry, 4-th Edition, NewYork John Wiley& SonsInc. 492 (2011).

[56] R.E. Dickerson, I. Geis, Stereo Supplement to The Structure and Action of Proteins by Richard E. Dickerson and Irving Geis: Supplement, Harper & Row, 1969.

[57] A. Lesk, Introduction to protein science: architecture, function, and genomics, Oxford university press, 2010.

[58] H.B. Lodish, A. Berk, A., Zipursky, SL, Matsudaira, P., Baltimore, D., Darnell, J, Mol. Cell Biol. (2000).

[59] J. Yan, D. Wu, P. Sun, X. Ma, L. Wang, S. Li, K. Xu, H. Li, Binding mechanism of the tyrosine-kinase inhibitor nilotinib to human serum albumin determined by 1H STD NMR, 19F NMR, and molecular modeling, J. Pharm. Biomed. Anal. 124 (2016) 1–9. https://doi.org/10.1016/j.jpba.2016.02.024.

[60] B. Meyer, T. Peters, NMR Spectroscopy Techniques for Screening and Identifying Ligand Binding to Protein Receptors., ChemInform. 34 (2003) 864–890. https://doi.org/10.1002/chin.200319274.

[61] C. Bertucci, S. Cimitan, A. Riva, P. Morazzoni, Binding studies of taxanes to human serum albumin by bioaffinity chromatography and circular dichroism, J. Pharm. Biomed. Anal. 42 (2006) 81–87. https://doi.org/10.1016/j.jpba.2005.12.002.

[62] Y. Zhang, S. Shi, X. Chen, W. Zhang, K. Huang, M. Peng, Investigation on the interaction between ilaprazole and bovine serum albumin without or with different c-ring flavonoids from the viewpoint of food-drug interference, J. Agric. Food Chem. 59 (2011) 8499–8506. https://doi.org/10.1021/jf201796x.

[63] M.L. Hall, W.L. Jorgensen, L. Whitehead, Automated ligand-and structure-based protocol for in silico prediction of human serum albumin binding, J. Chem. Inf. Model. 53 (2013) 907–922. https://doi.org/10.1021/ci3006098.

[64] Y. Yue, J. Liu, J. Fan, X. Yao, Binding studies of phloridzin with human serum albumin and its effect on the conformation of protein, J. Pharm. Biomed. Anal. 56 (2011) 336–342. https://doi.org/10.1016/j.jpba.2011.05.018.

[65] D.N. Wang, G. Kuhlbrandt, V.E. Sarabia, R.A.F. Reithmeier, Two-dimensional structure of the membrane domain of human Band 3, the anion transport protein of the erythrocyte membrane, EMBO J. 12 (1993) 2233–2239. https://doi.org/10.1002/j.1460-2075.1993.tb05876.x.

[66] D.L. Spector, Macromolecular domains within the cell nculeus, Annu. Rev. Cell Biol. 9 (1993) 265–315. https://doi.org/10.1146/annurev.cb.09.110193.001405.

[67] L.D. Dickerson, A. Sauer-Masarwa, N. Herron, C.M. Fendrick, D.H. Busch, The electron-transfer mechanism of autoxidation for hemoglobin, myoglobin, and their iron(II) cyclidene models, J. Am. Chem. Soc. 115 (1993) 3623–3626. https://doi.org/10.1021/ja00062a028.

[68] G. di Prisco, E. Cocca, S.K. Parker, H.W. Detrich, Tracking the evolutionary loss of hemoglobin expression by the white-blooded Antarctic icefishes, Gene. 295 (2002) 185–191. https://doi.org/10.1016/S0378-1119(02)00691-1.

[69] H. Michel, The mechanism of proton pumping by cytochrome c oxidase, Proc. Natl. Acad. Sci. 95 (1998) 12819–12824. https://doi.org/10.1073/pnas.95.22.12819.

[70] G.-F. Shen, T.-T. Liu, Q. Wang, M. Jiang, J.-H. Shi, Spectroscopic and molecular docking studies of binding interaction of gefitinib, lapatinib and sunitinib with bovine serum albumin (BSA), J. Photochem. Photobiol. B Biol. 153 (2015) 380–390. https://doi.org/10.1016/j.jphotobiol.2015.10.023.

[71] S. Rudra, S. Dasmandal, C. Patra, A. Kundu, A. Mahapatra, Binding affinities of Schiff base Fe(II) complex with BSA and calf-thymus DNA: Spectroscopic investigations and molecular docking analysis, Spectrochim. Acta Part A Mol. Biomol. Spectrosc. 166 (2016) 84–94. https://doi.org/10.1016/j.saa.2016.04.050.

[72] S. Ghosh, J. Dey, Interaction of bovine serum albumin with N-acyl amino acid based anionic surfactants: Effect of head-group hydrophobicity, J. Colloid Interface Sci. 458 (2015) 284–292. https://doi.org/10.1016/j.jcis.2015.07.064.

[73] G. Sudlow, D.J. Birkett, D.N. Wade, The characterization of two specific drug binding sites on human serum albumin, Mol. Pharmacol. 11 (1975) 824–832.

[74] G. Sudlow, D.J. Birkett, D.N. Wade, Further characterization of specific drug binding sites on

human serum albumin, Mol. Pharmacol. 12 (1976) 1052–1061.

[75] P.G. Squire, P. Moser, C.T. O'Konski, The Hydrodynamic Properties of Bovine Serum Albumin Monomer and Dimer, Biochemistry. 7 (1968) 4261–4272. https://doi.org/10.1021/bi00852a018.

[76] C. Tanford, Protein denaturation, Adv. Protein Chem. 23 (1968) 121–282.

[77] D.P. Cistola, D.M. Small, J.A. Hamilton, Carbon 13 NMR studies of saturated fatty acids bound to bovine serum albumin. I. The filling of individual fatty acid binding sites., J. Biol. Chem. 262 (1987) 10971–10979. https://doi.org/10.1016/s0021-9258(18)60913-5.

[78] M.L. Wagner, H.A. Scheraga, Gouy diffusion studies of bovine serum albumin, J. Phys. Chem. 60 (1956) 1066–1076. https://doi.org/10.1021/j150542a012.

[79] M.J. Hunter, A method for the determination of protein partial specific volumes 1, J. Phys. Chem. 70 (1966) 3285–3292. https://doi.org/10.1021/j100882a043.

[80] D.E. McMillan, A comparison of five methods for obtaining the intrinsic viscosity of bovine serum albumin, Biopolymers. 13 (1974) 1367–1376. https://doi.org/10.1002/bip.1974.360130708.

[81] A.K. Wright, M.R. Thompson, Hydrodynamic structure of bovine serum albumin determined by transient electric birefringence, Biophys. J. 15 (1975) 137–141. https://doi.org/10.1016/S0006-3495(75)85797-3.

[82] T. Peters Jr, Serum albumin, The Plasma Proteins,. 1 (1975) 133–181.

[83] J.F. FOSTER, Chapter 6 - Plasma Albumin, in: F.W.B.T.-T.P.P. PUTNAM (Ed.), Academic Press, 1960: pp. 179–239. https://doi.org/https://doi.org/10.1016/B978-1-4832-2810-5.50013-X.

[84] E.J. Cohn, W.L. Hughes, J.H. Weare, Preparation and Properties of Serum and Plasma Proteins. XIII. Crystallization of Serum Albumins from Ethanol-Water Mixtures, J. Am. Chem. Soc. 69 (1947) 1753–1761. https://doi.org/10.1021/ja01199a051.

[85] J.K.F. Noel, M.J. Hunter, Bovine Mercaptalbumin and Non-mercaptalbumin Monomers: INTERCONVERSIONS AND STRUCTURAL DIFFERENCES, J. Biol. Chem. 247 (1972) 7391–7406. https://doi.org/10.1016/S0021-9258(19)44641-3.

[86] M. Sogami, J.F. Foster, Isomerization reactions of charcoal-defatted bovine plasma albumin. The N-F transition and acid expansion, Biochemistry. 7 (1968) 2172–2182. https://doi.org/10.1021/bi00846a020.

[87] J. Emsley, Very strong hydrogen bonding, Chem. Soc. Rev. 9 (1980) 91–124. https://doi.org/10.1039/CS9800900091.

[88] P.A. Giguere, Comment on the strongest type of hydrogen bond, Chem. Phys. Lett. 80 (1981) 207–209. https://doi.org/10.1016/0009-2614(81)80091-7.

[89] J. Stuart, B. Wyithe, A. Loeb, Magnification of light from many distant quasars by gravitational lenses, Nature. 417 (2002) 923–925. https://doi.org/10.1038/nature00794.

[90] G. Graziano, G. Barone, Group additivity analysis of the heat capacity changes associated with the dissolution into water of different organic compounds, J. Am. Chem. Soc. 118

(1996) 1831–1835. https://doi.org/10.1021/ja9521942.

[91] A. Ben-Naim, Statistical mechanical study of hydrophobie interaction. i. interaction between two identical nonpolar solute particles, J. Chem. Phys. 54 (1971) 1387–1404. https://doi.org/10.1063/1.1674979.

[92] W. Kauzmann, Some Factors in the Interpretation of Protein Denaturation, Adv. Protein Chem. 14 (1959) 1–63. https://doi.org/10.1016/S0065-3233(08)60608-7.

[93] C. Tanford, The Hydrophobic Effect: Formation of Micelles and Biological Membranes, Charles Tanford, Wiley-Interscience, New York, 1980, 233 pp. Price: $18.50., J. Polym. Sci. Polym. Lett. Ed. 18 (1980) 1980.

[94] C.N. Pace, B.A. Shirley, M. McNutt, K. Gajiwala, Forces contributing proteins of, Faseb J. 10 (1996) 75–83.

[95] N. Shahabadi, A. Khorshidi, N.H. Moghadam, Study on the interaction of the epilepsy drug, zonisamide with human serum albumin (HSA) by spectroscopic and molecular docking techniques, Spectrochim. Acta - Part A Mol. Biomol. Spectrosc. 114 (2013) 627–632. https://doi.org/10.1016/j.saa.2013.05.092.

[96] N. Seedher, S. Bhatia, Interaction of Non-Steroidal Anti-Inflammatory Drugs, Etoricoxib and Parecoxib Sodium, with Human Serum Albumin Studied by Fluorescence Spectroscopy, Drug Metabol. Drug Interact. 22 (2006) 25–46. https://doi.org/10.1515/DMDI.2006.22.1.25.

[97] S. Yasmeen, Riyazuddeen, G. Rabbani, Calorimetric and spectroscopic binding studies of amoxicillin with human serum albumin, J. Therm. Anal. Calorim. 127 (2017) 1445–1455. https://doi.org/10.1007/s10973-016-5555-y.

[98] R. Liu, R. Pidikiti, C.E. Ha, C.E. Petersen, N. V. Bhagavan, R.G. Eckenhoff, The role of electrostatic interactions in human serum albumin binding and stabilization by halothane, J. Biol. Chem. 277 (2002) 36373–36379. https://doi.org/10.1074/jbc.M205479200.

[99] T.E. Creighton, 3.2. Evolutionary Divergence of Proteins, Proteins Struct. Mol. Prop. 2nd Ed., WH Free. Co., New York, NY. (1993) 108–114.

[100] E. Maltas, Binding interactions of niclosamide with serum proteins, J. Food Drug Anal. 22 (2014) 549–555. https://doi.org/10.1016/j.jfda.2014.03.004.

[101] Y.Z. Zhang, B. Zhou, X.P. Zhang, P. Huang, C.H. Li, Y. Liu, Interaction of malachite green with bovine serum albumin: Determination of the binding mechanism and binding site by spectroscopic methods, J. Hazard. Mater. 163 (2009) 1345–1352. https://doi.org/10.1016/j.jhazmat.2008.07.132.

[102] L.M. Salonen, M. Ellermann, F. Diederich, Aromatic rings in chemical and biological recognition: Energetics and structures, Angew. Chemie - Int. Ed. 50 (2011) 4808–4842. https://doi.org/10.1002/anie.201007560.

[103] G.B. Mcgaughey, M. Gagné, A.K. Rappé, G.B. Mcgaughey, M. Gagne, A.K. Rappe, PROTEIN CHEMISTRY AND STRUCTURE : π -Stacking Interactions : ALIVE AND WELL IN PROTEINS, (1998) 1–7. https://doi.org/10.1074/jbc.273.25.15458.

[104] S.A. Hudson, H. Ecroyd, F.C. Dehle, I.F. Musgrave, J.A. Carver, (-)-Epigallocatechin-3-Gallate (EGCG) Maintains κ-Casein in Its Pre-Fibrillar State without Redirecting Its Aggregation Pathway, J. Mol. Biol. 392 (2009) 689–700.

https://doi.org/10.1016/j.jmb.2009.07.031.

[105] Y. Porat, A. Abramowitz, E. Gazit, Inhibition of amyloid fibril formation by polyphenols: Structural similarity and aromatic interactions as a common inhibition mechanism, Chem. Biol. Drug Des. 67 (2006) 27–37. https://doi.org/10.1111/j.1747-0285.2005.00318.x.

[106] D.D. Boehr, A.R. Farley, G.D. Wright, J.R. Cox, Analysis of the π-π stacking interactions between the aminoglycoside antibiotic kinase APH(3′)-IIIa and its nucleotide ligands, Chem. Biol. 9 (2002) 1209–1217. https://doi.org/10.1016/S1074-5521(02)00245-4.

[107] J.P. Gallivan, D.A. Dougherty, Cation-π interactions in structural biology, Proc. Natl. Acad. Sci. 96 (1999) 9459 LP – 9464. https://doi.org/10.1073/pnas.96.17.9459.

[108] E. V. Pletneva, A.T. Laederach, D.B. Fulton, N.M. Kostić, The role of cation-π interactions in biomolecular association. Design of peptides favoring interactions between cationic and aromatic amino acid side chains, J. Am. Chem. Soc. 123 (2001) 6232–6245. https://doi.org/10.1021/ja010401u.

[109] M. Nys, D. Kesters, C. Ulens, Structural insights into Cys-loop receptor function and ligand recognition, Biochem. Pharmacol. 86 (2013) 1042–1053. https://doi.org/10.1016/j.bcp.2013.07.001.

[110] V.P. Santarelli, A.L. Eastwood, D.A. Dougherty, C.A. Ahern, R. Horn, Calcium block of single sodium channels: Role of a pore-lining aromatic residue, Biophys. J. 93 (2007) 2341–2349. https://doi.org/10.1529/biophysj.107.106856.

[111] J. Heinze, Cyclic voltammetry—"electrochemical spectroscopy". New analytical methods (25), Angew. Chemie Int. Ed. English. 23 (1984) 831–847.

[112] A. Ševčík, Oscillographic polarography with periodical triangular voltage, Collect. Czechoslov. Chem. Commun. 13 (1948) 349–377.

[113] J.E.B. Randles, A cathode ray polarograph, Trans. Faraday Soc. 44 (1948) 322–327. https://doi.org/10.1039/TF9484400322.

[114] R.S. Nicholson, Theory and application of cyclic voltammetry for measurement of electrode reaction kinetics., Anal. Chem. 37 (1965) 1351–1355.

[115] A.J. Bard, L.R. Faulkner, Fundamentals and applications, Wiley New York, 2001.

[116] S. Chatterji, On the applicability of Fick's second law to chloride ion migration through portland cement concrete, Cem. Concr. Res. 25 (1995) 299–303. https://doi.org/10.1016/0008-8846(95)00013-5.

[117] R.G. Ehl, A.J. Ihde, Faraday's electrochemical laws and the determination of equivalent weights, J. Chem. Educ. 31 (1954) 226. https://doi.org/10.1021/ed031p226.

[118] H.S. Lim, D.J. Barclay, F.C. Anson, Formal potentials and cyclic voltammetry of some ruthenium-ammine complexes, Inorg. Chem. 11 (1972) 1460–1466. https://doi.org/10.1021/ic50113a003.

[119] Y. Xiao, G. Han, Y. Li, M. Li, J.-Y. Lin, Three-dimensional hollow platinum–nickel bimetallic nanoframes for use in dye-sensitized solar cells, J. Power Sources. 278 (2015) 149–155. https://doi.org/10.1016/j.jpowsour.2014.12.068.

[120] A.R. Tigor, N. Sakiynah, H. Setyawan, A versatile electrochemical method to produce nanoparticles of manganese oxides by KMnO4 electrolysis, in: World J. Chem. Educ, 2014: pp. 124–126. https://doi.org/10.1063/1.4866744.

[121] W.H. Reinmuth, Electrochemical relaxation techniques, Anal. Chem. 40 (1968) 185–194.

[122] C.Q. Xiao, F.L. Jiang, B. Zhou, R. Li, Y. Liu, Interaction between a cationic porphyrin and bovine serum albumin studied by surface plasmon resonance, fluorescence spectroscopy and cyclic voltammetry, Photochem. Photobiol. Sci. 10 (2011) 1110–1117. https://doi.org/10.1039/c1pp05008g.

[123] L. Fotouhi, S. Banafsheh, M.M. Heravi, Electrochemistry of the interaction of furazolidone and bovine serum albumin, Bioelectrochemistry. 77 (2009) 26–30. https://doi.org/10.1016/j.bioelechem.2009.05.011.

[124] F. Xue, C.-Z. Xie, Y.-W. Zhang, Z. Qiao, X. Qiao, J.-Y. Xu, S.-P. Yan, Two new dicopper(II) complexes with oxamido-bridged ligand: Synthesis, crystal structures, DNA binding/cleavage and BSA binding activity, J. Inorg. Biochem. 115 (2012) 78–86. https://doi.org/10.1016/j.jinorgbio.2012.05.018.

[125] P. Krishnamoorthy, P. Sathyadevi, A.H. Cowley, R.R. Butorac, N. Dharmaraj, Evaluation of DNA binding, DNA cleavage, protein binding and in vitro cytotoxic activities of bivalent transition metal hydrazone complexes, Eur. J. Med. Chem. 46 (2011) 3376–3387. https://doi.org/10.1016/j.ejmech.2011.05.001.

[126] P.W. Atkins De Paula, Julio., Atkins' Physical chemistry, Oxford University Press, Oxford; New York, 2006.

[127] H.A. Benesi, J.H. Hildebrand, A Spectrophotometric Investigation of the Interaction of Iodine with Aromatic Hydrocarbons, J. Am. Chem. Soc. 71 (1949) 2703–2707. https://doi.org/10.1021/ja01176a030.

[128] J. Zhang, H. Yang, D. Li, J. Dou, Copper(II) Complexes Based on Aminohydroxamic Acids: Synthesis, Structures, In Vitro Cytotoxicities and DNA/BSA Interactions, Crystals. 8 (2018) 201. https://doi.org/10.3390/cryst8050201.

[129] P. Khanvilkar, R. Pulipaka, K. Shirsath, R. Devkar, D. Chakraborty, Organometallic binuclear Ru(II) complexes: Design, synthesis, DNA/BSA binding interactions and in-vitro cytotoxicity against HeLa cell line, Inorg. Chem. Commun. 102 (2019) 134–140. https://doi.org/10.1016/j.inoche.2019.02.023.

[130] R.S. Mulliken, The interaction of electron donors and acceptors, J. Chim. Phys. 61 (1964) 20–38. https://doi.org/10.1051/jcp/1964610020.

[131] E. Thiriot, Modélisation de la reconnaissance et de la catalyse enzymatiques: Développements méthodologiques et détermination du mécanisme des Métionine Sulfoxyde Réductases de classe A, Université Henri Poincaré-Nancy 1, 2009.

[132] S.F. Sousa, P.A. Fernandes, M.J. Ramos, Protein-ligand docking: Current status and future challenges, Proteins Struct. Funct. Bioinforma. 65 (2006) 15–26. https://doi.org/10.1002/prot.21082.

[133] A. Hernández-Santoyo, A.Y. Tenorio-Barajas, V. Altuzar, H. Vivanco-Cid, C. Mendoza-Barrera, Protein-protein and protein-ligand docking, IntechOpen: London, UK, 2013.

[134] S. Grosdidier, J. Fernández-Recio, Docking and scoring: applications to drug discovery in the interactomics era, Expert Opin. Drug Discov. 4 (2009) 673–686. https://doi.org/10.1517/17460440903002067.

[135] D.B. Kitchen, H. Decornez, J.R. Furr, J. Bajorath, Docking and scoring in virtual screening for drug discovery: methods and applications, Nat. Rev. Drug Discov. 3 (2004) 935–949.

[136] I.D. Kuntz, J.M. Blaney, S.J. Oatley, R. Langridge, T.E. Ferrin, A geometric approach to macromolecule-ligand interactions, J. Mol. Biol. 161 (1982) 269–288. https://doi.org/10.1016/0022-2836(82)90153-X.

[137] D.S. Goodsell, A.J. Olson, Automated docking of substrates to proteins by simulated annealing, Proteins Struct. Funct. Genet. 8 (1990) 195–202. https://doi.org/10.1002/prot.340080302.

[138] V. Patel, J. Shah, A.K. Gupta, Design and In-silico study of bioimaging fluorescence Graphene quantum dot-Bovine serum albumin complex synthesized by diimide-activated amidation, Comput. Biol. Chem. 93 (2021) 107543. https://doi.org/10.1016/j.compbiolchem.2021.107543.

[139] Y. Lv, Q. Liang, Y. Li, X. Liu, D. Zhang, X. Li, Study of the binding mechanism between hydroxytyrosol and bovine serum albumin using multispectral and molecular docking, Food Hydrocoll. 122 (2022) 107072. https://doi.org/10.1016/j.foodhyd.2021.107072.

[140] W.L. DeLano, The PyMOL molecular graphics system, Http//Www. Pymol. Org. (2002).

[141] L. Jendele, R. Krivak, P. Skoda, M. Novotny, D. Hoksza, PrankWeb: a web server for ligand binding site prediction and visualization, Nucleic Acids Res. 47 (2019) W345–W349. https://doi.org/10.1093/nar/gkz424.

[142] L. Jendele, R. Krivak, P. Skoda, M. Novotny, D. Hoksza, Supplementary material for PrankWeb: web server for ligand binding site prediction and visualization, Proteins. 420 (n.d.) 4009.

[143] O. Rahim, A. Khelef, B. Terki, M.S. Mahboub, T. Lanez, N -Ferrocenylmethyl-2-nitroaniline, Acta Crystallogr. Sect. E Struct. Reports Online. 68 (2012) m1318–m1318. https://doi.org/10.1107/S1600536812039177.

[144] C. Boubekri, A. Khelef, B. Terki, T. Lanez, Synthesis and Electrochemical Properties of N-(Ferrocenylmethyl)Aminobenzonitrile and N-(Ferrocenylmethyl)Nitroaniline Derivatives, Int. Lett. Chem. Phys. Astron. 49 (2015) 27–34. https://doi.org/10.18052/www.scipress.com/ILCPA.49.27.

[145] S.M. Batterjee, M.I. Marzouk, M.E. Aazab, M.A. El-Hashash, The electrochemistry of some ferrocene derivatives: Redox potential and substituent effects, Appl. Organomet. Chem. 17 (2003) 291–297. https://doi.org/10.1002/aoc.414.

[146] R.R. Gagne, C.A. Koval, G.C. Lisensky, Ferrocene as an Internal Standard for Electrochemical Measurements, Inorg. Chem. 19 (1980) 2854–2855. https://doi.org/10.1021/ic50211a080.

[147] D. Li, T. Zhang, C. Xu, B. Ji, Effect of pH on the interaction of vitamin B12 with bovine serum albumin by spectroscopic approaches, Spectrochim. Acta Part A Mol. Biomol. Spectrosc. 83 (2011) 598–608. https://doi.org/10.1016/j.saa.2011.09.012.

[148] A. Khennoufa, L. Bechki, T. Lanez, E. Lanez, N. Zegheb, Spectrophotometric, voltammetric and molecular docking studies of binding interaction of N-ferrocenylmethylnitroanilines with bovine serum albumin, J. Mol. Struct. 1224 (2021). https://doi.org/10.1016/j.molstruc.2020.129052.

[149] H. Benamara, T. Lanez, E. Lanez, BSA-binding studies of 2- and 4-ferrocenylbenzonitrile: voltammetric, spectroscopic and molecular docking investigations, J. Electrochem. Sci. Eng. 10 (2020) 335–346. https://doi.org/10.5599/jese.861.

[150] J.-B.M. Leuna, S.K. Sop, S. Makota, E. Njanja, T.C. Ebelle, A.G. Azebaze, E. Ngameni, A. Nassi, Voltammetric behavior of Mammeisin (MA) at a glassy carbon electrode and its interaction with Bovine Serum Albumin (BSA), Bioelectrochemistry. 119 (2018) 20–25. https://doi.org/10.1016/j.bioelechem.2017.08.008.

[151] S. Hashemnia, F. Khajavi Fard, Z. Mokhtari, A study of the interactions between ephedrine and human serum albumin based on spectroscopic, electrochemical and docking assessments, J. Mol. Liq. 348 (2022) 118058. https://doi.org/10.1016/j.molliq.2021.118058.

[152] X. Chu, G.L. Shen, J.H. Jiang, T.F. Kang, B. Xiong, R.Q. Yu, Voltammetric studies of the interaction of daunomycin anticancer drug with DNA and analytical applications, Anal. Chim. Acta. 373 (1998) 29–38. https://doi.org/10.1016/S0003-2670(98)00362-6.

[153] M. Aslanoglu, G. Ayne, Voltammetric studies of the interaction of quinacrine with DNA, Anal. Bioanal. Chem. 380 (2004) 658–663. https://doi.org/10.1007/s00216-004-2797-5.

[154] G. Richer, C. Sandorfy, The far-ultraviolet absorption spectra of ferrocene, cobaltocene, and nickelocene, J. Mol. Struct. THEOCHEM. 123 (1985) 317–327. https://doi.org/10.1016/0166-1280(85)80174-3.

[155] K.A. Majorek, P.J. Porebski, A. Dayal, M.D. Zimmerman, K. Jablonska, A.J. Stewart, M. Chruszcz, W. Minor, Structural and immunologic characterization of bovine, horse, and rabbit serum albumins, Mol. Immunol. 52 (2012) 174–182. https://doi.org/10.1016/j.molimm.2012.05.011.

[156] Z. Tian, L. Tian, M. Shi, S. Zhao, S. Guo, W. Luo, C. Wang, Z. Tian, Investigation of the interaction of a polyamine-modified flavonoid with bovine serum albumin (BSA) by spectroscopic methods and molecular simulation, J. Photochem. Photobiol. B Biol. 209 (2020) 111917. https://doi.org/10.1016/j.jphotobiol.2020.111917.

[157] R.N. El Gammal, H. Elmansi, A.A. El-Emam, F. Belal, M.E.A. Hammouda, Exploring the molecular interaction of mebendazole with bovine serum albumin using multi-spectroscopic approaches and molecular docking, Sci. Rep. 12 (2022) 11582. https://doi.org/10.1038/s41598-022-15696-4.

[158] Y.-J. Hu, Y. Liu, J.-B. Wang, X.-H. Xiao, S.-S. Qu, Study of the interaction between monoammonium glycyrrhizinate and bovine serum albumin, J. Pharm. Biomed. Anal. 36 (2004) 915–919.

[159] F. Korkmaz, D.A. Erdogan, Ş. Özalp-Yaman, Interaction of a novel platinum drug with bovine serum albumin: FTIR and UV-Vis spectroscopy analysis, New J. Chem. 39 (2015) 5676–5685. https://doi.org/10.1039/C5NJ00785B.

[160] A.K. Parpart, P.B. Lorenz, E.R. Parpart, J.R. Gregg, A.M. Chase, The osmotic resistance (fragility) of human red cells, J. Clin. Invest. 26 (1947) 636–640.

[161] Buffy Coat- Definition, Preparation, Uses - Microbe Notes, (n.d.). https://microbenotes.com/buffy-coat/ (accessed April 25, 2022).

[162] N. Maurya, J.K. Maurya, M. Kumari, A.B. Khan, R. Dohare, R. Patel, Hydrogen bonding-assisted interaction between amitriptyline hydrochloride and hemoglobin: spectroscopic and molecular dynamics studies, J. Biomol. Struct. Dyn. 35 (2017) 1367–1380. https://doi.org/10.1080/07391102.2016.1184184.

[163] F. Ding, B.-Y. Han, W. Liu, L. Zhang, Y. Sun, Interaction of Imidacloprid with Hemoglobin by Fluorescence and Circular Dichroism, J. Fluoresc. 20 (2010) 753–762. https://doi.org/10.1007/s10895-010-0618-0.

[164] Z. Chi, R. Liu, B. Yang, H. Zhang, Toxic interaction mechanism between oxytetracycline and bovine hemoglobin, J. Hazard. Mater. 180 (2010) 741–747. https://doi.org/10.1016/j.jhazmat.2010.04.110.

[165] M. Bhattacharyya, U. Chaudhuri, R.K. Poddar, Studies on the interaction of chlorpromazine with haemoglobin, Int. J. Biol. Macromol. 12 (1990) 297–301. https://doi.org/10.1016/0141-8130(90)90017-5.

[166] B.L.M. de Assis, A.D. Groto, V.H.S. da Mota, G.C. Peiter, K.N. Teixeira, Drug-protein in vitro and in silico interaction analysis with hemoglobin as a study model, (n.d.). https://doi.org/11606.

[167] E. Lanez, L. Bechki, T. Lanez, Antioxidant Activities, Binding Parameters, and Electrochemical Behavior of Superoxide Anion Radicals Twords 1-Ferrocenylmethylthymine and 1-Ferrocenylmethylcytosine, Curr. Phys. Chem. 10 (2020) 10–22. https://doi.org/10.2174/1877946809666190424143752.

[168] T. Lanez, H. Ben Amara, A. Adaika, E. Lanez, A. Khennoufa, N. Zegheb, IN VITRO AND IN SILICO ANTIOXYDANT ACTIVITY, TOXICITY PREDICTION, AND MOLECULAR DOCKING STUDY OF 3-AND 3, 3'-NITROPHENYLFERROCENE AND THEIR REDUCED AMINES, J. Fundam. Appl. Sci. 14 (2022) 417–430.

[169] N. Thuaud, B. Sebille, M.H. Livertoux, J. Bessiere, Determination of diazepam—human serum albumin binding by polarography and high-performance liquid chromatography at different protein concentrations, J. Chromatogr. A. 282 (1983) 509–518. https://doi.org/10.1016/S0021-9673(00)91628-5.

[170] G.-C. Zhao, J.-J. Zhu, J.-J. Zhang, H.-Y. Chen, Voltammetric studies of the interaction of methylene blue with DNA by means of β-cyclodextrin, Anal. Chim. Acta. 394 (1999) 337–344. https://doi.org/10.1016/S0003-2670(99)00292-5.

[171] C. Brett, A.M. Oliveira Brett, Electrochemistry: principles, methods, and applications, 1993.

[172] R.P. Rastogi, S.P. Singh, D.-P. Häder, R.P. Sinha, Detection of reactive oxygen species (ROS) by the oxidant-sensing probe 2′,7′-dichlorodihydrofluorescein diacetate in the cyanobacterium Anabaena variabilis PCC 7937, Biochem. Biophys. Res. Commun. 397 (2010) 603–607. https://doi.org/10.1016/j.bbrc.2010.06.006.

[173] M. Ozsoz, A. Erdem, P. Kara, K. Kerman, D. Ozkan, Electrochemical Biosensor for the Detection of Interaction Between Arsenic Trioxide and DNA Based on Guanine Signal, Electroanalysis. 15 (2003) 613–619. https://doi.org/10.1002/elan.200390077.

Publication